Development of an Annular Array Through-Transmission System for Non-Contact Inspection Applications

JIE GAO

Submitted in November 2018

For the degree of Doctor of Philosophy

Centre for Ultrasonic Engineering

Department of Electronic and Electrical Engineering

University of Strathclyde

The copyright of this Thesis belongs to the author under the terms of the United Kingdom Copyright Acts as qualified by University of Strathclyde Regulation 3.51. Due acknowledgements must always be made of the use of any material contained in, or derived from, this Thesis.

Content

Acknowledgements

Firstly, I would like to express my thanks to my supervisor Professor Anthony Gachagan for the assistance, encouragement, patience and time during the whole PhD research. The fact that he gave me the chance to do this work in the first place is also greatly appreciated.

There are several other people that I also wish to thank in the Centre for Ultrasonic Engineering (CUE) especially, Jerzy Dziewierz, Charles MacLeod, Richard O'Leary and the others for their support. Technical assistance has been an important part of this research and big thanks must go to all those involved, Tommy McCunnie, Walter Galbraith, Grant Smillie and the Engineering workshop staffs for their manufacturing skill and expertise in manufacturing the transducers.

I would like to thank my mum and dad, for their patience, encouragement, support and love during my stay in Glasgow. And I would like to thank my cousin who takes care of my dad when he is in surgery.

I also want to thank my friends in Glasgow for sharing happiness and distress. I cannot imagine my life without their help and support. I would finally like to extend a special thanks to my boyfriend, Fangzhou Xu, for his help and pressure relief throughout the work of this Thesis.

Abstract

Ultrasound has found application in many different sectors, including inspection in the aerospace industry to investigate component structural integrity. In many cases, a liquid coupling medium is used to efficiently transfer energy between the transducer and the sample under investigation. There are some materials which are not suitable for liquid coupling, either through material properties or the complexity of the surface geometry. The alternative of using an air-coupled approach is inherently challenging due to a large acoustic impedance mismatch between the transducer and air, resulting in low system signal-to-noise ratio (SNR). This Thesis will consider an air-coupled inspection system, using an annular array and efficient matching layer combination.

The matching layer is an important key transducer component to bridge the acoustic impedance mismatch between the transducer and the load medium. For air-coupled piezoelectric devices this is a critical factor in the transducer design. This work has concentrated on improving the manufacture methodology for an existing hybrid matching layer design, comprising membrane filter and silicone rubber. The key issue is to ensure repeatability of the fabrication process and reliability in the operating behaviour. Moreover, the developed approach has reduced the manufacture time for these layers and offers an opportunity for volume manufacture.

A segmented annular array system has been designed for non-contact inspection applications, which provides control of the depth focussing within the sample coupled with a degree of beam steering off the central axis. A pitch-catch transducer system has been implemented, with the operating frequency of the transmitter and receiver matched to improve system SNR. Full characterisation of both arrays has been performed, with good correlation between theory and experiment. Unfortunately, the fabricated array devices only provided beam steering capability on-axis, but when combined with the matching layer designs, were able to be evaluated on fibre-reinforce composite and honeycomb samples. Assessment of the inspection capability of the developed array system was undertaken through manual scans of sandwich composite structures. Reasonable quality images have been acquired which indicate surface damage and impact damage within several samples, with the results correlating well with corresponding Scanning Acoustic Microscope measurements.

List of Figures

List of Tables

List of symbols

Symbol	*Definition*	*Unit*
N_0	Near-far field boundary	Meter
R_p	Reflection coefficient	
T_p	Transmission coefficient	
d_n	Travelled distance in air for n^{th} element	Meter
k_t	Electromechanical coupling co-efficient	
t_n	Focal law time delay for n^{th} element	Second
γ_0	Angle of divergence of the sound energy	Degree
ε_r	Dielectric constant	
h	Membrane filter thickness	Meter
α	Attenuation coefficient	dB/m
A	Signal amplitude	Volt
D	Diameter of the transducers	Meter
F	Lens radius	Meter
L	Distance in air path	Meter
P	Atmospheric pressure	N/m^2
T	Temperature	Kelvin
Z	Acoustic impedance	Rayl
c	Velocity	m/s
f	Frequency	Hertz
m	Silicone rubber's mass	kg
λ	Wavelength	Meter

CHAPTER 1 Introduction

1.1 Project Context

Non-destructive evaluation (NDE) methods are used in a variety of applications and plays an essential role nowadays in the quality control for materials, structures and can be used for defect testing, manufacturing process improvement, cost saving and safety improvements [1, 2]. There are many techniques available to achieve these goals, such as ultrasound, microwave, infrared, laser, X-ray and electromagnetic techniques [3]. Compared with other approaches, ultrasound has the following advantages: (a) broad application range; (b) reasonable cost; (c) high flexibility. Ultrasound has a good ability to operate through liquid and solid media, and can provide information on both surface and subsurface features [4].

A good transducer is the core component in an ultrasonic testing system. Based on the load medium properties, the ultrasonic transducer is divided into three groups: designed for operation into solid, liquid or gas media. Interestingly, for most applications coupling into a solid material, a liquid coupling material is required between the transducer and the sample surface. In certain conditions, liquid coupling is not permitted or advisable, such as testing certain aerospace materials, paper, wood, art objects and precision electrical instrumentation, because the inspection through the use of a liquid coupling interface may cause permanent damage to the material under test. In such cases, an air-coupled transducer system would be the preferred option and would have a large range of potential applications.

An air-coupled transducer is a type of sensor which uses gas (typically air) as the coupling medium. The past two decades has seen a large increase in research on air-coupled transducer technologies and such designs offer great potential in certain NDE inspection applications through reducing the difficulty of operation by having a completely non-contact transduction system. The air medium can also offer more efficient set up procedure especially for inspecting complex shaped components and large specimens. These advantages have led to the development of a number of commercial air-coupled systems, although these are not used in typical industrial inspection scenarios.

Importantly, the significant challenge for piezoelectric based non-contact transducer inspection systems is the large acoustic impedance mismatch at all solid/gas interfaces. When this is combined with the power loss due to airborne attenuation, it is clearly evident that design of such a system requires careful consideration. To tackle these issues, this Thesis focusses on improving the system-to-noise (SNR) of the inspection system by applying ultrasonic array technology, coupled with high efficiency matching layer technology. Importantly, the application of an annular array configuration should provide a highly focussed, controllable inspection approach to improve the efficiency of non-contact NDE. Figure 1-1 shows the air-coupled ultrasonic through transmission system.

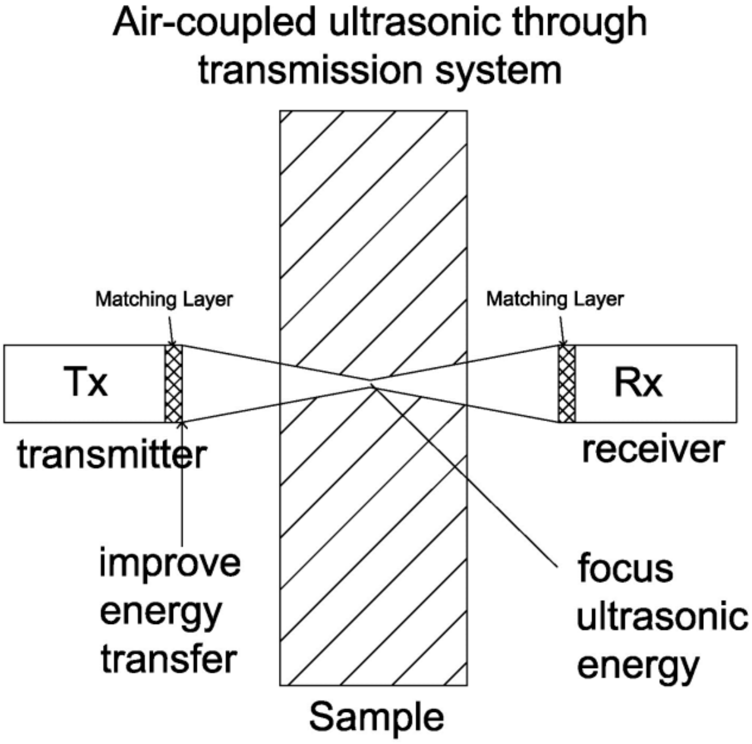

Figure 1-1 Air-coupled ultrasonic through transmission system

1.2 Overview of Thesis

Chapter 2: Review and Applications of Air-Coupled Transducers

This Chapter introduces the fundamental properties of air-coupled ultrasonic systems and discusses the challenging requirements for an inspection system operating in an air medium. In the air-coupled environment, different transducer technologies are used in different applications, including piezoceramic, piezopolymer, piezocomposite and single crystal transducers. The main technologies contributing to an air-coupled non-destructive evaluation (NDE) array scanning system are introduced. Moreover, the key technologies utilised in this Thesis, namely matching layer design and array transducer design, are described in detail. The two commercial phased array controllers used to acquire the results presented in this Thesis are introduced at the end of this Chapter.

Chapter 3: A Robust and Reliable Fabrication Process for Air-Coupled Matching Layers

It was accepted that in order to develop an efficient air-coupled system, it would be necessary to develop a suitable matching layer to improve the energy coupling between the transducers and the air medium. This Chapter explores the fabrication process for a multi-layered matching layer, which is a combination of silicone rubber and a membrane filter. An update to the traditional manufacturing method and a new manufacturing method are introduced in detail and a variety of influencing factors discussed. A series of comparisons are used to compare the matching layers' performance when fabricated using different fabrication processes. Consequently, a more reliable manufacture method is introduced with the following improvements: significantly shortening fabrication time; providing better manufacturing success rate; is easier to handle; and capable of delivering similar performance compared to the traditional method. The matching layers' performances in through transmission mode of operation are demonstrated to provide approximately 36 dB improvement in received signal magnitude.

Chapter 4: Characterisation of Air-Coupled Transducers and Annular Array Design

In this Chapter, the design and fabrication process for two air-coupled annular array transducers are introduced. Air-coupled transducers, incorporating the 1-3 connectivity piezocomposite configuration, are employed in a through transmission system. Two annular arrays are designed to be 1.5-D arrays and the manufacturing process is detailed to provide evidence of a robust procedure. To ensure the validity in the fabrication process, the transducer characteristics at every stage in the process has been tested and compared to modelled results. An unusual phenomenon happened when the piezocomposites were connected to the Hypertronics connector using 3 m long micro-coax cable. The fundamental operating frequency shifted due to the cable's capacitance and a pre-amplifier stage was introduced to remedy the frequency shift problem. Importantly, the pre-amplifier also provides better power efficiency and a reduction in system noise to produce a good system SNR. For the specified focusing distance for the array, a table of focal time delays was calculated and tested. Overall, good correlation between theory and experimental results were obtained.

Chapter 5: Array System Experimental Evaluation

In this Chapter, the experimental set up and results from the 1.5-D annular array are presented. The FlawInspecta phased array controller (Diagnostic Sonar Ltd, Livingstone, UK) was used to drive the transducer with a tone burst sine wave excitation function, which can offer more power to drive the transducer. Importantly, this phased array controller (PAC) software has no individual focal law module which can meet the requirements for applying the focal law to annular array transducers directly. Hence, for the transmitter, a time delay table has been produced by MATLAB and applied to the control software, and for the receiver, a superposition has been calculated in MATLAB after the receiver acquires the signals. A number of experimental results are presented. The air-coupled annular array transducer configuration resolution is tested by using an aluminium plate with through thickness holes, and the focal law applied in this experiment obtained a satisfactory resolution, down to approximately 2 mm. Next, a sandwich structure honeycomb material with known defects has been scanned and the results are extremely encouraging. Finally, a carbon fibre reinforced polymer (CFRP) material was tested and was shown to have a relatively weak SNR, although it is still possible to identify defects in the images.

Chapter 6: Matching Layer Performance in Pulse-Echo Configuration

In this Chapter, the matching layer system performance in a pulse-echo configuration was simulated and compared to experiment results. For this work, a single crystal transducer design has been used, as this should demonstrate superior performance in terms of sensitivity and bandwidth than the traditional piezocomposite approach. For pulse-echo operation, a series of investigations were completed to find the most suitable matching layer combination to maximise the received amplitude. Consequently, the matching layer, which again is a combination of silicone rubber and membrane filter, performs well in terms of amplitude improvement in both pulse-echo mode and pitch-catch mode system.

Chapter 7: Conclusions and Suggestions for Future Work

The conclusions Chapter presents a brief review for each Chapter and a general synopsis of the major results of the work will be presented. Although every attempt has been made to cover the aspects of the work presented in this Thesis as fully as possible, there are certain cases where further work would be of benefit and suggestions of where this work could be most useful directed are made within this Chapter.

1.3 Aims and Outputs of the Thesis

1.3.1 Aims of the Thesis

The key objectives of this Thesis were:

- Provide fundamental information on applications of a range of air-coupled transducers, matching layers and key technologies utilised in this Thesis, to provide the framework for the research on an array based air-coupled scanning system.

- To improve the manufacturing reliability for air-coupled matching layers, designed for piezocomposite configurations, and develop a new manufacturing approach to reduce the fabrication time, improve performance, fabricate more reliable matching layer structures and offer ability for volume manufacturing in industry requirements.

- To determine a suitable transducer technology for use within an air-coupled through transmission scanning system and evaluate on industrial samples.

- To investigate a suitable matching layer approach to apply to transducers developed in an aligned pulse-echo air-coupled transduction project.

1.3.2 Contributions to Knowledge

- A statistical analysis of the performance of an air-coupled hybrid matching layer (~200 fabricated samples) to assess manufacturing success rate and reliability of fabrication process.
- A robust and reliable manufacturing approach for fabrication of a combined silicone rubber and membrane filter matching layer has been developed. Detailed analysis of matching layer microstructure, characteristic and operational performance demonstrates potential for application in air-coupled inspection systems.
- Design, fabrication and implementation of an air-coupled array-based inspection system, incorporating the developed matching layer technology. Using 1-3 connectivity piezocomposite active material, two 1.5-D annular array configurations have been developed for use in a through-transmission inspection system, offering the operational flexibility to adjust the focal point electronically during the inspection process.
- Evaluation of annular array through-transmission system, including selected matching layers, on industrial samples demonstrated the inspection capability of the system, with excellent results produced on a honeycomb sandwich carbon fibre reinforced polymer sample.

CHAPTER 2 Review and Applications of Air-Coupled Transducers

Abstract

This Chapter will summarise the fundamental information related to piezoelectric air coupled ultrasonic systems and discuss the specific details of the challenging requirements for an inspection system caused by operating in an air medium. There are various proposed transducer designs for the generation and detection of ultrasonic energy in an air-coupled environment. Work in this field has encompassed several transducer technologies: single-crystal, piezoceramic, piezopolymer, piezocomposite and CMUT. The main technologies in an air-coupled NDE array scanning system are introduced. Moreover, the key technologies utilised in this Thesis are the matching layer configuration and the array transducer design and these are described in detail.

2.1 Related Fundamental Properties Regarding Air-coupled Ultrasound NDE

2.1.1 Air attenuation

All wave propagation will undergo some form of attenuation, with the amplitude equation for a decaying plane wave expressed as:

$$A = A_0 e^{-\alpha L} \qquad 2\text{-}1$$

In Equation 2-1, A is the reduced amplitude after the wave travels a distance L. A_0 is the initial value of the amplitude of plane wave. e is the Napier's constant which is equal to approximately 2.718. α is the attenuation coefficient of the coupling medium. The expressions shown in Equations 2-2 and 2-3 have been proposed in [5, 6] for the calculation of the α in an air load.

$$\begin{aligned} \alpha = f^2\{1.84 \times 10^{-11} \frac{P_o}{P}\left(\frac{T}{T_o}\right)^{0.5} \\ + \left(\frac{T_o}{T}\right)^{2.5}\left[1.278 \times 10^{-2} \frac{e^{-\frac{2239.1}{T}}}{f_{r,o} + \left(\frac{f^2}{f_{r,o}}\right)}\right. \\ \left. + 0.1068 \frac{e^{-\frac{3352}{T}}}{f_{r,n} + \left(\frac{f^2}{f_{r,n}}\right)}\right]\} \end{aligned} \qquad 2\text{-}2$$

Where f is the operation frequency (Hz). T is the air temperature (K). $T_o = 293.15$ K which is equivalent to room temperature at 20 ℃. P is the atmospheric pressure (N/m^2). $P_o = 1.013 \times 10^5\ \mathrm{N/m}^2$ which is the standard atmospheric pressure. $f_{r,o}$ and $f_{r,n}$ are the rotational relaxation frequencies (Hz) for oxygen and nitrogen respectively.

$$f_{r,o} = \left(\frac{P}{P_o}\right)\left\{24 + \left[4.04 \times 10^4 \times h \times \left(\frac{0.02 + h}{0.391 + h}\right)\right]\right\} \qquad 2\text{-}3$$

$$f_{r,N} = \left(\frac{P}{P_o}\right)\left(\frac{T}{T_o}\right)^{0.5}[9 + \left(280 \times h \times e^{-4.17\left(\frac{T_o}{T}-1\right)^{1.5}}\right)]$$

This algorithm is accurate to +/- 5 % for the range of temperature 0 ℃ - 40 ℃; the range of relative humidity 0 – 100 %; the range of the frequency 50 Hz – 10 MHz; and the range of the pressure from 1 atmosphere to a few hundreds of an atmosphere.

Using Equations 2-2 and 2-3, Figure 2-1 can be generated, which estimates that the attenuation coefficient α is generally proportional to the square of the propagating sound frequency [6, 7]. Thus, the higher operating frequency utilised, the larger the attenuation will be and the resultant received signal amplitude will be lower. When the frequency reaches 1 MHz, the attenuation is around 160 dB/m which is more than 700 orders of magnitude larger when compared with 0.22 dB/m for 1 MHz wave propagation in a water load [8]. Importantly, the frequency can also influence the precision of the inspection. In general, the higher frequency used, the shorter the wavelength, as shown in Equation 2-4, and a resultant higher spatial precision can be achieved. Typically for an air-coupled ultrasonic inspection system, the balance between attenuation and precision results in an operating frequency range from 400 kHz to 650 kHz.

$$\lambda = \frac{velocity}{frequency} \tag{2-4}$$

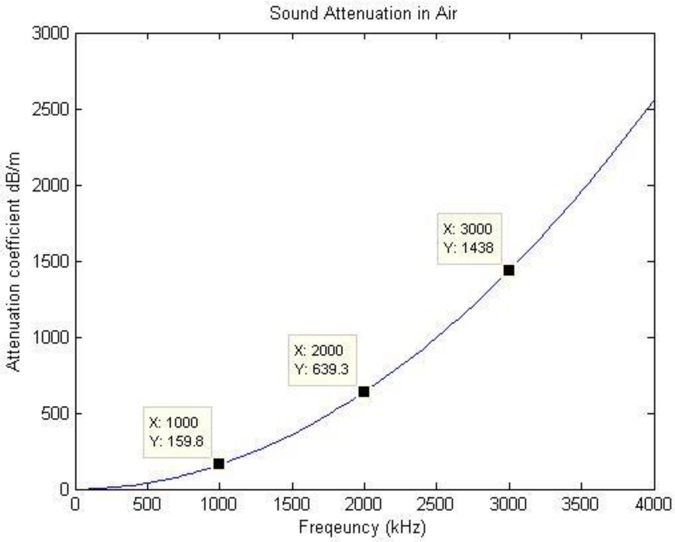

Figure 2-1 Air attenuation with frequency in 20 ℃ room temperature and standard atmosphere pressure

2.1.2 Air/Solid interface reflection loss

The main signal loss comes from the acoustic impedance mismatch at the transducer/air and air/sample boundaries. The acoustic impedance of air is much lower at 430 Rayl when compared to liquids and solids, which have acoustic impedances in the MRayl range. Table 2.1 shows the specific acoustic impedances of some typical ultrasonic system components [6, 8].

Table 2.1 Typical acoustic impedances

Material	*Acoustic Impedance*
Piezoelectric ceramic	33 MRayl
Air	430 Rayl
Water	1.5 MRayl

The transmission and reflection coefficients are related to the material acoustic impedances according to the following equations [8, 9, 10]:

Transmission coefficient:

$$T_p = \frac{P_t}{P_i} = \frac{2Z_L}{Z_L + Z_T} \tag{2-5}$$

Reflection coefficient:

$$R_p = \frac{P_r}{P_i} = \frac{Z_L - Z_T}{Z_L + Z_T} \tag{2-6}$$

Where Z_T is the specific acoustic impedance of the transmission medium, Z_L is the specific acoustic impedance of the load medium, and P_i, P_t and P_r are the incident, transmitted and reflected pressures respectively, as shown in Figure 2-2.

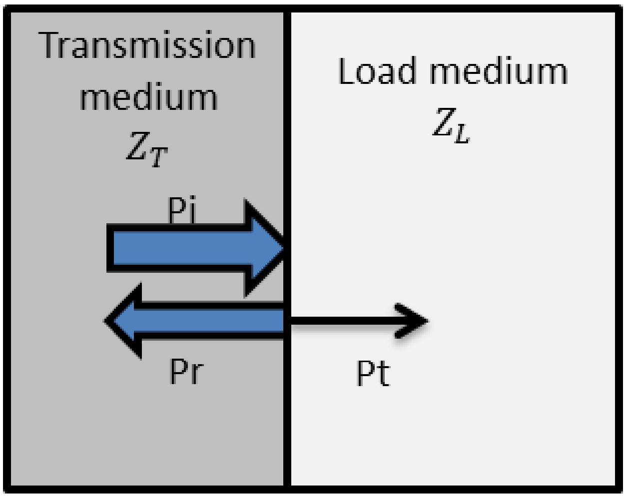

Figure 2-2 Pressures and impedances used in the calculation of transmission and reflection coefficients

Figure 2-3 shows the typical pitch-catch system which can be adopted when testing a sample in an air coupling medium. The energy received by the receiver is only a small proportion of that transmitted. For a 17 MRayl sample, the calculated values for the four transmission coefficients at each interface and the resulting insertion losses are given in Table 2.2. Transmission coefficients T1, T2, T3 and T4 were calculated using Equation 2-5 and the through transmission insertion loss can be calculated by multiplying the pressure transmission coefficients at the four boundaries. Operating in an air load has a much higher insertion loss 165.6 dB which is compared with 26.1 dB in water.

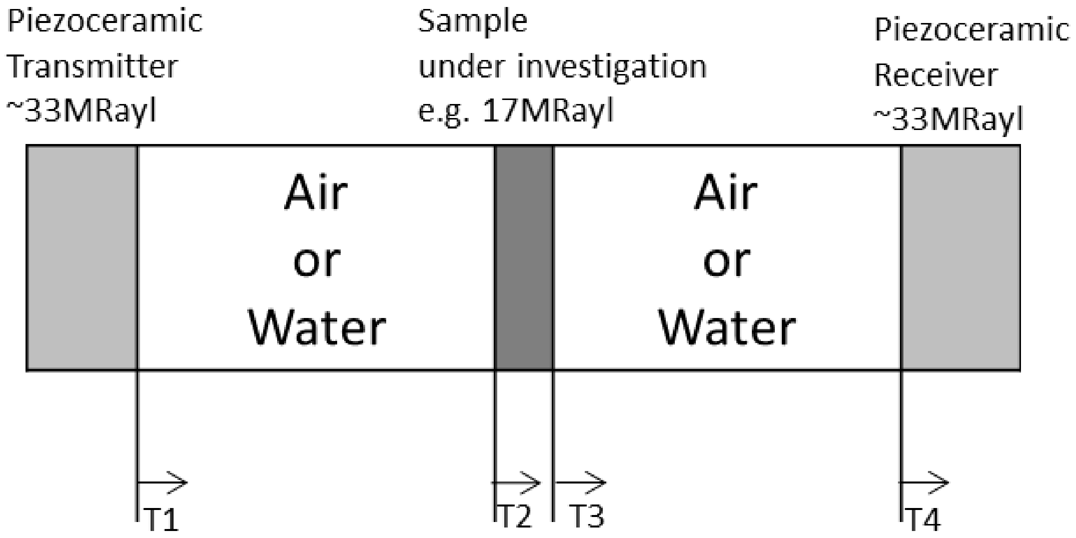

Figure 2-3 The influence of the acoustic impedance mismatch at typical interface boundaries for a NDE through transmission system [6]

Table 2.2 Transmission coefficients and calculated insertion losses for both air and water coupling medium in through transmission systems

Transmission coefficient	*Air load*	*Water load*
T1	2.606×10^{-5}	0.087
T2	1.9999	1.8378
T3	5.059×10^{-5}	0.1622
T4	1.9999	1.9130
Total	5.273×10^{-9}	0.0496
Insertion loss =20*$\mathbf{log_{10}}$(Total)	-165.56 dB	-26.09 dB

2.2 Transducer technologies utilised in air-coupled ultrasound systems

2.2.1 Piezoelectric transducers

Figure 2-4 shows the structure of a typical piezoelectric transducer. In transmission, an electrical excitation signal will be used to vibrate the piezoelectric material and generate the ultrasound, whereas in reception, the piezoelectric disk will convert any incident pressure wave to an electrical signal, which will be transferred to the signal conditioning instrumentation. The typical materials of the piezoelectric disk are $(1-x)Pb(Mg_{1/3}Nb_{2/3})O_3-xPbTiO_3$ (PMN-PT, single crystal material), piezoceramics, piezoelectric polymers and piezocomposites (ceramic/crystal and polymer).

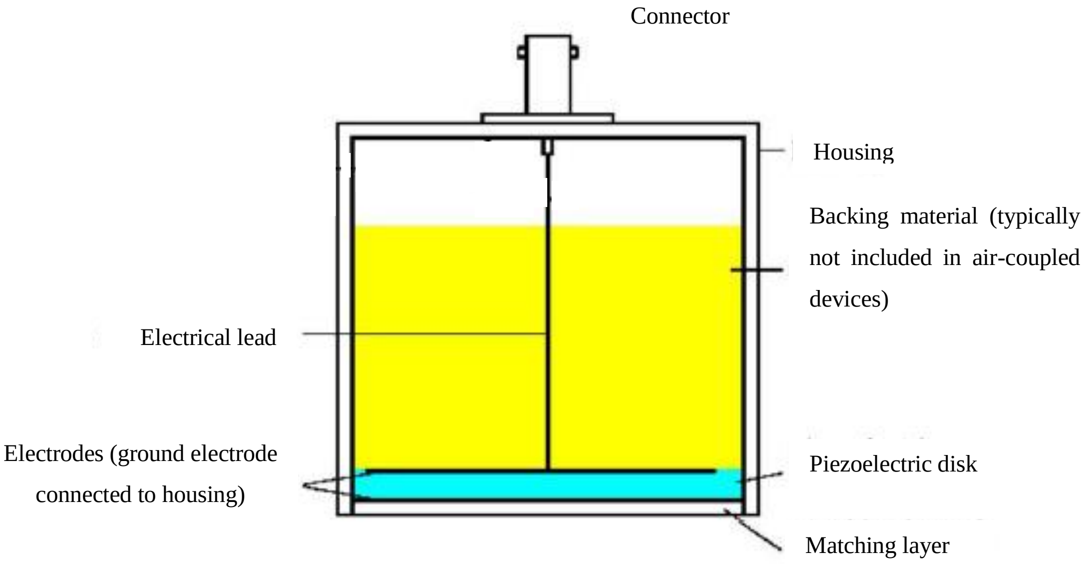

Figure 2-4 Schematic diagram of the structure of a standard piezoelectric transducer

2.2.1.1 Piezoceramics

Originally, crystals made from quartz were used for piezoelectric crystal transducers. In the early 1950s, naturally occurring quartz crystals started to give way to man-made piezoceramic as the primary transducer material. The advantages offered by a ceramic transducer when compared to other materials (PMN-PT and piezoelectric polymers) include the ability to fabricate ceramic in a wide range of shapes and sizes, its capability of operating efficiently even at low excitation voltages, and its ability to work at temperature up to 300 ℃. Piezoceramic materials are found in a large number of devices covering a large frequency range, including operating in a water load at frequencies up to 100 MHz [11]. Hence, ceramic transducers have been dominant in NDE applications for many years [12].

Conventionally, piezoceramics are created by a mixture of a ceramic powder and binders, then pressed and sintered at high temperature. A poling process is required as the dipole orientation inside the ceramic is initially random. By applying a high DC field at a temperature close to the ceramic's Curie point, the domains are aligned with the field direction. Normally, piezoceramic transducers make use of the piezoelectric thickness extension mode of the material.

Piezoceramic transducers have been reported for many non-contact applications in non-destructive evaluation (NDE) [13], such as piezocomposite material property measurement [14, 15] and paper roughness measurements [16]. Deka has demonstrated both through transmission and pulse-echo methods to evaluate material properties using a 450 kHz transducer [14]. One experiment demonstrates the identification of a fish-tail shape defect in an aluminium plate when operating in pitch-catch mode. Another experiment shows the internal bonded property of a laminated sheet. With a third experiment demonstrating that the transducers have adequate sensitivity to perform proximity sensing and gauging. Rogovsky [15] described an experiment concerning the application of focused piezoelectric transducers for NDE of piezocomposite materials. Neither paper has shown the detail about the design of transducers employed in their study, but the results reported are still important and lay a foundation for the following studies.

The main restriction to the use of piezoceramic for air-coupled applications is its narrow operational bandwidth, which is typically less than 5 % [12], and additional problems may occur when matching to the air medium due to its high characteristic acoustic impedance, $Z \approx 33$ MRayl.

2.2.1.2 Piezoelectric polymers

In 1969, the piezoelectric effect in the polymer polyvinylidene fluoride (PVDF) was discovered [12, 17, 18], which offers attractive options for air-coupled ultrasound applications. It exhibits good mechanical matching with air, a wide operating bandwidth, is lightweight and offers the capability to be configured as a flexible membrane. Piezoelectric polymer transducers show excellent dynamic properties due to its thin vibrating membrane and high mechanical damping compared to the piezoceramic material, which results in generation of short duration wave pulses [12].

PVDF material has been incorporated into a diverse range of devices covering a large frequency range, including operating in water conditions with a high operating frequency up to 120 MHz [19]. In the ultrasound range, Fiorillo has employed PVDF for robotic applications, where the operational frequencies of the transducers are higher than 380 kHz [20]. Gachagan compared the PVDF transducers' working conditions in both water and air with a 25 μm thickness PVDF film and also experimentally evaluated its wide-band and narrow-band characterisation [6]. Takahashi and Ohigashi managed to obtain imaging by using air-coupled PVDF transducers at a 2 MHz operating frequency [21]. Wang, Tanaka and Chonan developed a human's in-sleep cardiorespiratory monitoring with the sensory material PVDF, which is 140 mm in width, 200 mm in length and 28 μm thick [22]. The total sensor has a thin thickness which is 2 mm and the sensor is flexible. This system is suitable for measuring both respiration and heartbeats.

Different designs have been utilised to enhance the performance of PVDF: the use of multi-layered piezoelectric polymer through a parallel connection configuration was estimated to increase system sensitivity [23]; the micro-pillar sensor array shown in Figure 2-5 is reported to improve the sensitivity and measured stress constant with an accuracy more than 60 times better than a commercial PVDF transducer [24]; and Jeong and Shung reduced the reverberation in the device by removing the adhesive layer between PVDF film and the backing materials (silver epoxy was used as backing with ~2.6 MRayl impedance) [25, 26].

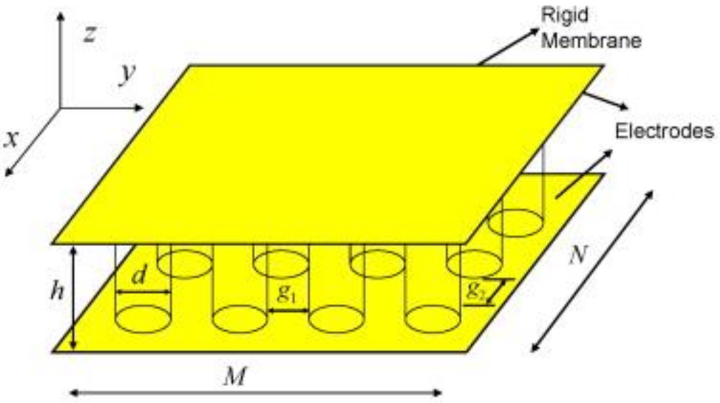

Figure 2-5 PVDF micro-pillar sensor based on full electrodes [24]

The main limitation for the use of PVDF is its narrow operating temperature range, low dielectric constant $\varepsilon_r \approx 10$ and electromechanical coupling co-efficient $k_t \approx 0.2$ which will result in poor transmission performance. Importantly, when used in typical ultrasonic systems, the piezoelectric polymer-based transducers have to be driven by much higher voltage levels than comparable piezoceramic devices.

2.2.1.3 Piezoelectric crystal

Before piezoceramics were developed, the most common piezoelectric materials were single crystals such as quartz. However, their use in transducers was superseded by the introduction of piezoceramics, which have much larger piezoelectric responses. This situation lasted until Shrout et al. reported a new family of single-crystal piezoelectric materials, based on lead magnesium, grown specifically for actuation applications in 1990 [27]. Four years later, $Pb(Mg_{1/3}Nb_{2/3})O_3$-$xPbTiO_3$ (PMN-PT) piezocrystal material was used in an ultrasonic probe for the first time [29]. Its outstanding performance was widely recognized and was considered a revolution for ultrasound transducers by Oakley [28]. The main benefits of using piezocrystal over piezoceramics are the improved sensitivity, higher coupling coefficient $k_{33} \approx 0.9$ and wider bandwidth when the material is operating in the thickness mode [29, 30]. One significant drawback is the upper working temperature limit, which has been reported to be as low as 60 ℃.

Due to the attractive properties of single crystal, Silverman et al fabricated a plate of $LiNbO_3$ that is 30 µm thick to produce a 75 MHz lithium niobate transducer with 2 mm aperture and 6 mm focal length and used this to image the anterior segment of eye. They also compared the results with a 35 MHz lithium niobate transducer of similar fractional bandwidth [31]. The results demonstrate that high-frequency ultrasound can provide high resolution images of the detailed structure of the eye. A 40 MHz PMN–PT single crystal needle transducer was used to monitor the blood flow velocity near the occlusion site in a vein to determine the effect of sonothrombolysis [32]. The single crystal materials not only have applications in the biomedical field, but they have also been utilized in an accelerometer with a resonance frequency of 19.4 kHz, which has 15 dB improvement in the signal-to-noise ratio (SNR) by adding a castellated layer under the piezoelectric material [33]. The single crystal has also applications in sonar, for uses including oceanographic research, oil and mineral prospecting, salvage, and undersea equipment inspection and maintenance [34].

However, the cost of the raw single crystal material is much higher than for piezoceramics. In 2007, the price of PMN-PT material was as high as $\$15/mm^3$ due to the difficulties in growing useable amounts of crystal, while comparable ceramic was around $\$0.01/mm^3$ [35]. Growing large crystals with uniform properties repeatable is also challenging and is the focus of many research papers [36, 37, 38]. The price of single crystal material has come down recently, but is still prohibitively high for incorporating into standard inspection systems.

2.2.1.4 Piezoelectric composites

In many fields of ultrasonic engineering, the standard piezoelectric ceramic and single crystal transducers are superseded by a multi-phase structure which comprises both active piezoelectric materials and passive polymeric materials: piezoceramic composites (will now be referred to as piezocomposites in remainder of Thesis). These new structures aim to maximise the advantages of piezoceramic and single crystal materials by controlling the device microstructure. Typically, the piezocomposites transducers' bandwidth can be around 30 %, which is a significant improvement when compared with some conventional piezoceramic materials, which can be down at 5 % bandwidth [12]. Moreover, the shape and size can still be easily adapted to a wide variety of industrial applications; the damping property associated with the polymer can reduce mechanical cross-talk within the structure; the electromechanical coupling co-efficient k_t is controllable; and the acoustic impedance matching to air is improved through inclusion of the low acoustic impedance polymer phase.

There are two types of configuration which are usually used: 1-3 and 2-2 connectivity piezoelectric composite, as depicted in Figure 2-6. The configuration name is related to the material connectivity: the first number means the connectivity of the active piezoelectric phase; and the second number refers to the connectivity of the passive polymer phase [39].

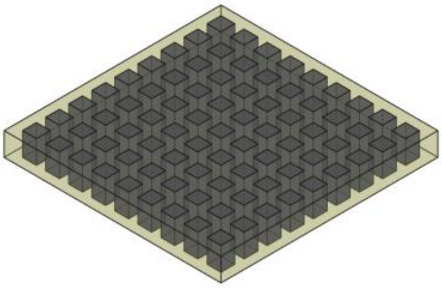

(a)

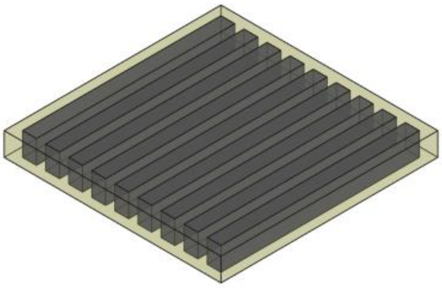

(b)

Figure 2-6 Schematic diagram of main piezocomposite configurations

(a)1-3 connectivity (b)2-2 connectivity

In the early 1990's, for 1-3 piezocomposite transducers, Hossack and Hayward assessed different pillar geometries include square, circular, triangular, and tapered using finite element analysis [40, 41]. W. A. Smith and Auld modelled the piezocomposite's material parameters in terms of the volume fraction to support the trade-off between minimizing the acoustic impedance and maximizing the electromechanical coupling efficiency [42]. Towards the end of the 1990's, Ritter et al designed a single-crystal polymer 1-3 piezocomposites transducer with a higher extensional coupling efficiency k_{33}, larger bandwidth, and higher electromechanical coupling coefficient k_t[43]. Gachagan improved the bandwidth by using lateral mode coupling [44]. Reynolds, Hyslop, and Hayward investigated the influence of boundary conditions on transducer surface displacement with a 1-3 piezocomposite transducer operating at 395 kHz [45]. Zukauskas, Cicenas and Kazys presented the performance of an air-coupled focused piezocomposite transducers in the through transmission mode [46]. This research reported the results of testing 0.6 mm thick aluminium plates and carbon fibre reinforced plastic (CFRP) delamination type defect in multi-layered materials by using 445 kHz air-coupled transducers. The focal spot of the transducers is 1 mm. The errors when estimating the dimensions of defects are -0.11 mm, 0.13 mm and 0.52 mm for the single layer aluminium test sample, the double layer aluminium test sample, and the CFRP test sample, respectively. The paper doesn't give the detail about the transducer's parameters, but the results are still significant because the experimental results showed that the measurement of the dimensions of defects in multi-layered structure using air-coupled ultrasonic technique can be performed with a relatively high accuracy compared to the traditional low frequency air-coupled transducer.

2-2 piezocomposite transducer configurations are often applied to linear array transducers due to its microstructure. In 1990, Smith, Engeler, O'Donnell, and Piel recorded the impulse response of array elements with different heights made from both 1-3 and 2-2 piezocomposite. The experiments show that the 2-2 piezocomposite has a benefit that the influence of changing the pillar height is small on impulse response ring down length [47]. The bandwidth of the 2-2 piezocomposite remains relatively unchanged also. Huebner, Reidmeyer and Stevenson described an alternate approach for fabricating 2-2 connectivity piezocomposite with fine scales unachievable by conventional dice-and-fill method in 1995 [48], using alternately stacked PZT plates and PVDF films and then laminating the device by heating in a vacuum. Transducers were fabricated out of the piezocomposite block, electroded and then poled. Wang et al produced a high power linear array transducer by using a 2-layer stacked 2-2 connectivity piezocomposite structure in 2012 [49].

One of the deficiencies is that the piezocomposite manufacturing process introduces additional fabrication difficulty and is time consuming, due to the complex combination of both active piezoceramic and passive polymer materials. Fortunately, more advanced technologies are appearing to support complex manufacturing such as 3-D printing [50]. This approach will alleviate such concerns in the future.

2.2.2 Key parameters for designing a 1-3 piezocomposite

2.2.2.1 Constituent materials

Single crystal and PZT materials can be used for the active phase in piezoelectric composite designs. Selection is typically made on the basis of availability and ease of manufacture, as well as performance. The advantages of using the ceramic materials rather than single crystal are that it is relatively inexpensive, exhibits high stiffness and is thermally robust, with a Curie temperature greater than 200 ℃. Previous work at Strathclyde developed a specification for a standard air-coupled piezoceramic composite transducer for operation at 600 kHz [51].

There is a wide range of active piezoelectric and passive polymers available for application in a 1-3 piezocomposite device. At Strathclyde, the primary piezoceramic materials used are PZT5H and PZT5A, with three polymer filler materials covering a wide range of acoustic and mechanical properties: the hard-set material CIBA-GEIGY CY1301/HY1300, the medium-set setting CY221/HY956 and a conformable, soft-set one CY208/HY956. Appendix A gives the main material characteristics of these ceramic and epoxy materials. Of these material combinations, Hayward and Gachagan confirms PZT5H with hard-set piezocomposite has the largest pressure for the transmission performance and PZT5A with hard-set can produce the largest received voltage, from their range of material combinations [51, 52]. In general, using a hard setting polymer produces more uniform surface motion and higher displacement because the damping is low; and the soft setting polymer introduces increased attenuation, reduced centre frequency and increased bandwidth [51, 53, 57].

2.2.2.2 Ceramic volume fraction

In an air-coupled 1-3 piezocomposite design the most influential design parameter is the ceramic to polymer volume fraction (CVF). At very high volume fractions (about 80 %), increased pillar lateral clamping is evident which has large effect on the elastic and piezoelectric behaviour, and at very low volume fractions (below 20 %), increased damping of the ceramic has an influence on sensitivity. Gachagan and Hayward presented the results that in transmission the PZT5H with hard set piezocomposite should have a CVF between 50 % and 70 %, and for reception, PZT5A with hard set should have a CVF between 10 % and 30 % [51]. Kelly et al [8] proved the results that the peak performance occurred at 70 % and 40 % for transmission and reception respectively with a silicone rubber matching layer applied, and 70 % and 20 % for transmission and reception respectively without matching layer [54]. In this work, a PVDF hydrophone was chosen to measure the pressure produced in air by the transmitters of varying volume fraction and a PVDF transmitter was used to produce an impulsive pressure to determine the air-coupled receivers' sensitivity across the range of volume fractions.

2.2.2.3 Electromechanical coupling coefficient

Electromechanical coupling coefficient k_t is an important property for a piezoelectric material. A higher k_t means an increase in the transfer efficiency between the electrical and mechanical domains. If $k_t = 1$, it means there is no energy loss between the electrical signal and mechanical energy transfer. A lower k_t will cause a energy loss which has an influence on the transducer performance, such as a lower signal to noise ratio. For a 1-3 piezocomposite material the value of k_t varies as a function of CVF, with a good k_t usually having a value around 0.6, as shown in Figure 2-7 [6]. At the CVF extremities, the value of k_t reduces due to the elastic loading of the polymer at low volume fraction and lateral clamping by the polymer at high volume fraction values. Importantly, this material structure has a reasonably stable k_t between 30 % and 80 % volume fraction.

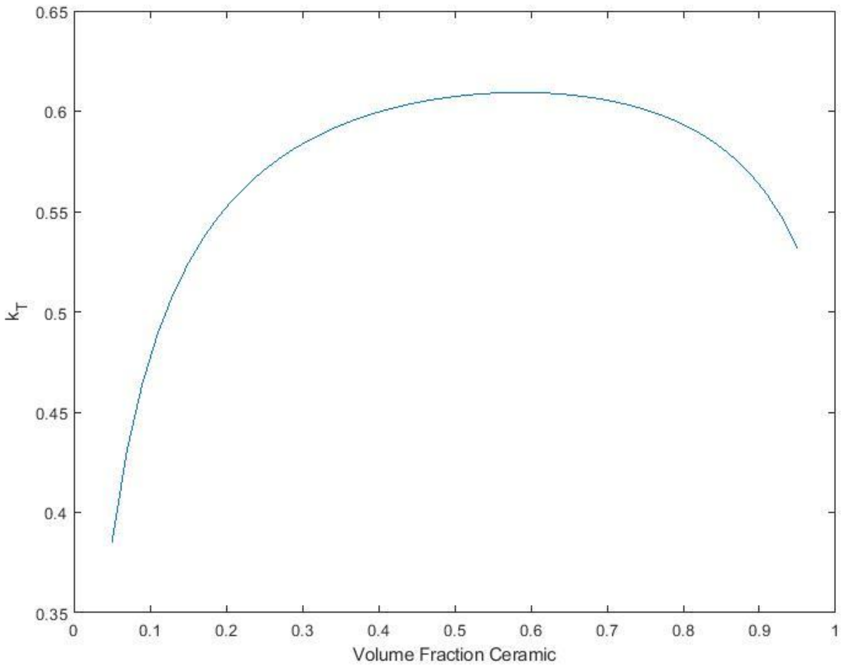

Figure 2-7 Variation with ceramic to polymer volume fraction and electromechanical coupling coefficient for a 1-3 piezocomposite, as predicted by Smith's model [42]

2.2.2.4 Aspect ratio and pillar geometry

Aspect ratio is one of the most important parameters for designing a 1-3 piezocomposite transducer and is defined in equation 2-7. Careful consideration must be taken on the shape and dimensions of the ceramic pillars, as these can have significant influence on the strengths of both inter- and intra-pillar parasitic lateral modes of vibration. The inter-pillar mode arises due to the standing wave patterns associated with the periodic composite pillar structure, whereas the intra-pillar mode is the standing waves within a pillar due to the waves reflected at the piezoelectric material boundaries. For both modalities, there will be a displacement in the lateral dimensions in addition to the thickness direction vibration. Importantly, correct design of the piezocomposite microstructure will remove these modes from the thickness mode vibration frequency.

$$Aspect\ ratio = \frac{ceramic\ pillar\ width}{composite\ thickness} \tag{2-7}$$

Electromechanical coupling coefficient k_t was found to increase as the aspect ratio reduces, which relates to an increase in piezoelectric coefficient [55]. Kim et al [56] presents the relationship detail between k_t and the aspect ratio. For the case of PZT, if the aspect ratio is larger than 0.862, the vibration will be associated with the lateral mode, while for an aspect ratio smaller than 0.862, it will be represented as a thickness mode vibration. Hayward et al [57] defined a maximum pillar aspect ratio (MPAR) from different piezocomposite material combinations: PZT and both hard and soft setting polymer materials. The key criterion in this work was to maximise the surface vibration dilation quality, which is effectively a measure of how uniform the surface vibration is for various piezocomposite configurations. In general, a lower aspect ratio will offer better vibrational performance, at the cost of producing fragile and thin pillars which carries a risk of manufacture failure. Moreover, when a polymer with low mechanical loss is assumed for improved dilation quality, strong lateral vibrations can occur [57].

Hossack and Hayward also reported on the pillar shape [41]. Circular pillars have no obvious advantage, especially compared with the square geometry. The triangular pillar geometry has a higher MPAR compared with square pillar, but should avoid facing parallel surfaces. Tapered pillars offer no significant reduction in lateral mode vibrations [41]. In summary, considered the cost, difficulties in manufacturing and the piezocomposite performance, the square pillar geometry is typically recommended.

2.2.2.5 Operation frequency for transmitter and receiver

For transducer manufacture, the thickness of the piezocomposite for operating at its thickness mode is mainly determined by the device fundamental resonance frequency [42], which can be calculated from the wavelength as this is equal to twice the thickness of the transducer.

The transmitter's resonance frequency is named as the electrical resonance (f_e) which represents the minimum electrical impedance associated with the fundamental operating mode of the device. The receiver's resonance frequency is named as mechanical resonance (f_m) which is the natural mechanical frequency associated with the fundamental operating mode.

It has been reported that the f_e of the transmitter should match with f_m of the receiver in a pitch-catch mode system to maximise system sensitivity [6, 8] as shown in Figure 2-8.

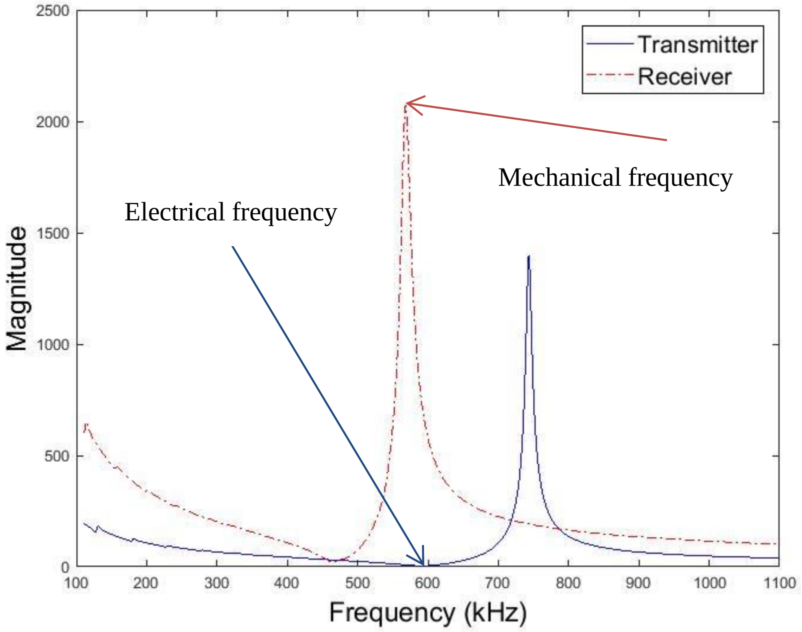

Figure 2-8 Operation electrical frequency of transmitter should match with the mechanical frequency of the receiver

2.2.3 Capacitive micro-machined ultrasonic transducer

Capacitive micro-machined ultrasonic transducer (CMUT) is an alternative transducer design for application in the air-coupled NDE area, although most of the commercial ultrasonic transducers are based on piezoelectric materials. CMUTs have a superior performance than the traditional piezoelectric transducers in some ways. It has wider bandwidth and higher operational frequency due to smaller fabricated dimensions. The most important aspect is that it has better acoustical matching to air, when compared to ceramic-based transducers.

Different from the standard ultrasonic piezoelectric transducers, CMUTs produce energy transduction as a result from changes in capacitance. The thin membrane will vibrate after it is excited by an alternating voltage signal, although a DC bias voltage is typically also applied to tension the membrane. The trapped gas provides a displacement space for the membrane and the device capacitance is established between the electrodes either side of this air gap. The larger the membrane displacement the more power is transmitted into the load. In reception mode, the membrane will be vibrated by external ultrasound waves and the changing capacitance can be detected as an electrical signal [58, 59]. Figure 2-9 shows the principle of operating a CMUT.

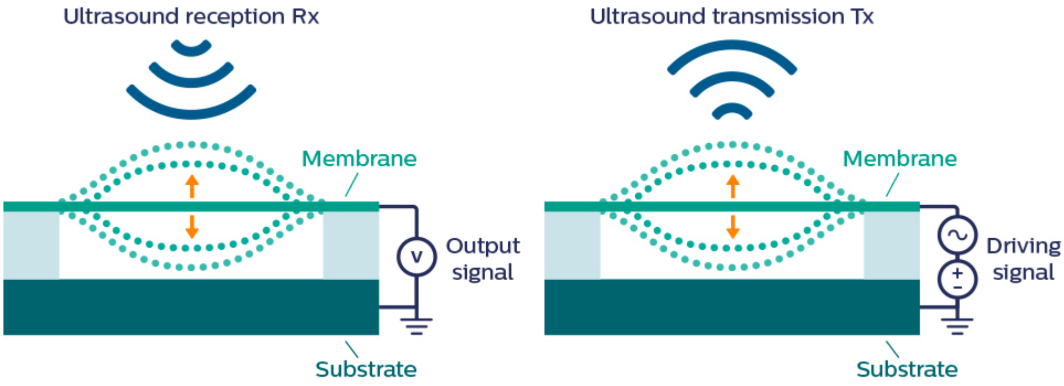

Figure 2-9 Principle of operating a CMUT [60]

Schindel and Hutchins manufactured a wideband CMUT with the -6 dB bandwidth from lower than 100 kHz to 2.3 MHz in 1995, although its insertion loss in air has not been measured [61]. Haller and Khuri-Yakub built a pitch-catch system by using two electrostatic transducers. The measured one way insertion loss is 26 dB and a 3-dB bandwidth of 20 % was measured which is compared to 20-dB insertion loss and 4 % bandwidth for a reference piezoelectric transducer [62]. Buhudorf, Ahrens and Binder introduced a new technology - partial doping of polysilicon membranes to reduce the parasitic and offset capacitances which offers an enhancement of the transducer sensitivity by over 30 % and also enables fabrication with an identical structure, but different resonance frequencies on the same transducer [63]. Octavio et al achieved a further improvement of the output pressure by using a resonant cavity, which is 11 dB greater than the traditional CMUT device and also increased its bandwidth with a Q factor (Q = f / bandwidth) of 4.5 compared with 7.75 for the traditional device [64].

CMUT transducers offer a big advantage for non-contact applications due to their good acoustic impedance match to air, which can produce efficient devices [65]. But the primary limitation is that the front face membrane is extreme fragile so that it is easily damaged. The complicated manufacturing process leads to increase in cost and higher potential for failed manufacture. Due to the micro-machined structure, the surface will become contaminated if left open to the environment, including the water vapour, dust, and other airborne contaminants, with these particles getting into the small spaces and leading to permanent device damage. Another weak point is the membrane can be too thin to produce a high energy output which is an essential requirement in the air load due to the large air attenuation. Moreover, the sensitivity and resolution still need to improve compared to piezoelectric-based transducers.

2.3 Phased array transducer configurations

For phased array transducer configurations, the array elements are electrically independent from each other, which allow for individual control of transducer operation through application of different excitation signals to each array element. Each array element will generate a discrete ultrasonic waveform which then will interfere with ultrasonic waves from other array elements in a pre-defined way to generate a desired beam profile, such as focusing to a point in space. There are a wide variety of array configurations [66], for example annular, linear, Mill's cross, hemisphere [67], and random/sparse. The most common phased array transducers are divided in to six types: 1-D linear, annular, 2-D matrix, 2-D segmented annular, 2-D sparse and 1.5-D matrix.

The 1-D linear array is characterised by array elements which have much smaller width than length, as shown in Figure 2-10. It generates a beam with elliptical shape, which offers the ability for beam control in the vertical and horizontal direction (relative to the array front face). The advantages of this configuration are their simple structure, ease of manufacturing, and relatively simple beam control [68]. But its simple structure is also a weak point since it can't satisfy the high demand for complex beam control. g is element gap, p is pitch size, w is element width, A is the element length, and e is one element size which should smaller than the half of wavelength.

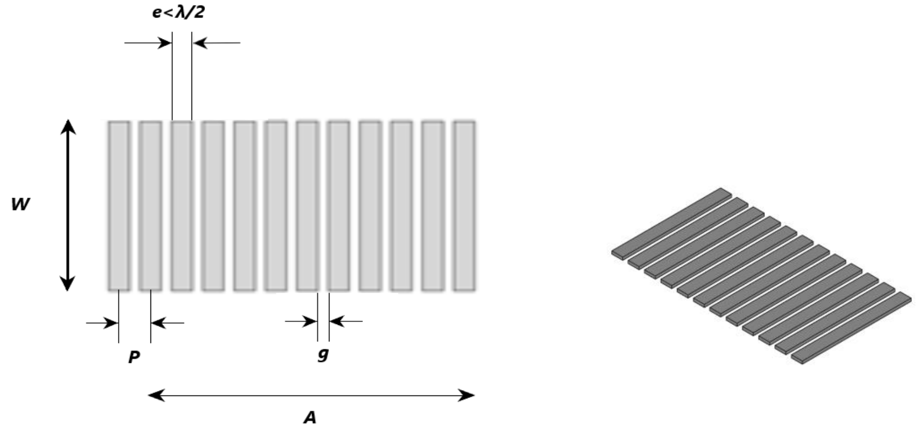

Figure 2-10 1-D linear array phased array layout

An annular array configuration is composed of elements with a concentric ring shape, as shown in Figure 2-11. It projects a spherical geometry beam and electronic control can steer the beam along the central axis in front of the device. It has a better focusing performance than the 1-D linear phased array transducers [69], but the geometry makes it impossible to steer the beam in an angle outside the central axis by electrical focusing method without moving the transducer.

Figure 2-11 Annular phased array layout

The 2-D matrix configuration, which is shown in Figure 2-12, projects an elliptical shape of ultrasonic beam from each element. The array permits three-dimensional imaging, and thus energy focusing area can be chosen across a wide spatial range [70]. The limitations of this 2-D array are its complex manufacturing process, complicated beam steering process and small array element size, which is not appropriate for applications that required a high power transduction scheme.

Figure 2-12 2-D matrix phased array layout

The 2-D segmented annular array as illustrated in Figure 2-13 is the combination of the concepts between the annular array and 2-D matrix array configurations. The beam shape is spherical or elliptical and can not only vary the depth but also the angle [71], thus providing more controllability of the beam operation. The drawbacks are the same as 2-D matrix array-complex manufacturing process, complicated beam control and low power due to the small elements size.

Figure 2-13 2-D segment annular phased array layout

The 2-D sparse array is a technique which is ideal for element number reduction from the standard 2-D matrix array configuration [72]. There are many potential array configurations, with a random arrangement illustrated in Figure 2-14 [73]. This technique can ease the complexity when manufacturing, although this is at the cost of deteriorating the beam pattern compared to the matrix array. Therefore, beam pattern optimization can be necessary to correct some of the drawbacks, mainly the side lobe artefacts. An additional benefit of using a sparse arrangement is the minimisation of grating lobes, which may be present in the array due to the periodicity within the 2-D matrix configuration.

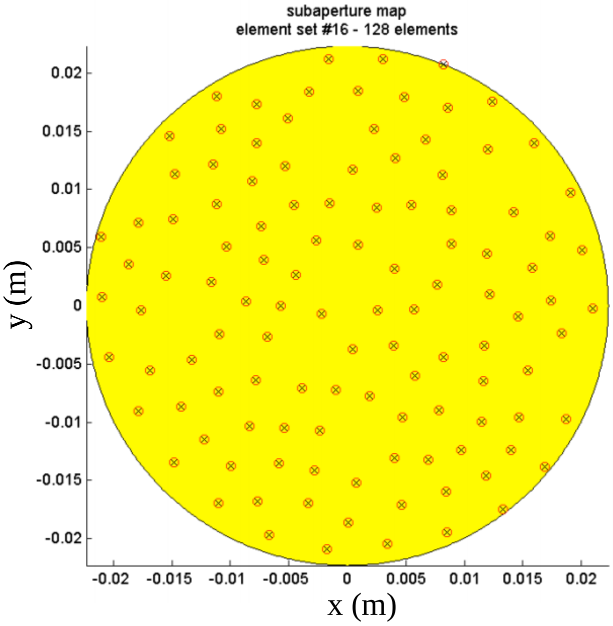

Figure 2-14 2-D random 128 elements sparse array [73]

A 1.5-D matrix array configuration is a compromise between beam steering ability and complex manufacturing process, such that it is a combination of 1-D linear and 2-D matrix array arrangements. As shown in Figure 2-15, every linear element based on 1-D linear array configuration has been split into a small number of sub-elements each with a different designed length. The probe produces an elliptical ultrasonic field projection and enables limited three-dimensions steering [74]. This design is a balanced product and has both advantages and disadvantages of 1-D linear array and 2-D matrix array configurations.

Figure 2-15 1.5-D matrix phased array layout

2.4 Beam steering for circular shaped transducers

2.4.1 Natural air-coupled acoustic field characteristics and excitation power supply

For free-field propagation, the space in front of the transducer is divided into two regions: near-field zone and far-field zone, as shown in Figure 2-16. In the near-field zone, the interference pattern produces an area of constructive and destructive interference, which makes it not an ideal zone for conventional feature detection in this range. Meanwhile, the far-field zone is a stable area, but the problem is that the amplitude may be low if the coupling medium exhibits a large attenuation, such as air. Equations 2-8 and 2-9 can be used to assess the near-far field boundary N_0, and the angle of divergence of the sound energy γ_0, respectively, where, D_{probe} is the diameter of the transducer and λ is the wavelength of the ultrasound in the load medium.

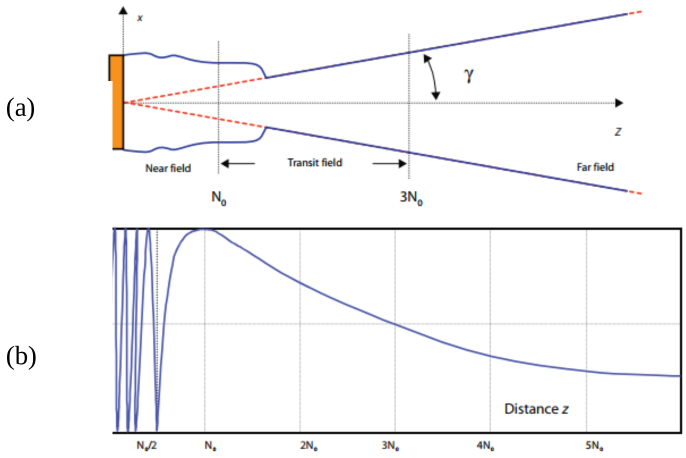

Figure 2-16 Illustration of near-far field pressure regions for a circular transducer: (a) general top view of pressure field regions and (b) on-axis z direction sound pressure profile under ideal conditions with distance [75]

$$N_0 = \frac{D_{probe}^2 - \lambda^2}{4\lambda} \qquad \text{2-8}$$

$$\sin\gamma_0 = 1.22\frac{\lambda}{D_{probe}} \quad 2\text{-}9$$

Table 2.3 illustrates the predicted near-far field boundary and divergence angle for a 40 mm diameter disc-shaped ceramic plate, operating at 600 kHz in both water and air media. The influence of air attenuation has not been included in the table for the purposes of comparison. The narrow beam divergence in air medium may be considered a benefit to a traditional single element system, but not for an array transducer. The near-far field boundary is further away when operating in the air medium, compared with a water load, resulting in low energy available for detection in the far field zone. Therefore, for operation in air, the transducer system target region will typically be in near field, albeit care should be taken to ensure the system does not operate at a null in the field profile.

Table 2.3 Comparison between theoretically predicted near-far boundary and divergence angle in both water and air medium operating at 600 kHz

	Water	*Air*
c	1500 m/s	345 m/s
λ	2.5 mm	0.575 mm
N_0	160 mm	695.5 mm
γ_0	4.37 °	1 °

The on-axial air-coupled field profile in a rigid infinite baffle can be considered by combining standard beam theory and the air attenuation theory, as described in Equation 2-2. This theoretical approach has been used to predict the air-coupled field behaviour under two conditions: an ideal air load without attenuation for a disc shape ceramic plate, and a standard air load with airborne attenuation for a disc ceramic, as shown in Figure 2-17. For both conditions, they are driven by continuous wave conditions at an operating frequency of 600 kHz. The airborne attenuation reduces the amplitude by approximately one half after a 100 mm propagation distance, as illustrated in Figure 2-17. This clearly demonstrates the attenuation problem associated with air-coupled operation.

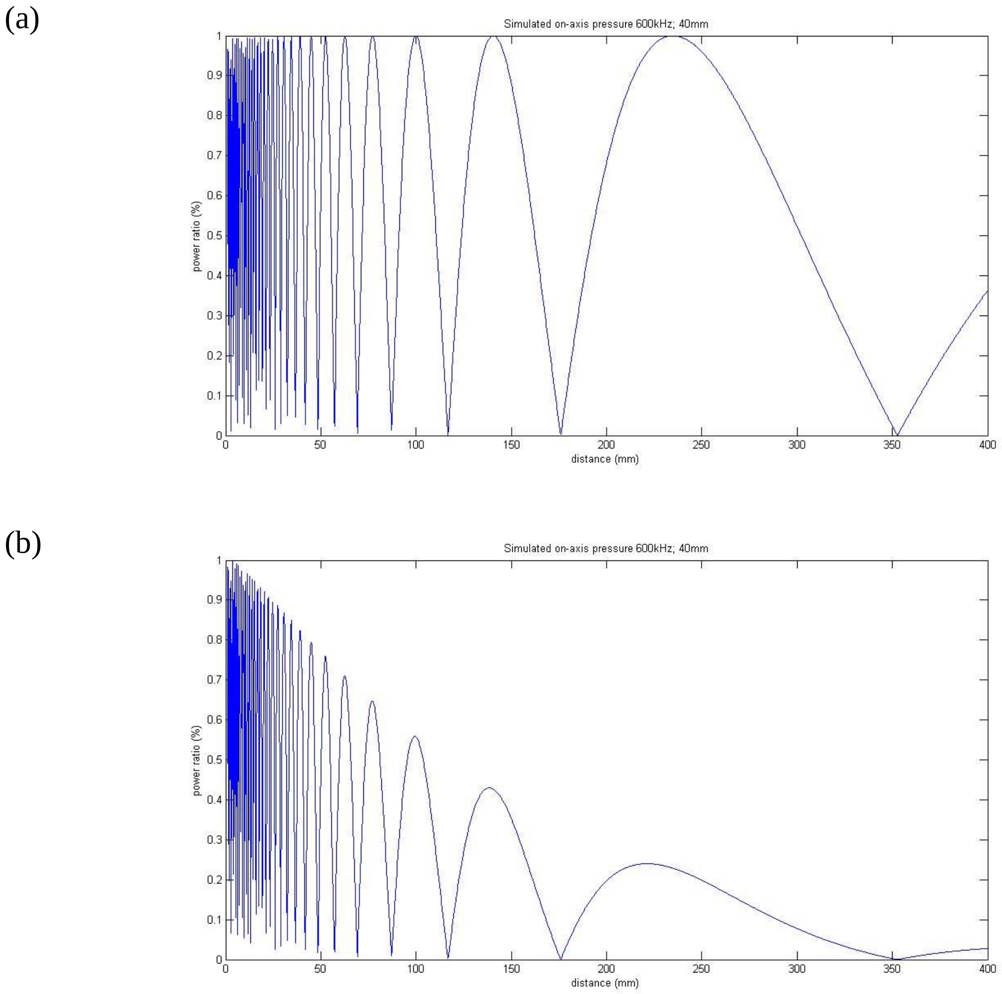

Figure 2-17 On-axis directivity profile for a 40 mm ceramic disc operating in air

(a) ideal conditions; (b) including air attenuation factors

The excitation signal also has influence on the field interference pattern as well. A conventional imaging system will use the pulse, which has low interference influence, as shown in Figure 2-18(e). The main issue associated with pulse excitation is that the signal does not have enough energy for operation in high attenuating load materials. Continuous wave excitation, as illustrated in Figure 2-18 (a), would solve the issue of maximising energy for air-coupled operation, but is unusable for imaging applications. Hence, the excitation waveform will be a compromise between these conditions, as illustrated in Figure 2-18 (b) – (d). Importantly, using an excitation signal with more than one-cycle is often chosen and Figure 2-18 (b) and (c) illustrate this concept.

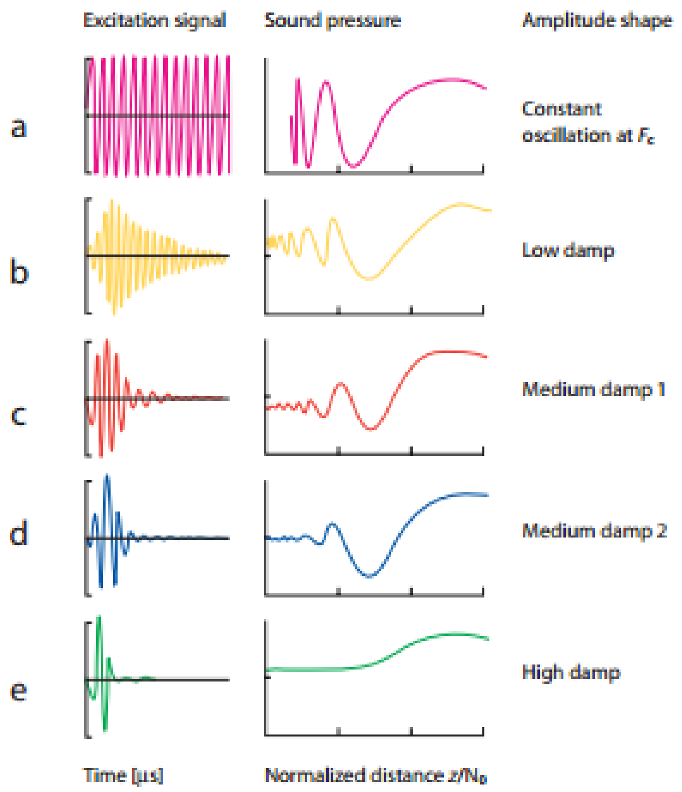

Figure 2-18 Sound pressure under different pulse shape excitation for plane disc-shaped piezoelectric transducer [75]

2.4.2 Beam focusing methodology

In air-coupled system, the air attenuation and the acoustic impedance mismatch are both large as mentioned in Section 2.1. The beam focusing is critical to maximise the energy transfer, increase signal to noise ratio and improve the detection sensitivity. Two main methods which have been used in the beam focusing are physical focusing method and electrical focusing method.

2.4.2.1 Physical focusing method

The physical focusing method, also known as passive focusing technique, uses additional components to achieve the desired focusing beam pattern. Lenses are the most commonly used, as shown in Figure 2-19 (a), with the beam steering achieved using refraction theory. Kelly [8] shows the results of a clear focusing at 40 mm distance by using a Perspex lens with a 40 mm radius. Robertson et al designed a wideband cylindrical transducer to focus with maximum intensity at a distance of 28 mm from the transducer when operating with a central frequency 500 kHz [76]. An apodization cone allows narrowing of the ultrasound beam to achieve focusing, at the expense of signal amplitude reduction and energy losses, as shown in Figure 2-19 (b). Off-axis parabolic mirrors are illustrated in Figure 2-19 (c) and have been used to focus the ultrasonic beam by using a reflection technique. Unfortunately, such devices are difficult to align during operation as there is no evident propagation axis. Figure 2-19 (d) is the Fresnel zone plate (FZP), in which the radii are calculated using Equation 2-10. Focusing is achieved through diffraction generated from the transmitter rings producing constructive interference. Different from the cumbersome devices such as lenses, apodization cone or mirrors, a device incorporating the FZP approach can have a low profile. However, only a fraction of the ultrasound beam reaches the focus point due to the masking effect of the opaque rings mask.

$$r_n = \sqrt{\lambda F n + \frac{\lambda^2 n^2}{4}} \quad n = 1, 2, 3 \ldots. \tag{2-10}$$

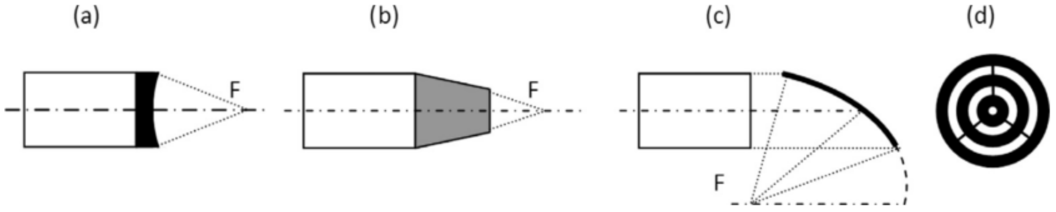

Figure 2-19 Physical focusing techniques

(a)lens; (b) apodization cone; (c) off-axis parabolic mirror and (d) Fresnel zone plate [77]

Álvarez-Arenas proposed a novel method in 2016 based on a variation of the Newtonian telescope. The transducer itself plays the role of the second mirror. The focus distance X can be calculated by Equation 2-11, where F is half of the lens' curvature radius and L is the primary mirror's location. This arrangement provides low noise, low losses and symmetrical beam [77].

$$X = F - 2L \tag{2-11}$$

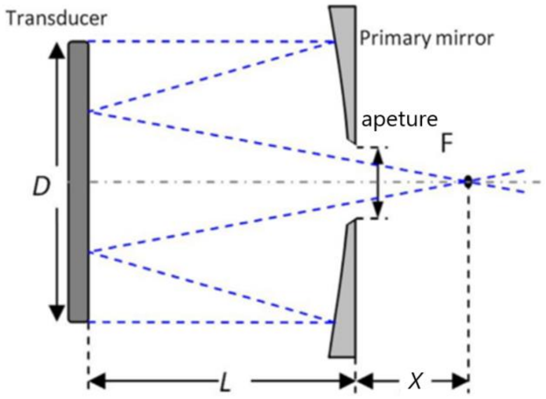

Figure 2-20 Newtonian-Cassegrain focusing principle. The focusing can be achieved through the primary mirror and the transducer itself plays the role of the second mirror. [77]

For the physical focusing method, one problem is that the focal distance is fixed. The approach to perform a scan is by moving the transducer to ensure full coverage of the component. Moreover, the only way to change the focal distance is by changing the mirror or lens which will increase the manufacturing complexity. Another drawback is that all the additional parts will make the transducers more bulky than the original transducer itself.

2.4.2.2 Electrical focusing method for annular array / focal law calculation

Electrical focusing methods use a series of pre-calculated excitation signals to fire each element in an array configuration. The focusing is achieved through superposition of the propagating waves from each array element. The time delays associated with the entire array elements in a transducer is called the focal law, which is based on fundamental trigonometric rules.

i. Trigonometric rules for one medium

Normally, for one medium, focal laws are easily calculated using simple trigonometric rules as shown in Figure 2-21 [78,79]. The centre points of each element are used as the exit point of the beam. Equations 2-12 and 2-13 describe this calculation for the one medium method.

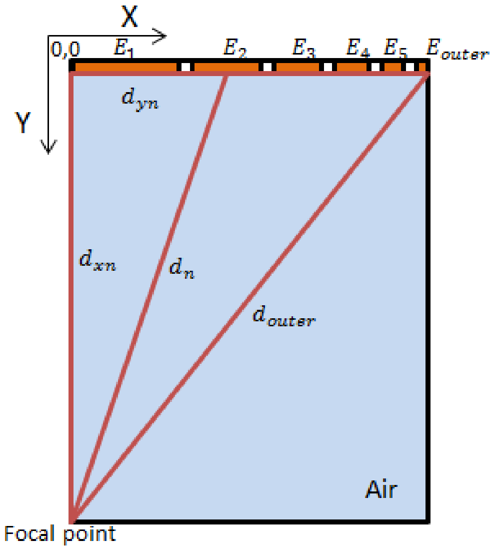

Figure 2-21 Sketch of the simple trigonometric rules to calculate the focal law for one medium. The distance differences between each elements (E1, E2, E3, E4, E5 and Eouter) and the focal point caused the arrival time differences.

$$d_n = \sqrt{d_{xn}^2 + d_{yn}^2} \tag{2-12}$$

Where: n is the number of the element

d_n is the travelled distance in air for nth element

d_{xn} is x axial projection of d_n

d_{yn} is y axial projection of d_n

$$t_n = \frac{d_{outer} - d_n}{c_{air}} \tag{2-13}$$

Where: t_n is the focal law

d_{outer} is the travelled distance for the outer elements

c_{air} is the sound velocity of air which is 345 m/s

ii. Trigonometric rules for multimedia propagation

In many real experimental conditions, there are often multi-layers of materials in the detection path. Due to the different sound velocities in different materials, the focal law calculation will be more complex when compared with the single medium case. Fermat's principle states that the sound beam travels the shortest distance in a medium [80]. Figure 2-22 demonstrates the main principles for operation through three media. The most difficult part is to locate x_1 and x_2 ($x_3 = radius - x_1 - x_2$).

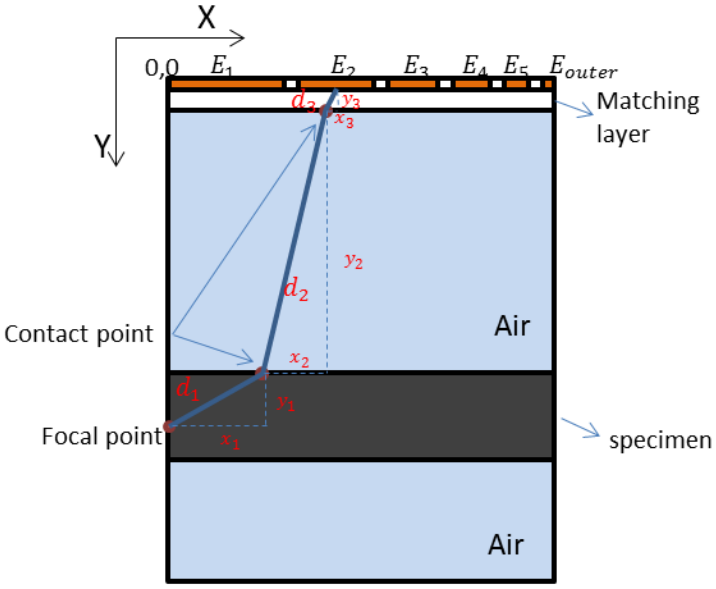

Figure 2-22 Sketch of the main focal law principle for operating through three media. The distance between the element and the focal point is not a straight line.

$$d_1 = \sqrt{x_1^2 + y_1^2}\ ;\ d_2 = \sqrt{x_2^2 + y_2^2}\ ;\ d_3 = \sqrt{x_3^2 + y_3^2} \qquad 2\text{-}14$$

Where: y_1 is the depth of the focal point under the specimen

y_2 is the front air thickness

y_3 is the thickness of the matching layer

x_1 and x_2 is the beam propagation contact points calculated by matlab

x_3 is calculated by the centre of each element minus x_1 and x_2

d_1 is the distance that the beam travels in the specimen

d_2 is the distance that the beam travels in the front air

d_3 is the distance that the beam travels in the matching layer

$$T_n = \frac{d_1}{c_{specimen}} + \frac{d_2}{c_{air}} + \frac{d_3}{c_{ml}} \tag{2-15}$$

Where: $c_{specimen}$ is the sound velocity for a particular specimen

c_{ml} is the sound velocity in the matching layer

c_{air} is the sound velocity of air which is 345m/s

T_n is the total time of the beam travels for nth element in this equation

$$t_n = T_{outer} - T_n \tag{2-16}$$

Where: t_n is the focal law

T_{outer} is the total time of the beam travels for the outmost element in this equation

2.5 Matching Layer Design for Air-Coupled Devices

For a high acoustic impedance transducer designs, incorporating piezoceramic or single crystal active materials, the mismatch between the transducer material and the air coupling medium is immense. One way of reducing the mismatch is to incorporate matching layers to the outer surface of the transducer, as illustrated in Figure 2-23. The figure indicates that the matching layer solution can comprise one or many layers. A good matching layer can improve the transducer's performance and increase the power transmitted into the medium. It has been noted from Table 2.2 that the removal of the water will increase the system insertion loss from 165.56 dB to 26.09 dB, hence the requirement for efficient acoustic matching within an air-coupled system is of vital importance.

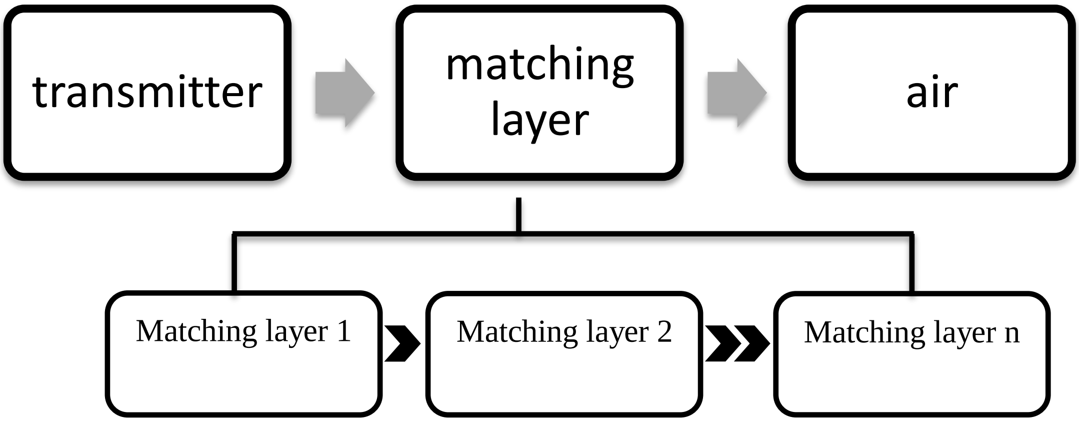

Figure 2-23 Transmitter's matching layer

Toda presented a new type of matching layer in 2002 [81]. A reflective layer structure is set up between the transducer and medium with a small air space. The transducer's impedance can then be matched with the medium by adjusting the air space. The reflective layer consists of a thin membrane, or a perforated thick plate. In either the thin-membrane or the perforated thick plate case, the received signal has an improvement up to 10 dB, but only in a narrow frequency band around 40 kHz. In 2004, Kelly et al. developed a multilayer matching layer with a combination of membrane filter (MF) and silicone rubber (SR) which has been found to be an appropriate matching layer material for air-coupled piezocomposite configurations [82]. The two constituent materials are easy to obtain and relatively inexpensive. The MF is nylon microporous membrane filter with a pore size around 0.45 μm resulting in a low acoustic impedance material. Moreover, it has the added benefit of a relatively simple manufacturing process. The silicone rubber is a room temperature vulcanizing (RTV) rubber resulting in an elastomeric material – the nature of the RTV facilitates the manufacture of shapes, forms and thicknesses for the construction of the matching layers. A significant signal gain of 30 dB has been achieved with the most efficient matching layer designs when applied to a pitch-catch air-coupled system. Álvarez-Arenas introduced an active outer layer material, ferroelectret film, which has a stable piezoelectric response and is also thin [83, 84]. Its heterogeneous structure results in significant low acoustic impedance, which is lower than 0.1 MRayl, but at the same time, it has a high attenuation property of 2600 Np/m. There are no results showing how large a gain could be achieved after the matching layer being attached, but good time domain results displayed indicate that the polypropylene foam ferroelectret film is a good candidate material for air-coupled transducer designs.

The MF and SR combination matching layer will be discussed in more detail in the next Chapter, with the objective to improve the reliability of manufacture process and get better performance matching layer systems.

2.5.1 Impedance and thickness design for the matching layers

The Equation 2-17 shows the fundamental calculation for the impedance of a single layer matching layer.

$$Z_l = \sqrt{Z_P Z_a} \tag{2-17}$$

Where Z_p represents the acoustic impedance of transducer, which would be 21 MRayl for a 70 % CVF piezocomposite, and Z_a is the impedance of air which is 430 Rayl, as shown in Table 2.1. So for a single layer material, the matching layer material acoustic impedance Z_l should be 0.095 MRayl. However, there is no standard material currently suitable to facilitate ideal matching to an air load with low impedance and low attenuation. Therefore, most matching layer research focuses on a multiple layer matching layer approaches. Equation 2-18 shows the basic “n” stack matching layers calculation.

$$Z_{l(i)} = \sqrt[n+1]{Z_p^{n-i+1} Z_a^i} \tag{2-18}$$

Where i indicates the layer number with respect to the surface of the transducer. For a double-matching layer:

$$Z_{l(1)} = \sqrt[3]{Z_p^2 Z_a} \qquad Z_{l(2)} = \sqrt[3]{Z_p Z_a^2} \tag{2-19}$$

Alvarez-Arenas and Diet showed that for ideal matching layer situations, more layers will produce better performance, but in reality, the ideal outer matching layer is not realisable, and the number of layers can increase the insertion loss for each layer. So a matching layer with 3 or 4 layers is considered to achieve the best performance [85].

The thickness of the matching layers should also be optimized for the best performance. When the matching layer has a quarter wavelength thickness at the operational frequency, the coupling performance is maximized [8, 82, 86,]. Figure 2-24 shows the transmitter’s signal reflection results when the matching layer thickness is a quarter of wavelength, half wavelength and three quarter wavelengths. The black sine wave is the original transmitted signal, the red line is the reflected signal from the matching layer/air boundary, and the blue line is the reflected signal from the matching layer/transmitter boundary. The odd number of a quarter wavelength thickness has a signal cancellation phenomenon which minimises the influence of the reflection from each matching layer/air boundary and matching layer/transmitter boundary.

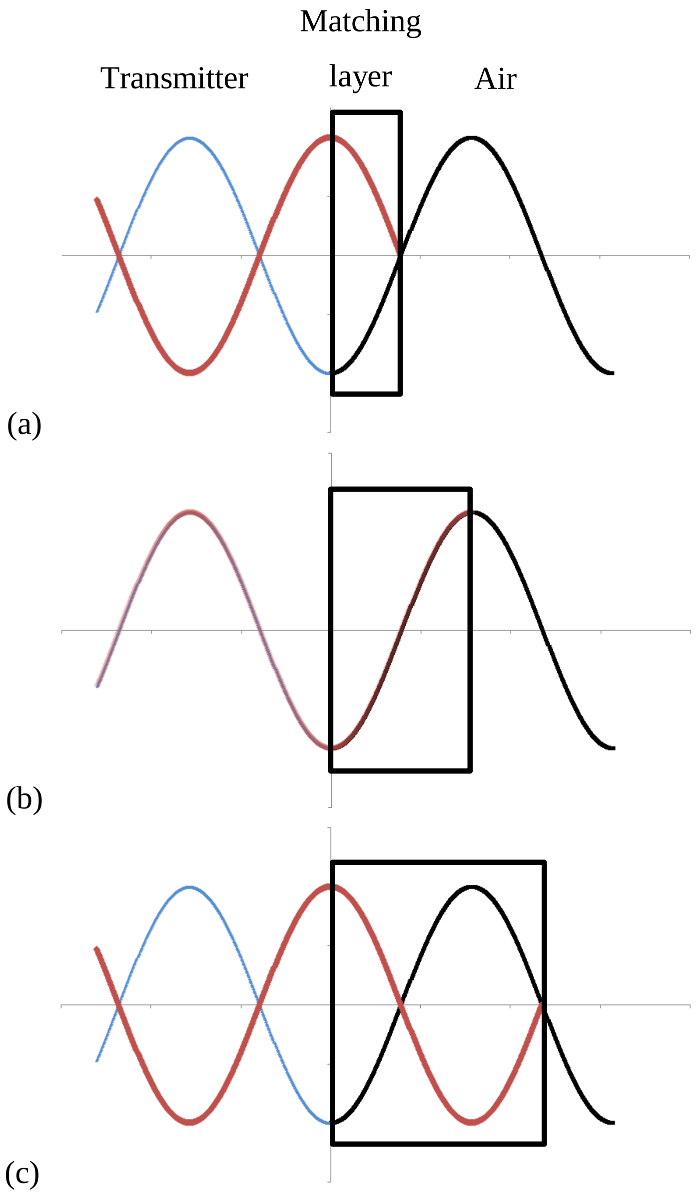

Figure 2-24 The cancellation principle of using the odd number of quarter wavelength thickness matching layers: (a) λ/4 wavelength thickness, (b) λ/2 wavelength thickness, (c) 3λ/4 wavelength thickness. The black sine wave is the original transmitted signal, the red line is the reflected signal from the matching layer/air boundary, and the blue line is the reflected signal from the matching layer/transmitter boundary.

2.6 Phased Array Controller Instrumentation

For single channel transmitter and receiver systems, a basic function generator and oscilloscope are often used for ease of setting up and conducting basic tests. However, for array transducers, the phased array controller (PAC) should be used for beam steering and image processing. Some researchers build their own array controller [87], but there are many commercial instruments available and two have been used in this Thesis.

2.6.1 Zetec Dynaray

The Zetec Dynaray-256/256PR, as shown in Figure 2-25, is an ultra-high performance phased array ultrasonic technology instrument. The Dynaray instrument can drive across wide range frequencies from 0.5 MHz to 20 MHz, with a pulser voltage up to 200 V.

The controlled software platform, named UltraVision, offers the chance to set up the focal laws and drives the active elements up to 256 simultaneously. This provides a 3-D work environment to create the components structure and realise the data visualization immediately.

Figure 2-25 Dynaray-256/256PR instrument from Zetec Inc. [88]

2.6.2 Diagnostic Sonar Ltd InspectaFlaw (DSL)

The DSL instrument, as shown in Figure 2-26, is a real time phased array instrument which is designed for high performance ultrasound systems. It offers different hardware configurations based on National Instruments technology and can drive up to 256 active elements. It also has accessories, such as position sensor trolley, which is a small device mounted on the transducer which can provide accurate positional information when moving the transducer to generate a C-scan or B-scan through real time imaging.

The software platform, named DSLFITfocusStream or DSLFITacquire, allows the adjustment of the parameters of the pulse, which is a specified number of half cycles at a desired frequency. This is configurable and can be set up to deliver tone burst excitation or a linear chirp, for example. The power supply drives the system in a range from -100 V to + 100 V.

Figure 2-26 DSL instrument [89]

2.6.3 Dynaray and DSL PAC comparison

Both of these two instruments are high performance devices which can drive the array transducers in a range of 200 V. The different is the Dynaray can only send a mono cycle pulse with a specific pulse width up to 200 V, and the DSL can control the number of half cycles with a specific frequency from – 100 V to + 100 V.

These two instruments allow bespoke module set up and patchboards are available for different connectors. Dynaray-256/256PR has four Hypertronics ports which can satisfy the requirements for the pulse-echo mode and pitch-catch mode systems. Whereas, DSL requires different hardware for different transducers and the DSL has only one port when connecting to a Hypertronics connector.

For focal law set up, both of these two instruments have focal law modules, but they are designed for linear array configurations. However, both software modules allow for loading personal focal law set ups to control each element in the array. For linear array operation, both instruments have facilities to calculate the focal law and only need to set up the focusing point in the software. For complex shapes array, Dynaray is the more powerful module for focal law control, as it can apply different time delay for each elements of transmitter and receiver, separately. DSL can only set up the transmitter's focal law in pitch-catch mode system. For the scanning data acquisition, the Dynaray's data visualization property can show the received signal with receiver's focal law data immediately. For DSL, the result needs further data processing or the software needs to link to a bespoke programme associated with the specific receiver's focal law.

2.7 Summary

An air-coupled transducer system has a lot of challenges due to the air medium, which has a higher attenuation compared with water medium and the reflection losses at solid/gas interfaces are significant due to the acoustic impedance mismatch. Traditional transducer technologies have been discussed. The advantages and disadvantages of three different piezoelectric material types, namely piezoceramic, piezopolymer and single crystal materials, have been introduced. The piezocomposite 1-3 configuration is considered a good choice for use in an air-coupled system rather than 2-2 structure.

This Thesis will design and evaluate annular array configurations and hence, the range of array configurations was presented and their relative merits discussed. 2-D patterns offer a superior performance on controllability, but increase the complexity in manufacturing at the same time. For operation in air, standard phased array operation using pulse excitation is not appropriate as this results in a lower energy compared to the tone burst excitation signal. Therefore, tone burst excitation will be chosen for the experiments in this Thesis as it can provide higher energy transmission levels. However, this will cause a complex interference pattern in near field and is characteristic of a very narrow operational bandwidth. For array technology, beam control is introduced electrical methods, where specific time delay laws are applied to drive the individual elements in the array device. The annular array design, fabrication and evaluation will be discussed in Chapters 4 and 5.

To improve air-coupled piezocomposite performance, a matching layer system must be included into the design. There are a number of potential options and the fabrication and evaluation of a hybrid SR and MF configuration will be the subject of Chapter 3.

CHAPTER 3 A Robust and Reliable Fabrication Process for Air-Coupled Matching Layers

Abstract

Ultrasonic piezoelectric transducers typically have a matching layer attached to the front face to improve both sensitivity and bandwidth performance. In particular, air-coupled piezoelectric transduction requires the application of a multi-layer matching layer assembly to provide a useable SNR. These matching layer assemblies are attached to both the transmitter and receiver for pitch-catch operation and efficiency gains of ~15 dB have been reported for each device [82].

This Chapter will explore the fabrication process for a multi-layered matching layer, which is a combination of silicone rubber and a membrane filter. This configuration can provide excellent improvement in sensitivity [82], but reliable and repeatable manufacture is challenging to achieve. Consequently, a more reliable manufacture method is introduced, significantly shortening fabrication time, is easier to handle, and capable of delivering similar performance compared to the traditional method.

A series of modelling and experimental results will be presented and compared to determine the appropriate thickness of the matching layer applied to a 600 kHz air-coupled single-element piezocomposite transmitter and receiver.

3.1 Introduction

The requirement for manufacturing an appropriate matching layer with satisfactory performance for inclusion in an air-coupled system is widely recognized due to the acoustic impedance mismatch, especially when compared with an immersion system, as explained in Section 2.1. There have been many promising research projects carried out regarding air coupling medium systems. In particular, the quality of matching layer attached to the transducer will influence the transducer's performance. Stephen Kelly and Gordon Hayward [82] demonstrated that a combined silicone rubber and membrane filter approach provides good efficiency for air-coupled piezoelectric composite transducers. Unfortunately, the manufacturing process was not considered in detail and repeatable manufacture of this matching layer technique is challenging.

This Chapter builds on the previous manufacturing process [8], and a quantitative analysis has been taken to test the reliability of the process with a large number of manufactured matching layers. An efficient and new method to manufacture matching layers with the same constituent materials is introduced, using a K coated machine (K202 control coater manufactured by Print Coat Instruments Ltd.). The new method makes the silicone rubber cure quicker; hence, shortening the processing time significantly and the curing process which is exposed to air directly can be easily monitored. Microscope tests to extract the cross-section detail confirm the internal microstructure of the latest matching layer materials is consistent with the original reported structure. A reliability test follows, as well as an experimental comparison between the traditional pressure method and the coated method.

3.2 Air-coupled matching layer approach

In Section 2.5, the basic thickness design matching layer theory was introduced, which indicates that the best coupling performance can be achieved when the matching layer acoustic impedance is the geometric mean between the transducer and the load and has a quarter wavelength thickness at the transducer operational frequency. For a piezoelectric transducer operating into an air load, this standard theory is not applicable as the acoustic impedance of the required matching layer material is difficult to obtain. One successful approach was developed by Kelly et al [8, 82], in which a multi-layer, matching layer structure was manufactured and a series of experiments undertaken to decide the appropriate layer thickness for both a 600 kHz transmitter and receiver pair. The two constituent materials SR and MF are easy to obtain and relatively inexpensive. The MF is nylon microporous membrane filter, with a 0.45 μm pore size, 47 mm diameter and 0.12 mm thick (HNWP04700 manufactured by Merck Millipore Ltd.). The SR compound (RS 692-542 and manufactured by RS components Ltd.) specifications indicate that the curing time is 7 days at 23 ℃. This will be addressed during the manufacturing description later in this Chapter. In addition, the operating temperature range for the SR is between -65 ℃ to 180 ℃ which is suitable for most inspection conditions for an air-coupled system.

Figure 3-1 shows the structure of these matching layers. MSR is short for modified silicone rubber which is a transition layer between the silicone rubber, SR, and membrane filter, MF, and the SF indicates the part of the membrane filter which has become saturated with silicone rubber, because the MF is microporous. Note that the SF layer does not extend through the full MF thickness. Due to the thin nature of SF and MSR, these two layers in this thesis will be considered as one layer in modelling, and hence, there is a three layer graduation in acoustic impedance from the silicone rubber through to the porous membrane filter outer layer. The fusion layer comprises SF and MSR and is important as it will offer a great inner graduation between SR and MF and transmit more power.

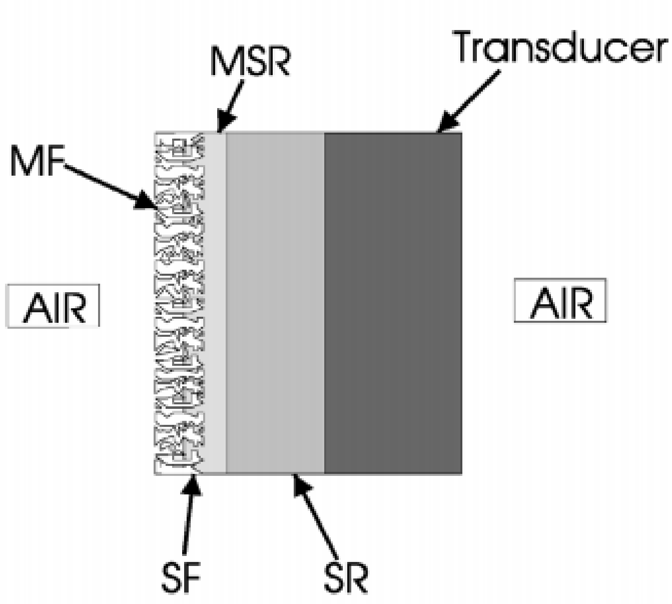

Figure 3-1 Structure of air-coupled matching layer using a combination of membrane filter and silicone rubber [82]

3.3 Development of the matching layer manufacturing process

The matching layer is a combination of SR and MF. The manufacture process is mainly introducing SR onto the MF. Different manufacture tools and methods are introduced in this section.

3.3.1 Fabrication tool development based on an extension of the original methodology

The original fabrication tools are two Perspex plates covered with cling film and fixed on a mechanical frame which is introduced by Kelly [8]. The thickness of the finished matching layer is controlled using mechanical spacers inserted between the plates to set the layer thickness. The main drawback in using cling film is the inconsistency in achieving a 100 % smooth coverage across both plates, which will cause a defective feature in the matching layer, as shown in Figure 3-2. Moreover, only one or two matching layers can be produced at a time with this approach, which is time-consuming, albeit the demand for matching layers is relatively low.

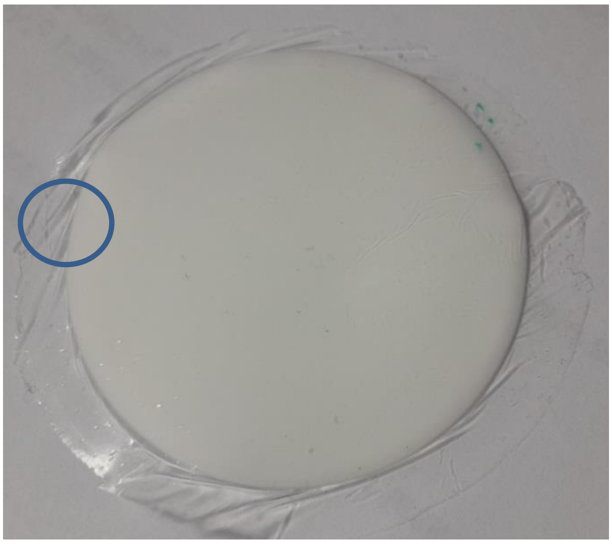

Figure 3-2 Example of a matching layer made using the Perspex plates approach. Note the ripples in the cling film encapsulating the matching layer structure

To remove the issue associated with the use of cling film, which is used to prevent adhesion of the SR phase onto the Perspex plates, a PVC plate is utilised on the silicone rubber side. The second plate is still made from Perspex as this transparent material can allow monitoring of the process and ensure the silicone rubber does not seep entirely through the MF layer. The PVC surface is non-stick, from which it is possible to peel the matching layer off easily in a clean working environment. Figure 3-3 illustrates this set-up, where two matching layers are produced simultaneously.

1. Metal frame
2. Matching layers
3. Spacers

Figure 3-3 Modified matching layer fabrication rig

3.3.1.1 PVC plate and Perspex plate manufacturing process

The manufacturing steps involved in this matching layer process are now detailed:

1) *Clean the surface areas*

   Use fine grade sandpaper (grade - P600) to clean any residual SR from the PVC plate surface. Followed by removing the fine dust layer by wiping the surface with isopropanol alcohol (IPA) - this is achieved by spraying the IPA onto a tissue.

2) *Press the cling film onto the Perspex plate*

   Take a piece of cling film which should large enough to cover the plate. Pull the cling film to make it as smooth as possible and adhere the edges to the top of the plate. Cut four holes using a scalpel, aligned with existing holes in the Perspex, to enable attachment to the metal frame.

3) *Calculate SR fabrication parameters*

   These calculations ensure consistent application of the SR phase into the matching layer system. This calculation, Equation 3-1, will be undertaken for different MF diameters or a different SR. For the current configuration, the calculation is:

   The parameters of the MF used are:
   Diameter: D = 47 mm
   Thickness: H = 0.12 mm

   The diameter of SR should be larger than 47 mm to ensure it fully covers the MF material and 50 mm in diameter is suitable for use in the calculation. The fabrication parameters for the SR phase are:

   $r = 25$ mm 3-1
   h = final matching layer thickness design value – H,
   SR density: $\rho = 1.03\ \mathrm{g}/cm^3$
   SR volume: $V = \pi \times r^2 \times h$
   SR mass: $m = \rho \times V$

   Where: r is the radius of the silicone rubber
   h is the thickness of the silicone rubber
   H is the thickness of the membrane filter

4) *Choose spacers*

Based on the matching layer design thickness, choose suitable spacers and place them towards the edge and close to the centre of each side of the PVC plate, as shown in Figure 3-3.

5) *Apply SR phase*

Put the PVC plate on the weighing scales and reset the scale to zero. Use scales to monitor the weight of SR applied onto the plate until it reaches the calculated mass in step 3 for the desired matching layer thickness.

6) *Air bubble removal*

Use a sharp tool to prick/release any air bubbles trapped inside the SR.

7) *Apply MF phase*

Place the membrane filter on the top of the silicone rubber. Next apply the Perspex plate, with cling film side down, and press it down slowly onto the MF and SR materials to let the SR spread evenly.

8) *Apply pressure*

Then use a metal weight to ensure a consistent pressure during the curing phase.

9) *Material curing*

Curing time varies with the mass of the SR. It should be more than 12 hours, normally overnight. This is less than the 7 days defined in the specification, but has been deemed appropriate through experimental evaluation of many matching layer assemblies.

10) *Peel off the matching layers*

Separate the PVC and Perspex plates and peel off the matching layer from the PVC plate gently.

Even though the steps of making matching layers are clear and easy to follow, there are still many uncertain factors in every step and they will influence the final product.

- The PVC surface should be clean and smooth, otherwise the SR will stick on the plate and the surface of the SR face on the matching layer will not be sufficiently smooth. The roughness of the PVC is controlled by the roughness of the applied sandpaper.

- The volume of the SR not only has influence on the curing time, but also guarantees the SR covering the MF completely. It should be calculated accurately. During Step 7, the MF should entirely cover the SR, ensuring that the SR mass is in the approximate middle area of the MF for uniform spreading of the SR.
- Using this approach, the thickness of matching layer has to be maintained between 0.3 mm and 0.8 mm. It is hard to peel off if its thickness is lower than 0.3 mm, and it can become uneven if its thickness is larger than 0.8 mm.
- Any air bubbles inside the SR will cause scattering of the ultrasound and should never appear in a good qualified matching layer.
- The key to the pressing method is slow application, waiting for the SR to spread. The wrong operation may cause the SR spread onto the upper face of the MF or fully saturate the MF layer. The metal frame plate can be only allowed to press down with a continuous and constant pressure.
- Peel off the matching layer gently from one side with a constant power and movement, noting that a sudden change in strength can rip the matching layer or cause permanent deformation.
- Manufacturing the matching layer in a fixed environment which maintains stable temperature and humidity is the basic requirement of the laboratory environment.

3.3.1.2 Curing time investigation

The previous matching layer work always indicated that the curing time should be overnight, but there were no experiments, or trials, to investigate the curing process. The curing time can be determined through a series of manufacturing runs, and initial results indicate that the waiting period should be 12-16 hours, which equates to a standard overnight time period. An increased matching layer thickness will require an increased volume of SR and the curing time will be longer. The following work is to determine how to manufacture a 0.47 mm thickness matching layer in a typically lab environment.

Initially, the quality of SR can be calculated using Equations 3-1 and described in Step 3.

$r=25$ mm

h = final matching layer thickness design value – H

$\rho=1.03$ g/cm^3

$H=0.12$ mm

$$V = \pi \times r^2 \times h = 3.14 \times 2.5^2 \times (0.047 - 0.012) = 0.667 \ cm^3$$

$$m = \rho \times V = 1.03 \times 0.667 = 0.69 \ g$$

The same process was repeated for identical SR and MF conditions, with different cure times applied in order to assess the matching layer quality. The first experiment waited for a 3 hours cure time and the produced matching layer is presented in Figure 3-4. It is obvious that 3 hours curing time is not enough for completing the matching layer. The rectangle section shows that the silicone rubber on the membrane filter is not cured. Next, a 5.5 hours test has been implemented, and the image of the produced matching layer is shown in Figure 3-5. This result showed considerable improvement compared to the 3 hours cure result, although there is a small area which has not fully cured, as indicated by the circle in the Figure. Consequently, slightly increasing this cure time to 6.5 hours produced a fully cured matching layer, as presented in Figure 3-6.

These results show that the original 12-16 hours curing time, and the manufacturers recommended curing time are both too long for this process. However, the cure time will increase with an increase in matching layer thickness and when operating in a research environment, overnight curing is always recommended.

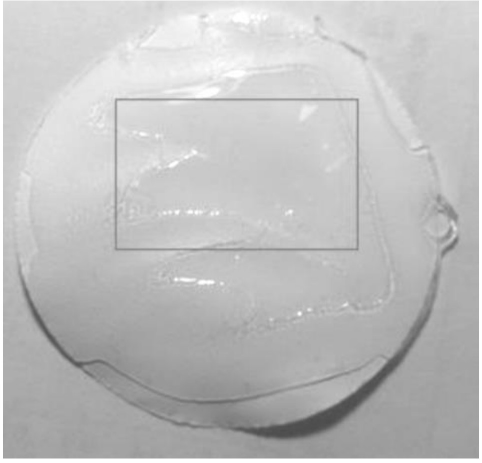

Figure 3-4 Matching layer manufacture with curing time of 3 hours and large area shown in rectangle is not fully cured

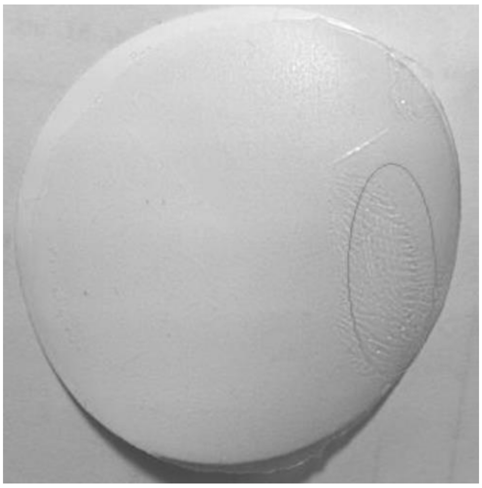

Figure 3-5 Matching layer manufacture with curing time of 5.5 hours and a small area shown in oval is not fully cured

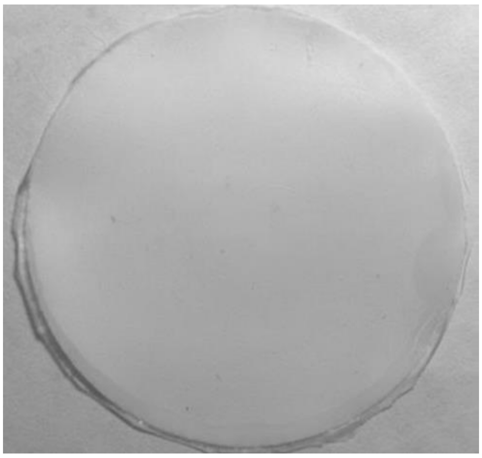

Figure 3-6 Matching layer manufacture with curing time of 6.5 hours which is totally cured

3.3.2 K coated machine manufacturing method

A new method to manufacture the combined silicone rubber and membrane filter matching layer is through the use of the K coated control machine (K202 control coater manufactured by Print Coat Instruments Ltd.). This machine can provide a simple but effective method of applying paints, printing inks, adhesive and other surface coatings onto many substrates such as paper, plastic films, metal plates, etc. The main features for using this coating machine are simple, economical, good repeatability, and stainless steel highly polished bed. Moreover, this method can coat multiple products simultaneously for comparison and offer an opportunity for volume production in the future. Another benefit is that the curing time can be shortened significantly because the silicone rubber is exposed to the air directly, shortening the cure time by up to 3 hours. In addition, it is also possible to fully observe the curing process and monitor for any issues during the process. An image of the K control coating machine is shown in Figure 3-7.

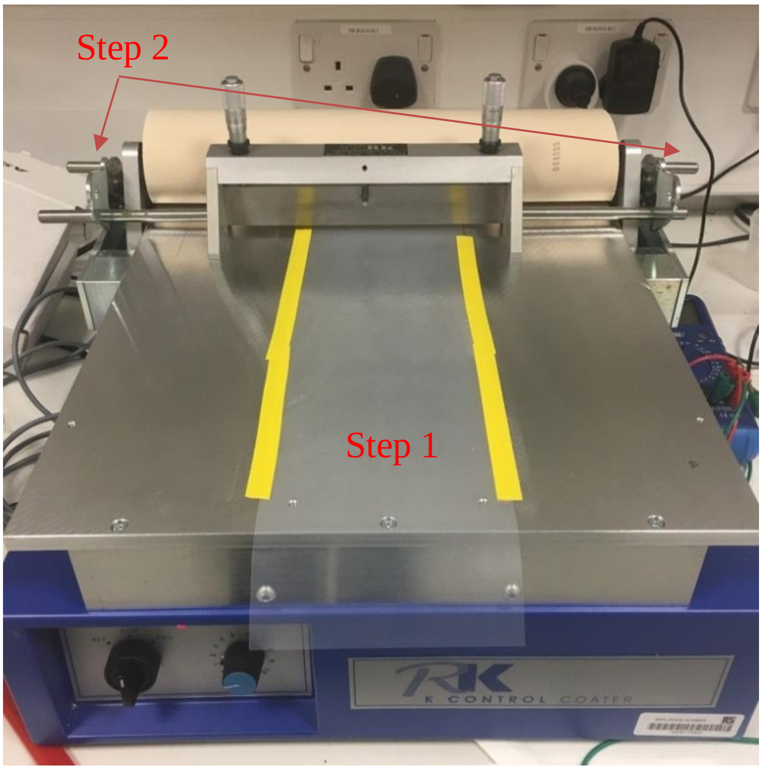

Figure 3-7 K control coated machine, including indications of Steps 1 and 2 of the fabrication process

3.3.2.1 Coating machine manufacturing process

The manufacturing steps involved in the K control coating matching layer process are now detailed:

1) *Machine preparation*

   Fix non-stick sheeting (e.g acetate) onto the steel bed using tape and make sure this is flat, as shown in Figure 3-7.

2) *Lock the coating blade*

   Figure 3-7 shows where the hooks are located to lock the blade tightly into position (indicated as Step 2 in Figure).

3) *Adjust material thickness control*

   The rotary knobs, shown in Figure 3-8, control the gap height between the blade and the steel bed which means they control the thickness of the matching layer afterwards. The height of the gap should be adjusted by following the parameters detailed in Table 3.1 in Section 3.3.2.2, noting that the thickness of the acetate is taken into account.

4) *Apply the membrane filter*

   Tape should be on the top of the membrane filter as the SR will spread from the top or the SR may push away the membranes. A maximum 6 matching layers can be manufactured at one time using this machine.

5) *Application of silicone rubber*

   Squeeze an excess value of SR at the top of the MF in a line as shown in Figure 3-9. What is important is to ensure that the length of the line is longer than the diameter of the membrane filter which is at least 50 mm to make sure the SR can fully cover the membrane filter. When the silicone rubber has been deposited, immediately start the coating machine at its lowest speed setting (position 1), to minimise risk of SR curing while exposed to the air.

6) *Air bubble removal*

   Figure 3-10 illustrates the newly formed MF and SR combination. At this stage, one can use a sharp tool to prick/burst any air bubbles observed inside the SR.

7) *Material curing*

   Curing time varies with the mass of the SR. It typically only needs 3 hours for the SR to fully cure.

8) *Peel off the matching layers*

The matching layer is easily peeled off from the non-stick acetate, as shown in Figure 3-11. Trim the extra SR of the matching layer assembly as required.

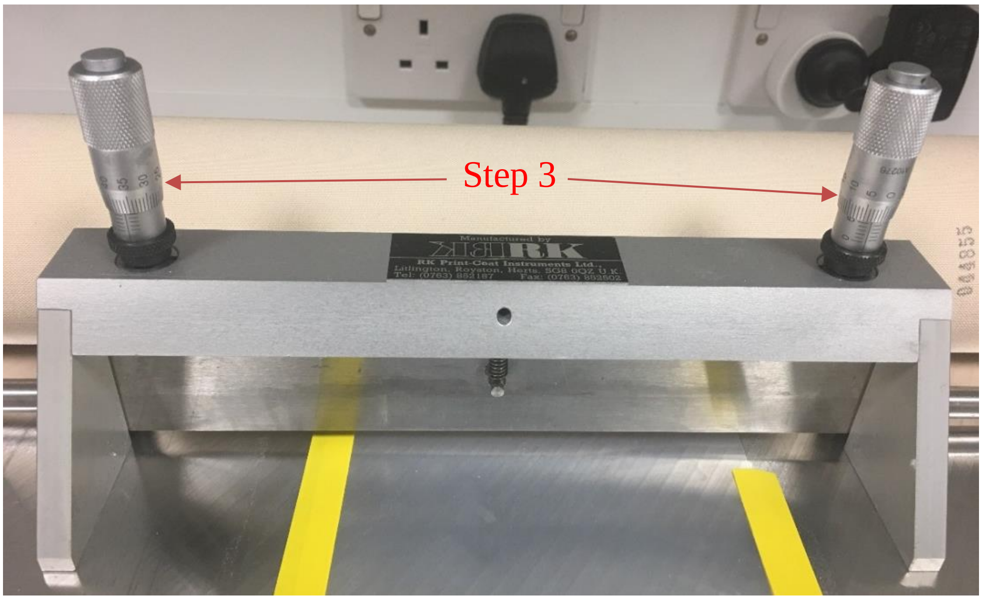

Figure 3-8 Rotary knobs and coating blade of the K control coating machine

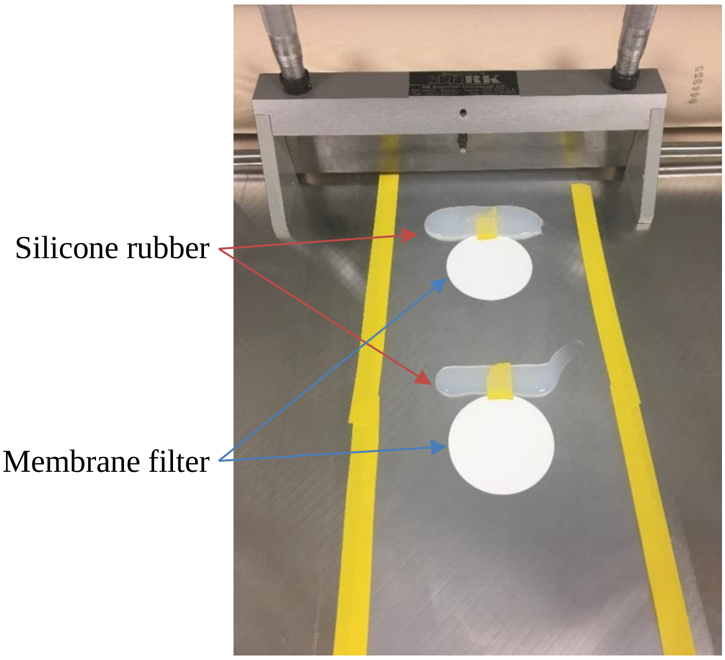

Figure 3-9 Membrane filter and silicone rubber preparation in the K control coating machine. Note that the length of the SR line is wider than the MF diameter and that the SR is placed on top of the tape holding the MF in place.

Figure 3-10 Silicone rubber spread pattern after application using the K control coating machine

Figure 3-11 Removal of the matching layer assembly

Uncertainty factors still exist in the new method.

- There will be machine control errors due to quality of the equipment.
- The metal frame of the K machine should be in the horizontal position and a spirit level can be used to measure this before starting the process.
- The quantity of SR must be sufficient to cover the membrane filter. In this process, there will always be excess SR and hence, the SR line must be wider than the MF diameter so that an excess in the volume/mass of SR applied is suggested.
- Any air bubbles inside the SR will cause scattering of the ultrasound, and should never be allowed to appear in a good qualified matching layer.
- The SR outer layer is exposed to the air directly and can be easily contaminated. It is recommended to use a protective cage/cover over the products and maintain a good laboratory environmental condition, as discussed in Section 3.3.1.1.

3.3.2.2 Qualifying the blade gap thickness adjustment

The blade gap distance in the K machine can control the matching layer's thickness. But the blade gap is not the final thickness of the matching layer due to the shrinkage during the curing process. A series of fabrication experiments has been done to find the relationship between the blade gap height and the produced ML thickness. The matching layer thickness is measured by digital calliper. Due to the deformation of the SR material when measured by the calliper, the measuring tolerance has been tested by 20 repeat measurements with one matching layer, and the tolerance is in the range of ± 0.01 mm. For each gap adjustment, two ML have been manufactured at the same time with same thickness. For each matching layer, the thickness is measured three times. Therefore, the results shown in Table 3.1 represent a total of 6 averages. Plotting these results, see Figure 3-12 (a), shows that the relationship is approximately linear with the polynomial fitting. The Figure 3-12 (b) shows the linear fitting residuals and more than 80% residuals are less than the measure tolerance ± 0.01 mm.

Another ± 0.01 mm tolerance may be caused by the uneven acetate and the adjustment of rotary knobs which is considered acceptable.

Table 3.1 K coated machine's blade gap adjustment guide

Blade gap (mm) – acetate sheet thickness (mm)	*ML thickness ± 0.01 (mm)*
0.38	0.28
0.48	0.34
0.53	0.37
0.55	0.38
0.58	0.40
0.60	0.41
0.67	0.43
0.68	0.46
0.73	0.47
0.75	0.49
0.78	0.50
0.80	0.53
0.83	0.53
0.88	0.54
0.98	0.61

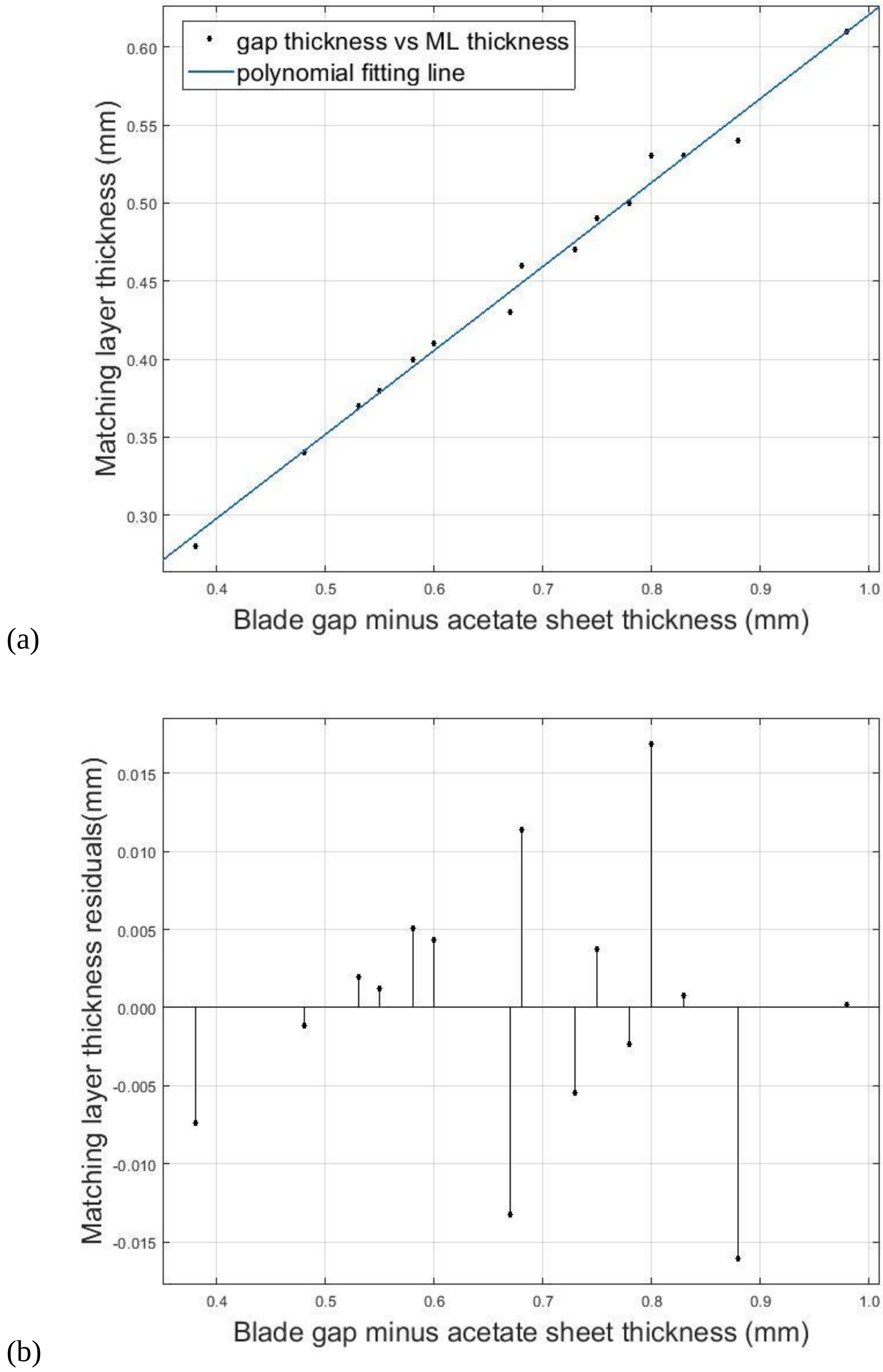

Figure 3-12 Blade gap adjustment guide, (a) linear relationship between the blade gap and the finished matching layer thickness, (b) linear fitting residuals

3.4 Comparing the matching layer fabrication methods

After introducing the fabrication principles and process methods for making an air-coupled matching layer comprising silicone rubber and a membrane filter, this Section will discuss their microstructure and operational characteristics to make a comparison and decide on the best fabrication approach for a reliable matching layer performance.

3.4.1 Matching layer structure and surface roughness comparison

The K coated machine process for matching layer manufacture is 4 times faster in terms of curing, easier to handle, simpler to set up, effortless to peel off, easier to clean the equipment and more reliable than the applied pressure method. However, what is most important is determining how well the new matching layer performs when attached to an air-coupled transducer. It is obvious that if the new matching layer process cannot produce material with at least the same performance characteristic as the original matching layer process, then the case to change the process is unpersuasive.

The microstructure of the matching layers has been investigated through an optical microscope (ML7100 Halogen Trinocular Metallurgical Microscope, Meiji). The setup and sample preparation are shown in Figure 3-13. The image output, with x20 magnification, from the microscope is shown in Figure 3-14 and Figure 3-15, where the side view and the SR surface view are presented for matching layers fabricated using the pressure method and K coating machine method, respectively. The goal is to produce a matching layer with the structure as presented in Figure 3-1, as this has been shown to produce a strong air-coupled transducer performance. These high resolution images reveal the different layers of the microstructure and highlight the interface between the SR and MF materials. As shown in Figure 3-1, the intended microstructure should contain a boundary containing the interface transition layer, MSF, and ingress of the silicone rubber into the porous membrane filter microstructure, SF. These are highlighted in the Figures. These interlayers provide a coupling mechanism between the SR and MF. Interestingly, the matching layer made using the pressure technique has a wider MSR/SF area. The surface view, Figure 3-14(b) and Figure 3-15(b), demonstrates a clear difference in surface finish quality. The matching layer made using PVC and Perspex plates which have some imperfections on the surface as a result of the application of fine grade sandpaper to remove excess silicone rubber between processes, and K coated material has a high quality finish, when compared to the structures produced using the press technique. Whereas with the applied pressure technique, there are clear ripples in the surface finish, which could be detrimental to the acoustic performance of the matching layer and the ripples are too small to seen by visual checking. These microstructural image results indicate that both methods produce similar quality matching layers, with the K coating method producing a slightly more consistent SR outer face.

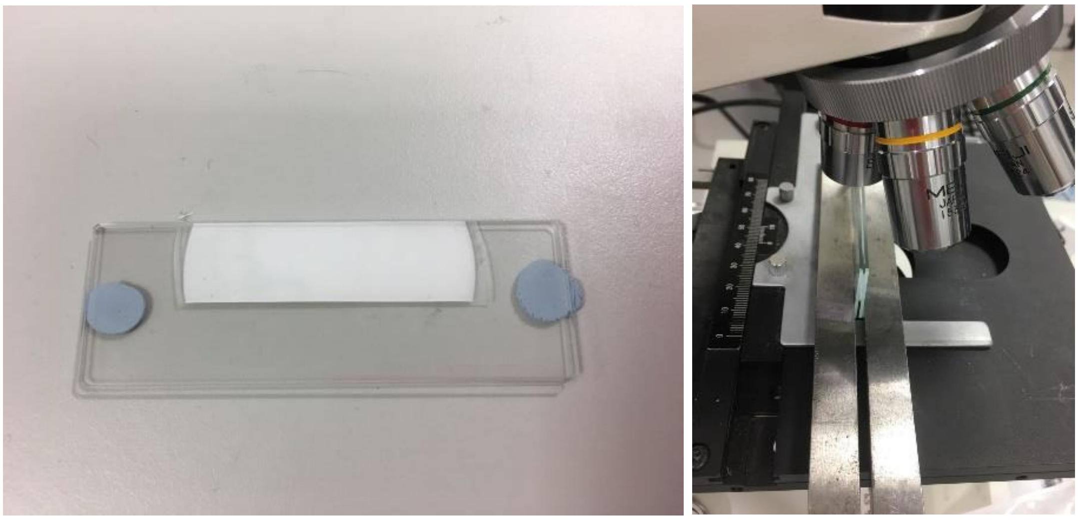

(a) Glass slide with sample of air-couple matching layer attached (b) Close up of the microscope head

Figure 3-13 Images of material to be evaluated and optical microscope equipment used for the evaluation

(a) Image of side view of pressure fabricated matching layer

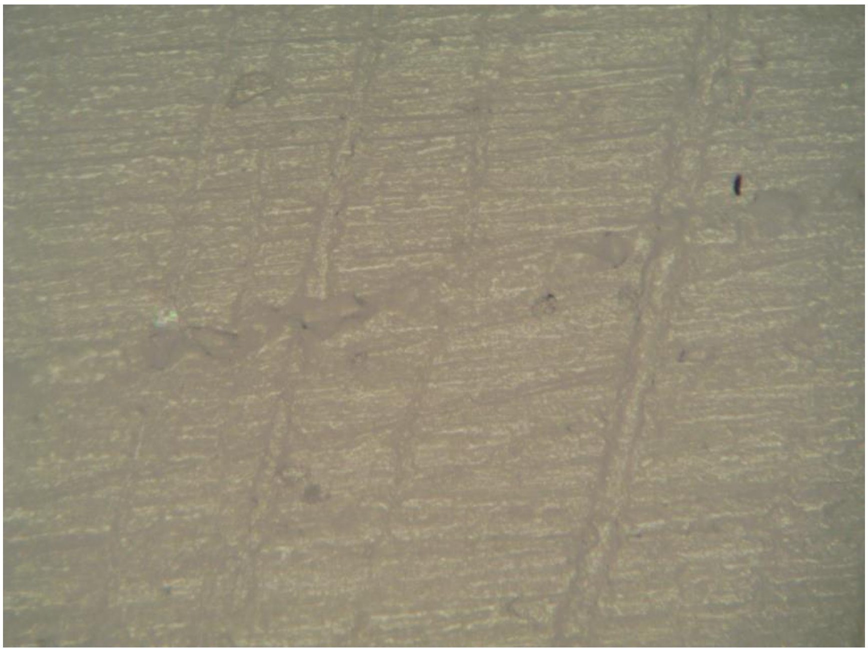

(b) Image of top view of pressure fabricated matching layer

Figure 3-14 Matching layer (a) side view and (b) surface view of material made using pressure method with x20 magnification

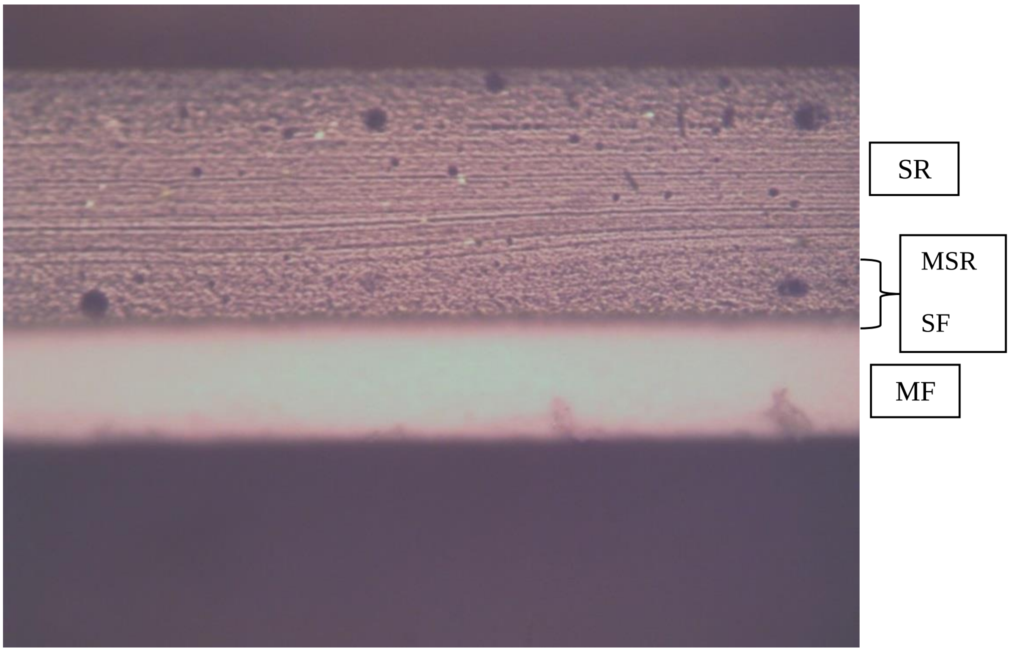

(a) Image of side view of K machine fabricated matching layer

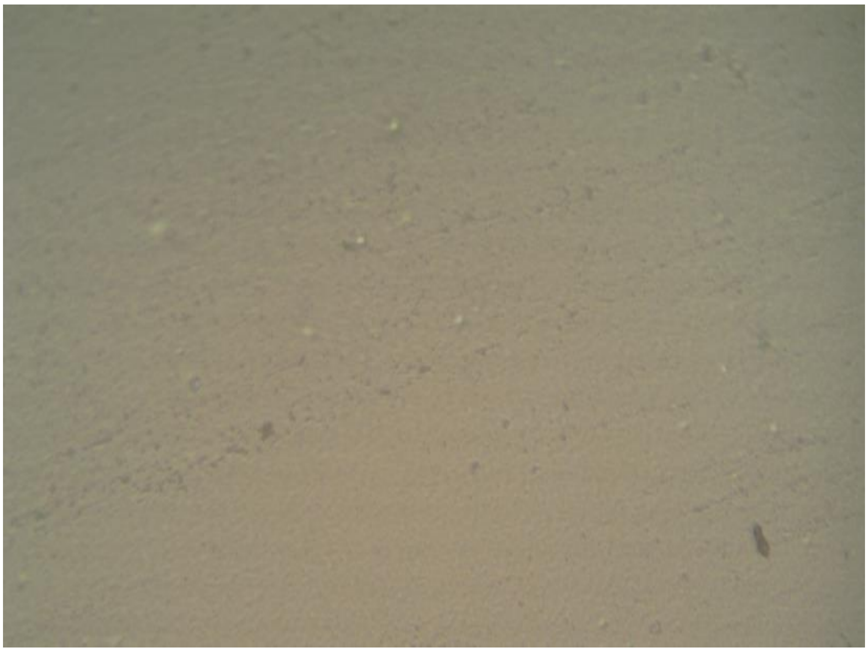

(b) Image of top view of K machine fabricated matching layer

Figure 3-15 Matching layer (a) side view and (b) surface view of material made using K coated machine with x20 magnification

3.4.2 Ultrasonic evaluation experimental arrangement of the matching layer systems

To conduct an experimental evaluation, two 600 kHz 1-3 piezocomposite transducers have been used in the experimental arrangement shown in Figure 3-16. From previous work at Strathclyde, the design for single element air-coupled transducer made using 1-3 piezocomposite technology and operating at a frequency of 600 kHz has been established [8, 82]. These transducers have been used here to test a variety of fabricated matching layer materials. Although, not using the optimum bonding condition, each matching layer has been attached to the transducer surface by using ultrasonic gel. This provides the ability to interchange between matching layers using the same transmitter or receiver device. Full details of the transducers used for this evaluation are provided in Appendix B.

First, the transducer performance was predicted using PZFlex with a matching layer applied and evaluated for the amplitude improvement. The extrapolation method has been used as the speed in the air is too slow and the air path is too long for practical simulation. Extrapolation is a process in which the value is estimated beyond the specific range of given variable. It provides the estimate of the observation below or above the given values. So, a 5 mm modelling distance has been set to obtain the existing trends and this trend will be applied for the 50 mm air path simulation later. A 2-D model in air medium has been built comprising the 1-3 piezocomposite structure, with active and passive materials as shown in Figure 3-17. The matching layer will be added to the model at the top of the piezocomposite. The system is driven by a 600 kHz frequency 5 V, 10 cycle sine wave.

Next, the experimental pitch-catch measurement was acquired as shown in Figure 3-16, which is a quite simple experimental arrangement. A 10-cycle tone burst with 10 V peak-to-peak at 600 kHz was generated by a traditional function generator (33210A Function Generator, Keysight Technologies) to drive the transmitter. And the receiver connect to the oscilloscope (TDS 1002B, Tektronix) to record the received pitch-catch signal.

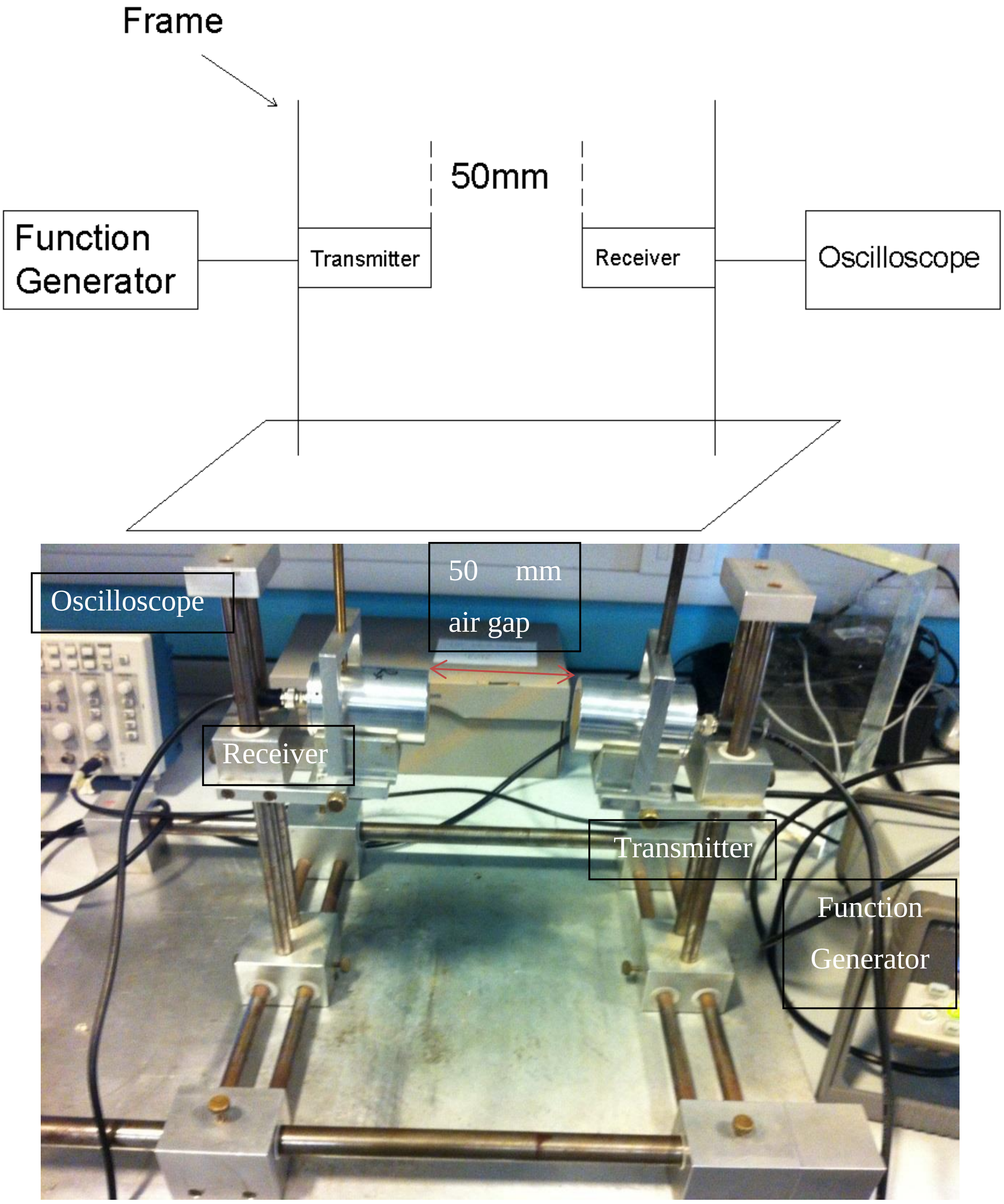

Figure 3-16 Matching layer testing set up using two standard air-coupled 1-3 piezocomposite devices operating in pitch-catch mode through a 50 mm air gap

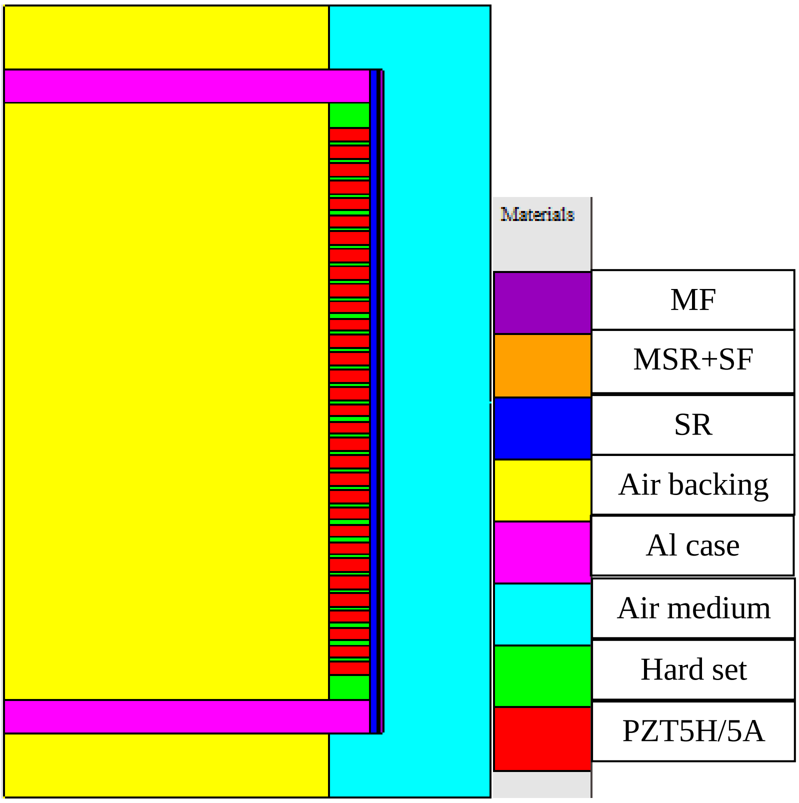

Figure 3-17 PZFlex 2-D extrapolation model to investigate thickness matching layer's performance for the amplitude improvement for air-coupled 1-3 piezocomposite transducers

3.4.3 Investigating matching layer thickness

The structural comparisons introduced in Section 3.4.1, demonstrated an appreciation of the similarities and differences in the fabricated matching layers using either the pressure or K machine approaches. With the matching layer applied on the surface of the transducers, the additional gain in a pitch-catch configuration should be ~30 dB if the matching layer is to be considered suitable for this air-coupled system [82], which will improve the SNR of the air-coupled inspection application. This section is to ascertain the optimum matching layer thickness for both transmission and reception devices operating around 600 kHz and the aim is to find the most suitable thickness range for applying to transmitter and receiver with these two different manufacturing methods. Hence, the experimental set up is shown in Figure 3-16, with a variety of matching layer configurations attached to the transducer front faces to determine their effect on the system sensitivity. In this work, as the MF is a fixed thickness material, which is 0.12 mm, then the overall matching layer thickness is controlled by the SR thickness. In Kelly's thesis [8], his experiment results shown that 0.28 mm SR thickness performs best for transmitter and 0.54 mm SR thickness matching layer performs best for receiver. Therefore, a range of 0.1 mm to 0.5 mm SR thickness matching layers have been manufactured with approximate 0.02 mm steps and applied to the transmitter. A range of 0.2 mm to 0.7 mm with 0.02 mm steps SR thickness matching layers have been made and attached to the receiver. One thing should be mentioned that all measured matching layer thickness has a measurement tolerance ± 0.01 mm, as introduced in Section 3.3.2.2.

For a fixed frequency, the most suitable matching layer thicknesses for transmitter and receiver have been modelled separately, using PZFlex, as shown in Figure 3-17 for the amplitude improvement. For both model and experiments, when finding the suitable matching layer on transmitter, there is no matching layer on receiver. And, when finding the suitable matching layer on receiver, there is no matching layer on the transmitter.

An evaluation has been undertaken for the transmitter device and for operating at 600 kHz frequency, the most suitable matching layer thickness for transmission has been modelled as shown in Figure 3-18. The amplitude improvement is largest when the

SR thickness is 0.36 mm and the gain is useable when the thickness in the range of 0.33 mm to 0.38 mm. The smoothing fitting line uses the smoothing parameter 0.9999887578312688 in both Figure 3-19 and Figure 3-20 which display the relationship between the received amplitude ratio (ratio of maximum sensitivity recorded with and without matching layer) and SR thickness for both manufacturing methods. For this work, the receiver has no matching layer and a variety of matching layers are applied to the transmitter. Hence, the measured data in these graphs represents an improvement in the transmitter efficiency. Interestingly, in all three Figures the optimum matching layer thickness is in the range of 0.30 mm to 0.38 mm, and this will be used going forward for the matching layers used in the transmitter devices designed in the later stages of this Thesis.

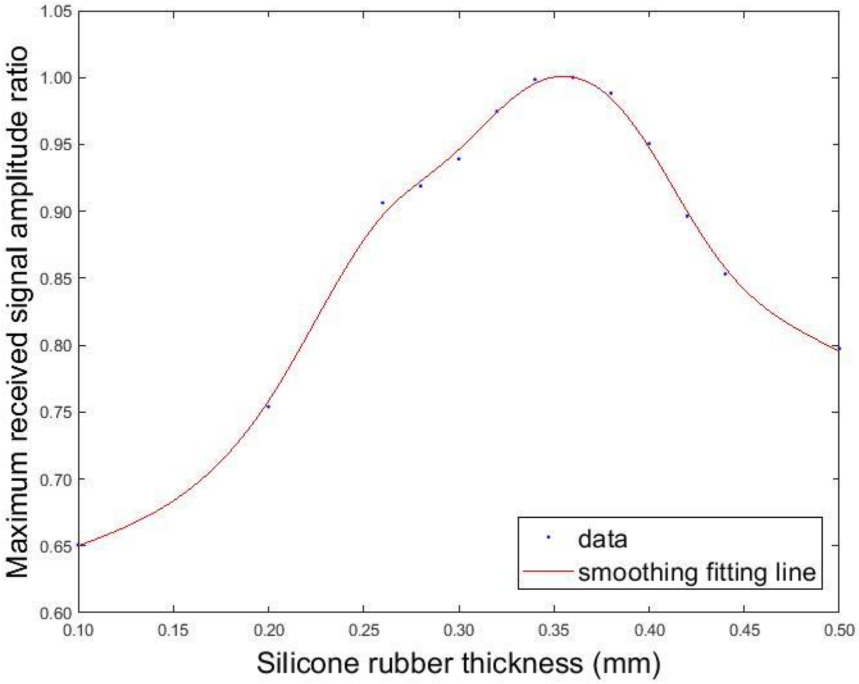

Figure 3-18 Simulated relationship between SR thickness and transmitter efficiency when operating at 600 kHz

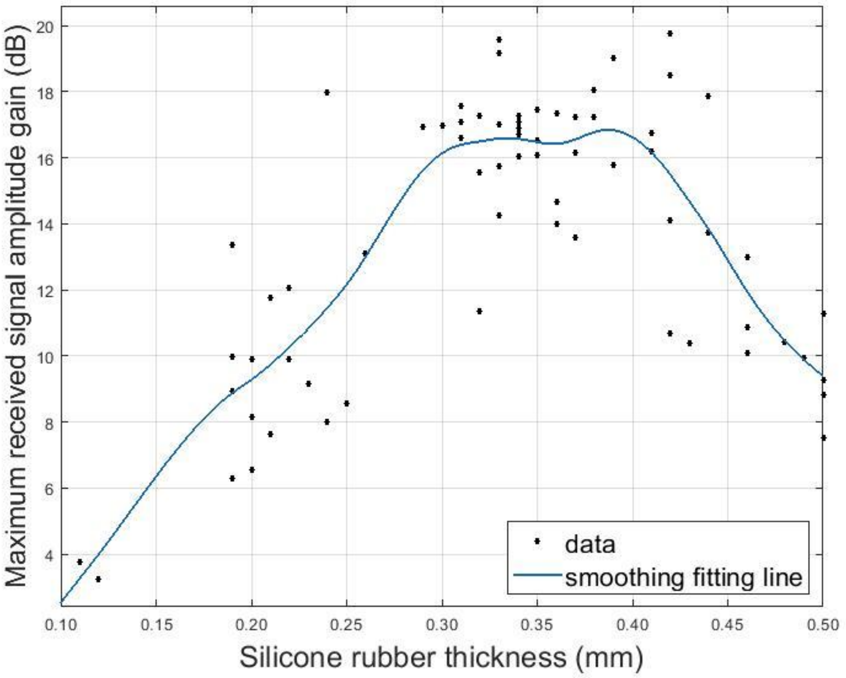

Figure 3-19 Measured relationship between silicone rubber thickness and transmitter efficiency for pressure loading method matching layers by operating on 600 kHz

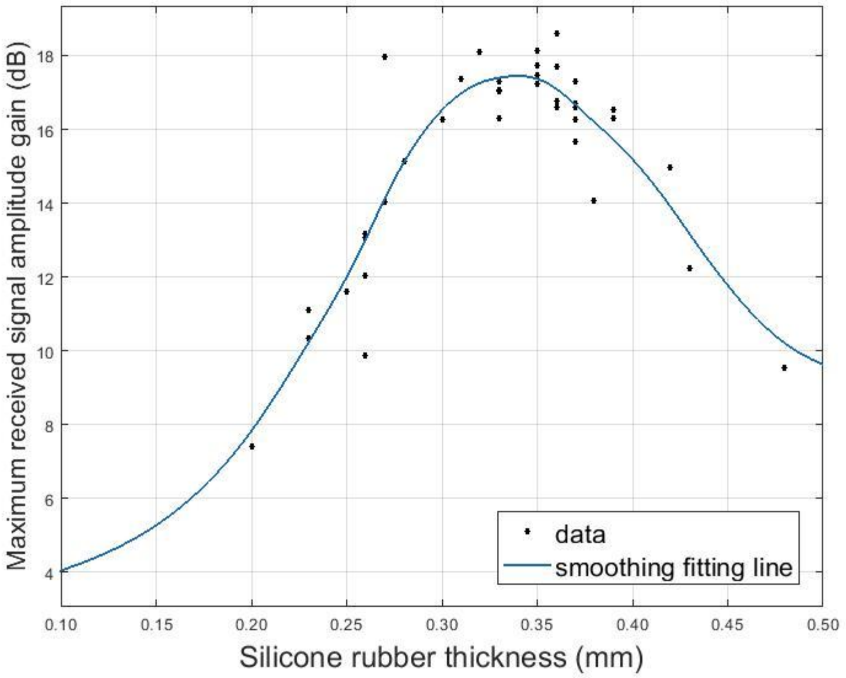

Figure 3-20 Measured relationship between silicone rubber thickness and transmitter efficiency for K coated machine method matching layers by operating on 600 kHz

A similar evaluation has been undertaken for the receiver device, although in this case the transmitter has no matching layer and a variety of matching layers attached to the receiver. Firstly, for operating at 600 kHz frequency, the most suitable matching layer thickness for receiver has been modelled as shown in Figure 3-21. The amplitude improvement is largest when the SR thickness is 0.49 mm and the gain is useable when the thickness in the range of 0.40 mm to 0.53 mm. The smoothing fitting line uses the smoothing parameter 0.9999887578312688 in both Figure 3-22 and Figure 3-23 which display the relationship between the receive sensitivity and SR thickness for both manufacturing methods. The important information from these graphs are that optimum SR thickness for matching layers produced by the pressure method is between 0.37 mm and 0.45 mm and the K machine method is between 0.4 mm to 0.5 mm, which overlaps with the theoretical range. Overall, the receiver experimental results are not as reliable as the data presented for the transmitter and the measured peak sensitivity improvement of 10 dB which is lower than the transmitter's maximum gain of 18 dB.

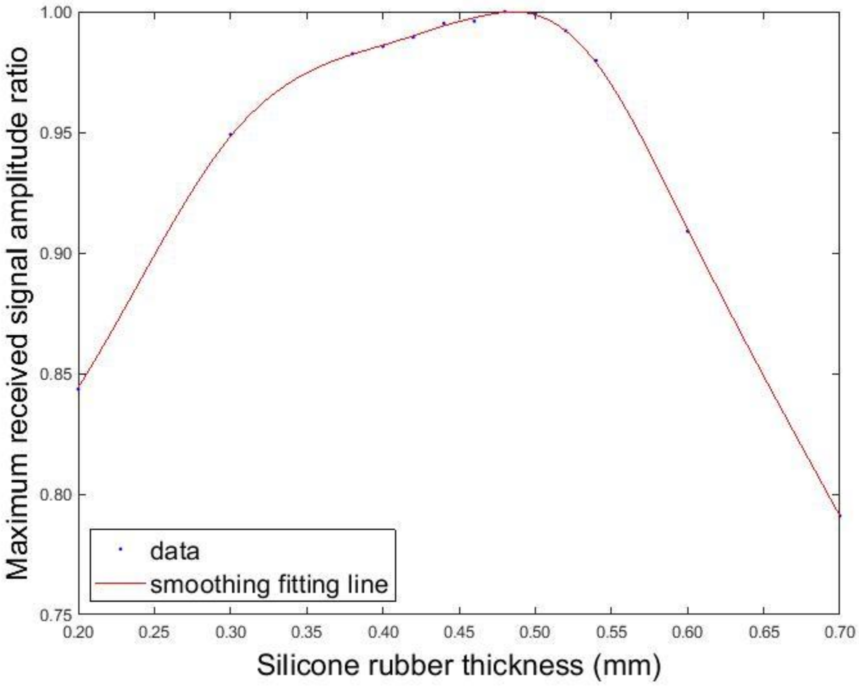

Figure 3-21 Simulated relationship between SR thickness and receiver efficiency when operating at 600 kHz

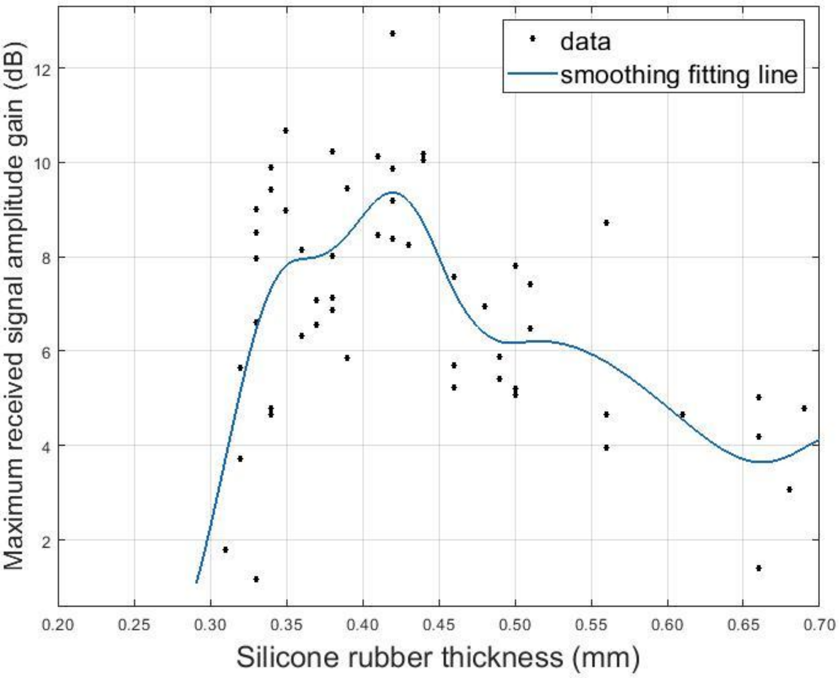

Figure 3-22 Measured relationship between silicone rubber thickness and receiver efficiency for matching layers fabricated using the pressure method by operating on 600 kHz

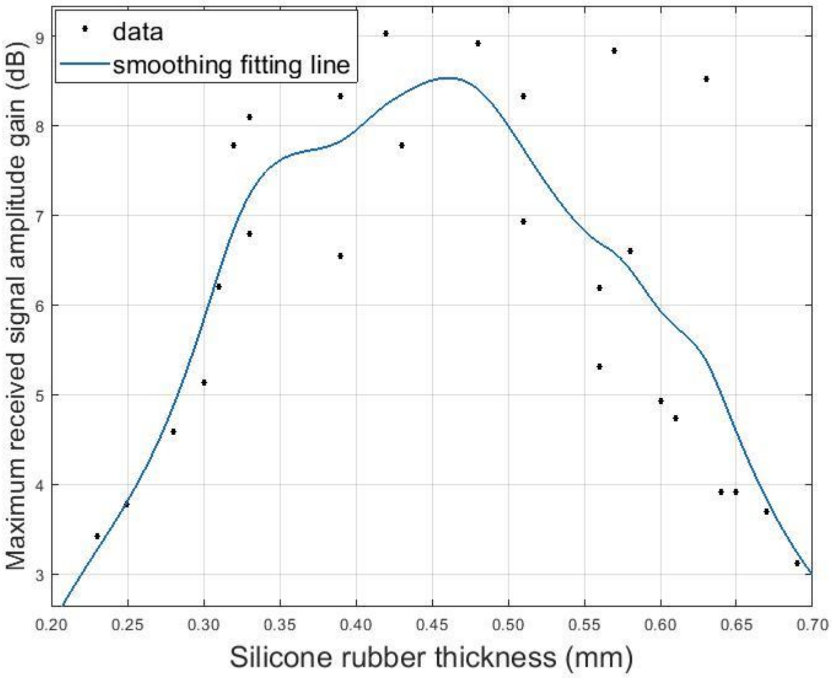

Figure 3-23 Measured relationship between silicone rubber thickness and receiver efficiency for matching layers fabricated using the K coated machine method by operating on 600 kHz

3.4.4 Reliability tests

In this section, statistical analysis is discussed to compare the reliability of these two different manufacturing methods.

Figure 3-24 and Figure 3-25 are two residual analysis figures for the matching layers produced for the transmitter and correspond to the results presented in Figure 3-19 and Figure 3-20, respectively. Figure 3-19 and Figure 3-20 indicate that both of the fabrication methodologies can offer a maximum gain of around 18 dB. The pressure method can offer a little larger maximum gain to 19.5 dB in some cases as it has wider hybrid layers as shown in microscope results Figure 3-14. Figure 3-24 and Figure 3-25 are two tolerance figures are the differences between the experiment results' point and the fitted line. For the pressure method to manufacture the matching layer assemblies, the largest tolerance is 6.3 dB, whereas, the K coated machine matching layers produce a smaller maximum tolerance of 3.9 dB. The R-square value have been recorded which is a statistical measure of how close the data matches to the fitted regression line, where a larger value means the data is more close to the fitted line. The smoothing fitted line for pressure method has more scatter, with R-square value 0.7409 compared to 0.9189 for K coated machine method because the pressure loading method produces matching layers with poor consistency. Whereas, the K machine fabrication approach has less scatter, as shown in Figure 3-20, and produces more consistent matching layer assemblies.

For the receiver, both Figure 3-26 and Figure 3-27 are two residual analysis figures for the matching layers produced for the receiver and correspond to the results presented in Figure 3-22 and Figure 3-23, respectively. Figure 3-22 and Figure 3-23 indicate that both of the fabrication methodologies can offer a maximum gain of around 9 dB. For the pressure method to manufacture the matching layer assemblies, the largest tolerance is 5.1 dB, whereas, the K coated machine matching layers produced a smaller maximum tolerance of 3.1 dB. The smoothing fitted line for pressure method has more scatter with R-square value 0.5134 compared to 0.7389 for K coated machine method.

The receiver’s matching layer results show a scattering of results compared to the transmitter matching layer experimental results. This could be due to a lower SNR in the receiver’s matching layer experiment.

In addition to the whole thickness tolerance comparisons, the specific thickness comparisons of matching layers made by both methods are shown in Figure 3-28. Three thicknesses 0.49 mm, 0.50 mm and 0.51 mm have been chosen for testing on transmitter because the best SR thickness range is between 0.33 mm to 0.38 mm, as mentioned in previous section, which means matching layer thickness range is between 0.47 mm to 0.52 mm. The red data point is the gain performance made by the K coated machine and the blue data point is produced by the pressure method. This Figure shows that the K coated approach, identified in red line in the Figure, has better gain and a smaller tolerance range compare to the blue line. Therefore, the K coated machine method has more reliable performance in the specific thicknesses considered here.

One important issue should be noted that, all the matching layers applied on the transducers have no visual damage. The manufacturing success rate is still one key factor for the reliability test. For the statistics generated through this research, the pressure method’s success rate is less than 80 %, whereas the success rate for K coated machine method is larger than 90 %, which could improve further as a skilled worker gained additional experience.

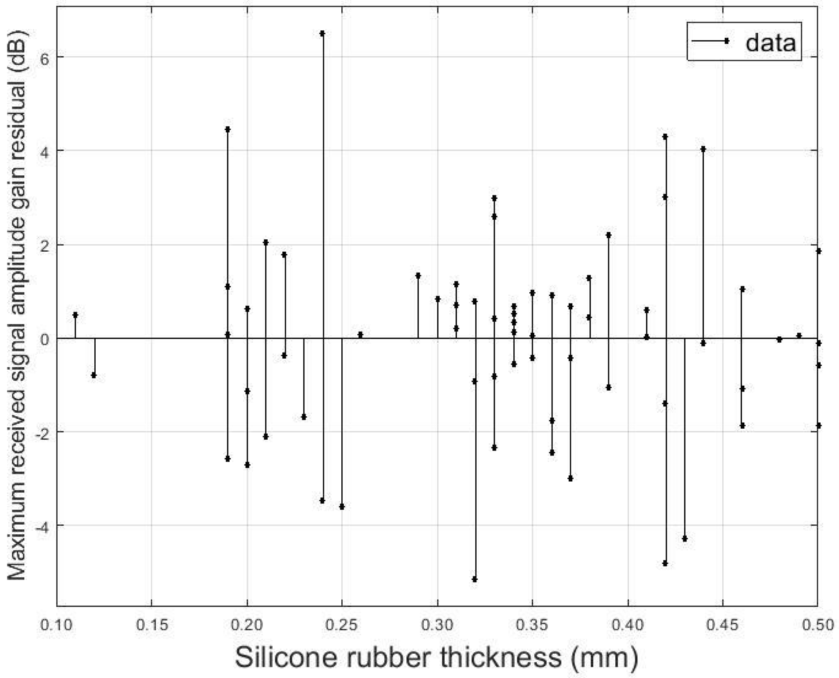

Figure 3-24 Tolerance analysis for transmitter's matching layers fabricated using pressure method

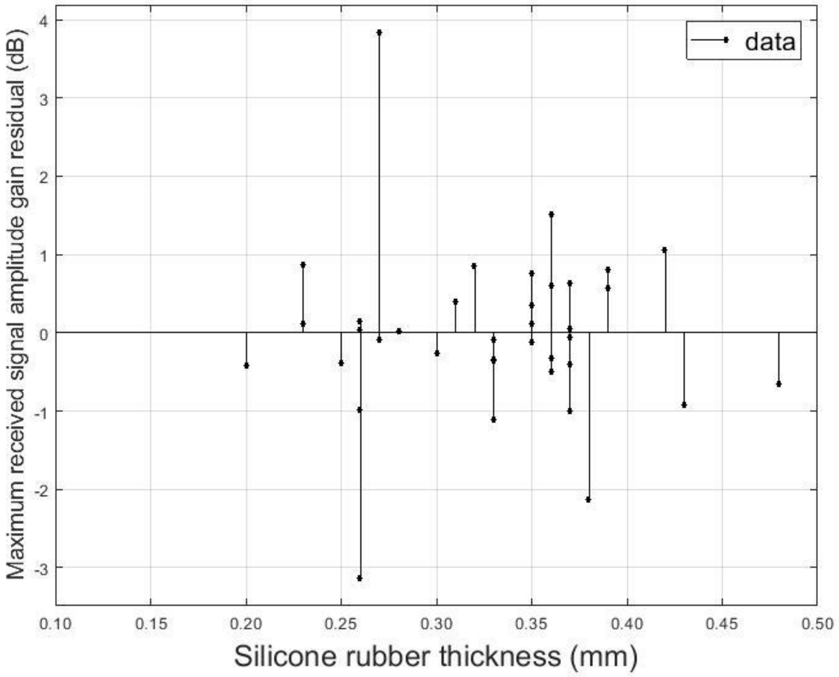

Figure 3-25 Tolerance analysis for transmitter's matching layers fabricated using the K coated machine scanning method

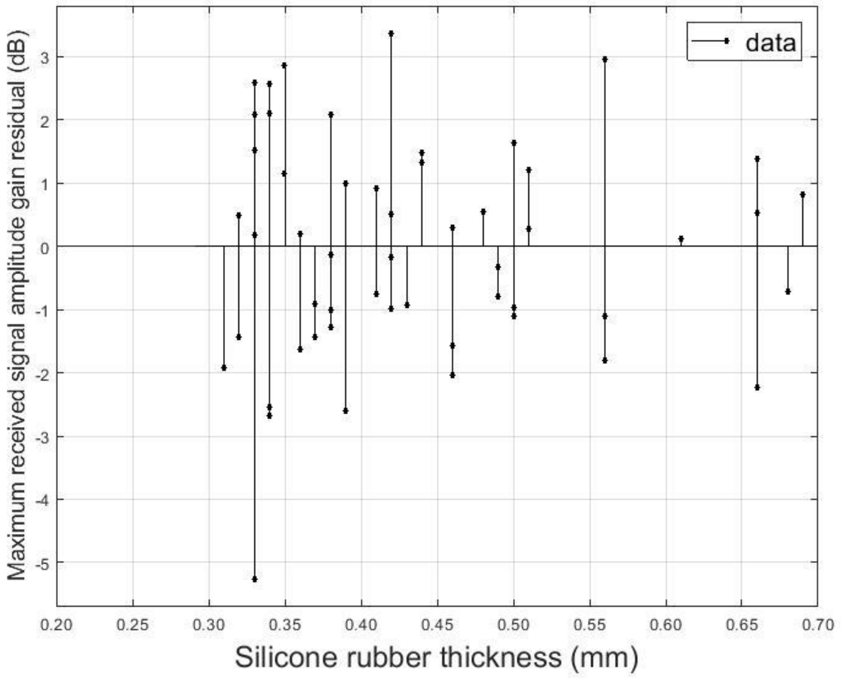

Figure 3-26 Tolerance analysis for receiver’s matching layers fabricated using pressure method

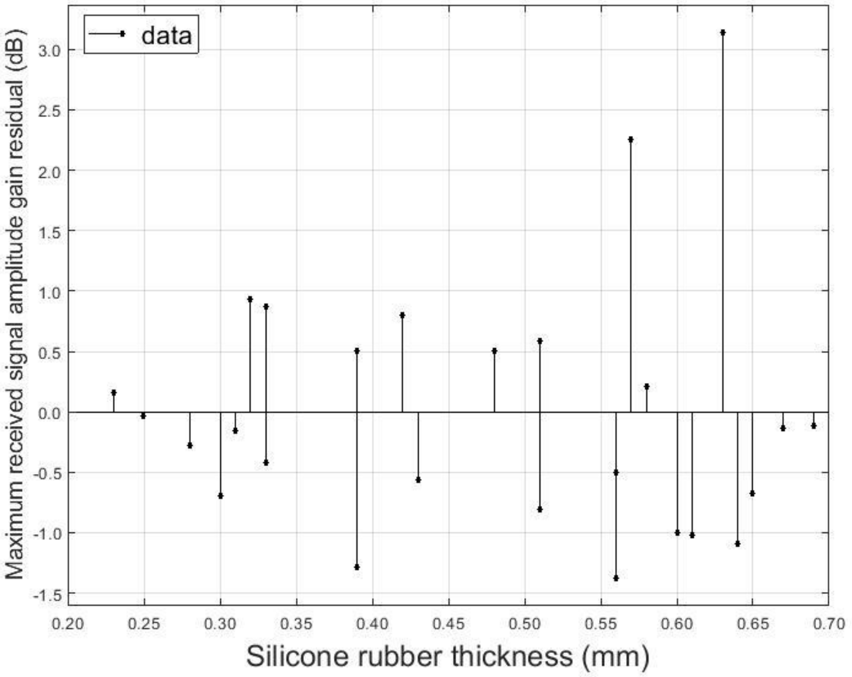

Figure 3-27 Tolerance analysis for receiver’s matching layers fabricated using the K coated machine scanning method

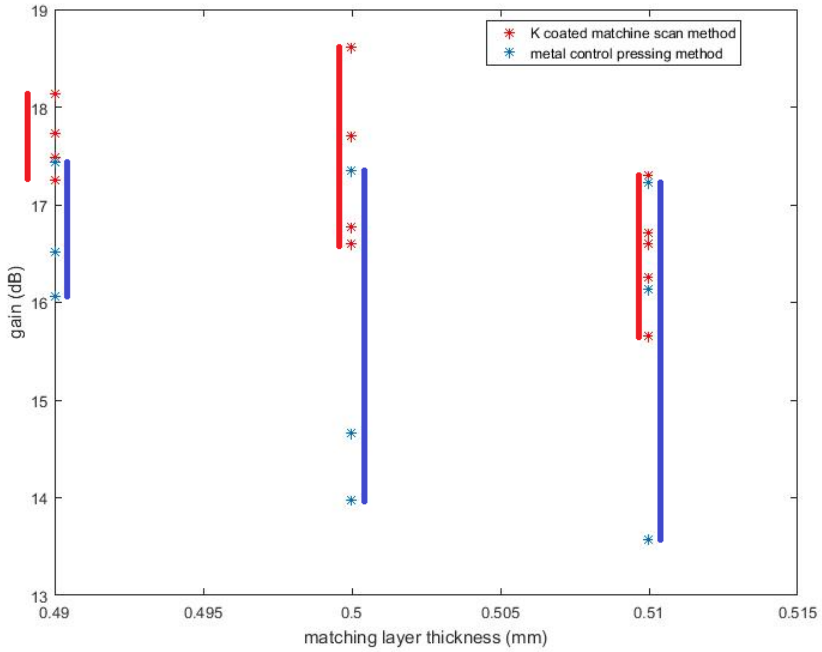

Figure 3-28 Specific thickness transmitter’s matching layer comparison for both fabrication methodologies, red line is the matching layer performance made by K coated machine and blue line is the matching layer performance made by pressure method

3.4.5 Experimental pitch-catch performance using K coated machine method matching layers

The K coated machine manufacturing method can provide similar performance characteristic, shorter curing time, and better manufacturing success rate than the pressure method. The transmitter efficiency is largest when the SR thickness is 0.36 mm and the receiver efficiency is largest when the SR thickness is 0.48 mm. In practise, it is necessary to apply these two matching layers on both transmitter and receiver separately to obtain the maximum gain for the air-coupled system.

Figure 3-29 (a) and (b) show the PZFlex modelling results indicating that this combined matching layer assembly can offer a 24 dB gain when applied to both transmitter and receiver devices in a pitch-catch operating configuration. The matching layer can not only increase the maximum received signal voltage at the designed frequency 600 kHz, but also it increases the signal at frequencies of 425 kHz and 650 kHz as shown in Figure 3-29 (c) and (d). The spectral domain figures show that the bandwidth and main frequency do not change significantly, which is not surprising due to the fact the device is operating in air and that the matching layer’s thickness has been designed to maximise operation at the transducer centre frequency.

Figure 3-30 (a) and (b) presents the measured through-transmitted signal results. In the practical case, the gain has exceeded the predicted value and was calculated at 35 dB. The frequency response, shown in Figure 3-30 (c) and (d), have a more complex characteristic than shown in the prediction. It is considered that this is due to practical variations in the key material properties and dimensions creating more individual resonant behaviour in the transduction system. The important and key characteristic is the improvement in sensitivity when the matching layers are applied to the transmitter and receiver devices, which is necessary due to the poor SNR associated with air-coupled piezoelectric systems. The spectral domain figures show vibrational modes at 400 kHz and 650 kHz, which is in agreement with PZFlex simulation, and the lower frequency has been introduced through the matching layer.

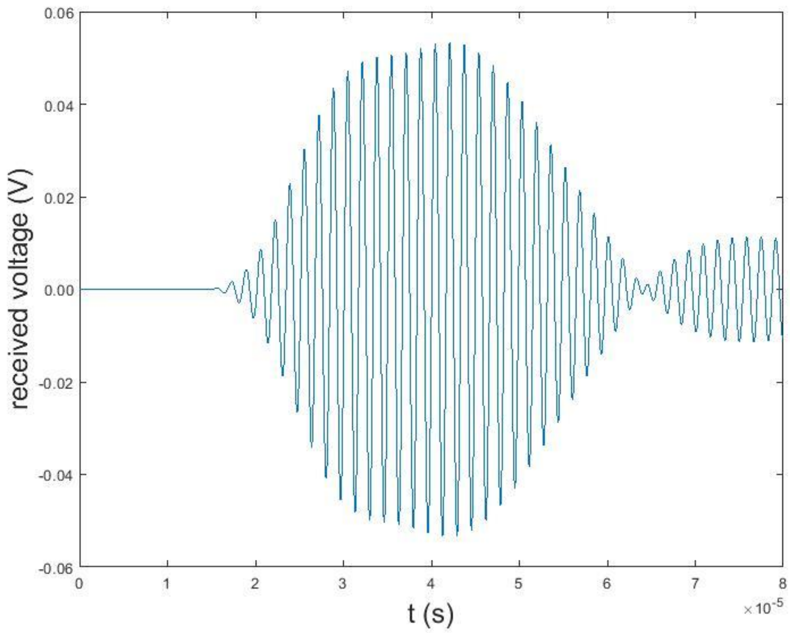

a) No matching layer applied - simulation time domain response for pitch-catch air-coupled transducer system

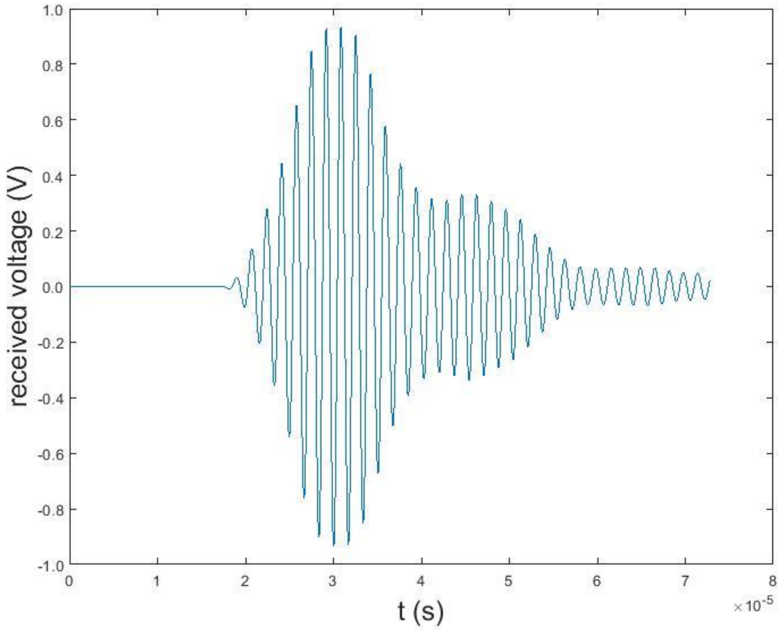

b) Matching layer applied on both transmitter and receiver - simulation time domain response for pitch-catch air-coupled transducer system

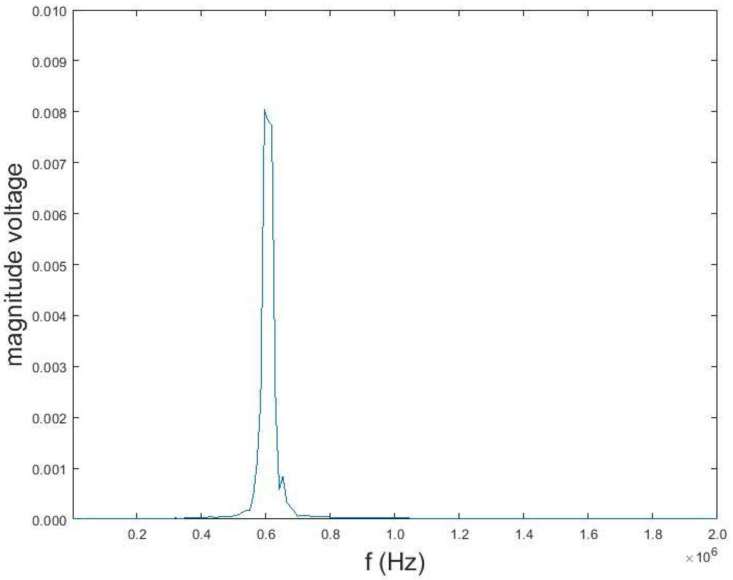

c) No matching layer applied - simulation spectral domain response for pitch-catch air-coupled transducer system

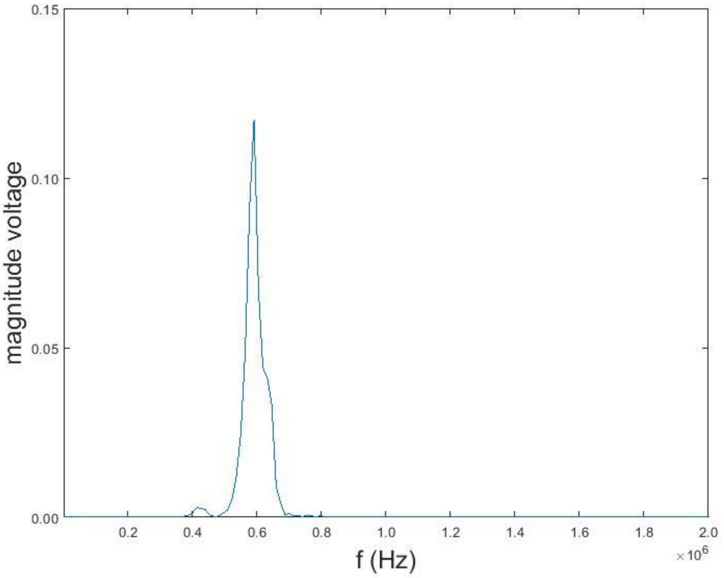

d) Matching layer applied on both transmitter and receiver - simulation spectral domain response for pitch-catch air-coupled transducer system

Figure 3-29 PZFlex simulation results of the air-coupled pitch-catch system both with and without matching layers whose gain is 24.87dB, (a) time domain response without matching layer; (b) time domain response with matching layers; (c) spectral domain response without matching layer; (d) spectral domain response with matching layers

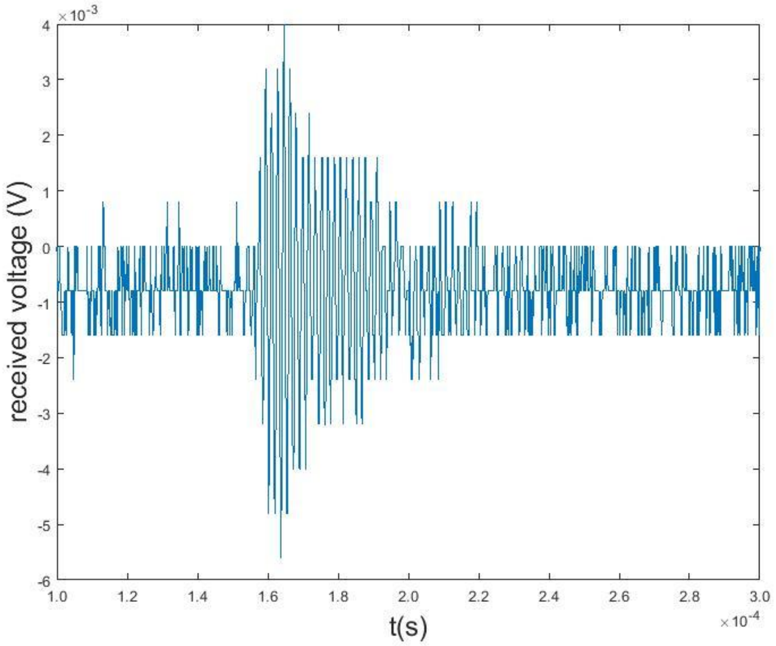

a) No matching layer applied - experimental time domain response for pitch-catch air-coupled transducer system

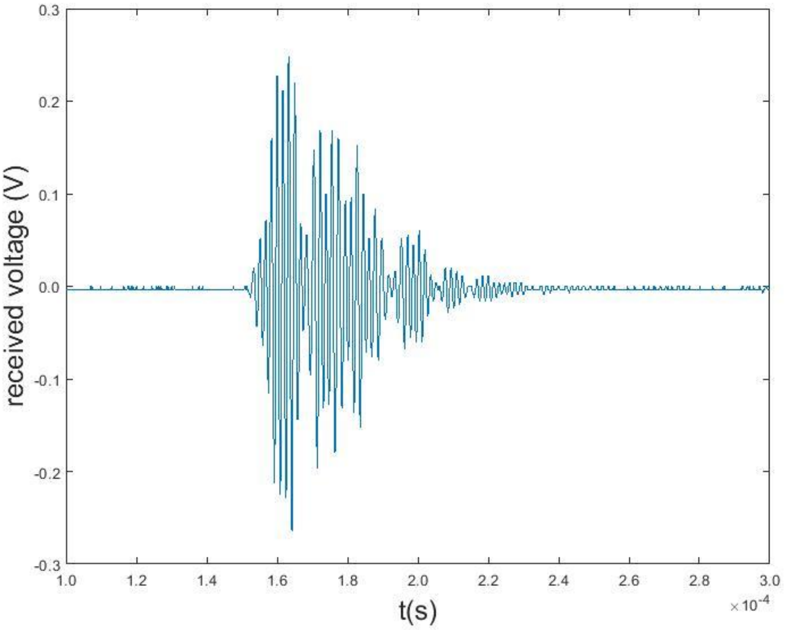

b) Matching layer applied on both transmitter and receiver - experimental time domain response for pitch-catch air-coupled transducer system

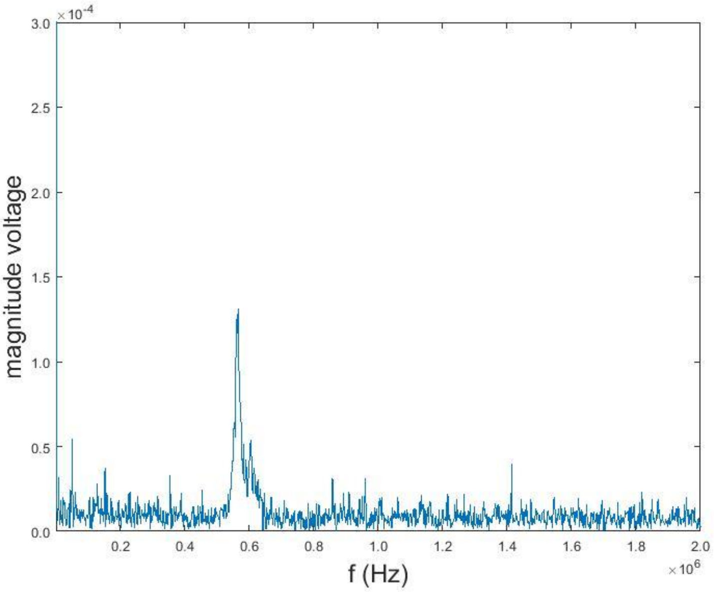

c) No matching layer applied – experimental spectral domain response for pitch-catch air-coupled transducer system

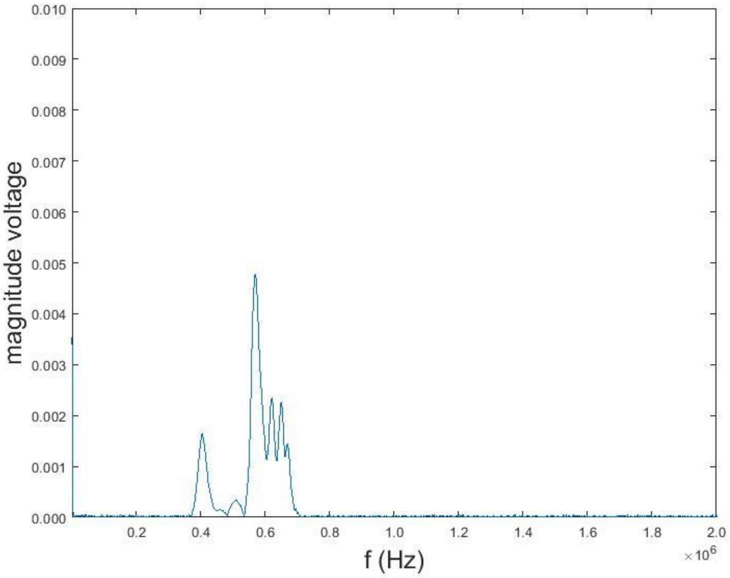

d) Matching layer applied on both transmitter and receiver - experimental spectral domain response for pitch-catch air-coupled transducer system

Figure 3-30 Experimental results of the air-coupled pitch-catch system both with and without matching layers whose gain is 35.84dB, (a) time domain response without matching layer; (b) time domain response with matching layers; (c) spectral domain response without matching layer; (d) spectral domain response with matching layers

3.5 Summary

This Chapter has developed a new technique to manufacture a previously reported matching layer combination, which has been shown to be appropriate for use with air-coupled piezoelectric transducer systems [82]. The K coated machine produces matching layers with greater consistency and better overall performance when compared to matching layers fabricated using the conventional pressure loading approach. The matching layer is a combination of silicone rubber and a membrane filter, and is effectively in acoustic impedance matching layer system.

Analysis of the transmit and receive performance of air-coupled 1-3 piezocomposite transducers using a range of matching layer thicknesses, highlighted the key thickness which should be used in all matching layers fabricated, using the K coating methodology, for use with the air-coupled devices developed and evaluated later in the Thesis. For the transmitter, the overall matching layer thickness, including membrane filter thickness, should be 0.46 mm to 0.5 mm, and for the receiver the range is 0.52 mm to 0.62 mm. Importantly, an overall gain in sensitivity of over 35 dB can be achieved when adopting this approach and these matching layer configurations will be used in the following Chapters to provide good SNR for the array based air-coupled inspection systems.

CHAPTER 4 Development and Evaluation of Air-Coupled Annular Array System

Abstract

This Chapter describes the fabrication process for two air-coupled annular array transducers and subsequently, describes a number of key experimental measurements acquired to determine the operational performance of the array transducer. Moreover, all experimental results are compared to simulated data to confirm the validity of the design process. Air-coupled transducers, incorporating the 1-3 connectivity piezocomposite configuration, are employed in a through transmission mode. Two annular arrays are designed to be 1.5-D annular arrays and the manufacturing process is detailed to provide evidence of a robust procedure. Within the characteristic pressure field profile for air-coupled disc transducers, the influence of air medium requires the operational region to be in the complex near field. These factors are significant for the operational accuracy of an air-coupled device and experimentally acquired field characteristics can be used to correctly position the transducer system. For the specified focusing distance, a table of focal time delays are calculated under the assumption that the matching layer thickness has uniform thickness. A shift in the fundamental operating frequencies was observed and simulation used to explain this phenomenon. Moreover, two pre-amplifier boards are designed to remedy the frequency shift problem, which can also provide better power efficiency and a reduction in system noise to produce a good system SNR. Overall, good correlation between theory and experimental results is obtained.

4.1 Introduction

Non-contact ultrasonic NDE, using air as the load medium, has a number of potential advantages, including the ease of set up, fast inspection of complex shaped specimens, protection for non-waterproof specimens, and enlarges the range of suitable working environments. The main drawback, as mentioned in Section 2.1, is that the attenuation and insertion loss for such inspection systems are large, so that the received signal is significantly weaker if compared to an identical inspection in a liquid load medium.

One of the solutions to improve air-coupled ultrasonic system performance is by using the matching layer approach introduced in Chapter 3. Another method to improve the signal strength is using beam steering technology to focus/enhance energy in a targeted region. Among all the different array geometries, the annular configuration offers good performance for focusing in the middle of the transducer central axis due to its symmetric configuration. There are two methods to achieve focusing in the central axis, one of them is physical alteration of the transducer itself and the other one is controlling the electrical excitation of an array configuration. For the physical focusing approach, the transducer will operate at a fixed focusing distance. Different specimens may require different focusing distances due to their thickness or material properties and hence, the physical approach is not reliable enough since it has to change the transducer set up every time. But for electrical focusing, the array transducer structure is unchanged and a focal law is applied across the array aperture, which can be adjusted for different the focal distances. Importantly, manipulation of the ultrasonic beam in the load medium is achieved by introducing time delays between each array element and using series superposition of these propagating waves in the load itself. Compared to the physical focussing method, electrical focusing can provide more controllability when performing focusing at different distances rather than moving the devices. For the proposed annular array configuration, it is desirable to design additional operational flexibility to enable operation when the target point is outside of the central axis. Hence, a 1.5-D annular array is designed based on the 2-D annular segmented array but with a limited number of sub-elements, which should provide limited focusing performance off-axis. Consideration has to be given to ensure that the array does not have too many elements which can lead to complex manufacturing procedure and hardware set up.

In this Chapter, a standard design process for 1-3 connectivity piezocomposite array transducers for operating at 590 kHz has been used [6, 41, 42, 51]. Two transducers are manufactured as transmitter and receiver for operating in the pitch-catch mode, in which the electrical resonance frequency of the transmitter and mechanical resonance frequency of the receiver are matched to maximise sensitivity of the air-coupled system. A series of initial characteristic tests are provided to make sure the piezocomposites operate as designed. Then, comparisons of the theoretical and experimental results are presented for a variety of test scenarios. Simulation results are predicted using PZFlex and includes the influence of the electrical cable on the array behaviour. This Chapter also provides the method for time delay calculation process for the desired focal law conditions. It should be noted that pre-amplifier boards are designed for receiver array to improve the performance and remedy a frequency shift phenomenon caused by introduction of the electrical interconnect cable.

4.2 1-3 Connectivity Piezocomposite Active Layers

4.2.1 1-3 piezocomposite design and manufacture

Two standard 1-3 piezocomposites are designed with operating frequency of 590 kHz, which is consistent with previous air-coupled transducer designs from the ultrasonic research group at Strathclyde University [6, 44]. The primary piezoceramic materials used are PZT5H and PZT5A, with three polymer filler materials covering a wide range of acoustic and mechanical properties: the hard-set material CIBA-GEIGY CY1301/HY1300, the medium-set setting CY221/HY956 and a conformable, soft-set one CY208/HY956 which were introduced in Section 2.2.2. Hayward and Gachagan confirms PZT5H with hard-set piezocomposite has the largest pressure for the transmission performance and PZT5A with hard-set can produce the largest received voltage by testing a series of different material combinations. Therefore, PZT5H is suitable for transmitter and PZT5A is suitable for receiver, these two materials are chosen as ceramic materials. Even though a hard epoxy filler material has lower attenuation/damping ratio which will result in a device with a higher level of mechanical cross-talk, this material was still chosen to maximise the output signal power. Moreover, there is no backing in these two air-coupled transducers for the same purpose to maximise the transducer output performance. The ceramic volume fractions are selected at 70 % and 30 % for the transmitter and receiver respectively [8]. These have been selected to improve the performance of the individual transmit and receive transduction aspects of the system and importantly, ensures that both devices operate with a high level of electromechanical coupling co-efficient k_t as shown in Figure 2-8. The diameter and saw width are decided based on the ease of manufacturing and the availability in the Centre for Ultrasonic Engineering (CUE) fabrication workshop. Table 4.1 gives the detail parameters for the final 1-3 piezocomposite manufacture which is calculated from Smith and Auld equivalent parameter model [42].

The piezocomposites are fabricated using the standard 'dice and fill' technique [48, 90] using the parameters in Table 4.1, and two piezoelectric composites have been manufactured for transmitter and receiver separately. This fabrication technique dices the ceramic plate in two perpendicular directions with a diamond or resin blade to produce a 2-D matrix of pillars. The bulk ceramic wafer is usually thicker than the required thickness, so that the ceramic pillar matrix is still attached to the uncut stock. Then a polymer fill technique is used to backfill the removed kerfs with a polymer phase. The excess ceramic stock and polymer can be lapped off from the bottom and top surfaces to produce the desired piezocomposite thickness.

Table 4.1 Manufacture specifications for the 1-3 piezocomposite designs operating at 590 kHz

	Transmitter	*Receiver*
Ceramic material	PZT5H	PZT5A
Polymer material	Hard set CY1301	Hard set CY1301
Volume fraction	66 %	30 %
Dimensions	40 mm × 40 mm	40 mm × 40 mm
Saw width	0.15 mm	0.2 mm
Saw pitch	0.85 mm	0.5 mm
Thickness	2.55 mm	2.98 mm
Aspect ratio	0.313	0.1

4.2.2 Characterising the 1-3 piezocomposite transducers

To ensure every manufacturing step is under control, the characteristic behaviours/performances of the two piezocomposites are checked throughout the fabrication process. To facilitate an electrical connection for preliminary characterisation of the full 1-3 piezocomposite, removable silver layers are printed by using a brush on both sides of transmitter and receiver's piezocomposites as shown in Figure 4-1.

For the initial behaviour check, the full 40 mm × 40 mm piezocomposite plate is used and the electrical impedance characteristic and vibration behaviour are tested to ensure the piezocomposite is manufactured as designed and increase the reliability for the next fabrication step moving towards the final transmitter device.

The important factor electromechanical coupling co-efficient k_t which is introduced in Section 2.2.2 can be described by equation 4-1 by means of electrical resonance (f_e) and mechanical resonance (f_m) for calculation.

$$k_t^2 = \frac{\frac{\pi f_e}{2f_m}}{\tan(\frac{\pi f_e}{2f_m})} \tag{4-1}$$

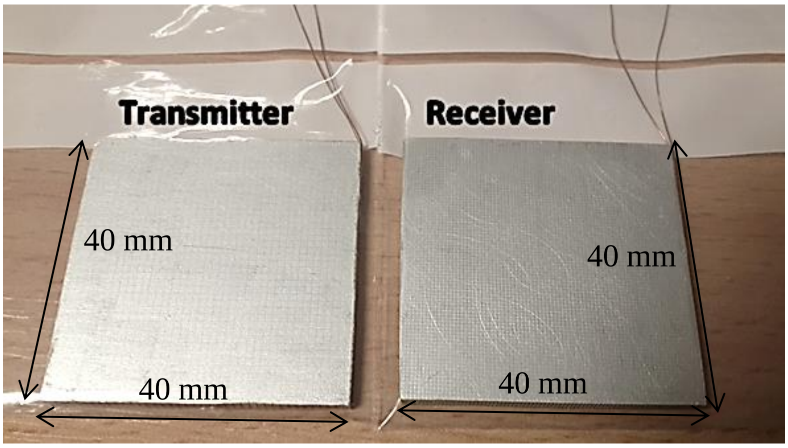

Figure 4-1 Silver paint electrodes on both sides of each 40 mm × 40 mm 1-3 piezocomposite, Transmitter: 2.55 mm thickness, 66% volume fraction, 0.7 mm pillar width and 0.15 mm saw width; Receiver: 2.98 mm thickness, 30% volume fraction, 0.3 mm pillar width and 0.2 mm saw width

4.2.2.1 Characterisation of full 1-3 piezocomposite transmitter

Figure 4-2 shows the theoretical and experimental impedance characteristic curve for transmitter before the array configuration is applied. The experimental electrical resonance frequency, f_e, is 588 kHz which is well matched to the designed frequency of 590 kHz. The mechanical resonance frequency, f_m, is 743.6 kHz and the k_t calculated by using Equation 4-1 is 0.65 ± 0.002, which is a good value as shown in Figure 2-7.Figure 4-3 is the vibrational characteristic for the transmitter when operated at its electrical frequency of 588 kHz. This was measured using a Polytec Laser Doppler Vibrometer (MSA-100-3D, Polytec Ltd.). The transmitter vibration is represented as a diagonal shape, which may be caused by many factors such as the pressure from the frame when holding the piezocomposite, non-uniform manufacturing or not facing to the camera in the parallel direction. But it is clearly that the material vibrates in phase.

In the initial behaviour test, the performance of piezocomposite for transmitter is overall good for the next stage.

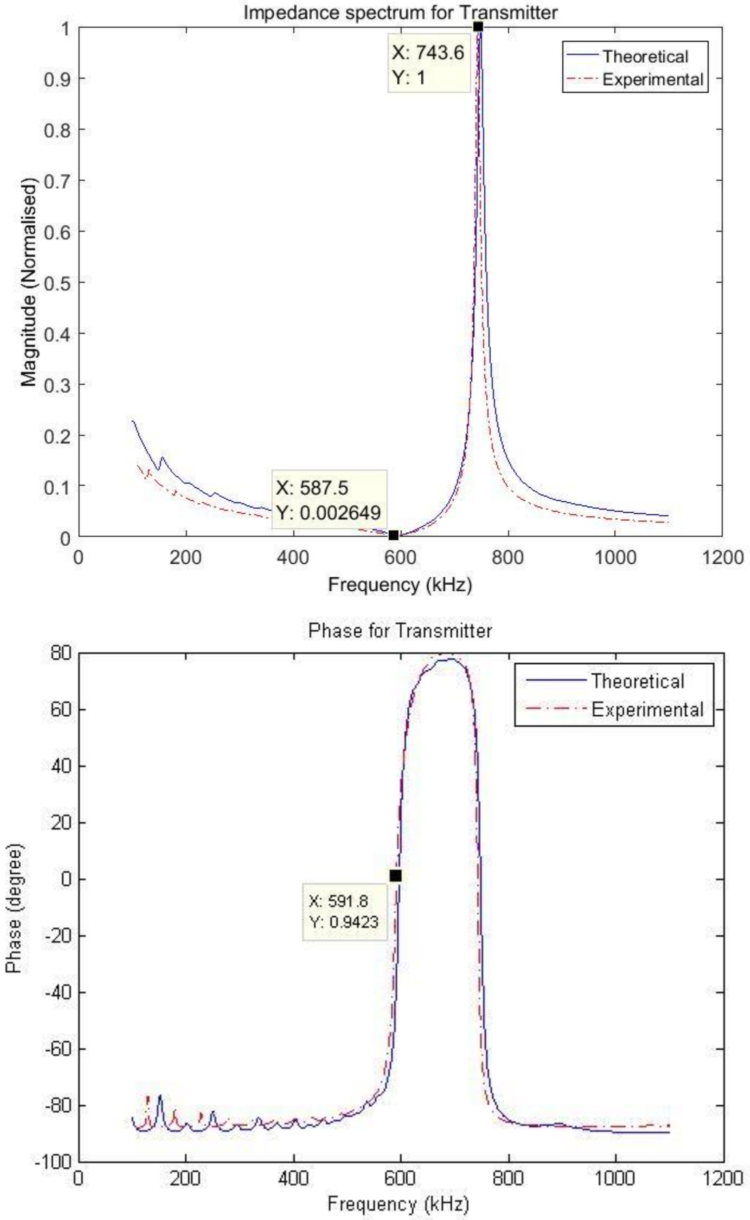

Figure 4-2 PZFlex simulation theoretical and experimental impedance and phase characteristic line for transmitter as a 40 mm × 40 mm plate, and the impedance figure normalised to its own maximum impedance

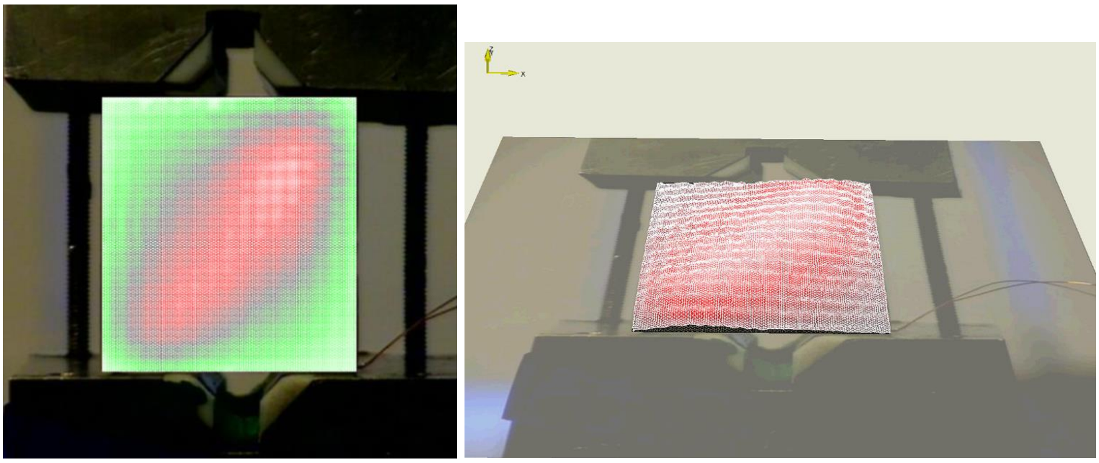

Figure 4-3 Laser vibration measurement for the 40 mm × 40 mm plate transmitter operating at 587 kHz

4.2.2.2 Characterisation of full 1-3 piezocomposite receiver

The same electrical impedance characteristic and vibration behaviour tests performed on the transmitter were repeated for the full 1-3 piezocomposite receiver.

Figure 4-4 shows the theoretical and experimental impedance characteristic curve for receiver before the array configuration was applied. The experimental results again match well with the theoretical results, where the measured mechanical resonance frequency, f_m, is 578 kHz which is only 12 kHz lower than designed 590 kHz frequency. The electrical resonance frequency, $f_{e,}$ is 473 kHz and the k_t calculated by using Equation 4-1 is 0.62 ± 0.002 which is another strong value as shown in Figure 2-7.

Figure 4-5 presents the vibration response for the receiver when operated at its electrical resonance frequency of 473 kHz, as determined from Figure 4-2. This is standard practice when characterising the vibrational behaviour of a reception device and provides an indication of the transduction performance of the piezoelectric material. The receiver has a high power concentrated in the middle section compared to the outer regions. There are three bad points in the middle of the piezocomposite, and can be identified as the 3 ‘stripes’ visible in Figure 4-5.

In these initial behaviour tests, the piezocomposite’s performance for receiver is considered acceptable for use in the next fabrication stages.

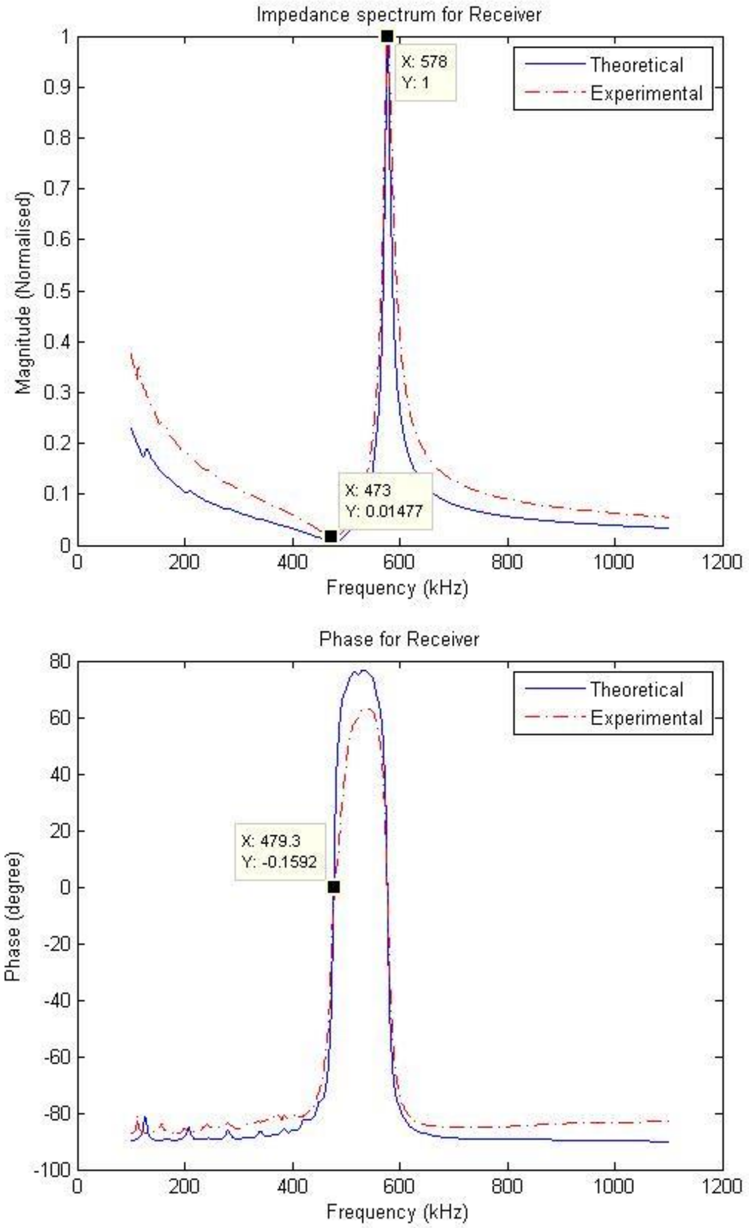

Figure 4-4 PZFlex simulation theoretical and experimental impedance characteristic line for receiver as a 40 mm × 40 mm plate, and the impedance figure normalised to its own maximum impedance

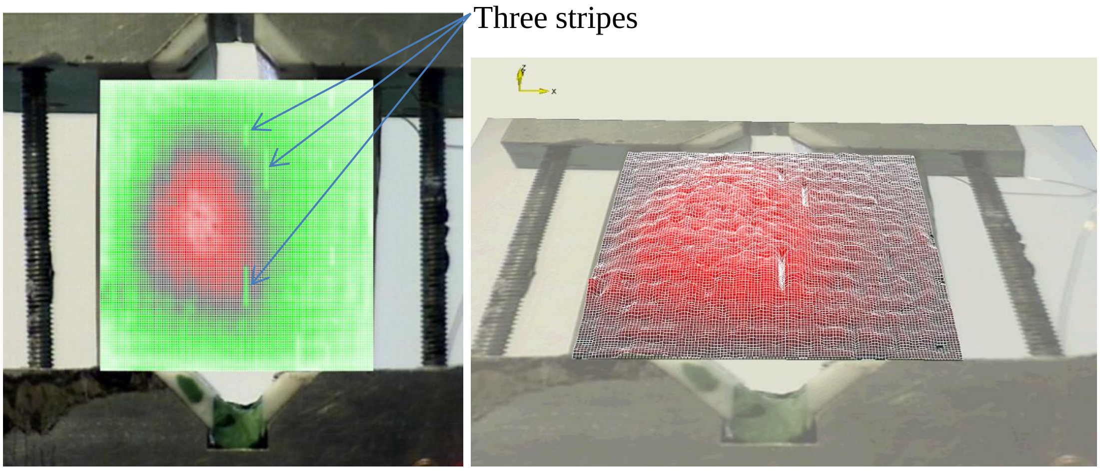

Figure 4-5 Laser vibration condition for the 40 mm × 40 mm plate receiver operating at 470 kHz

4.2.2.3 Transmitter's and receiver's resonance frequency alignment

The f_e of the transmitter should match with f_m of the receiver in a pitch-catch mode system to maximise system sensitivity as introduced in section 2.2.2.5. From the experimental results as shown in Figure 4-2 and Figure 4-4, the transmitter's resonance frequency, f_e, is located at 587 kHz and the receiver's resonance frequency, f_m, is 578 kHz. These two resonance frequency are reasonably aligned and hence, the pitch-catch mode system should work as designed.

4.3 Annular Array Technology

After the piezocomposite plates are manufactured and their acceptable performances acquired though preliminary characterisation, the annular array is designed because this configuration has a stronger ability for focusing on the central axis than linear array due to its symmetric structure. Table 4.2 is a summary of the normally used array types, which were introduced in Section 2.3. The concept of designing a 1.5-D annular array came is closely aligned to the 1.5-D matrix array, which is a compromise between standard 1-D and 2-D array configurations, and is effectively a subset of the 2-D annular segmented array configuration. This configuration has been selected to provide strong axial focal performance, with a limited steering capability around the focal axis.

Table 4.2 Typical phased array probe characteristics

Type	*Deflection*	*Figure*
1-D linear	2-D beam manipulation	Figure 2-10
Annular	Central axis beam manipulation	Figure 2-11
2-D annular segmented	3-D beam manipulation off central axis	Figure 2-13
2-D matrix	3-D beam manipulation	Figure 2-12
2-D random sparse array	3-D beam manipulation	Figure 2-14
1.5-D matrix	Weak 3-D beam manipulation	Figure 2-15
1.5-D annular	Weak 3-D beam manipulation	Figure 4-7

4.3.1 Conventional Annular Array Design

To calculate the individual radial dimensions for each element of the 1-D annular array, it should satisfy the following rules:

- Every element has an equal active area.

  Every element will deliver an equal power and it is easy to control. Each element constraints achieve approximately same electrical impedance and the same phase shift [91].

- The element size should be fairly large to transmit/receive more energy.

  Increasing element size produces better focusing and steering capability [92] which could offer more power at the point of interest on the component. The raw materials size is 40 mm × 40 mm, as chosen from CUE stock. Hence, the maximum diameter of the array should be lower than 40 mm.

- The gap width between each ring should be large enough to electrically isolate array elements.

  Primarily, the choice of array element gap should match the fabrication capabilities, but also ensure that the risk of an electrical short is minimised. For this work, a gap width of 0.6 mm has been selected.

- The width of each element should be determined relative to the ceramic pillar size to ensure at least 1 ceramic pillar across the smallest width array element.

  It is better to be no less than 0.85 mm as the saw pitch for transmitter is near 0.85 mm.

Using these four design criteria, a design script has been developed in MATLAB, as shown in Appendix C, to produce the annular array design with eight annular elements, as shown in Figure 4-6. Here, the value of each annular array elements' radius and the distribution of the elements are clearly illustrated. For clarity, the radii values used to define each array element are 5.900, 6.500, 8.778, 9.378, 11.080, 11.680, 13.086, 13.686, 14.903, 15.503, 16.588, 17.188, 18.172, 18.772, and 19.678 mm, working from the centre to the full diameter of the entire array (~39.400 mm).

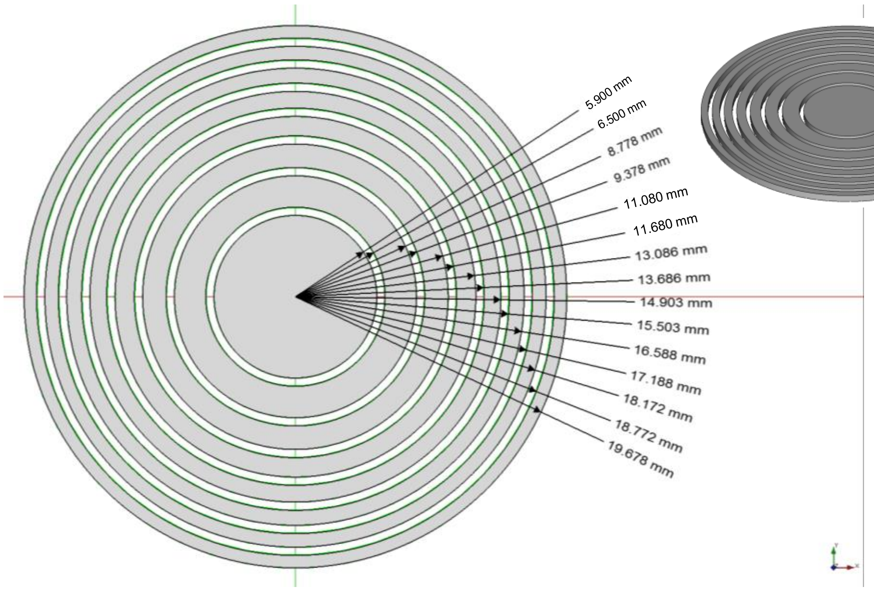

Figure 4-6 Annular array elements' radii and distribution

4.3.2 Extending the annular array to a 1.5-D configuration

In many practical applications, the exact location of the array focal point in/on the component being inspected is not always precisely known. This can be due to inaccuracies in the positional information in the automated deployment of the transducer system [93]. In addition, variations in the component geometry can also add to this issue. A standard annular array has the ability to move the focal point, but only on the central axis of the device. Hence, an additional degree of freedom in terms of manipulating the focal point was considered appropriate in order to enable fine movements of the array off the central axis of the array. In order to achieve this, each annular array element will be divided into equal sized sub-elements and each of the sub-elements will effectively be an active array element in a segmented annular array structure.

There are obviously many options for segmenting the annular array structure and in particular, the choice of number of sub-elements is important. For this application, the decision to be made considered the additional complexity in array manufacture when sub-dicing into a large number of array elements and the ability of the segmented annular array to provide some additional control in the location of the focal region off the central axis. Subsequently, a three-segment configuration was considered an acceptable option for investigating which is the minimum number for 3-D beam manipulation. Thus, each array element electrode, with the exception of the centre element, would be sub-diced at 120° intervals to create array elements of an equal area.

The distribution layout is presented in Figure 4-7 and displays that the array has been separated into three parts, u, d and l except the middle circle element named “1”. The elements are named by the part name followed with a number from 2 to 8 indicate the most inside to outside, for example l2, l3, l4, l5, l6, l7, l8 for l part.

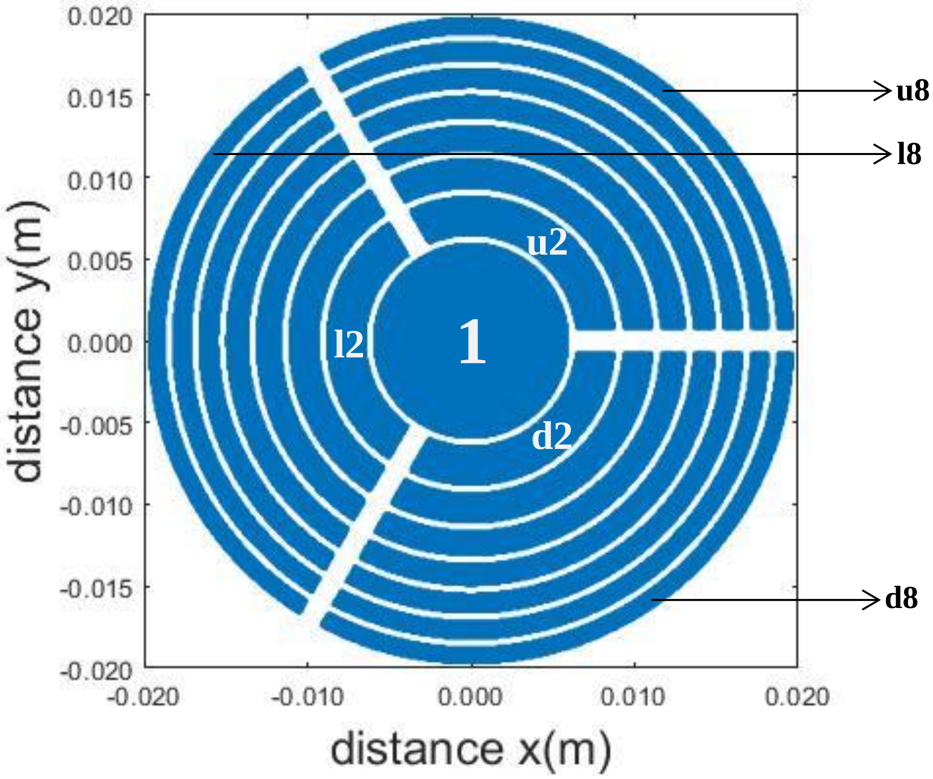

Figure 4-7 Segmented annular array configuration

4.3.3 Influence of number of annular elements on focal performance

For the desired 3-part segmented annular array, an evaluation of the impact on the beam profile as a function of the number of rings within the array has been modelled in Matlab, with the script shown in Appendix D. The initial design parameters produced an eight annular element design, hence modifying this to 6 and 10 rings were considered for comparison on the array performance. All three configurations are presented in Figure 4-8 and have been designed following the rules introduced in Section 4.3.1.

The simulated beam profile for testing the performance of the focusing ability is shown in Figure 4-9. The near far field boundary in air is 695.5 mm as calculated in Section 2.4.1. Therefore, the focusing distance will be located in the near field region. In this 3-D model, the focusing distance has been chosen at 65 mm as an example. The 6 rings annular array has the lowest power at the focusing region. The 10 rings annular array has the largest focusing power but the width of the outmost ring is only 0.65 mm which is smaller than the pillar size 0.85 mm. Therefore, the 8 rings annular array has been decided as appropriate for the next stage this research.

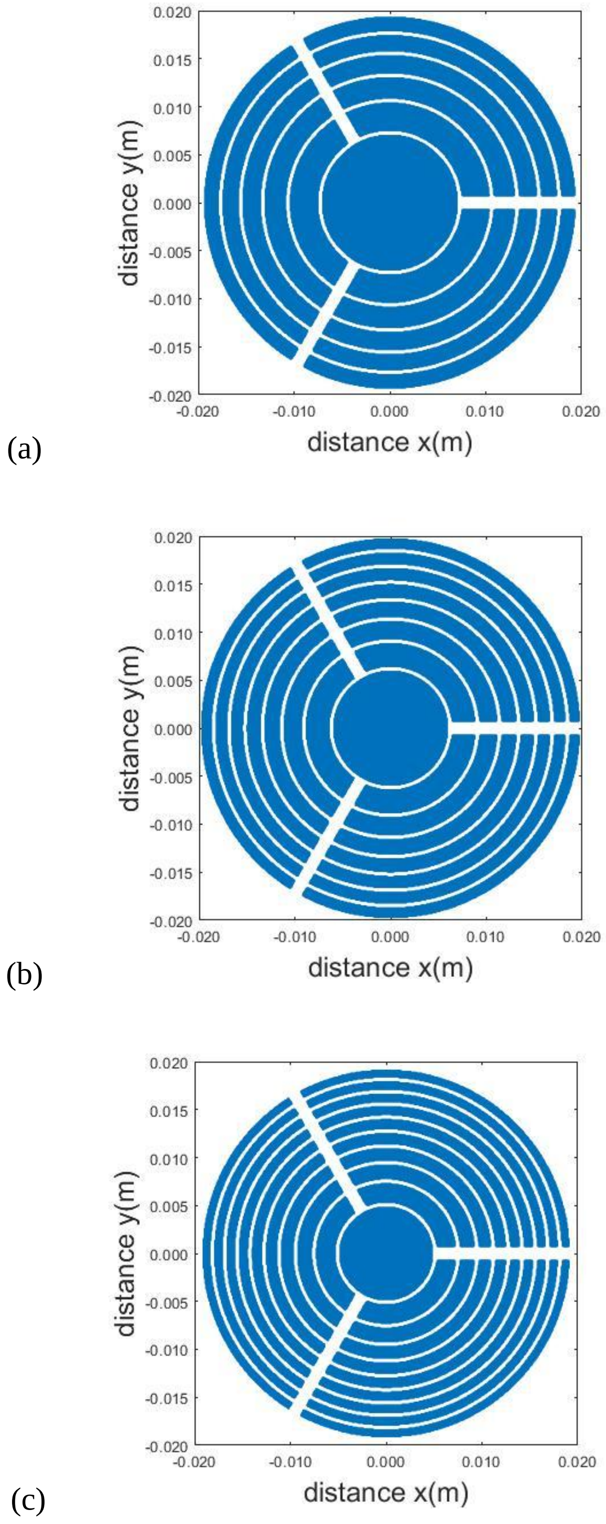

Figure 4-8 Patterns of (a) 6, (b) 8, (c) 10 annular segmented rings, within a 40 mm maximum diameter

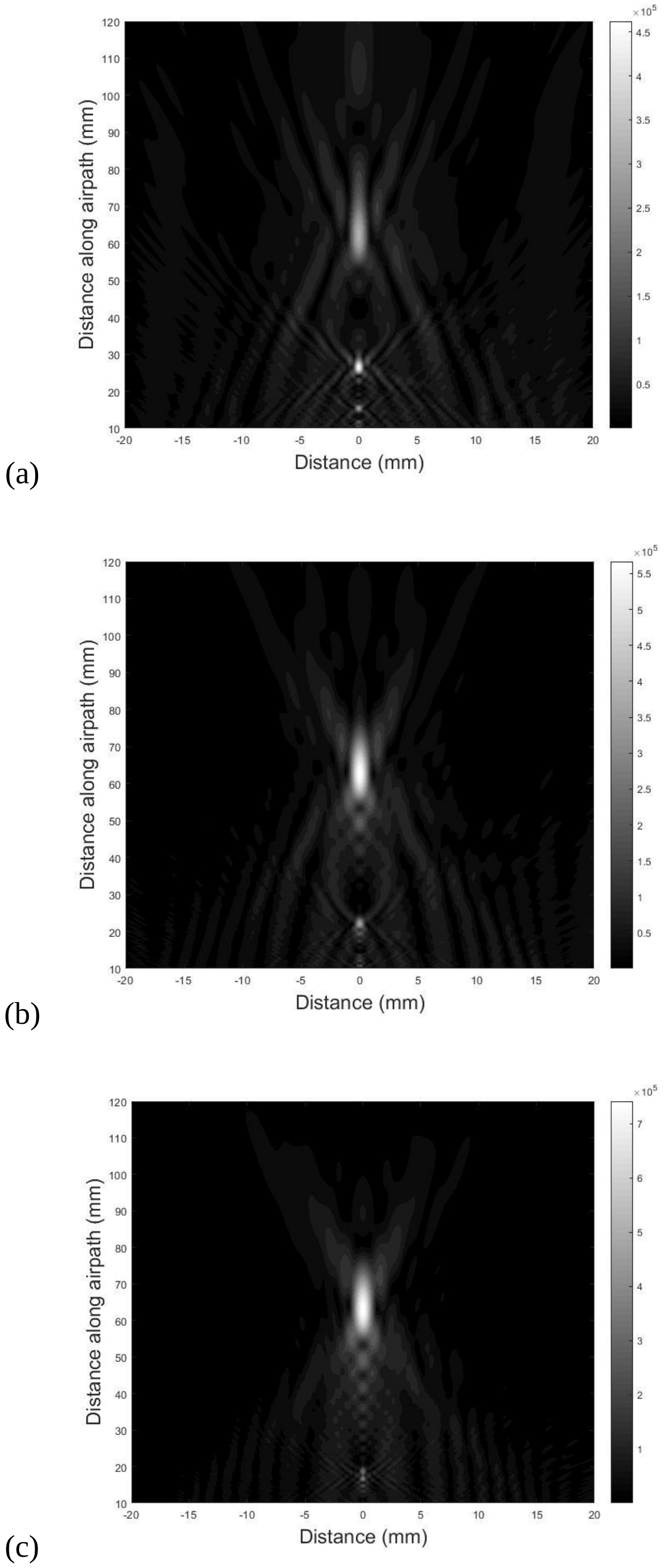

Figure 4-9 Simulated beam profiles for annular array configurations focusing at 65 mm depth, (a) 6 annular array configurations with 3.329e5 focusing power, (b) 8 annular array configurations with 5.903e5 focusing power, (c) 10 annular array configurations with 7.495e5 focusing power

4.3.4 Manufacturing process for the 22 elements annular array

An appropriate mask was designed and fabricated using laser cutting, as depicted in Figure 4-10. The annular array pattern is made on the transducer through thin film evaporation with the mask placed on the surface of the piezocomposite material. Figure 4-11 presents the gold (Au) metallic electrode on the transducer surface and the subsequent attachment of wire electrical connections. Each Au deposition has been separated into three parts to produce 22 array elements. Silver insulated wire (AG005845, by Goodfellow) has then been attached onto each array element using glue and then a fine coating of silver paint used to provide electrical connection between the wire and the array element.

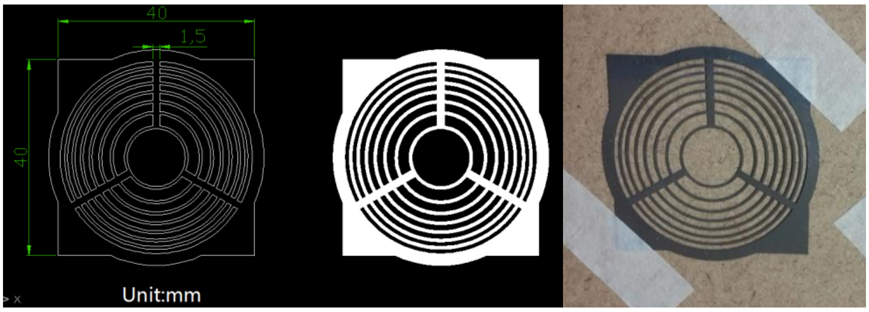

Figure 4-10 Mask of the annular array

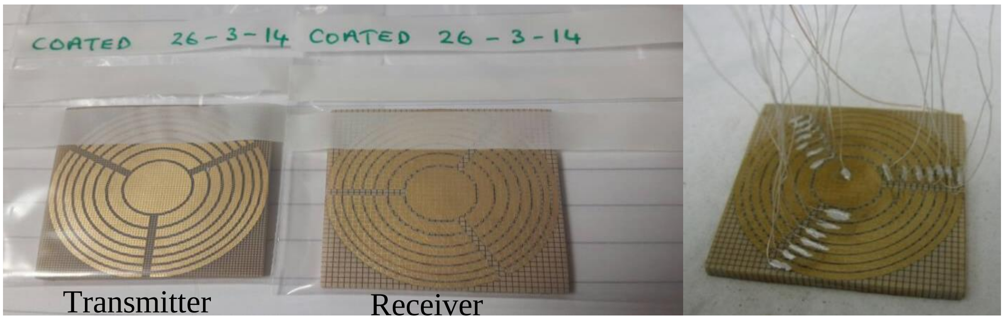

Figure 4-11 Array elements configuration for both receiver and transmitter, and fully wired for the transmitter device; Transmitter: 2.55 mm thickness, 66% volume fraction, 0.7 mm pillar width and 0.15 mm saw width; Receiver: 2.98 mm thickness, 30% volume fraction, 0.3 mm pillar width and 0.2 mm saw width

4.3.5 Electrical impedance characteristic of 1.5-D annular array

4.3.5.1 22 elements transmitter array impedance characteristic

Once the 22 elements array had been configured, the electrical impedance characteristic response for all 22 elements are both modelled and measured to make sure all elements behave as intended. For the transmitter, the primary operating frequency is located at the electrical resonance frequency. Figure 4-12 shows the electrical frequency results for all 22 elements, starting from the middle element '1' to the outmost ring 'l8, u8 and d8'. The theoretical impedance characteristic results are modelling in PZFlex and the experimental results for each array ring are detailed in Appendix E. The experimental results show a good match to the theoretical prediction, where both show an increasing tendency from the designed 590 kHz to 640 kHz.

4.3.5.2 22 elements receiver array impedance characteristic

Once the 22 elements array had been applied to the receiver, the electrical impedance characteristic responses were evaluated using the same approach as applied to the transmitter. Figure 4-13 shows the electrical frequency results for all 22 elements, starting from the middle element '1' to the outmost ring 'l8, u8 and d8'. The theoretical impedance characteristic results are modelled in PZFlex also and the experimental results for each array ring are detailed in Appendix E. For the receiver, the mechanical resonance frequency is the main check parameter as it will work at the mechanical frequency. The experimental result shows an increasing tendency, which is in contrast to the relatively stable theoretical results. The difference between the simulation and the experimental results is caused by the manufacturing tolerances as shown in Figure 4-4 (page 98), where the mechanical frequency is 578 kHz rather than the designed and simulated one at 590 kHz. Another reason is caused by the PZFlex model which doesn't separate the outside ring into three parts.

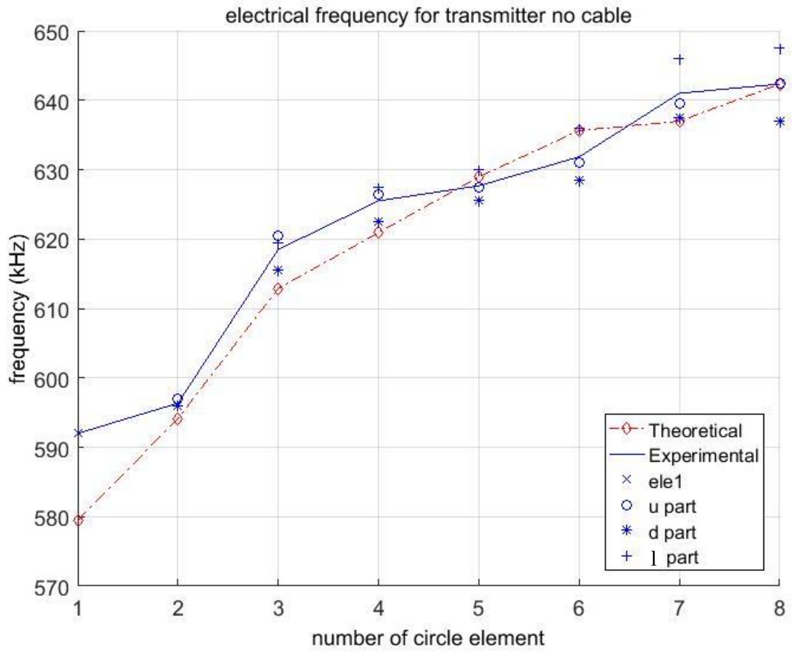

Figure 4-12 Theoretical and experimental electrical frequency for each ring/element of transmitter before put into the transducer’s case

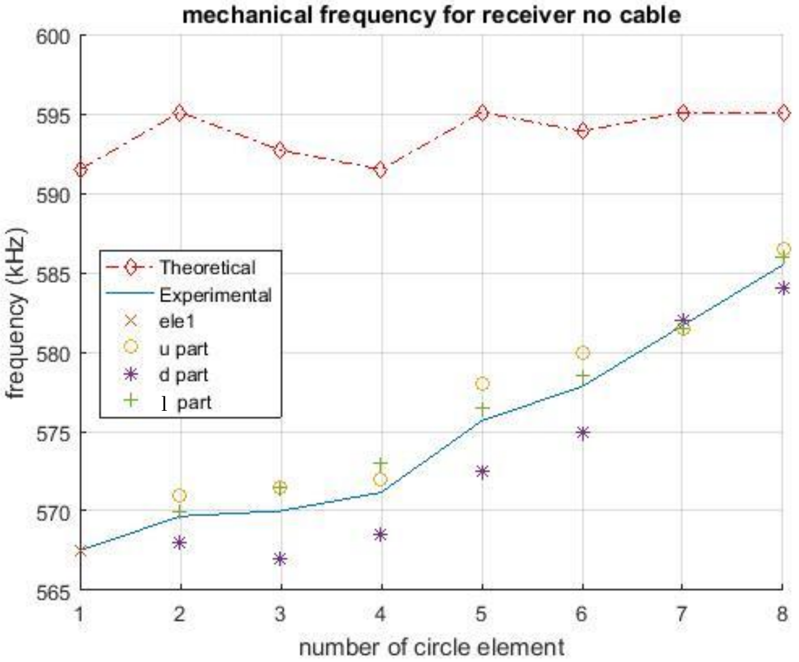

Figure 4-13 Theoretical and experimental mechanical frequency for each ring/element of receiver before put into the transducer’s case

4.4 Transducers Construction

4.4.1 Transducer Housing

The transducer housings are designed based on the dimension of the piezocomposite with 63 mm width, 63 mm length, and 270 mm high. The large height offers space for electrical interconnect PCB boards. The housing was fabricated in sections to allow access during the electrical wiring stage, as shown in Figure 4-14.

Two PCB boards are manufactured for connecting the individual wires from the 22 elements and the external coaxial cable. The connection details are depicted in Appendix F.

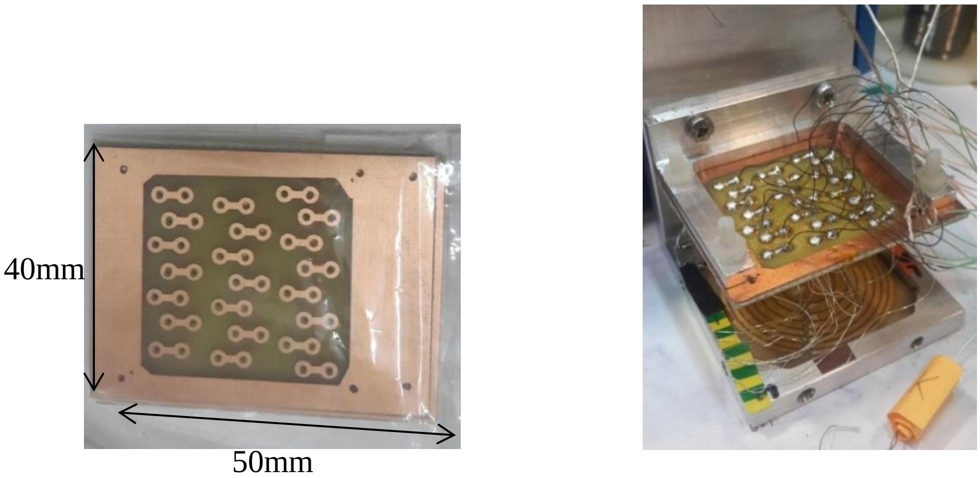

(a) Interconnect PCB

(b) Connecting wires from transducer to interconnect PCB

Figure 4-14 PCB boards layout and example of electrical wiring process

4.4.2 Micro-coax interconnect using Hypertonic

Due to availability of the standard Hypertronics (Hypertronics, Massachusetts, USA) phased array connector (Hypertac connector, Smiths Interconnect), both the transmitter and receiver are connected into one single Hypertronics connector as shown in Figure 4-15. The cables are separated into two distinct areas for both the transmitter and the receiver. The connection detail is shown in Appendix F.

Figure 4-15 Hypertronics connector

Table 4.3 details the electrical parameters of the micro-coax cable used for this work. The cable used was available in the CUE laboratory and was unlabeled. Hence, all the parameters were determined using a standard multi-meter. Importantly, the full 3 m length of cable has been measured as this will be connected to each array element and potentially can influence the electrical performance of the transducer array. With the cable attached, the transducer performance tests for both transmitter and receiver have been repeated to determine how the cable will influence the impedance characteristic and the vibrational conditions.

Table 4.3 Micro-coax cable measured electrical data

	3 meters long cable	*Parameters per meter length*
Inductance	0.158 mH	0.052 mH
Capacitance	846 pF	282 pF
Resistance	18 Ω	6 Ω
Conductance	0.056 S	0.167 S

4.4.2.1 Transducer electrical impedance and vibrational characteristics

It is obvious that manufacturing tolerances and repeatability of processes can introduce uncertainty factors which could influence the transducer performance. Hence, to ensure the finished transducers work as designed, the performance characteristics of each transducer will be re-tested after the micro-coax cable attached and the original measurements detailed in Section 4.3.5 repeated.

i. Transmitter evaluation

For the transmitter, the electrical resonance frequency is still the main testing parameter. In Figure 4-16, the f_e for each element is presented. The tendency for the frequency to increase as consecutive array rings are investigated is matched for both theoretical and experimental results. With the cable connected, the average value of f_e was reduced by about 10 kHz in experimental results compared to Figure 4-12, meanwhile the theoretical results remained at a similar value. The detailed electrical impedance characteristic for each measurement is shown in Appendix G.

Figure 4-17 presents the vibrational response for the transmitter and cable combination, for each array annual ring. All of the results show the array vibrating in phase, with low levels of mechanical cross-talk between array elements. Interestingly, the mechanical crosstalk is highest for the second ring and results in displacement in the inner element. As a hard-set epoxy has been used as the filler material, some degree of mechanical crosstalk was expected due to the low lateral attenuation associated with the polymer phase. Hence, overall these are very good results from an array operational perspective and the crosstalk between ring 2 (l2, u2 and d2) and the central element (1) may be due to the fact that there is minimal polymer material around the inner element to provide lateral damping as the inner radius is the smallest. It should also be noted that annular ring 8 (l8, u8 and d8) has a lower displacement characteristic when compared to the other rings. It is considered that this is due to the thinnest width than the inner rings which may not cover one piezoceramic pillar fully.

ii. Receiver evaluation

The mechanical frequency result for each element of receiver is shown in Figure 4-18. The trends of increasing frequency from the inner to outer elements for both theoretical and experimental results are consistent. Although, for this device the theoretical results are higher than the experimental result. With the cable connected, the average of the measured f_m is reduced by about 65 kHz to 500 kHz when compared with the original results presented in Figure 4-13. This will have implications for the efficiency and operational behaviour of the receiver array and this phenomenon is analysed in the Section 4.4.3. The detailed electrical impedance characteristics are shown in Appendix G.

Figure 4-19 presents the vibrational conditions for receiver with micro-coax cable connected and have been evaluated at the device electrical resonance frequency of 470 kHz. The devices have an overall poorer performance than the transmit array (Figure 4-17) in terms of uniform element displacement and higher mechanical crosstalk is clearly evident in the additional concentric rings visible in each measurement. This piezocomposite has a lower ceramic volume fraction compared to the transmit device and this will contribute to the poorer transmit performance. Importantly, each annular array element is operational and was considered to be useable as an air-coupled receiver for this work.

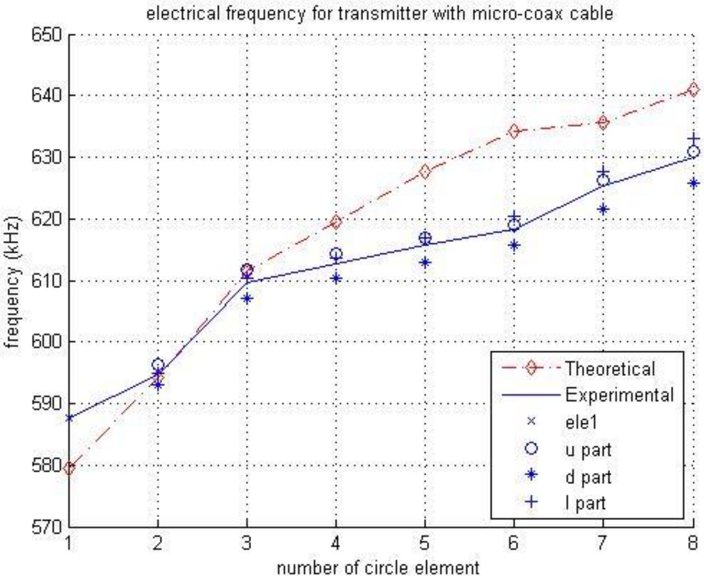

Figure 4-16 Theoretical and experimental electrical resonance frequency for each annular ring of the transmitter with 3 m cable connected

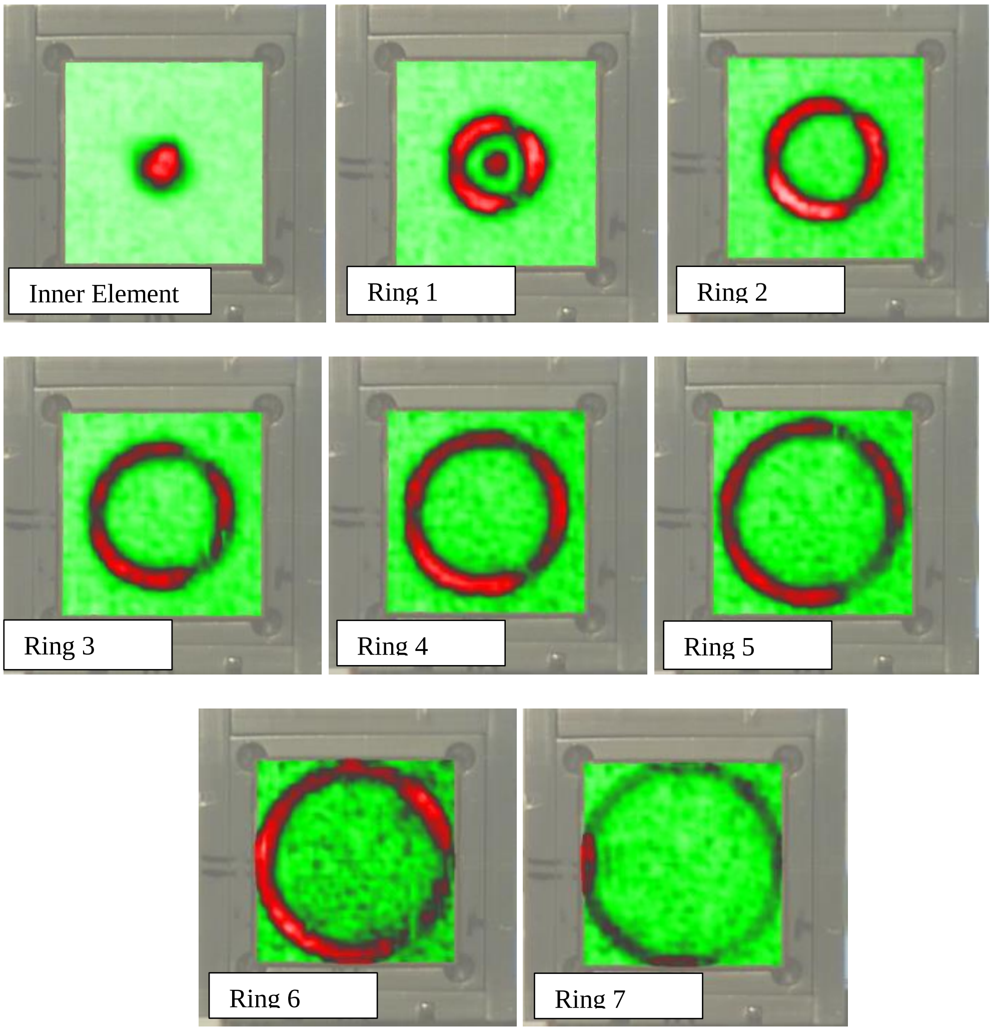

Figure 4-17 Vibrational conditions for 22 annular array elements of the transmitter with micro-coax cable connected for operating at 580 kHz

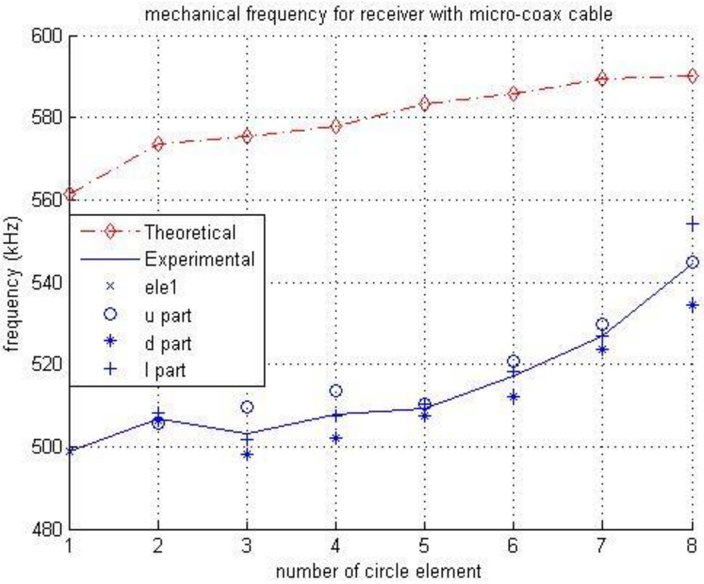

Figure 4-18 Theoretical and experimental mechanical resonance frequency for each annular ring of the receiver with 3 m cable connected

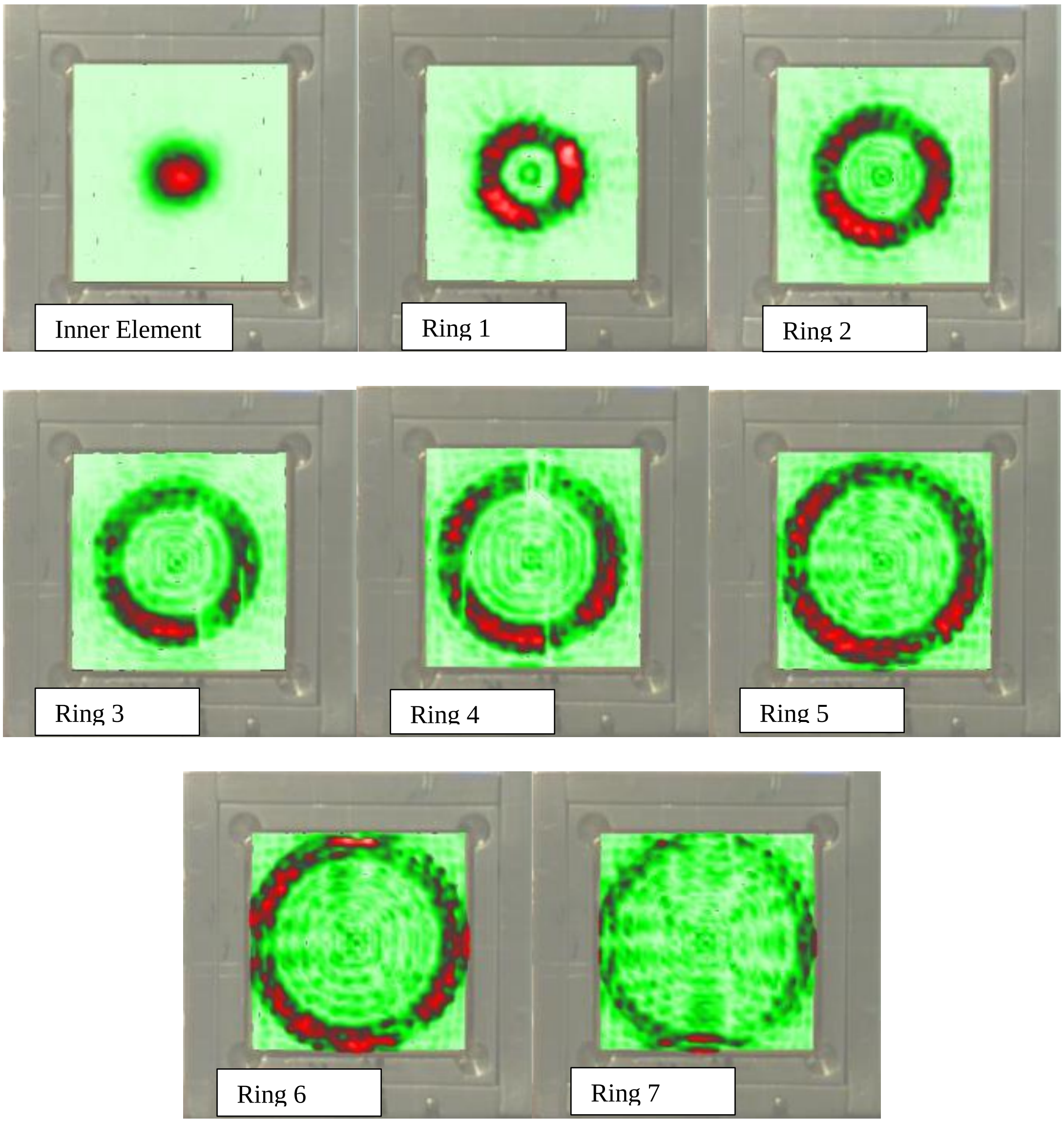

Figure 4-19 Vibrational conditions for 22 annular array elements of the receiver with micro-coax cable connected for operating at 473 kHz

4.4.2.2 Transmitter array focusing performance

i. Pressure profile simulation and experimental set up

Simulation of the segmental annular array pressure profile has been undertaken in MATLAB, initially without applying any focal law. The simulated layout is shown in Figure 4-20 and the spatial resolution is 0.1 mm. The air field pressure is calculated by the summing contributions in the field from each point on the transducer surface. The MATLAB code detail is based on Huygen's Principle and is presented in Appendix D.

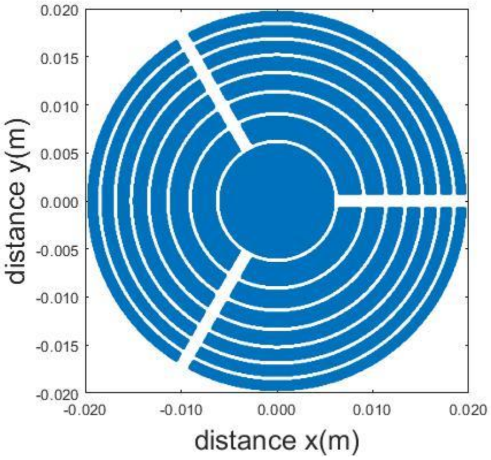

Figure 4-20 Air field pressure simulated layout in MATLAB

The Figure 4-21 shows the simulation on-axis profile for the 22 element transmitter array disc, which has a minima located at 30 mm and should be accounted for when operating the array. Moreover, it is clearly evident from the Figure that the air attenuation dominates the pressure field and it .

For the corresponding experimental focusing tests, the transmitter is excited by the Dynaray Phased Array Controller (Dynaray-256/256PR, Zetec Inc, Canada) and a pinducer is connected to an in-house x-y mechanical scanner to record the air field pressure with high spatial resolution. The experimental configuration is shown in Figure 4-22. The transmitter is fired by a 60 dB and 830 ns width pulse with 16 averages on reception.

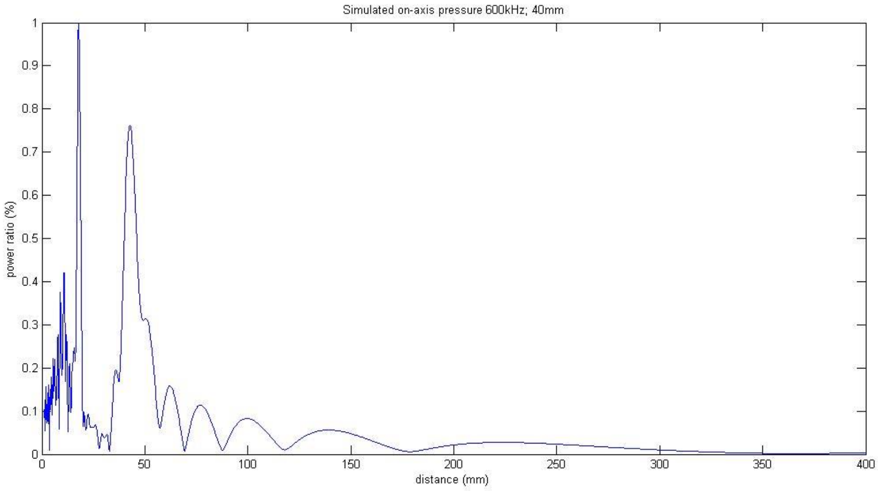

Figure 4-21 Simulation on-axis directivity profile for a 40 mm diameter transducer with 22 elements annular array

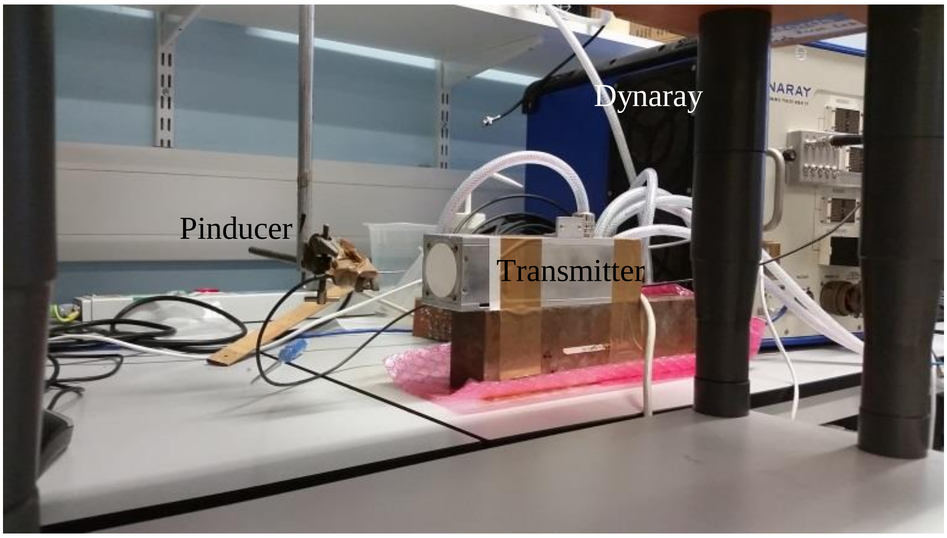

Figure 4-22 Experimental configuration for air field pressure test using Dynaray PAC

ii. Transmitter array focusing performance

To test the transmitter's focusing performance, appropriate time delays are incorporated into the MATLAB code and a series of simulations were conducted when the focusing point is located between 30 mm to 80 mm. Figure 4-23 shows the relationship between the focusing distance and the maximum air field pressure at the focal point. Importantly, the acoustic power is highest when operating in the range of 50 mm and 65 mm.

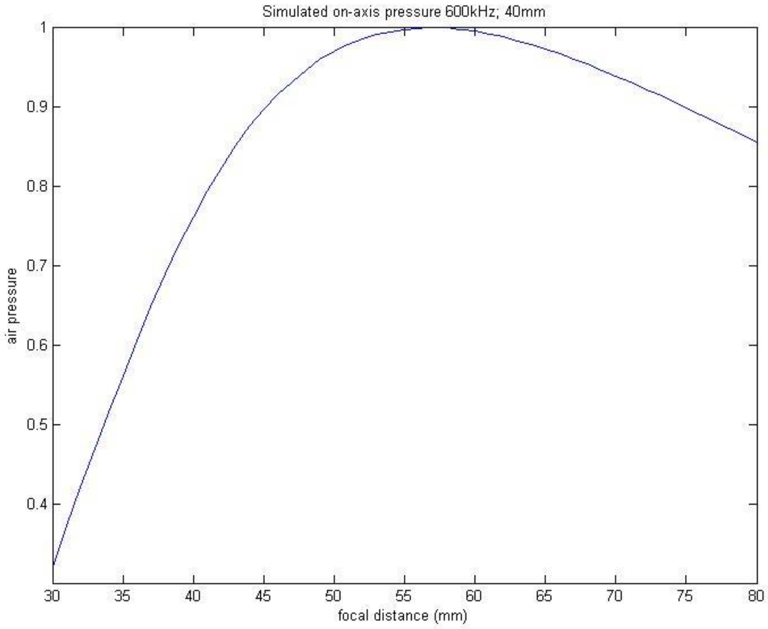

Figure 4-23 Simulated on-axis directivity profile for a 40 mm diameter, 22 elements annular array transmitter when focusing at different distances

Figure 4-24 illustrates the simulation on-axis air field pressure profile when focusing at 65 mm, 75 mm and 85 mm distances from the transducer front face which is based on the same MATLAB model in Appendix D. All of them have a clear focusing peak, with the highest peak pressure value predicted at the focusing depth of 65 mm. In addition, as the focal length is increased it can be observed that the focal region lengthens.

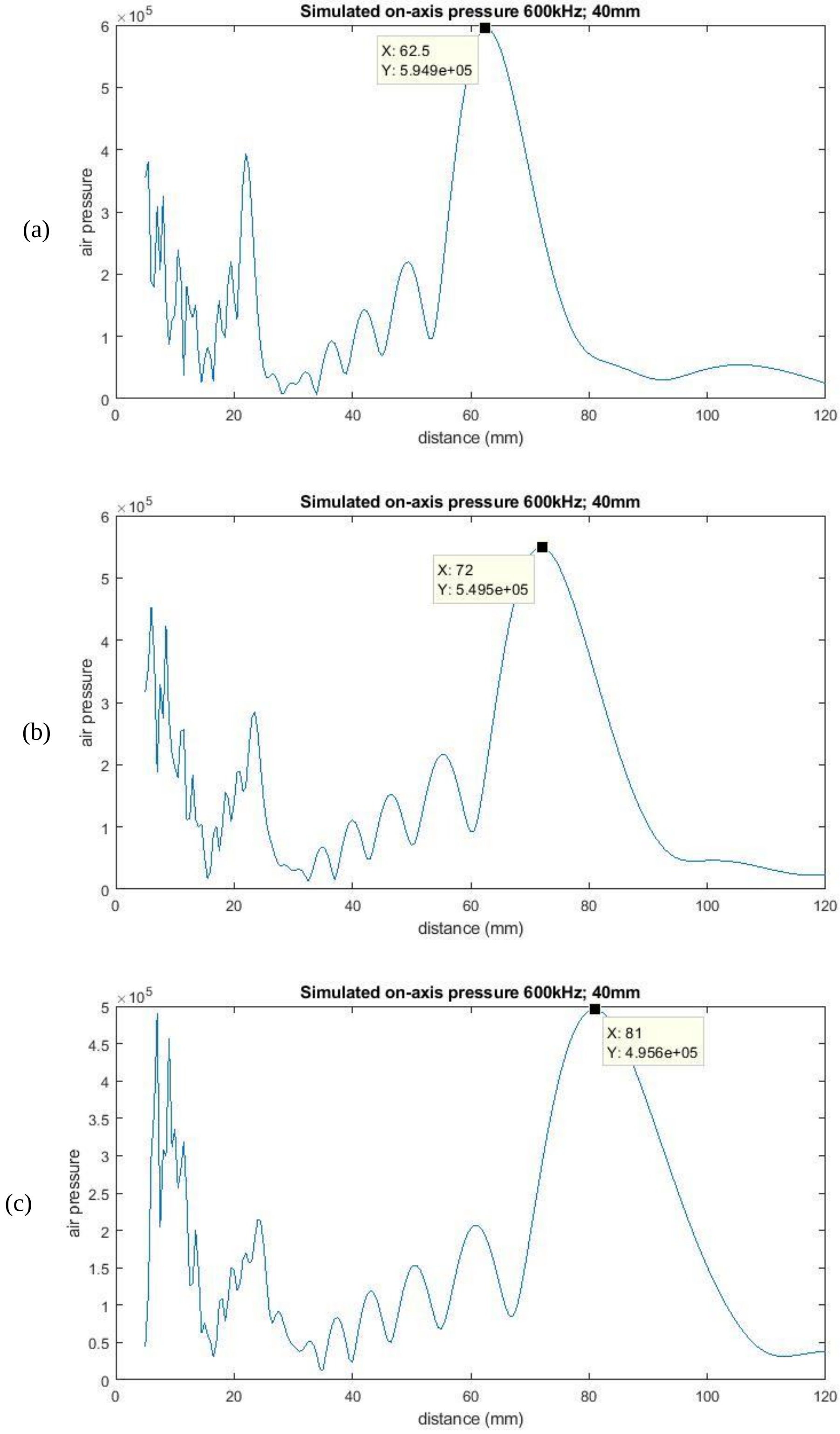

Figure 4-24 Simulated on-axis directivity profile for a 40mm diameter transducer with 22 elements annular array focusing at (a) 65 mm, (b) 75 mm and (c) 85 mm

Table 4.4 gives the focal law details when focusing at different distances. The middle element has the largest time delay for central axis focusing without consider the matching layer and the sample. The focal law calculation is based on the Trigonometric rule, which was introduced in Section 2.4.2.2. For the specific 22 elements array with designed thickness matching layer and specific sample material, a more complex MATLAB code has been written to calculate equivalent time delay table. The example shows the calculation process for the ring #1 and the code detail is presented in Appendix H. The main limitation for the focal law applied rather than the physical focusing method is that it increases the excitation demands on the signal generator to ensure that the anticipated operational performance is achieved.

Table 4.4 Time delay table for different focal distances

Annular ring number	Time delay(ns)		
	Focus at 65 mm	Focus at 75 mm	Focus at 85 mm
#1	8120	7068	6254
Ring#1	6817	5939	5258
Ring#2	5789	5046	4469
Ring#3	4709	4108	3640
Ring#4	3589	3133	2777
Ring#5	2429	2121	1882
Ring#6	1227	1073	952
Ring#7	0	0	0

Example: calculate the total travel time

This example illustrates the total travel time for the first circle elements (l2, u2, d2) with 7.64 mm radius as the middle point of the beam, which is the excitation reference point assumed in the calculations. The material of the test specimen is steel, in this example with a sound velocity of 5200 m/s and the sound velocity inside matching layer is assumed as 630 m/s [8]. The total focal distance is 50 mm (Thickness of matching layer is 0.48 mm, air is 36 mm and then the depth inside the specimen is 13.52 mm).

Figure 4-25 shows the travel time calculation, where x_1 and x_2 have a range from 0 mm to 7.64 mm. The minimum travel time has been calculated at 1.0805e-04 second, when x_1 is 6.57 mm and x_2 is 1.04 mm.

Figure 4-26, Figure 4-27 and Figure 4-28 are illustrations of the air field pressure simulations calculated in MATLAB, with experimental Dynaray C-scan results provided for comparison. Comparing the theoretical and experimental results in these Figures demonstrates that all of them have a clear focussed region, as designed, and noting that there is a 50 mm offset on the experimental results to minimise the scanning time by starting 50 mm from the front face of the transducer.

There is excellent correlation between the focal region size and shape for each focal law. Moreover, it is apparent that the experimental results are consistent with the predicted lengthen of the focal region as the focal point moves further from the transducer front face.

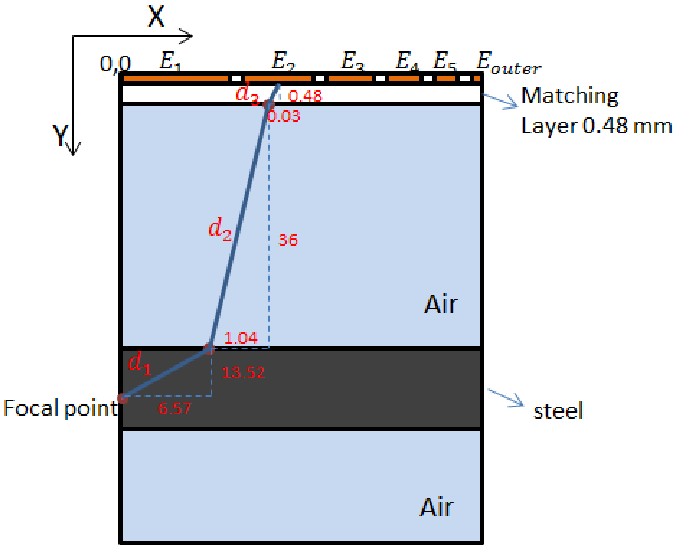

(a) Ray path from element (ring #1) to desired focal point in steel specimen

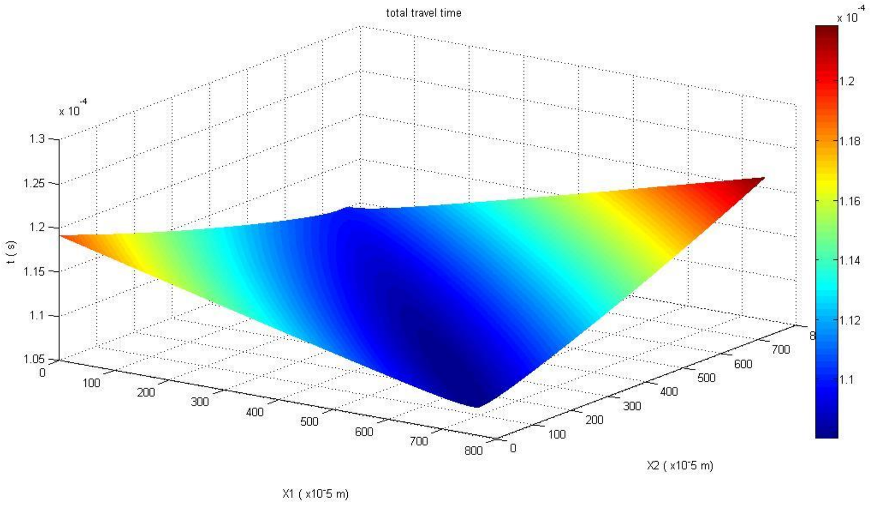

(b) Contour plot of all of the array element time delays to focus 13.5 mm into a steel specimen

Figure 4-25 An example focal law calculation which use MATLAB to calculate the shortest time for ultrasound propagation, (a) the shortest time ultrasound path when focusing inside the steel specimen; (b) the propagation time calculation to find the mininal value

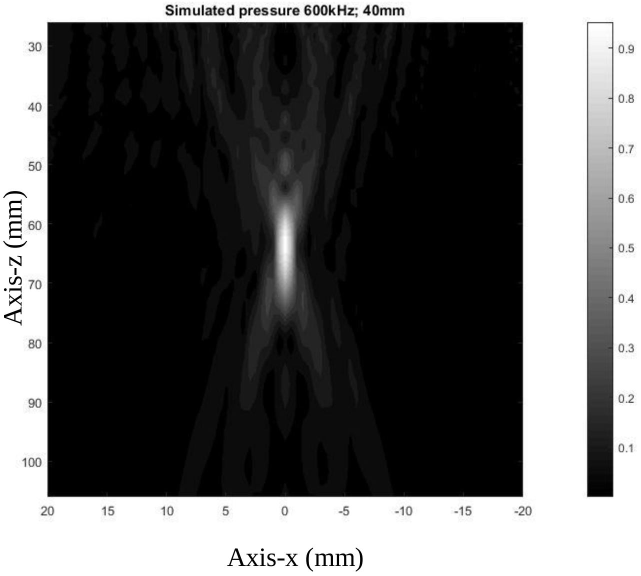

(a) Matlab 3-D simulation

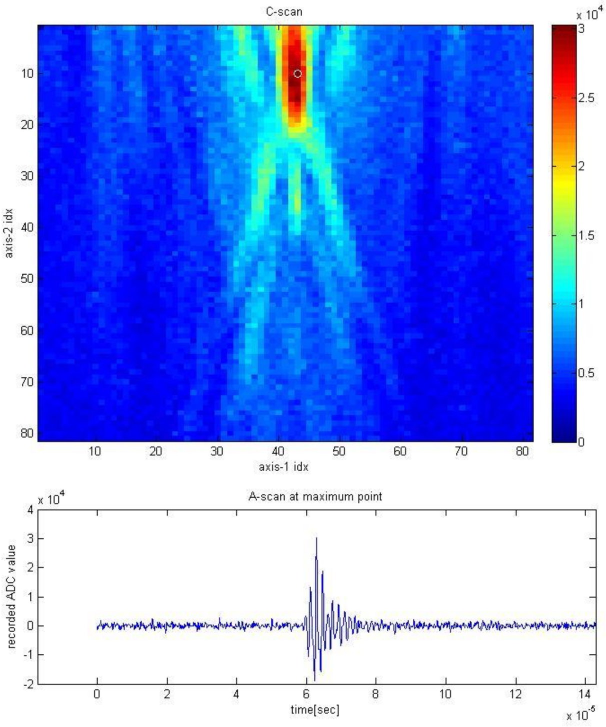

(b) Dynaray experiment

Figure 4-26 Beam profiles for 22 elements annular array focusing at 65 mm depth with matching layer applied, (a) MATLAB focusing simulation; (b) Dynaray experiment with 50 mm offset as the front area has too bright color/large air pressure which will mask the focusing area detail

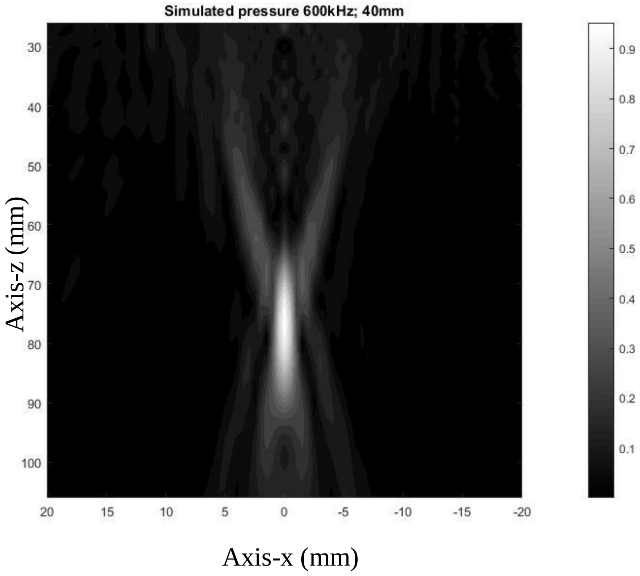

(a) Matlab 3-D simulation

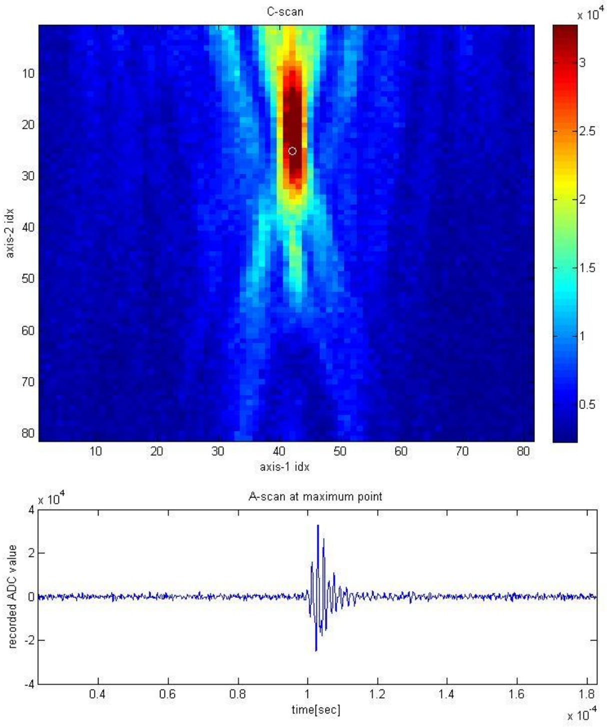

(b) Dynaray experiment

Figure 4-27 Beam profile for 22 elements annular array focusing at 75 mm depth with matching layer applied, (a) MATLAB focusing simulation; (b) Dynaray experiment with 50 mm offset as the front area has too bright color/large air pressure which will masks the focusing area detail

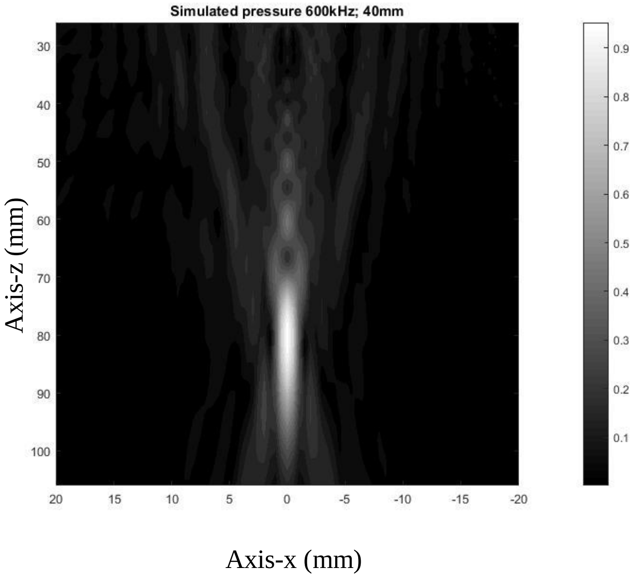

(a) Matlab 3-D simulation

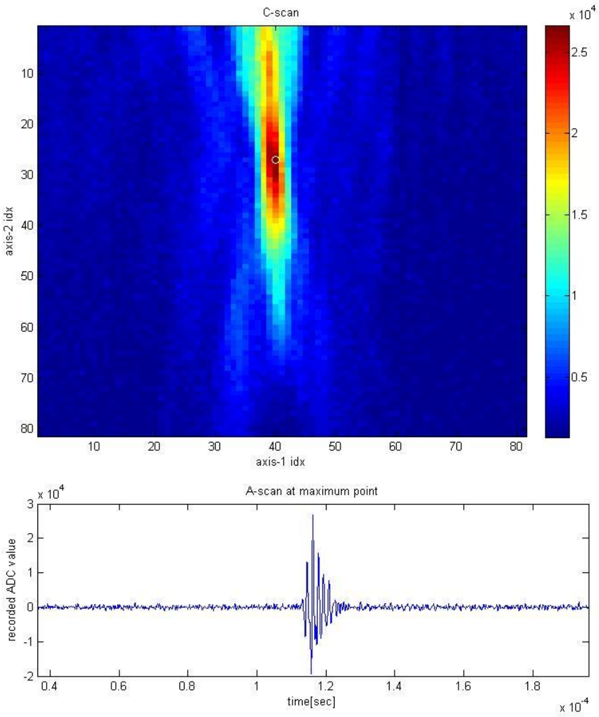

(b) Dynaray experiment

Figure 4-28 Beam profile for 22 elements annular array focusing at 85 mm depth with matching layer applied, (a) MATLAB focusing simulation; (b) Dynaray experiment with 50 mm offset as the front area has too bright color/large air pressure which will masks the focusing area detail

4.4.3 Analysis of frequency shift issue after cable attachment

In Section 4.4.2.1.ii, the experimental measurement shows a reduction in the mechanical resonance frequency for the receiver device was observed after the attachment of the micro-coax cable. Figure 4-29 presents the theoretical electrical impedance characteristic curves for the receiver's middle element with micro-coax cable when the capacitance is included in the PZFlex model as the measured value of 282 pF per meter. The full line is the impedance characteristic on the top of the electrode surface and the electrical impedance characteristic at the end of the cable is shown by the dashed line. Comparing with these two lines, the cable capacitance leads to a reduction in the mechanical resonance frequency, f_m, and a subsequent decrease in the value of the maximum electrical impedance. The f_m frequency shift is more than 50 kHz, the maximum impedance reduces to be lower than the half of the impedance on the surface of the receiver and the electrical resonance frequency, f_e, doesn't change. In fact, all of the mechanical resonance frequencies shift due to the inclusion of the cable capacitance, with the middle element demonstrating the largest shift range. Importantly, these results are consistent with the experimental results shown in Section 4.4.2.1.ii.

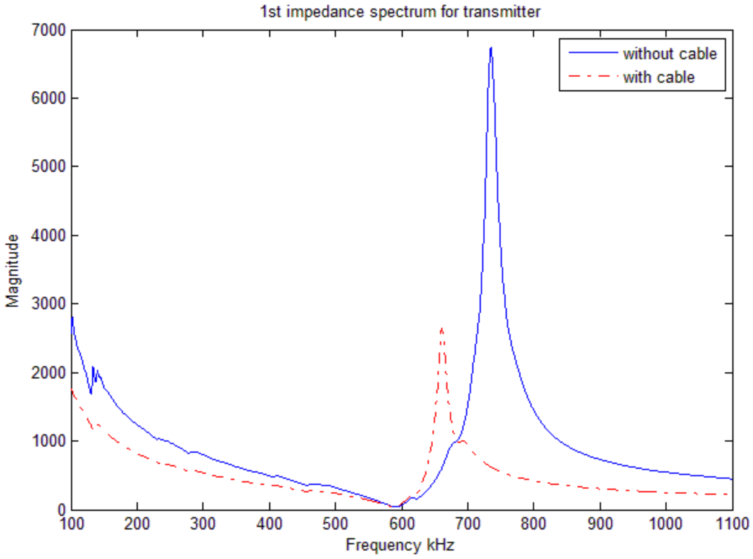

Figure 4-29 Simulated impedance characteristic for the receiver's middle element 1, with and without the inclusion of capacitance due to the micro-coax cable electrical connection

There are many methods that can be considered to compensate for the frequency shift, such as changing cable type, or shortening the micro-coax cable. However, using the Hypertonics plug is an easy way for the Dynaray to control each pin and cutting the cable shorter will restrict the transducers reach when being used for inspecting a large specimen. Accordingly, a decision to build a pre-amplifier stage between the active array elements and the micro-coax cable was considered a good option. Importantly, the pre-amplifier will enlarge the received signal/SNR and provide an impedance buffer to compensate for the frequency shift.

To remedy the frequency shift, a simple pre-amplifier has been designed as shown in Figure 4-30. The AD797 (RS, Stock No. 912-7407) is a very low noise, low distortion operational amplifier which is ideal for using inside the pre-amplifier. In addition, the AD797 has an excellent slew rate of 20 V/µs and a 110 MHz large gain bandwidth, which is highly suitable for low frequency ultrasound systems. The BUF634 is a high speed, unity-gain open loop buffer which is suitable for use as a pre-amplifier. The BUF634 device can be used inside the feedback loop of op amps to increase output current and improve capacitive load drive. Table 4.5 shows the amplifier frequency response. It shows that this array preamplifier is appropriate for lower frequency applications. For ease of the pre-amplifier installation in the limited space inside of the transducer’s case, the 3 segmented elements of 7 each outside ring element are connected together and hence, the array reverts back to a standard annular array.

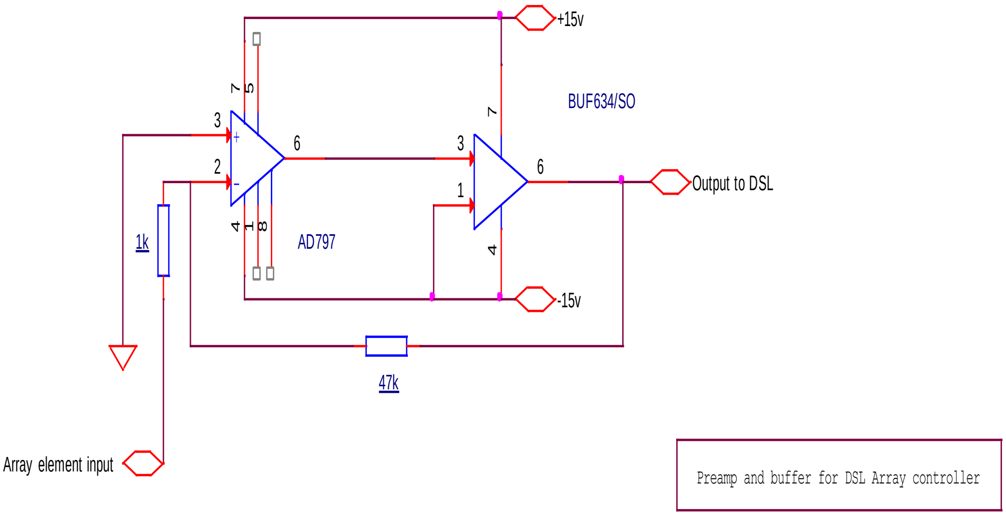

Figure 4-30 Schematic of the array pre-amplifier

Table 4.5 Frequency response table

Frequency	*Vin*	*Vout*
10 kHz - 1 MHz	10 mv	1 v
1.1 MHz	10 mv	0.95 v
1.2 MHz	10 mv	0.95 v
1.3 MHz	10 mv	0.85 v
1.4 MHz	10 mv	0.85 v
1.5 MHz	10 mv	0.825 v
1.6 MHz	10 mv	0.8 v
1.7 MHz	10 mv	0.75 v
1.8 MHz	10 mv	0.7 v
1.9 MHz	10 mv	0.6 v
2.0 MHz	10 mv	0.5 v

4.4.4 Connection to phased array controller for inspection trials

The Dynaray PAC can only use pulse excitation to drive the array elements and as such, it can’t offer enough power for practical testing in the air medium. A second PAC, Flawinspecta (Diagnostic Sonar Limited, UK) is a better choice for the delivery of a narrower bandwidth excitation signal for air-coupled inspection, such as firing by a 5 cycle sine wave tone burst. This will be referred to a DSL in the rest of the Thesis. Unfortunately, to connect to the DSL, the original Hypertronics connector was not suitable and the connection arrangement changed to two sets of SMB sockets for the transmitter and receiver elements, as shown in Figure 4-31. At this stage, the opportunity to change the micro-coaxial cable was available and a replacement cable, RG174 (RS stock No. 521-8206), was used as this was compatible with the SMB connectors.

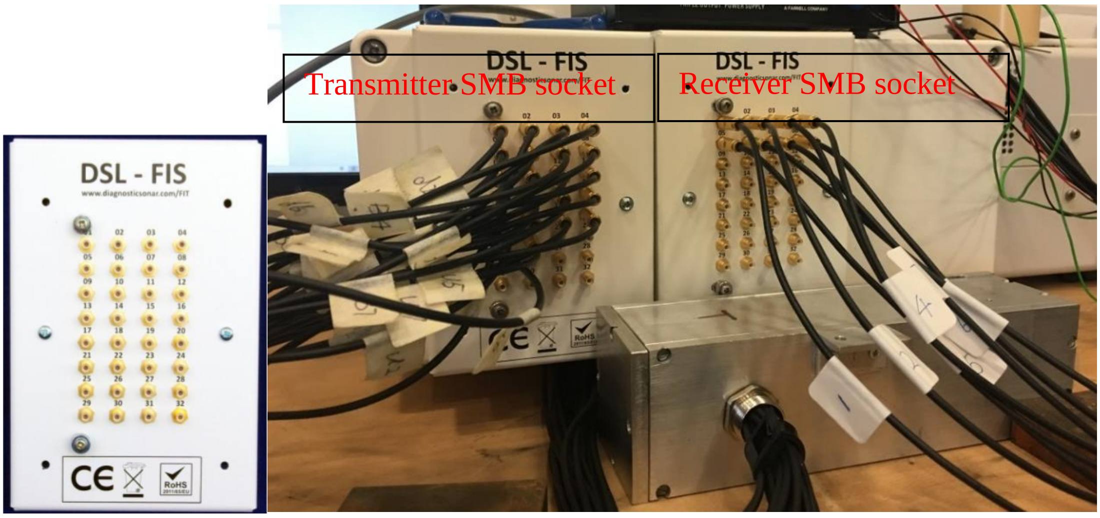

Figure 4-31 Two SMB sockets: one for transmitter and one for receiver

Table 4.6 shows the parameters of the RG174 cable datasheet. Again, as the cable will influence the performance of the receive transducer in particular, a shorter cable length of 2 meters was selected, which still enables the arrays to be evaluated on experimental samples. The performance tests for both transmitter and receiver have been carried out again to find how significant the cable capacitance will influence the impedance characteristic. As the capacitance is smaller than the micro-coax cable, the frequency shift is expected to be smaller as well.

Table 4.6 RG174 co-axial cable parameters

	Parameters per meter
Inductance	0.009 mH
Capacitance	111 pF
Resistance	0.4 Ω
Conductance	2.5 S

4.4.4.1 Transducers' impedance characteristic

To ensure the final transducers work as expected after changing the cable, the various performance metrics for the transducers are re-tested.

i. Transmitter's evaluation

For the transmitter, the electrical impedance characteristics are measured again. The electrical resonance frequency for each element is collated and presented in Figure 4-32. The increasing trend observed is the same as with the micro-coax cable. After the RG174 cable was connected, the average value of electrical frequency is reduced by no more than 5 kHz compared to the experimental results shown in Figure 4-12. The detailed electrical impedance characteristics for each annular array element are shown in Appendix G.

ii. Receiver's evaluation

After the 8 preamplifiers have been installed inside the receiver, the impedance characteristic cannot be tested directly. So a frequency sweep has been done to find at which frequency, the receiver can receive the largest power. The frequency shift still exists in the modified array, as originally reported for the micro-coax cable.

4.4.4.2 Operational frequency decision

Unfortunately, the final designs of transmitter and receiver annular arrays are not matched to a common operating frequency. This is a consequence of fabrication issues and the introduction of cable capacitance. This is sub-optimum in terms of maximising the operational performance of an air-coupled system, which has inherent SNR issues due to the acoustic impedance mismatch between the piezoelectric material and the load medium. Hence, it is necessary to decide on the best operating frequency for the practical system before conducting air-couple inspection tests. A frequency sweep test was therefore conducted to find the best operational frequency. The simple experimental configuration used previously, see Figure 3-16, was used with a separation distance around 50 mm and carefully direction and position adjustments undertaken to maximise the received signal. Figure 4-33 presents the maximum amplitude across a narrow frequency range. These frequency sweep results indicate that when the system operational frequency is 530 kHz, the system SNR will be maximised. This operational frequency will be used in the next Chapter where the system experimental evaluation will be described.

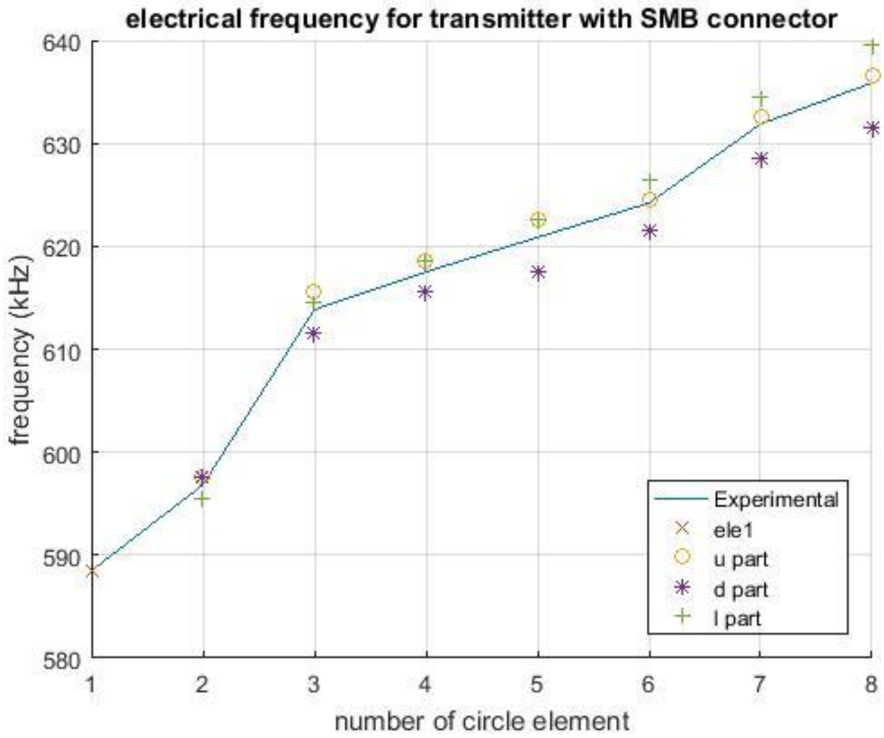

Figure 4-32 Experimental electrical frequency for each ring/element of transmitter with 2 m RG174 cable

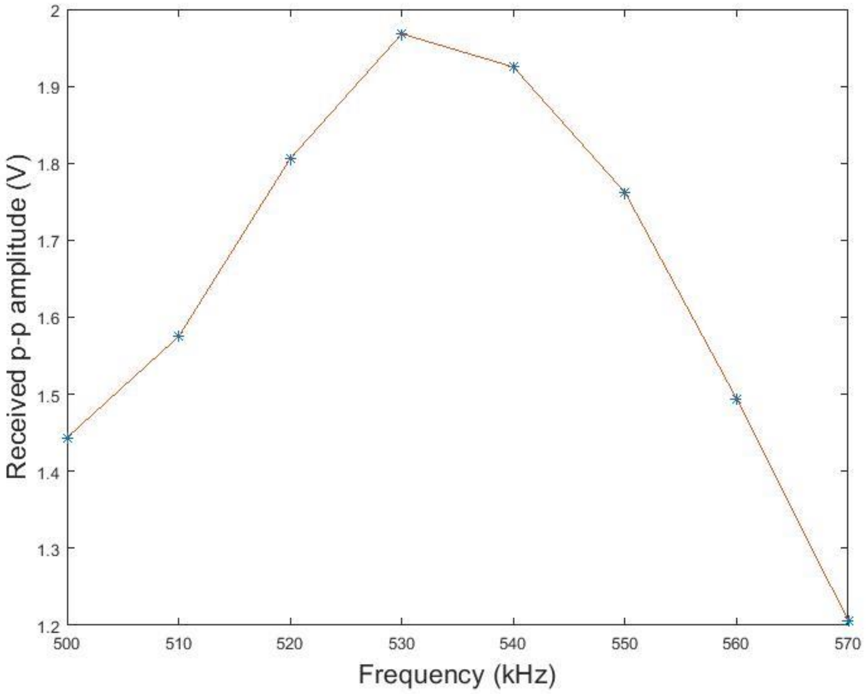

Figure 4-33 Frequency sweep for the best received signal which is maximum at 530 kHz

4.5 Summary

This Chapter describes the development of an annular array air-coupled inspection system. In this work, a separate transmitter and receiver were designed to operate in the frequency range 500-600 kHz. Moreover, an annular array configuration was selected to provide control of the focal depth, with a 1.5-D configuration selected to provide additional off-axis control. The manufacture and evaluation was split into two parts due to the specification and availability of two different phased array controllers within the CUE laboratory. The Zetec Dynaray PAC provided a convenient platform to test and characterise the operational performance of the transmitter. After this was complete, the electrical interconnect was modified to accommodate the DSL FlawInspecta PAC, which is capable of delivering a gated square wave burst to maximise the efficiency for air-coupled inspection operation.

For the basic transducer designs, good correlation between simulated and measured transducer performance metrics was achieved. Unfortunately, the addition of coaxial cable to connect the transducer to the PAC introduced cable capacitance which resulted in a frequency shift for the receiver array, in particular. A pre-amplifier stage was introduced, which increased the system SNR but did not overcome fully the frequency shift issue due to cable capacitance. In order for the fabricated air-coupled annular array system to be used in an experimental set-up, the best operational frequency for this transmit-receive pair was experimentally evaluated and will be set at 530 kHz in the next Chapter.

CHAPTER 5 Experimental Evaluation

Abstract

In this Chapter, the experimental set up and results from the annular array will be presented. The FlawInspecta (DSL) phased array controller will be used to drive the transducer with a multiple cycle, gated square wave excitation function. However, the DSL software (FIToolbox) has no individual focal law module which can meet the requirements for applying the focal law to annular array transducers. Consequently, a method to apply both transmitter and receiver focal laws are introduced in this Chapter. A number of experimental results are then presented. The air-coupled annular array transducer configuration resolution is first tested by using an aluminium plate with through thickness holes. Next, a sandwich structure honeycomb material with known defects has been scanned and the results are extremely encouraging. Finally, a carbon fibre reinforced polymer (CFRP) material was tested and was shown to have a relatively weak SNR, but it was still possible to identify defects in the images.

5.1 Experimental arrangement

To ensure consistency with respect to attenuation, the operating environment has to be kept at a constant status. The CUE laboratory was utilized to conduct all the air-coupled experimentation described in the Thesis, which provided a controlled environment, 20 ℃ ± 1 ℃ for temperature and 40 % ± 5 % for humidity.

The laboratory was equipped with two phased array controllers (PAC), Dynaray and DSL described in Section 2.6, for array transducers experiments. These were utilized in the transducer characterisation stage described in Chapter 4. Unfortunately, the Dynaray is only capable of generating a wideband pulse excitation. This means, the power driving the transmitter is not large enough to generate sufficient pressure in air to go through a sample to detect the damaged area. Therefore, this Chapter will only focus on the configuration for the DSL PAC.

There are several difficulties during the setting up process for the DSL PAC.

- As discussed in Chapter 4, there is a connector difference between the two PACs and the original Hypertronics connector was replaced with individual coaxial cables (RG174, RS stock No. 521-8206) with a SMB connector (RS stock No. 332-6686). For DSL, it is impossible to control a 22 element transmitter whose pin arrangement is out of order and trying to receive the signal in other 22 pins at the same time for the Hypertronics connector. To solve this problem, the DSL’s hardware setting has been separated into individual transmit and receive modules using two SMB interface units. Each interface unit has its own set of SMB connectors and the connect order can be controlled to ensure the correct array element order is maintained.
- Secondly, the annular array pattern is not consistent with the standard DSL software. The DSL pattern module works better for a linear shaped array, based on the number of elements and the pitch size, from which the software can draw the array element pattern automatically. But for special patterns, such as annular or triangle, it is not straightforward to inform the software of the position of each element. To solve the problem, it is necessary to control each pin/element individually.

- Third, the focal law application method. For the version of the DSL software used for this work (LV2013 : Tx=PXIe-7966R : Rx=PXIe-7966R : 7 May 2015 - 12:30 - Beta), the focal law application module is a basic implementation, which is specifically designed for linear array operation. This is similar to the second problem described previously, where the software cannot understand the position of each array element. Therefore, a special software version has been written to overcome this problem. The focal law has been calculated using a MATLAB routine (presented in Appendix D) and the generated transmitter's focal law table will be applied to each array individually through the DSL PAC interface. For the receiver, data mapping was also a problem needed to be solved. In this version of the DSL software, there is no individual module to set up the receiver's focal law. The solution is to apply the focal law in the post-processing of the data. Hence, during the experiment, each channel of the receiver will acquire the air-coupled signal at the same time and the post-processing applied in MATLAB. The main part of this functional code is shown in Appendix I.

The experimental arrangement is set up on a motorized XYZ scanner stage, as shown in Figure 5-1. The sample being inspected will be fixed on the scanning arm with 1 mm scan dimension per step as the beam width shown in Figure 4-26 and Figure 4-27 are both around 4 mm. Hence, the transducers are fixed into a stationary position and the sample is moved/scanned using the mechanism stage between two fixed transducers. This is a non-standard scanning arrangement but meant that the transducers' relative position is fixed and known for these experimental trials. The main drawback is that the scan area is limited with this set up. The power supply provides a split +15 V and -15 V DC voltage to the pre-amplifier located inside of the receiver housing. The DSL PAC is computer controlled and will fire the calculated time delays in the transmitter array, with the second SMB interface unit receiving the through-transmitted signals simultaneously on all receive array elements.

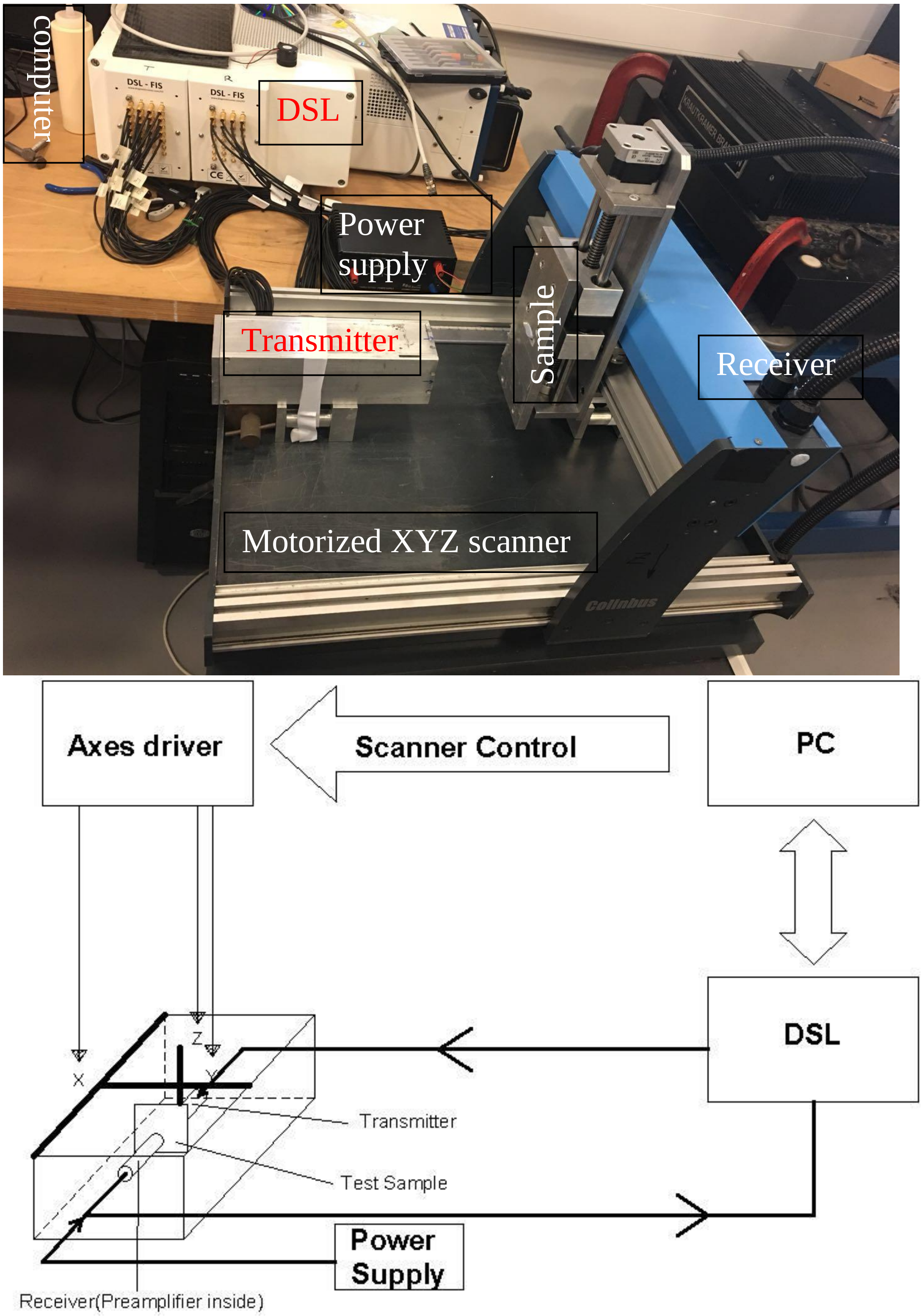

Figure 5-1 Photograph and schematic diagram of the through transmission system used to produce the sample C-scan test

5.2 Specimen inspection using air-coupled annular array transducer pair

C-scan figures are presented in this section for the specimen inspections which are composed of a series of A-scan saved data. The maximum received amplitude and arrival time information in A-scan results are the main extracting information for the C-scan figures. Because of the limited moving space of the XYZ scanner between two large transducers, as shown in Figure 5-1, the C-scan has a limited detection area. Therefore, all the defects have been centred close to the middle of the scanning area in three individual C-scans rather than one large C-scan of the entire sample.

5.2.1 Resolution evaluation using an aluminium plate

Figure 5-2 shows an aluminium test plate, with 5 through-thickness holes, used to initially evaluate the inspection performance of the air-coupled annular array system. A 3 mm thick plate with through-drilled holes of diameters 10 mm, 8 mm, 6 mm, 4 mm and 2 mm was used to evaluate the system resolution performance. For brevity only the C-scan images of the smaller holes in the plate, 4 mm and 2 mm, are presented. Figure 5-3 is the C-scan result across both holes, and it shows that the 4 mm hole position is clearly identified with the -6 dB contour line as the brighter pattern in the left-hand side of the image. The high intensity signal through the 4 mm hole dominates the signals recorded around the 2 mm hole. Hence, Figure 5-4 is a re-scaled image extracted from Figure 5-3 around the location of the 2 mm hole. Again, it is possible to observe and identify the 2 mm hole from this air-coupled dataset with the -6 dB contour line. Accordingly, it is considered that the developed air-coupled annular array system has a resolution of at least 2 mm, which is comparable with previous air-coupled inspection systems [6, 8].

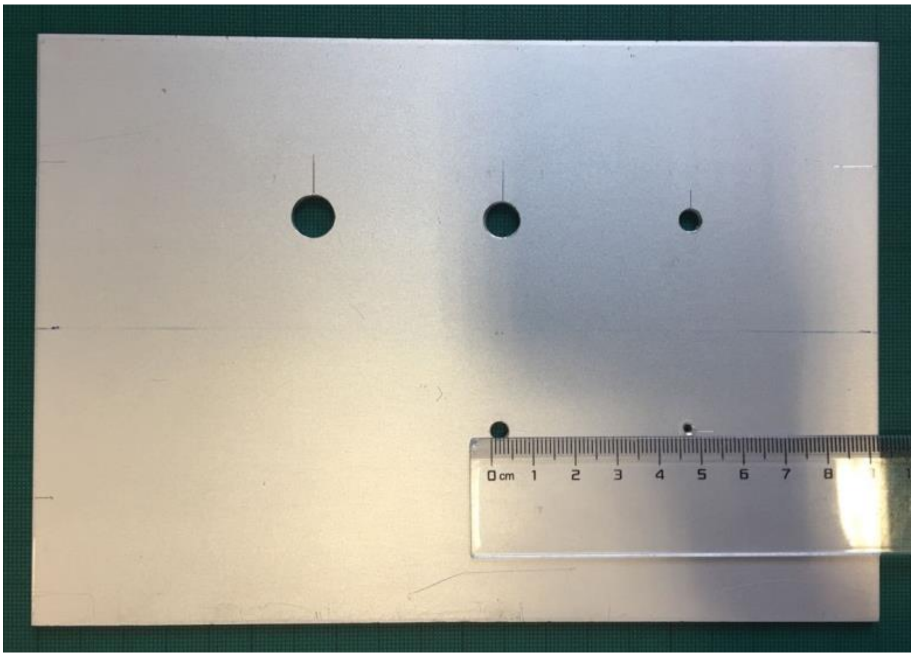

Figure 5-2 Aluminium plate with 5 holes whose diameter are 10 mm, 8 mm, 6 mm, 4 mm, and 2 mm

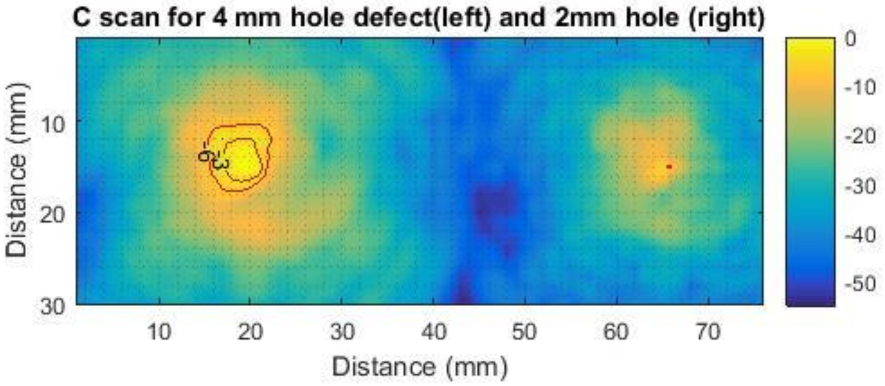

Figure 5-3 C-scan image showing both 4 mm hole (left) and 2 mm hole (right) comparison

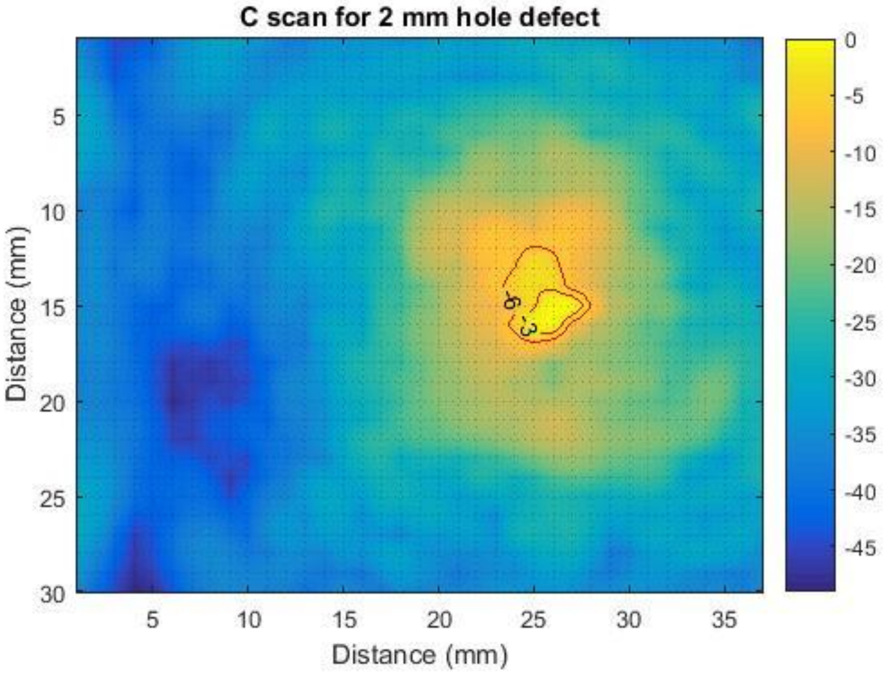

Figure 5-4 Re-scaled C-scan image extracted from Figure 5-3 of area around 2 mm hole

5.2.2 Inspection performance through honeycomb sample test

Sandwich composite structures comprising a ‘paper’ honeycomb core and carbon fibre reinforced polymer (CFRP) facesheets were often fabricated for aerospace industry. A graphical representation of this sandwich structure is provided in Figure 5-5. The structures offer a very high stiffness-to-weight ratio because the hexagon pattern is strong, light-weight and the carbon fibre outer layer, which is typically thin relative to the honeycomb layer, has very high strength [94]. Such sandwich composite structures are difficult to inspect due to the air-coupled honeycomb inner layer.

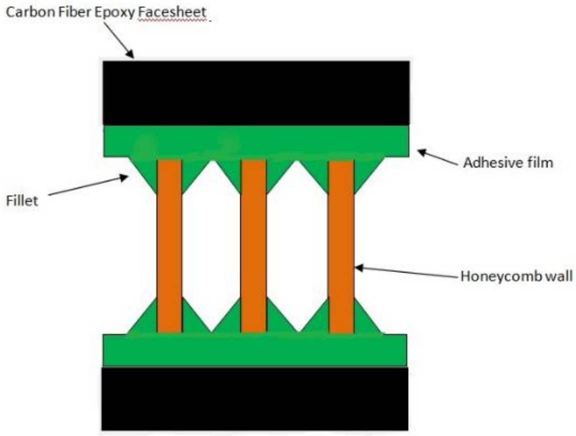

Figure 5-5 Sandwich composite structures with paper honeycomb core and CFRP facesheets [94]

The honeycomb material is not recommended to use with water for inspection scanning as the water will permeate through the honeycomb structure and destroy the material. What is more important is that the standard water medium inspection system cannot acquire useful information due to the air inside the hexagonal cylinder layer. So, an air-coupled inspection system is ideal in this situation. Compared to infrared thermography introduced by Triska and Bugajski [95] which performs well only at facing-side of the sample, the air-coupled transducer approach can locate any damage through the ultrasound propagation path.

5.2.2.1 Introducing defects into honeycomb sample

In order to assess the air-coupled annular array inspection performance, damage was introduced into the Honeycomb sample using a torque wrench and 20 mm diameter steel ball, as shown in Figure 5-6(a). In addition, the mechanical press in Figure 5-6(b) is used to apply pressure to the sample through the ball bearing. The wrench is used to rotate the screw, which will make the ball, placed under the screw, press down into the CFRP surface. When the torque reaches the desired value, the wrench will prevent the ball from pressing down further. The pressure damage will not only cause the visible surface damage, but also cause deformation of the inner structure of the carbon fibre outer layer and honeycomb structure. Therefore, the damage size might be larger than that observed through visual inspection. Two comparison dents were produced using 8 N.m. and 11 N.m. torque as shown in Figure 5-7. From visual inspection these two indentations on the surface of the sample are both ellipse in shape and are approximately 8 mm × 8 mm and 13 mm × 16 mm for the 8 N.m. and 11 N.m. cases respectively. Please note that there is damage at the edge of the sample directly in line with the 8 N.m. defect, which should be noted as this may influence the evaluation results.

Figure 5-6 Tools utilized to create damage in Honeycomb structure (a) torque wrench and ball bearing; (b) mechanical press

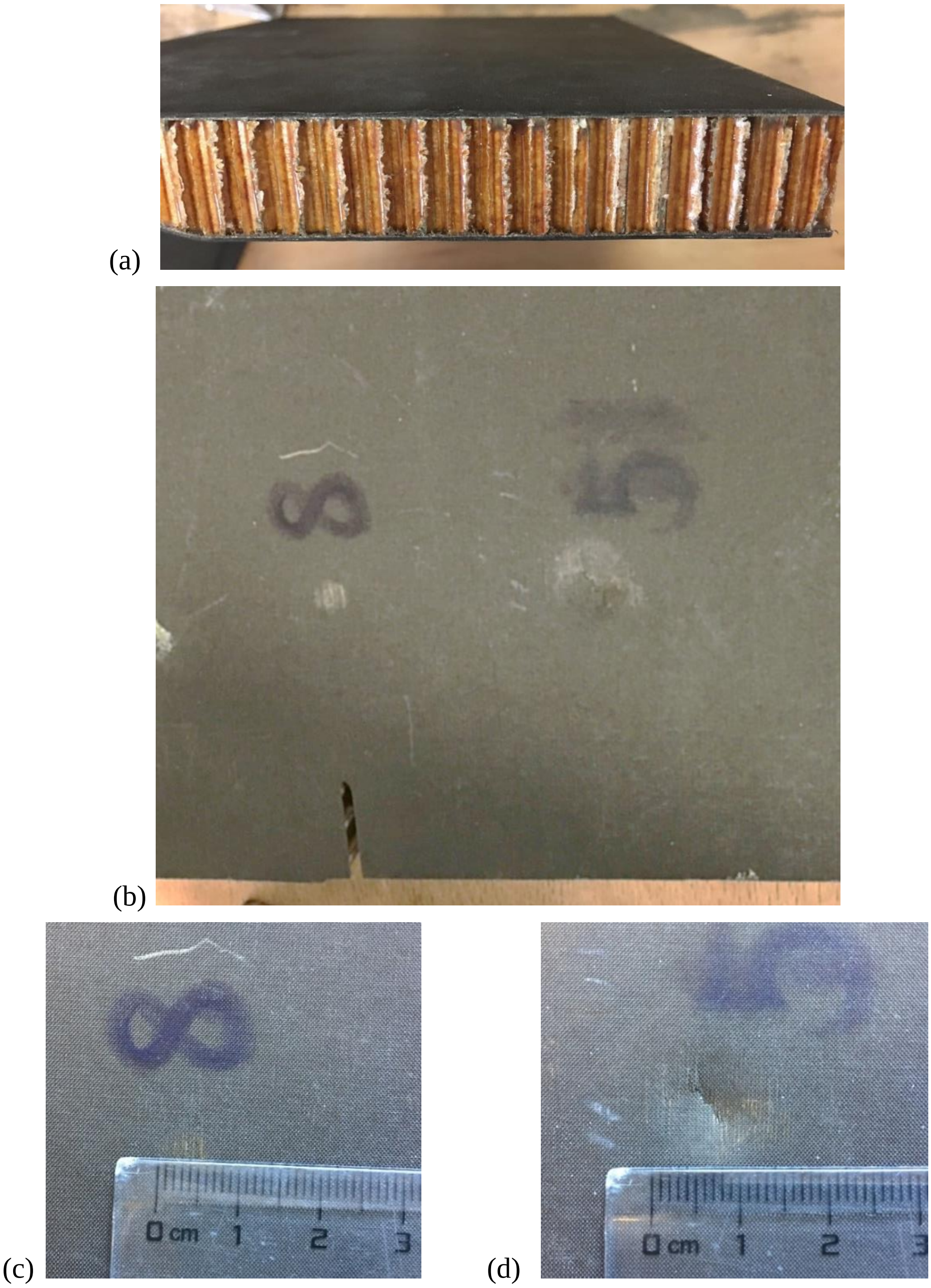

Figure 5-7 Images of Honeycomb plate and generated defects (a) Side view of honeycomb structure; (b) Top view of outer surface of honeycomb structure; (c) close-up image of defect induced by 8 N.m. press; (d) close-up image of defect induced by 11 N.m. press

5.2.2.2 Air-coupled NDE of CFRP and honeycomb plate

Figure 5-8(a) presents the amplitude C-scan image of both induced defects but is dominated by the direct signal through the damage at the edge of the plate. This damaged area allows ultrasound to go through easily and hence, the result shows much larger energy at this location, when compared to the rest of the plate. Obviously, this impacts on the quality of the image data acquired around the defects of interest. However, if the time-of-flight (ToF) information for the first arrival at the receiver elements is plotted instead of amplitude, then it should be possible to identify the defect areas from the through transmitted signals. Figure 5-8(b) presents the ToF image and the defect areas corresponding to the 8 N.m. and 11 N.m. induced defects can be clearly identified.

To locate the damage accurately, the delayed signal has been removed because the ultrasound speed in air is slow compared to the sample's speed, the amplitude and index results are shown in Figure 5-9. To identify and size the defects, -6 dB contour lines have been drawn onto the amplitude C-scan image, Figure 5-9(a), using red lines and the damaged areas are clearly displayed. The 8 N.m. torque induced defect was considered an 8 mm × 8 mm elliptical area defect from visual surface inspection, although the C-scan amplitude data indicates a defective elliptical area of approximately 22 mm × 24 mm in size. Also, for the 11 N.m. torque induced defect, the visual inspection defect size of 13 mm × 16 mm elliptical area defect has increased to approximately 32 mm × 40 mm in size with elliptical shape from the ultrasonic inspection data. As discussed previously, the pressing action of the ball bearing causes deformations inside the honeycomb layer which are much larger than the visual inspection indicates on the CFRP surface. What's more, in the amplitude figure, the honeycomb hexagon pattern has also been displayed, which demonstrates that this air-coupled transducer configuration operates with good resolution and accuracy. Furthermore, if the scan step distance is reduced from the 1 mm dimension used in this experiment, it is considered that the hexagon pattern can represented more accurately in the image. The benefit of being able to see the honeycomb pattern will allow checking of the material's hexagon structural integrity. The ToF figure shows a clear defect area, but it doesn't show out the hexagon pattern.

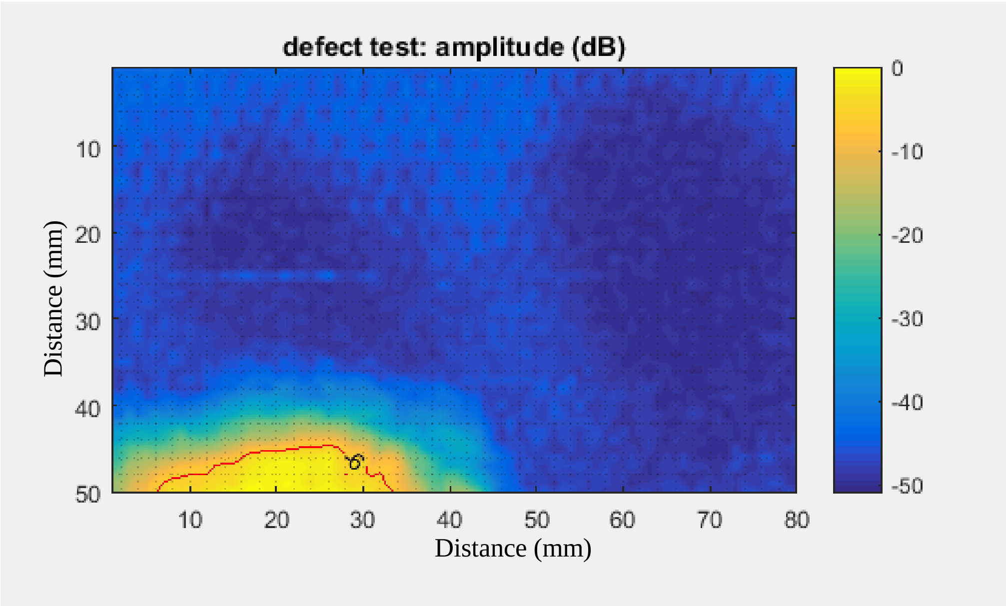

(a) Amplitude based C-scan image of sample

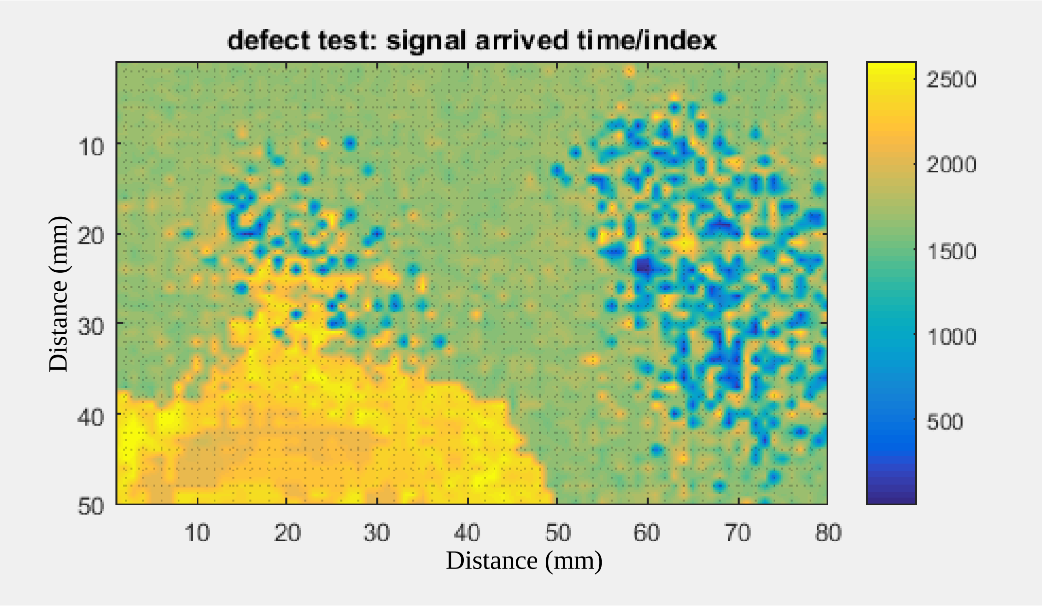

(b) Time-of-flight based C-scan image of sample

Figure 5-8 Air-coupled C-scan image of 50 mm × 80 mm area including both defects and edge damage in the Honeycomb plate sample

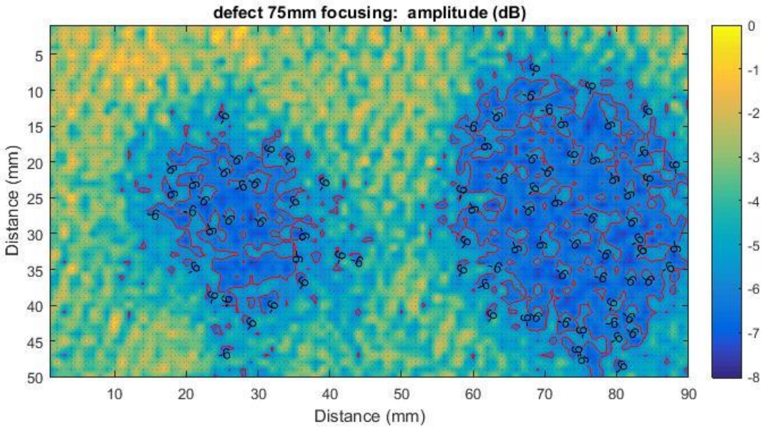

(a) Amplitude based C-scan image of sample

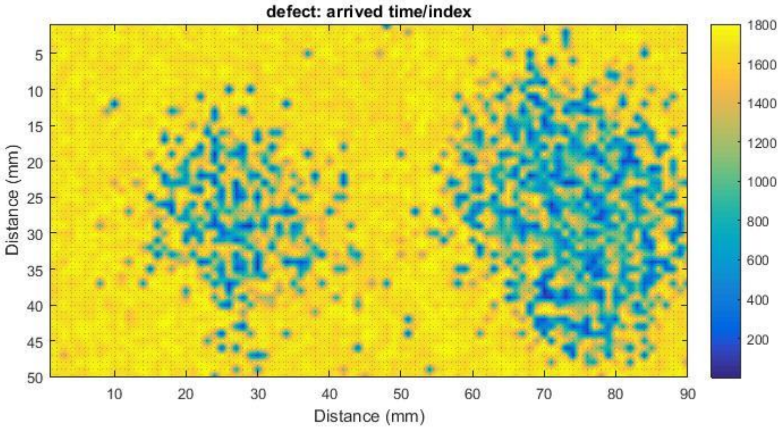

(b) Time-of-flight based C-scan image of sample

Figure 5-9 Air-coupled C-scan image of 50 mm × 90 mm area focusing on both defects in the centre of the Honeycomb plate sample

Interestingly, another project in CUE was working with a different air-coupled transduction system, comprising two commercial Curlin-AIR transducers which are offered by Rolls-Royce. This system operated at 50 kHz and was used to inspect the 11 N.m. induced defect, with the resulting amplitude C-scan image shown in Figure 5-10. Importantly, the measured size of the defect is approximately the same as for the air-couple annular array system, approximately 35 mm × 40 mm with elliptical shape.

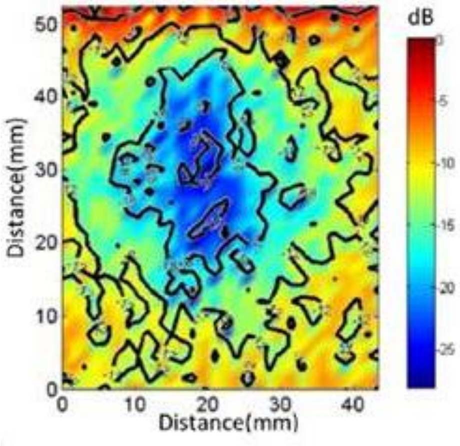

Figure 5-10 Comparative air-coupled C-scan image of 11 N.m. defect using a different air-coupled arrangement. This is used to validate the annular array results presented in Figure 5-9.

5.2.3 Carbon fibre reinforced polymer plate experiments

5.2.3.1 Defect manufacturing method

The torque wrench pressing approach to fabricate defects was trialled again on a 5 mm thick carbon fibre reinforced polymer (CFRP) sample. Unfortunately, due to the high stiffness of the carbon fibre material, the indent was too small to be inspected by the system, even with the wrench set to the highest torque scale of 33 N.m. Therefore, as an alternative, two pits were made using a table mounted rotary drill and an 8 mm drill bit, as shown in Figure 5-11. Defect 1 at the right side is deeper than the left defect 2. The defect in the middle, identified as Defect 3, was made by hammering a nail located in the small indent made by torque wrench technique. All the defects did not drill through the material. To prove the ability to test the defect inside the material, the damage side was chosen to be the face facing the receiver.

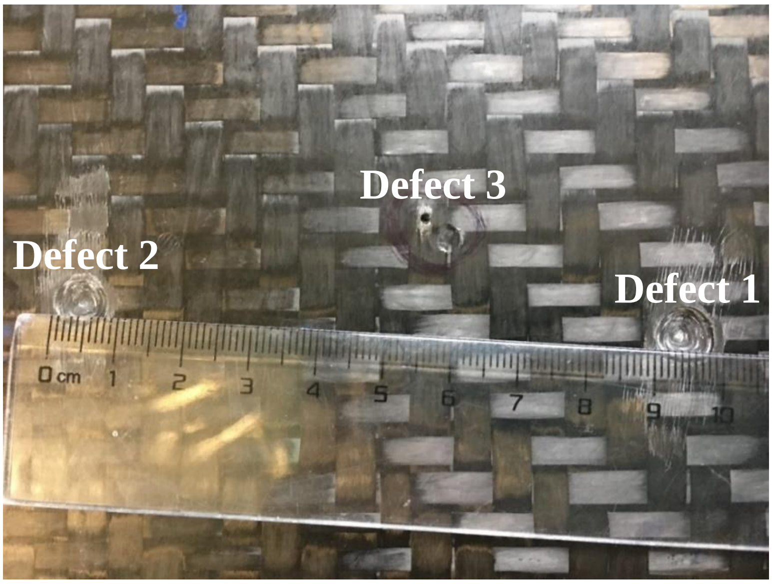

Figure 5-11 Carbon fibre reinforced polymer plate with three artificial defects induced by drilling (Defects 1 and 2) and hammering (Defect 3)

5.2.3.2 Scanning Acoustic Microscope (SAM) test comparison

To ensure the carbon fibre epoxy plate has no other defects inside the plate, a high-resolution Scanning Acoustic Microscope (SAM 300, PVA TePla Analytical Systems GmbH) scan of the plate was conducted before and after making the damage. The SAM uses high frequency (<30 MHz) scans through a water load and can produce information through the thickness of a sample. It addition, to checking the defects induced through the conventional mechanical approaches, this data can be used to compare with the images produced using the air-coupled annular array system.

Figure 5-12 shows that the original CFRP plate has no defects inside. The SAM scans start from the defect-free face and move towards the face with induced defects. Whereas, Figure 5-13 presents the SAM C-scan results after manufacturing the three defects. Interestingly, as defect 1 is deeper than the other two defects, it appears first in the SAM scan data, Figure 5-13(b). Importantly, the SAM has detected the small indentation made by torque wrench in defect 3 area, and it shows clearly that there are two closely spaced defects in defect 3 area corresponding to the torque wrench and hammer approaches.

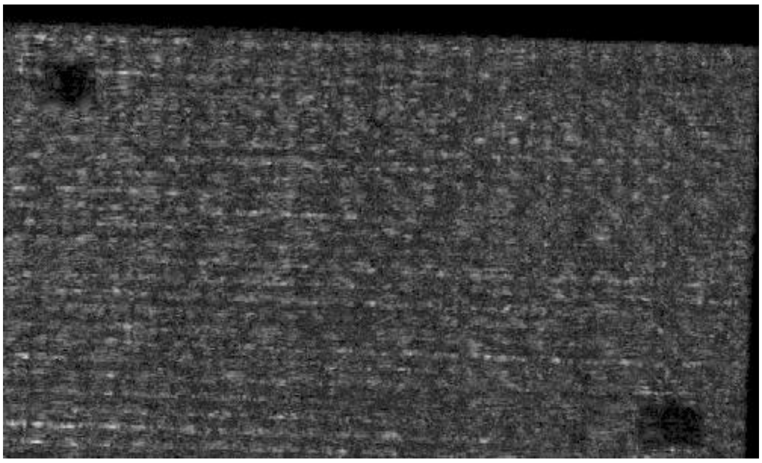

(a) Defect free surface layer

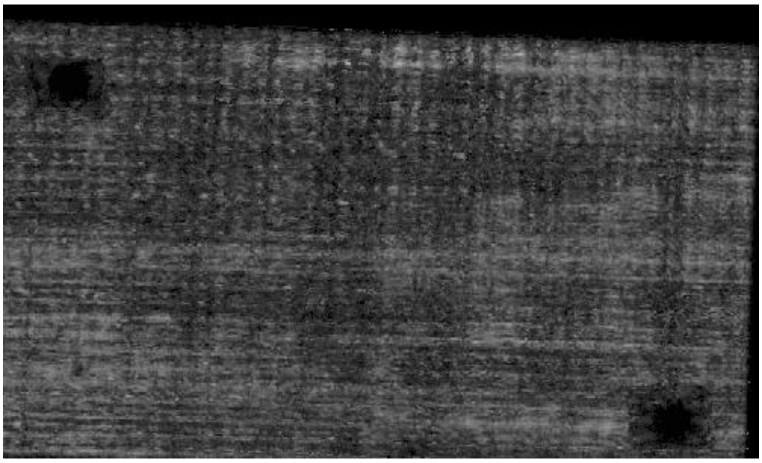

(b) Image from layer in middle of sample

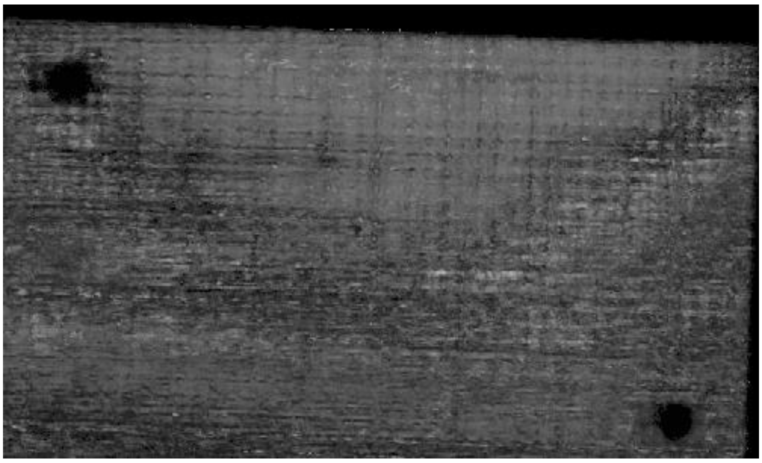

(c) Image from defect induced side (prior to defect process)

Figure 5-12 SAM image of CFRP plate before introducing damage and there is no original defect inside. Three scan has been shown from different depth (a) surface layer; (b) middle layer; (c) back side

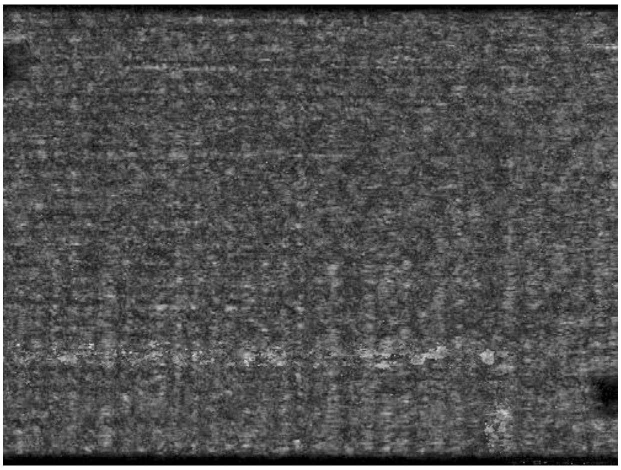

(a) Defect free surface layer

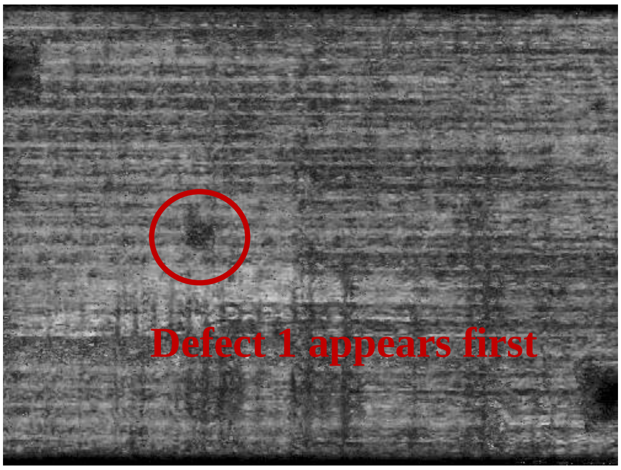

(b) Image from layer in middle of sample in which Defect 1 appears

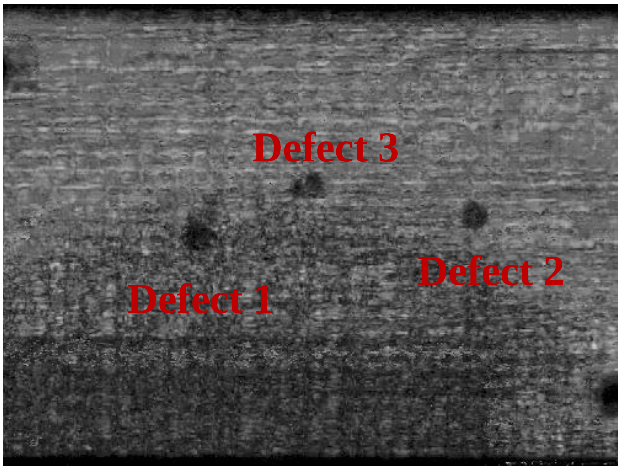

(c) Image from defect induced side

Figure 5-13 SAM image of CFRP plate after introducing damage and the defect shows out through the three scan from different depth (a) surface layer; (b) middle layer; (c) defect side

5.2.3.3 Air-coupled NDE of CFRP plate

Figure 5-14 presents the scan results for Defect 1 which is deeper than the other two defects. The defect's location is clearly identifiable using a -7 dB contour line as -6 dB contour line significantly overestimated the defect dimension. Compared to the diameter of the drill bit, which was 8 mm, the defect size measured from the air-coupled image is enclosed within an 8 mm × 10 mm footprint, which is a promising result.

Figure 5-15 is the air-coupled scan result for Defect 2. Again, the defect's location stands out after drawing up the -7 dB contour line, with the boundary indicating a defect size close to 8 mm × 5 mm, and the -6 dB contour line shows a confused result which cannot locate the defect position. Compared to Figure 5-14, the Defect 2's result has weaker response, with other features in the C-scan with a similar amplitude response and hence, the potential for false positives would be high.

As shown in Figure 5-13(c), there are two closely spaced defects in the area identified as Defect 3. Unsurprisingly, the air-coupled C-scan presented in Figure 5-16 doesn't show this. Due to the lower operating frequency of this air-coupled system, it is unable to discriminate between these two defects. The -6 dB contour line indicates one defect, likely from the hammered nail damage, which is approximately 2 mm in diameter. Again, there are other features in the C-scan image which have similar amplitude to the defect and could be identified as a false positive.

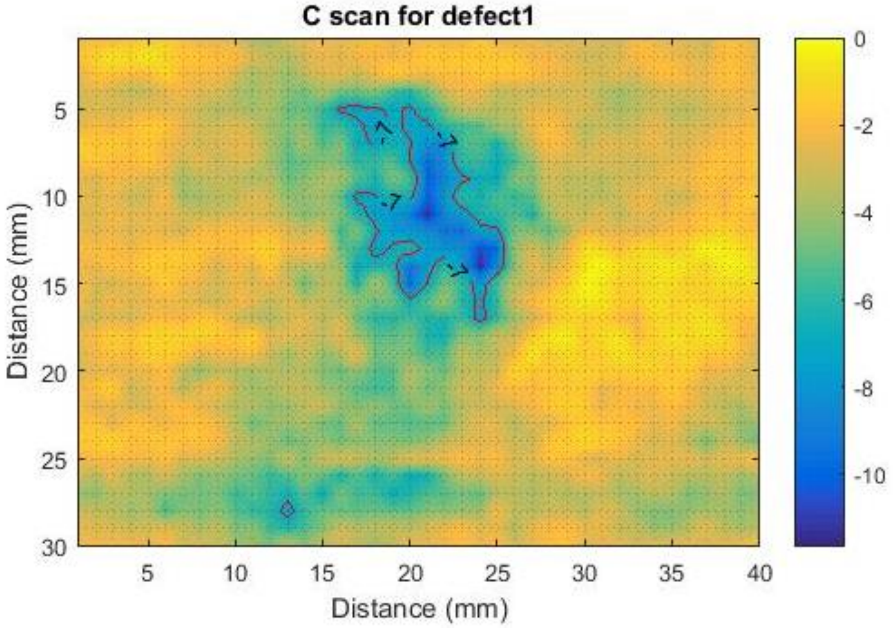

Figure 5-14 Air-coupled C-scan image of Defect 1 from the CFRP sample and -7 dB contour line has been drawn to show the defect area because -6 dB contour line is not consistent

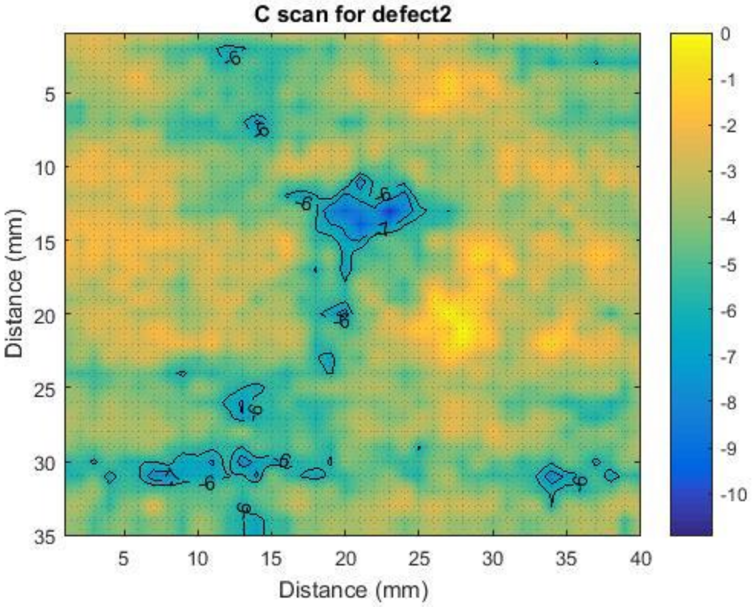

Figure 5-15 Air-coupled C-scan image of Defect 2 from the CFRP sample with -7 dB contour line shows the defect area more clearly and -6 dB contour line is not consistent.

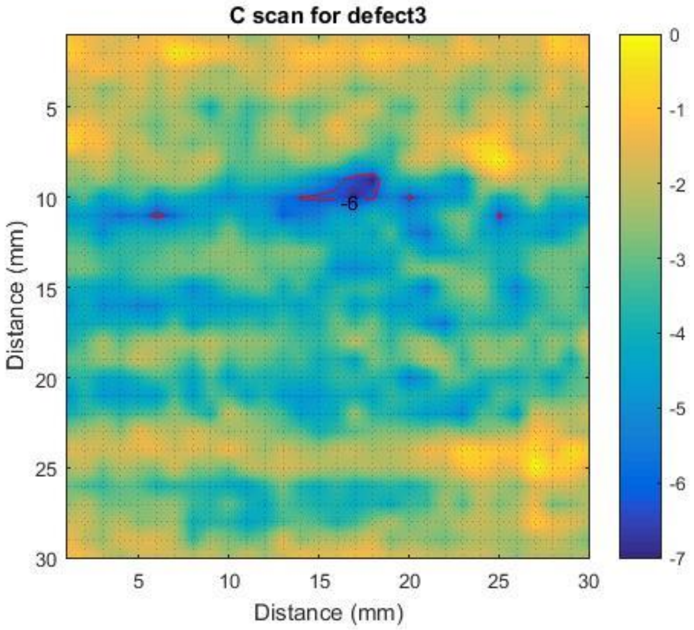

Figure 5-16 Air-coupled C-scan image of Defect 3 from the CFRP sample and -6 dB contour line shows predicted defect area.

5.3 Summary

The air-coupled annular array transducer system was evaluated using 3 different test samples. Artificial defects were introduced into each sample and the ability of the air-coupled annular array transducer pair to identify each defect was investigated. For this work, the DSL PAC was used to deliver a signal burst to each element of the transmitter, equivalent to a tone burst at the operating frequency of the device. Moreover, implementation of the focal law in reception was done during the post-processing stage due to limitations with the DSL software package.

In this work, the sample was scanned and the transducer pair fixed in place. Although, this is not the way such a system would be implemented in a practical inspection scenario, it was considered appropriate to evaluate the performance of the air-coupled transducers. All defects were identified, although the performance in the CFRP material also demonstrated other features in the amplitude C-scan which could be wrongly identified as a defect. The inspection performance when scanning a Honeycomb sample was highly encouraging. In fact, both amplitude and time-of-flight images were produced and shown to clearly identify the defects of interest, as well as highlighting the honeycomb structure in the middle layer of the sample.

CHAPTER 6 Matching layer performance in pulse echo system

Abstract

In Chapter 3, the matching layers performance in through transmission mode was presented which can offer nearly 36 dB gain in receiver amplitude. In this Chapter, the matching layers performance in a pulse echo system are simulated and compared to the experiment results. For this work, a piezocomposite based on single crystal piezoelectric material is used.

$(1\text{-}x)Pb(Mg_{1/3}Nb_{2/3})O_3\text{-}xPbTiO_3$ (PMN-PT) transducer has a superior performance in both sensitivity and bandwidth than the traditional PZT transducer [29, 30]. For pulse-echo operation, the final matching layer thickness is not decided by the number of quarter wavelengths, as the electrical mechanical frequencies differ and the transducer wide band operational property will be compromised using the standard frequency dependent matching layer design theory. The aim of this work is to find the most suitable thickness matching layer for this pulse-echo system. Consequently, a series of simulations and experiments have been conducted to investigate how the silicone rubber and membrane filter hybrid matching layer will perform in a pulse-echo system and how large amplitude improvement can be offered by the matching layers.

6.1 Introduction

The best matching layer thickness is mainly dominated by the transducers' operational frequency. That is the reason why the best matching layer thickness for amplitude improvement is different for the transmitter and receiver in a through transmission system. Therefore, determining a matching layer for incorporation into a pulse-echo transducer is more challenging and this is increased for an air-coupled pulse-echo system. Most research uses the 'resonance frequency' to calculate the quarter wavelength thickness, but it is not always accurate enough [96, 97]. In the case of a pulse-echo transducer the following questions are raised:

> *What is the right frequency to use in the calculation of the matching layer thickness, as the electrical and mechanical frequencies are different in a single device, pulse-echo system?*

In this work, a PMN-PT single crystal piezocomposite transducer has been used. PMN-PT based transducers normally offer larger sensitivity than traditional PZT-based transducers. Another project in the CUE, at the University of Strathclyde, has designed and fabricated a prototype PMN-PT piezocomposite transducer. The operational parameters of this device will be provided here, but the full design is not part of this Thesis and hence, a summary of the transducer design is given in Appendix J to assist the reader. The wider bandwidth characteristic of the normal PMN-PT material is beneficial in many applications, although this device uses air backing, which will not realise the full bandwidth potential. Therefore, this research pays more attention on the performance of the silicone rubber and membrane filter matching layer combination and assessing any improvement to the device sensitivity.

6.2 PMN-PT single crystal transducer operational parameters

The PMN-PT single crystal transducer, used in this work, is a 1-3 connectivity piezocomposite structure with medium set epoxy (HY956EN/CY221) used as the passive filler material. All the key fabrication and operational parameters are shown in Table 6.1 and Figure 6-1 presents the electrical impedance spectrum for the PMN-PT transducer.

Table 6.1 Transducer parameters for PMN-PT and medium set epoxy 1-3 piezocomposite

	PMN-PT and medium set 1-3 piezocomposite
Thickness	1.594 mm
Pillar width	0.478 mm
Polymer width	0.16 mm
Volume fraction	56 %
Electrical frequency	708 kHz
Mechanical frequency	1042 kHz
k_t	0.767

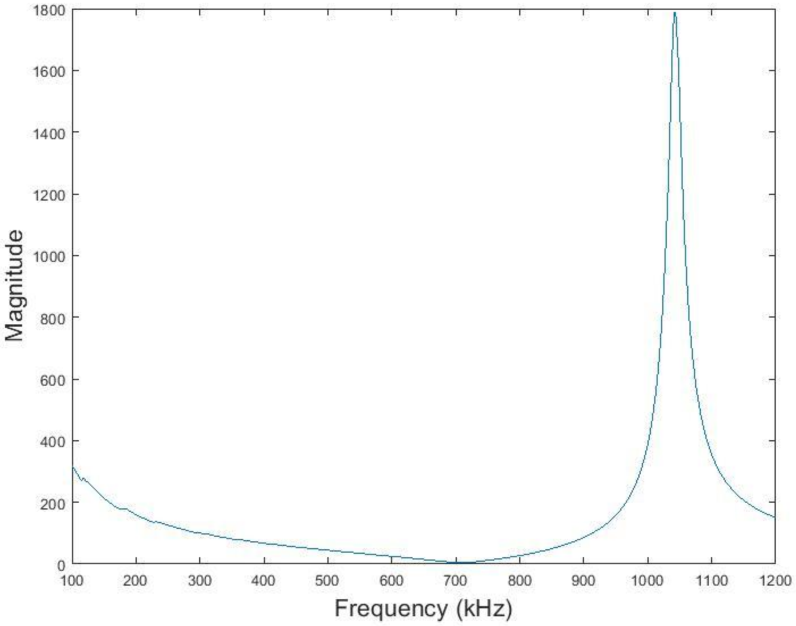

Figure 6-1 Measured electrical impedance magnitude characteristic for PMN-PT piezocomposite transducer with measured electrical frequency at 708 kHz and mechanical frequency at 1042 kHz

6.3 Experimental arrangement

The standard laboratory conditions are maintained at 20 ℃ ± 1 ℃ for temperature and 40 % ± 5 % for humidity. Figure 6-2 shows the experimental arrangement. A pulser-receiver (JSR Ultrasonics PR35 Pulser/Receiver, Imaginant Inc. Pittsford NY USA) has been used to drive the pulse-echo transducer. Temporary matching layers are attached on the outer surface of the transducer using coupling gel. The generated ultrasonic pulse will be reflected by a glass block set, at a fixed distance. The position and the orientation of the glass should be adjusted carefully to maximise the echo reflection. To ensure experimental consistency, the glass block and transducer were fixed into position and did not alter for the duration of the experiment. This is important as the position of the glass block should not be moved when changing the matching layer and hence, the space between the transducer and the glass block should be wide enough for manual changing of the matching layers, with a 50 mm distance chosen.

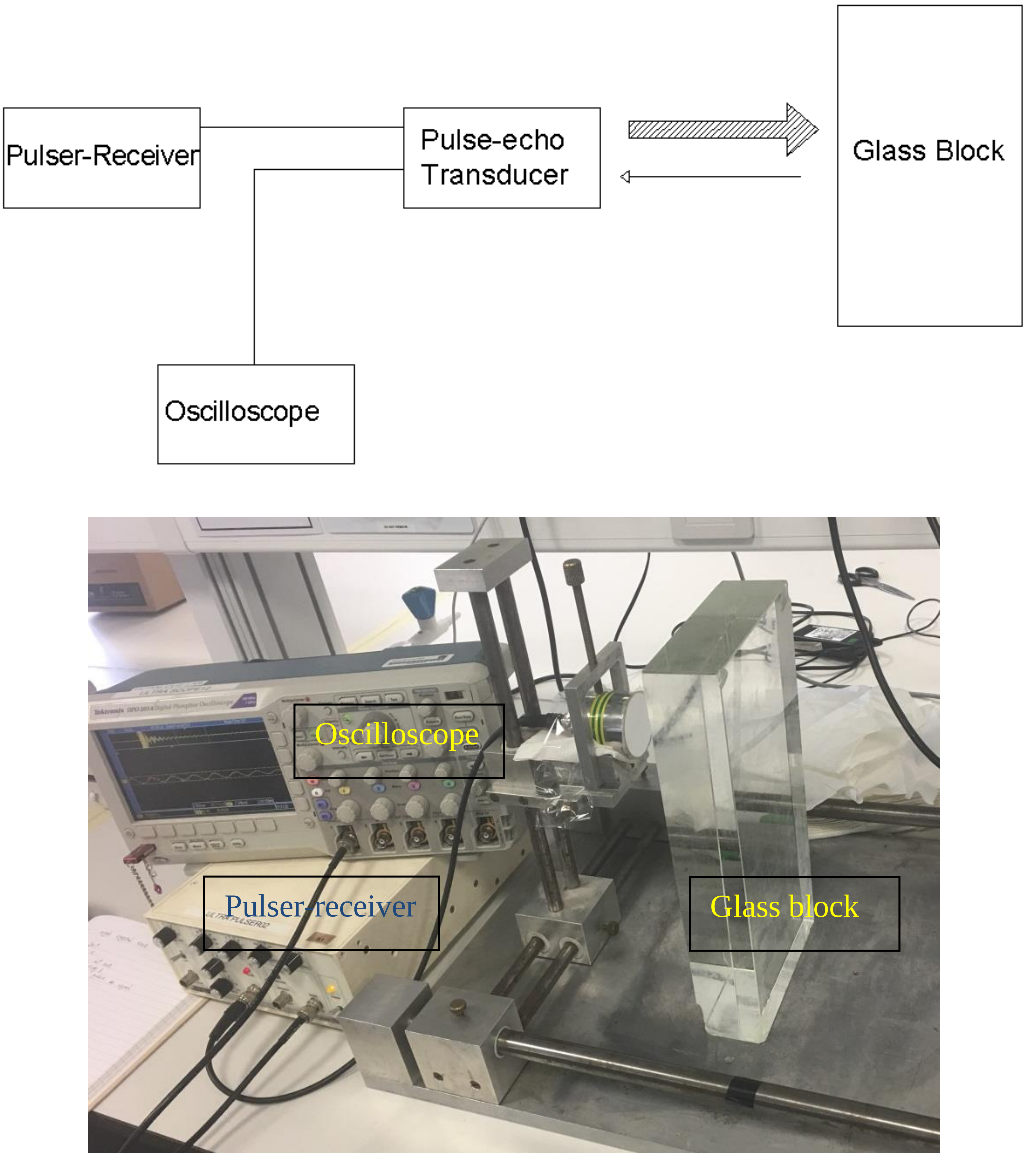

Figure 6-2 Experimental arrangement in pulse echo system and the pulse is reflected from the glass block

6.4 Matching layers performance in pulse-echo system

6.4.1 Transducer performance prior to matching layer attachment

Before applying the silicone rubber and membrane filter matching layers, the received echo signal has been recorded. As sound velocity in air is 344 m/s, the received signal should appear at approximately 0.29 ms in pulse-echo time domain signal results.

In Figure 6-3, the reflected signal is masked by the system noise. Moreover, in Figure 6-4, the FFT signal does not show a clear wideband transducer performance, with three amplitude peaks evident at 506 kHz, 875 kHz and 1.26 MHz. None of these frequencies match with the transducer resonant modes, as detailed in Table 6.1, and hence, this response is primarily noise.

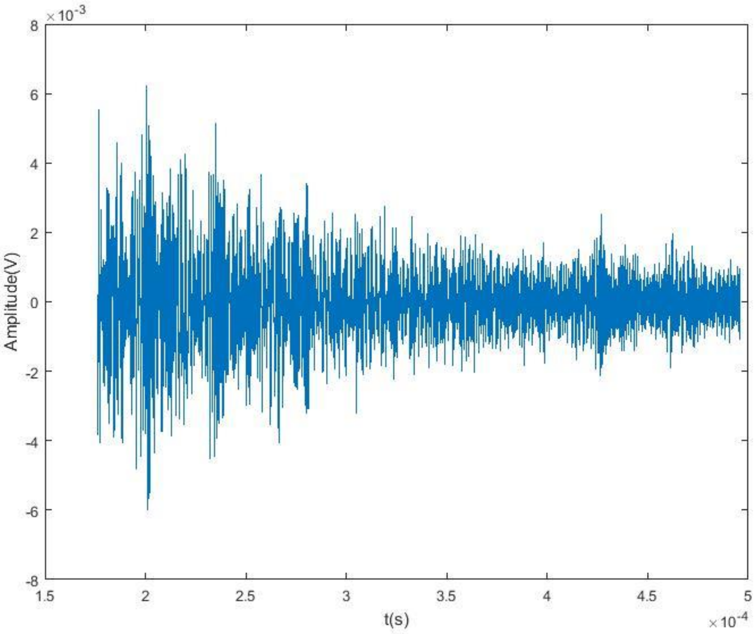

Figure 6-3 PMN-PT transducer time domain signal in pulse echo configuration without matching layer and the received signal should appear at approximately 0.29 ms

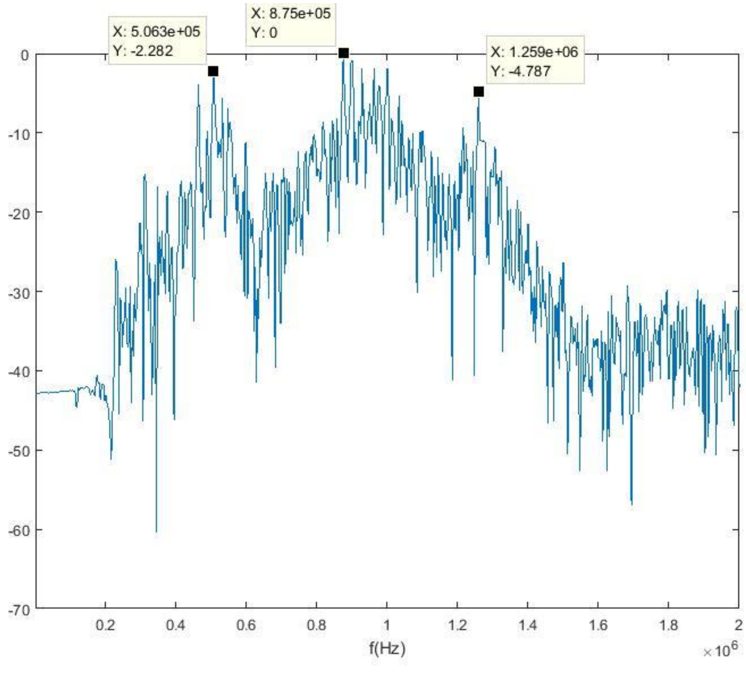

Figure 6-4 PMN-PT transducer spectral response in pulse-echo configuration without matching layer

6.4.2 Choosing suitable matching layer thickness for amplitude improvement

For the air-coupled transducers, the first concerned property is the sensitivity. Without a good signal amplitude improvement, the received signal is difficult to identify. Interestingly, no satisfactory signal is visible without a matching layer being applied in this pulse-echo transducer system, as shown in Figure 6-3. As the membrane filter's thickness is fixed at 0.12 mm, the silicone rubber thickness will be the variable parameter to determine a suitable matching layer thickness for this configuration.

PZFlex 2-D modelling has been used, as introduced in Chapter 3, to find the suitable matching layer thickness for the received echo amplitude improvement. Compared with the pitch-catch mode, the receiver configuration is set up identically to the transmitter. Again, the extrapolation method has been used, as the sound speed in the air is slow and the air path is too long for practical simulation. Moreover, extrapolation is a process in which the value is estimated beyond the specific range of given variable. It provides the estimate of the observation below or above the given values. So, a 7.5 mm modelling distance from the transducer has been set to obtain the characteristic of the emitted pressure wave and this information extrapolated for the full 100 mm air path to mimic the experimental set up. As shown in Figure 6-5, the 2-D model has been built using a 1-3 piezocomposite structure comprising the active PMN-PT and passive HY956EN/CY221 medium materials. On the top of the piezocomposite surface, the matching layer has been added to the modelling, comprising a membrane filter which is fixed at 0.12 mm, modified silicone rubber and saturated filter layer which is fixed at 0.02 mm, and the silicone rubber thickness will be the variable. The system is driven by a 708 kHz frequency 1 V, half-cycle, sinusoidal wave to simulate pulse excitation.

Comparing the modelling and the experimental results in Figure 6-6(a) and 6-6(b), respectively. The smoothing curve fitting line is drawing with the default setting smoothing parameter 0.999999141 for both modelling and experimental results. For the modelling results, it doesn't contain the coupling gel and the extrapolation method doesn't offer the exactly received signal amplitude, therefore, Figure 6-6(a) uses a modified received amplitude gain compare to the maximum modelling gain value. One of the uncertainties for the maximum value in experimental results is caused by the sample quantity as there are only 24 matching layers applied for the data recorded in Figure 6-6(b), that is to say, the real maximum value may appear around the experimentally measured value and it will not be the exact same thickness. Another influencing factor is the coupling gel differences each time when changing the matching layers. Even though there is slight difference which is around 0.04 mm between modelling and experiments results, it is clear that both sets of results have three clear amplitude peaks when the silicone rubber thickness are 0.26 mm, 0.33 mm and 0.40 mm.

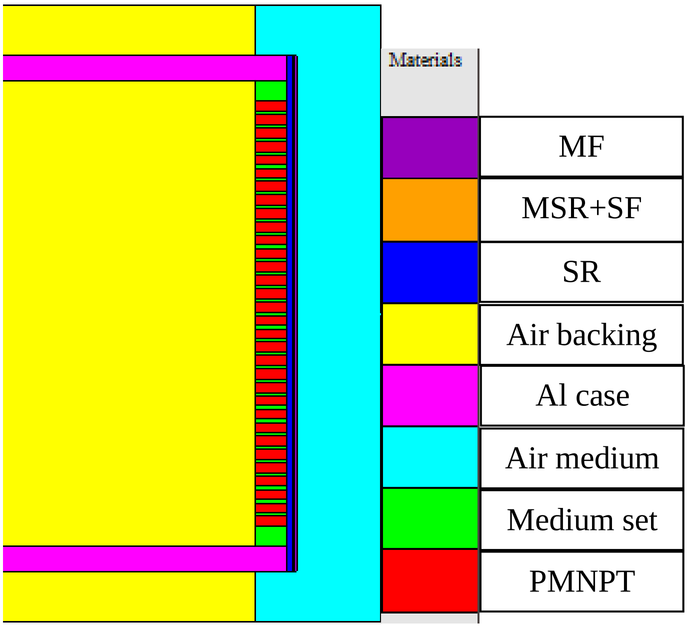

Figure 6-5 PZFlex 2-D extrapolation model to investigate suitable matching layer thickness for the amplitude improvement of an 1-3 PMN-PT piezocomposite transducer in the air-coupled pulse-echo PZFlex model

For the 0.26 mm silicone rubber thickness matching layer, Figure 6-7 shows the time domain signal for this matching layer configuration and importantly, the received echo signal is clearly visible at 0.29 ms, as expected. The maximum amplitude is

0.042 V. The pulse length is 0.047 ms. The peak of the received FFT signal is around 715 kHz as shown in Figure 6-8, which is the electrical frequency of the transducer as shown in Figure 6-1. However, it can be observed that it is not the best overall matching layer thickness for amplitude improvement. The bandwidth is 31.3 kHz.

For the 0.33 mm silicone rubber thickness matching layer, Figure 6-9 shows the time domain signal for this matching layer configuration. A clear received echo signal is visible at 0.29 ms also and this corresponds to the maximum amplitude improvement. The maximum amplitude is 0.058 V. The pulse length is 0.082 ms. The peak of the received FFT signal is around 612 kHz as shown in Figure 6-10 which indicates a narrow bandwidth operating system. This result is not surprising as the matching layer is designed to operate efficiently for a specified frequency. This received signal should be compared to the no matching layer case presented in Figure 6-3 to fully appreciate the improvement in system SNR. Overall, an approximate 19 dB gain has been realised without and with matching layer applied on when using a 0.33 mm silicone rubber thickness matching layer. The bandwidth is 18.7 kHz.

For the 0.40 mm silicone rubber thickness matching layer, Figure 6-11 and Figure 6-12 shows the time domain signal and the corresponding FFT spectrum, separately. The received echo signal appears at 0.29 ms as expected with 0.055 V maximum amplitude and the pulse length is largest compared to the other two thicknesses which is 0.115 ms. The received FFT signal is more narrowband than for the other two thicknesses which is only 12.5 kHz. The peak of the received FFT signal is around 550 kHz.

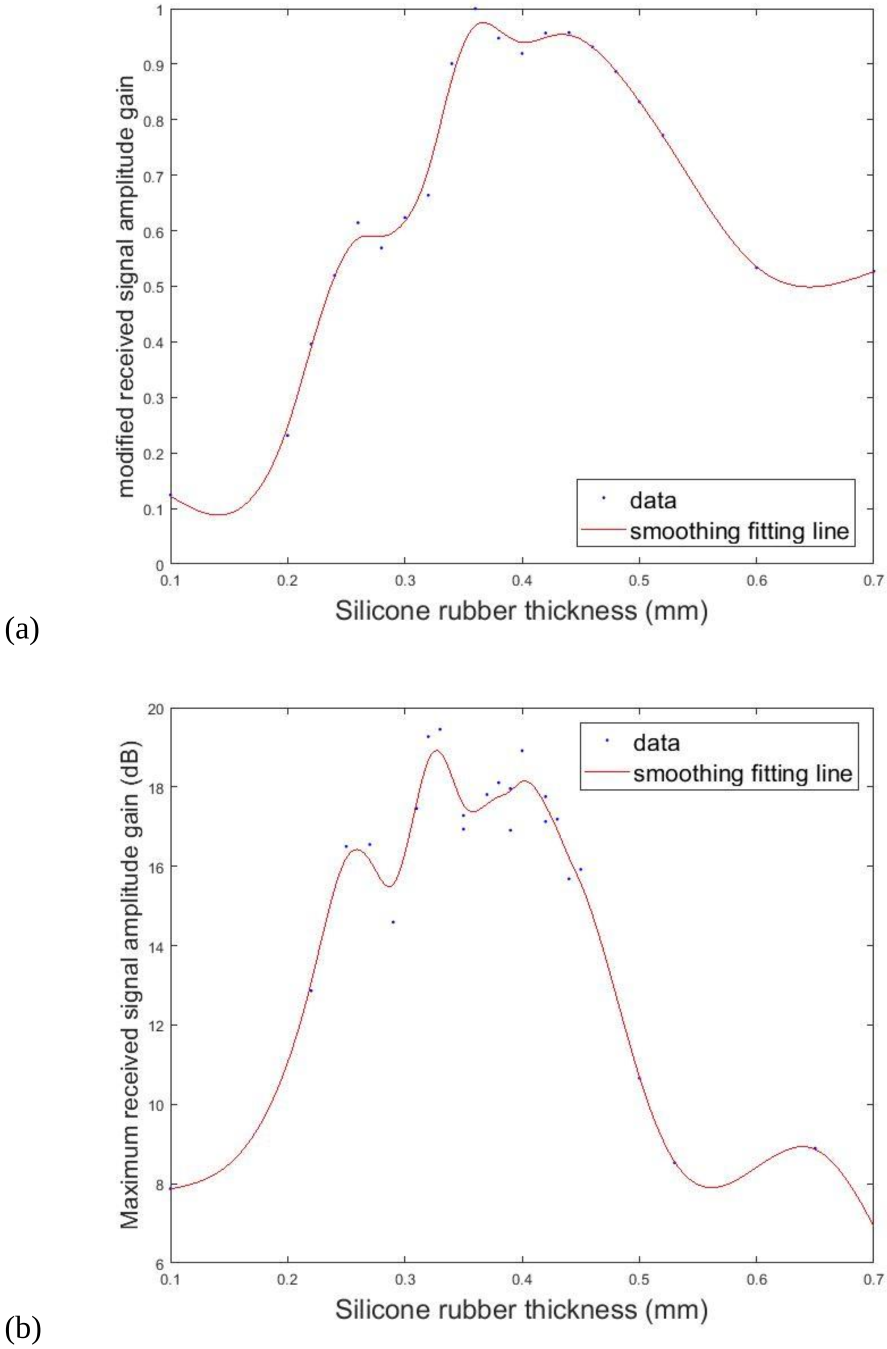

Figure 6-6 The relationship between silicone rubber thickness and the received signal amplitude gain for PMN-PT piezocomposite transducer in a pulse-echo system: (a) modelling results with three peaks at 0.265 mm, 0.363 mm and 0.438 mm; (b) experimental results with three peaks at 0.259 mm, 0.327 mm and 0.405 mm, the maximum gain at 0.327 mm is 18.72 dB

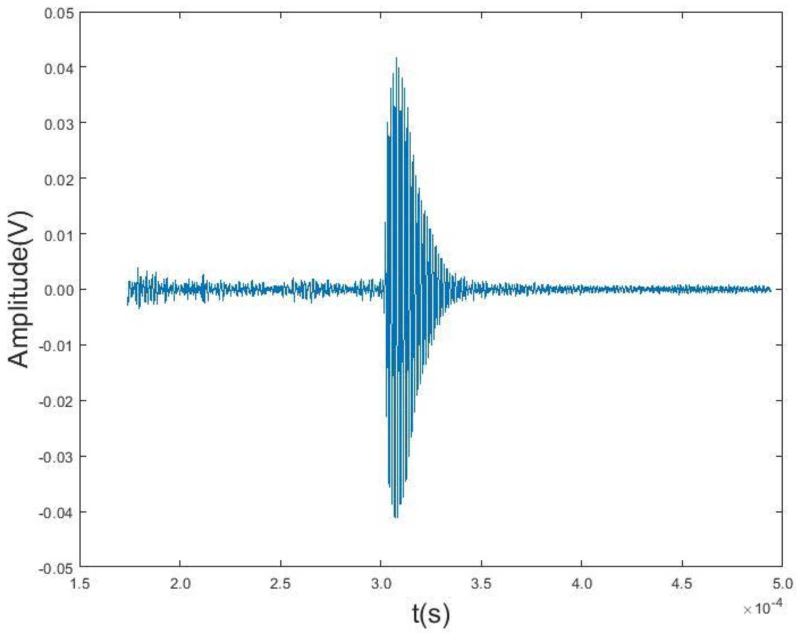

Figure 6-7 PMN-PT transducer’s time domain signal in pulse-echo system with 0.26 mm silicone rubber thickness: the arrived time is 0.29 ms, the maximum amplitude is 0.042 V and the pulse length is 0.047 ms

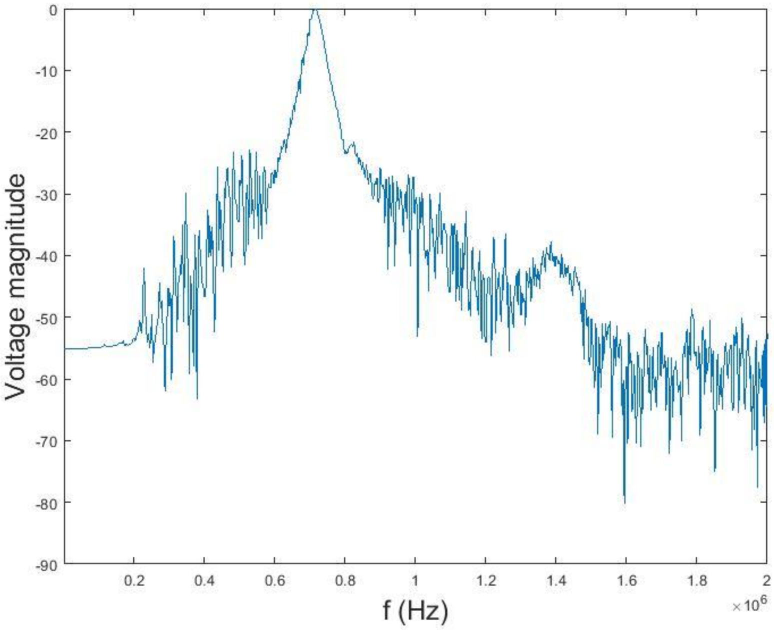

Figure 6-8 PMN-PT transducer’s FFT signal in pulse-echo system with 0.26 mm silicone rubber thickness: the peak frequency is 715.6 kHz and the bandwidth is 31.3 kHz

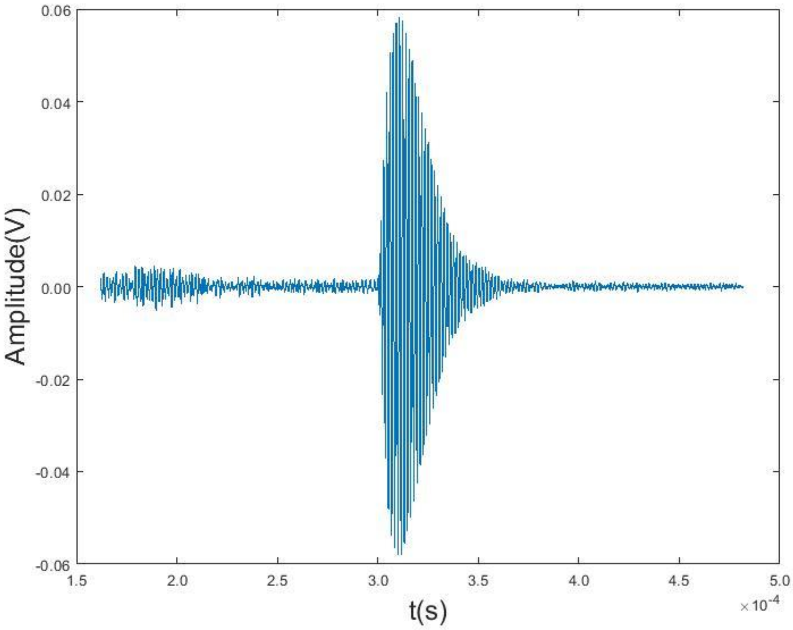

Figure 6-9 PMN-PT transducer's time domain signal in pulse-echo system with 0.33 mm silicone rubber thickness when the system has maximum amplitude 0.058 V , the signal arrives at 0.29 ms as expected and the pulse length is 0.082 ms

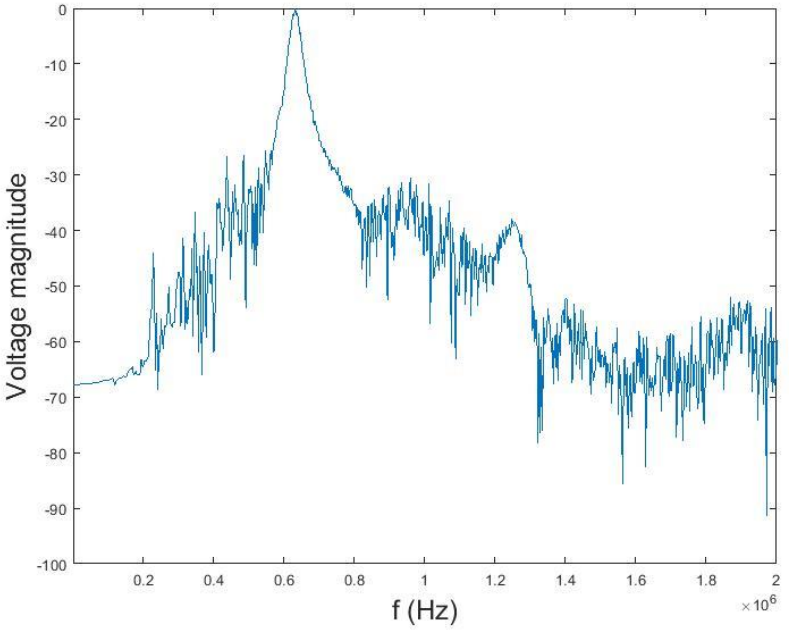

Figure 6-10 PMN-PT transducer's FFT signal in pulse-echo system with 0.33 mm silicone rubber thickness when the system has maximum amplitude: the peak frequency is 631.3 kHz and the bandwidth is 18.7 kHz

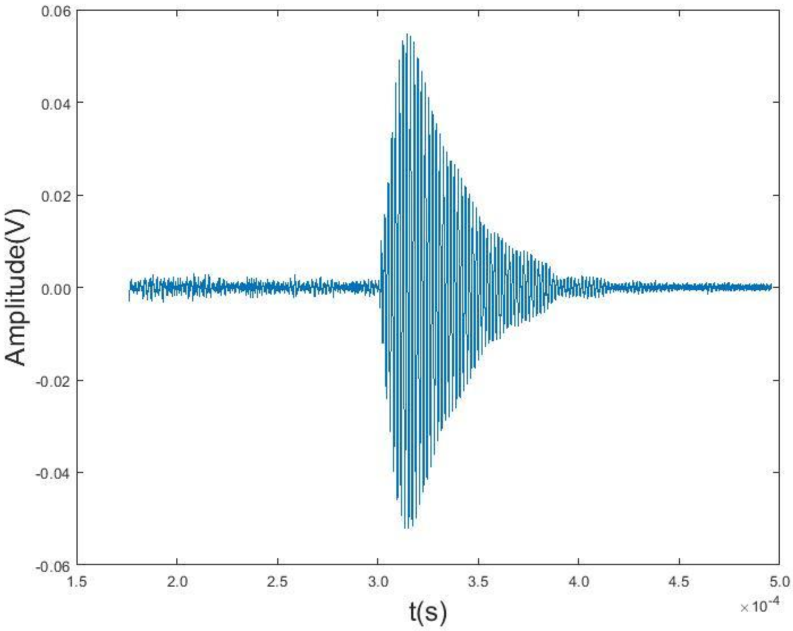

Figure 6-11 PMN-PT transducer's time domain signal in pulse-echo system with 0.40 mm silicone rubber thickness: the arrived time is 0.29 ms, the maximum amplitude is 0.055 V and the pulse length is 0.115 ms

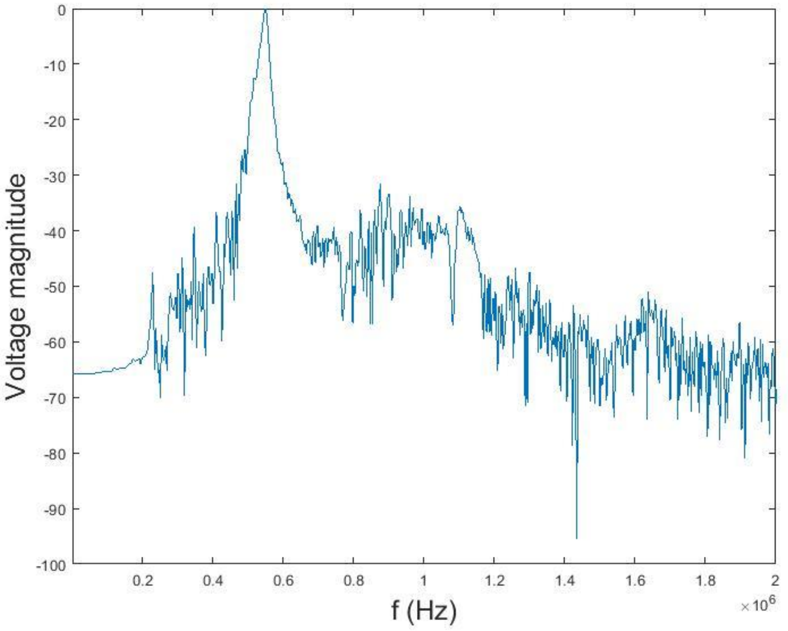

Figure 6-12 PMN-PT transducer's FFT signal in pulse-echo system with 0.40 mm silicone rubber thickness: the peak frequency is 550.0 kHz and the bandwidth is 12.5 kHz

6.5 Discussion

This Chapter has investigated the hybrid silicone rubber and membrane filter matching layer performance on an air-coupled pulse-echo transducer system. It is apparent that the transducer pulse-echo response is only evident when a matching layer is applied and hence, this method to enhance system SNR negates any potential performance benefits from utilising advance piezoelectric PMN-PT material as the active phase in a 1-3 piezocomposite.

For this transducer system, there are three maxima for choosing the most suitable matching layer thickness on a PMN-PT piezocomposite transducer in a pulse-echo system: 0.26 mm, 0.33 mm and 0.40 mm. For each of these maxima, the received echo signal is clearly visible at 0.29 ms as expected. For the 0.26 mm silicone rubber thickness matching layer, the maximum amplitude is 0.042 V. The pulse length is shortest compare to the other two peaks thickness at 0.047 ms. The peak of the received FFT signal is around 715 kHz with the largest bandwidth of 31.3 kHz. For the 0.33 mm silicone rubber thickness matching layer, the maximum amplitude is 0.058 V which can offer approximate 19 dB gain compared to the received signal without matching layer. The pulse length is 0.082 ms. The peak of the received FFT signal is around 612 kHz with a bandwidth of 18.7 kHz. For the 0.40 mm silicone rubber thickness matching layer, the maximum amplitude is 0.055 V and the pulse length is largest compared to the other two thicknesses at 0.115 ms. The received FFT signal is more narrowband than for the other two thicknesses at only 12.5 kHz. The peak of the received FFT signal is around 550 kHz.

In summary, for the amplitude improvement, the most suitable thickness is 0.33 mm silicone rubber thickness which can offer the largest gain and it can also offer a moderate bandwidth compared to thicker thickness matching layers.

Unfortunately, the system doesn’t show a wideband operation system and the matching layers are only recommended for narrow bandwidth devices. Overall, it would seem that for wideband operation in an air-coupled transducer system, then the capacitive micromachined ultrasonic transducer devices would still be the preferred option [98].

CHAPTER 7 Conclusions and suggestions for future work

7.1 Summary

7.1.1 General Thesis Overview

The development of an air-coupled inspection system for non-destructive performance testing in the aerospace industry has been completed successfully. The air-coupled scanning system provides the potential to perform testing on large samples quicker than an equivalent water-coupled system. Moreover, the air-coupled technology can provide an efficient method when scanning samples which cannot tolerate liquid contact.

In this Thesis, a number of developments have been made to produce a scanning system with adequate operational performance and which can overcome the large air attenuation and counter the acoustic impedances mismatch. The developments can be summarised as follows:

- A pair of annular arrays was designed for use within a through-transmission air-coupled inspection system. The array transducers were fully characterised and evaluated for their focussing ability along the transducer central axis.
- New manufacturing method for producing silicone rubber and membrane filter matching layer has been developed. A large numbers of matching layers have been fabricated to fully understand the manufacture process detail. Statistical analysis has been used to understand tolerance parameters for the fabricated materials.
- Matching layer performance has also been researched for a wideband transducer designed for pulse-echo operation. Although, the device sensitivity

significantly (~20 dB) improved through the use of the hybrid matching layer combination, this was at the expense of operational bandwidth.

- System evaluation using a variety of samples, metal and fibre composite, showed encouraging results, although system SNR was problematic on thicker CFRP material samples.

Nowadays, the development of a successful air-coupled inspection system could offer the potential opportunity for applications with some challenging materials and materials with complex geometry.

7.1.2 Annular array transducers

Building on current implementation of air-coupled piezocomposite transducers, two 1-3 piezocomposite transducers have been produced for operating in a pitch-catch air-coupled system, with an annular array configuration integrated into the design. The initial design specification was to enable beam steering capability around the central focal axis of the annular array, with a 1.5-D configuration implemented in which each array element ring was subdivided into 3 electrically independent parts. Unfortunately, due to the capacitance of the attached micro-coax cabling, a pre-amplifier unit had to be used with the receiver array and this limited the array operation to a standard 8-element ring annular configuration.

Overall, these two annular array transducers were successfully manufactured and the focusing performance evaluated to demonstrate a promising air-coupled pitch-catch system. The finished array system can be simply characterised as 40 × 40 mm devices, operating at a matched frequency of 530 kHz and capable of providing a strong axial focus in the range 45-75 mm from the transducer front surface.

7.1.3 Hybrid matching layer

For use with piezocomposite air-coupled device, a hybrid matching layer, which is composed of silicone rubber and membrane filter, has been previously reported to provide a two-way sensitivity gain in excess of 30 dB. The most significant challenge in using this material combination was the inconsistency of the manufacturing process. Hence, this Thesis has a developed robust and reliable fabrication process, which has been utilised in the array transducers designed and evaluated through this work.

The new manufacturing process uses a K-coated scanning machine and can produce up to 6 matching layer combinations during one fabrication process. Moreover, as the silicone rubber is exposed to the air directly, it will cure faster and the whole curing process can be monitored directly. This approach has the potential for large scale manufacturing for a commercial product in the future.

Approximately 200 matching layers have been evaluated through this work and a set of design guidelines, with appropriate graphs and tables have been presented for air-coupled piezocomposite transducer configurations. Consequently, a more reliable manufacture method has been introduced, significantly shortening fabrication time, is easier to handle, and capable of delivering excellent operational performance in the pitch-catch system approach utilised in this Thesis.

The matching layer approach has also been trialled on a wideband pulse-echo piezocomposite system, incorporating single crystal active material. While a large improvement in pulse-echo sensitivity was demonstrated, the desired bandwidth improvement associated with the active single crystal material was not observed and hence, this matching layer approach is primarily suited to a narrowband, pitch-catch system implementation.

7.1.4 Samples testing

Three test plates were used to evaluate the air-coupled annular array inspection system performances which were located mid-way between transmitter and receiver. The system defect resolution was examined using an Aluminium plate, with 5 through-holes, with the smallest diameter of 2 mm clearly detectable. A sandwich structure material, comprising a honeycomb centre between two CFRP thin plates, was next evaluated for detection of man-made defects using excessive pressure applied to a ball-bearing on the surface of one of the CFRP plates. The results are very encouraging, showing not only the defective areas, but also the honeycomb structure itself. The honeycomb structure size is 4 mm in width which is two times larger than the resolution tested on the Aluminium plate. Consequently, the defective area evaluated is larger than the visual measurement after the defect was introduced. This is due to the nature of the material where an externally induced defect propagates into the material and results in a larger defective volume. Both through-transmission amplitude and time-of-flight information have both been successfully used to produce NDE images of this sample. Finally, after these encouraging results, a more difficult material has been tested, which is thicker CFRP plate with 5 mm thickness. Again, artificial defects were introduced and evaluated using a high frequency scanning acoustic microscope and the air-coupled array system. In this case, although the defects were identified, the low SNR would produce false calls in terms of potential defects and hence, it was considered that this developed inspection system was not appropriate for use in this case.

7.2 Suggestions for further work

7.2.1 Further matching layer investigations

The matching layer comprising a combination of silicone rubber and membrane filter has a good performance on amplitude improvement for air-coupled transducers in both pitch-catch mode system and pulse-echo system. But for the wideband transducers, its properties lead to a quite limited range of applications.

O’Leary has investigated the use of multiple matching layers, with a stepped mechanical impedance profile which can provide more smooth transition from the transducer to the load medium [99, 100]. The schematic structure for multiple matching layer is shown in Figure 7-1. Increasing of number of the matching layers will lower the peak transmission response, but should create an increase in bandwidth. The gain bandwidth product can be greatly improved, with almost three times improvements reported. The manufacturing difficulty introduced in the paper is bonding the layers together, which uses a soft polymer phase between each layer. Interestingly, the research shows that the bondline thickness has very little effect on either the frequency or the time domain responses, with bondlines around 30 μm thick. Unfortunately, any trapped air within the bondline (air volume content of ~5 %) will cause a large bandwidth drop and increase the device ring down time. Therefore, the great care must be given to ensure the homogeneity of the bonds.

Inspired from the multiple matching layer performance, the silicone rubber and membrane filter still has potential improvement by seeking for more suitable materials to achieve such a multiple layered structure. Key here will be materials selection, with the outermost layer being the most challenging.

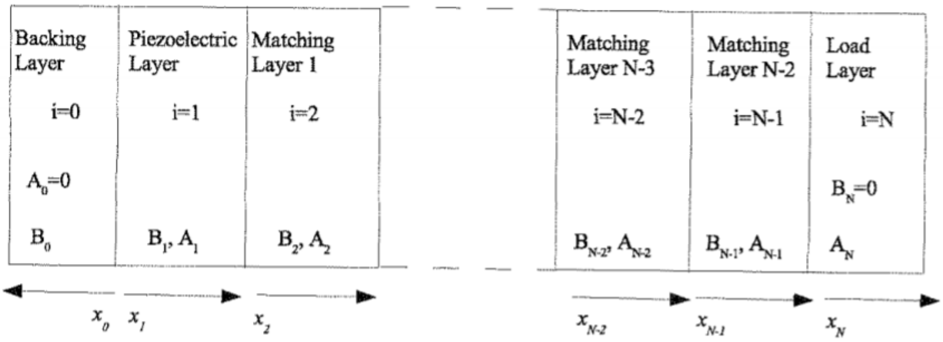

Figure 7-1 Schematic N-layered structure of the transducer, no reflected wave travel to the right in the backing layer, that is A_0=0 and infinite load without reflecting boundary, that is B_N = 0

7.2.2 Pre-amplifier for SNR improvement in receiver array

The pre-amplifier used in receiver presented in this Thesis, is an 8-channel simple pre-amplifier which can increase the amplitude of all the received signals including noise and therefore, it has limitation performance in increasing SNR. However, due to the challenging sensitivity issue associated with an air-coupled system, it is hard to separate the defect signal from the noise for inspection applications. Hence, an ultralow noise amplifier is required to increase the sensitivity of the air-coupled system and it gives the system capacitance compensation which will offer the opportunity to solve the frequency mismatch problem.

During this Thesis, an alternative preamplifier has been designed, but was unable to be manufactured and used in the array devices. Importantly, the receiver amplifier includes differential to single ended conversion, with an adjustable gain. Figure 7-2 shows the principle of the preamplifier, which is produced in 3 separate PCBs. It is envisaged that these amplifiers should be evaluated with the air-coupled array system to determine the optimum pre-amplifier approach. An overview of the three boards will now be provided, with more detail in Appendix K:

- Board one has 12 AD8432 [101] dual-channel ultralow noise pre-amplifier. Each amplifier allows two channel inputs. Each channel has a single-ended input, differential output and integrated input clamps as shown in Figure 7-3 (a). For the developed 22 elements annular array, 11 amplifiers are needed.

The AD8432 has a bandwidth of 200 MHz and can be implemented with four accurate gains, which are 12.04 dB, 18.06 dB, 21.58 dB and 24.08 dB. These parameters allow the amplifier well suited for many high-speed applications. The input impedance of the amplifiers can be adjusted to match the signal source impedance without compromising the noise performance by using a feedback circuit.

- The second board is the most complex board. It is a double-layer board and there are 11 AD8129 [102] for each layer. So, 22 AD8129 has been set up for 22 elements annular array. The AD8129 is a differential-to-single-ended amplifier with extremely high common-mode rejection ratio, which has significant influence on reducing the noise sources or crosstalk, as shown in Figure 7-3 (b). Moreover, the AD8129 is a low noise, high gain amplifier intended for applications over very long cables, where signal attenuation is significant.
- The third board is a power supply board. The ADP151 [103] is an ultralow noise, low dropout linear regulator that operates from 2.2 V to 5.5 V and provides up to 200 mA of output current. The ADM7151 [104] is a low dropout linear regulator that operates from 4.5 V to 16 V and provides up to 800 mA of output current to provide higher power supply rejection, and low noise performance.

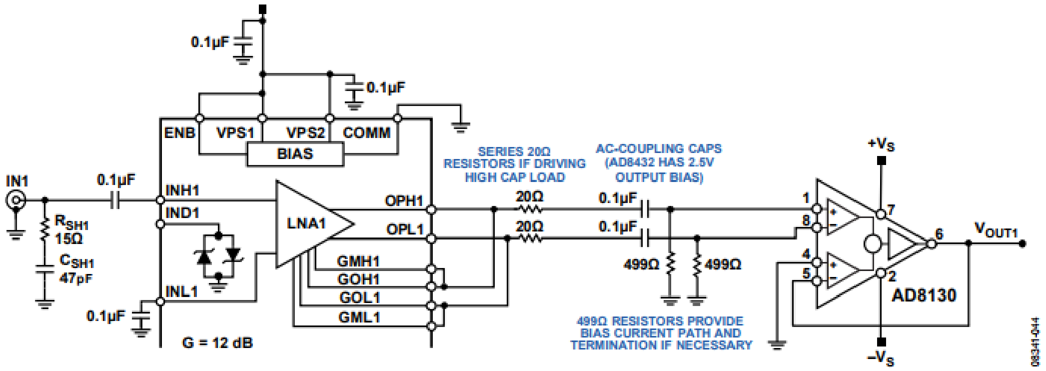

Figure 7-2 Principle of the pre-amplifier [101]; the left device is one channel of AD8432 and connect to one AD8129/AD8130

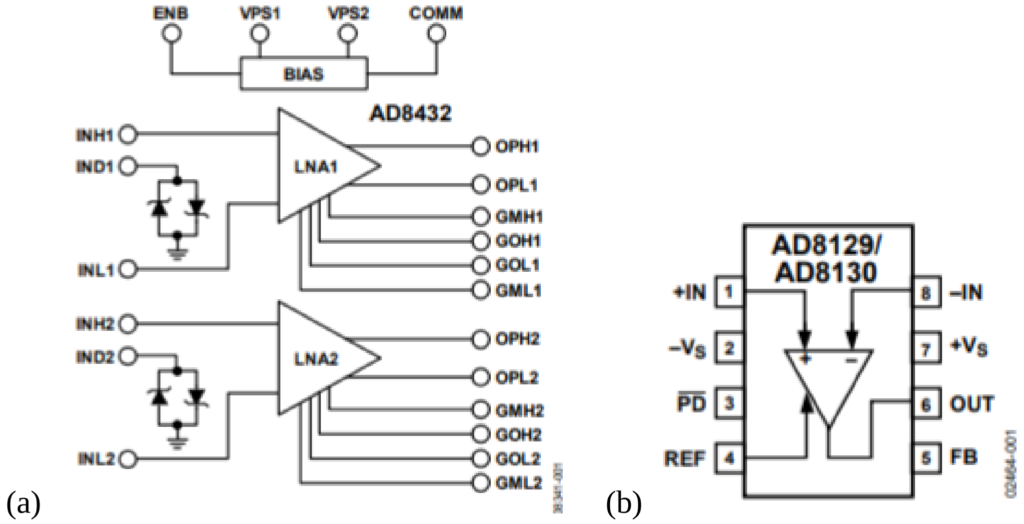

Figure 7-3 Function block diagrams for (a) AD8432 and (b) AD8129

Unfortunately, these three boards have problems when manufactured. Due to the complex design and precise pattern, it needs a long time to check the problem and fix it. But it will be the near future work to make a better performance receiver which will work as 22 elements array instead of 8 channels annular array.

7.2.3 Robotic arm application

The simple XYZ scanner's scanning area is limited and this has been further restricted by moving the sample instead of the transducer system for the work presented in this Thesis. Hence, the scanning system associated with a robotic platform would be a more suitable option.

For a future testing environment, using two 6-axis, fixed platform robotic arms to hold the transmitter and receiver on both sides of the sample and move in alignment with the component surface would be an ideal scenario. There have been significant developments in terms of robotic application of NDE over recent years and combining this with air-coupled array based inspection would be a powerful system.

A series of technologies have been introduced within CUE from sample geometric measurements through to visualisation of the inspection data [105]. The CAD model for a complex sample should be initially generated, using a coordinate measuring machine, such as FaroArm, which uses a laser probe to construct the sample's surface using metrology software, as shown in Figure 7-4. After the CAD model has been drawn, the tool path can be generated automatically in MasterCAM X6 and the robotic arm will follow the desired tool path as shown in Figure 7-5. The processed inspection results can then be superimposed onto the measured CAD representation of the sample to provide structural integrity information, as presented in Figure 7-6.

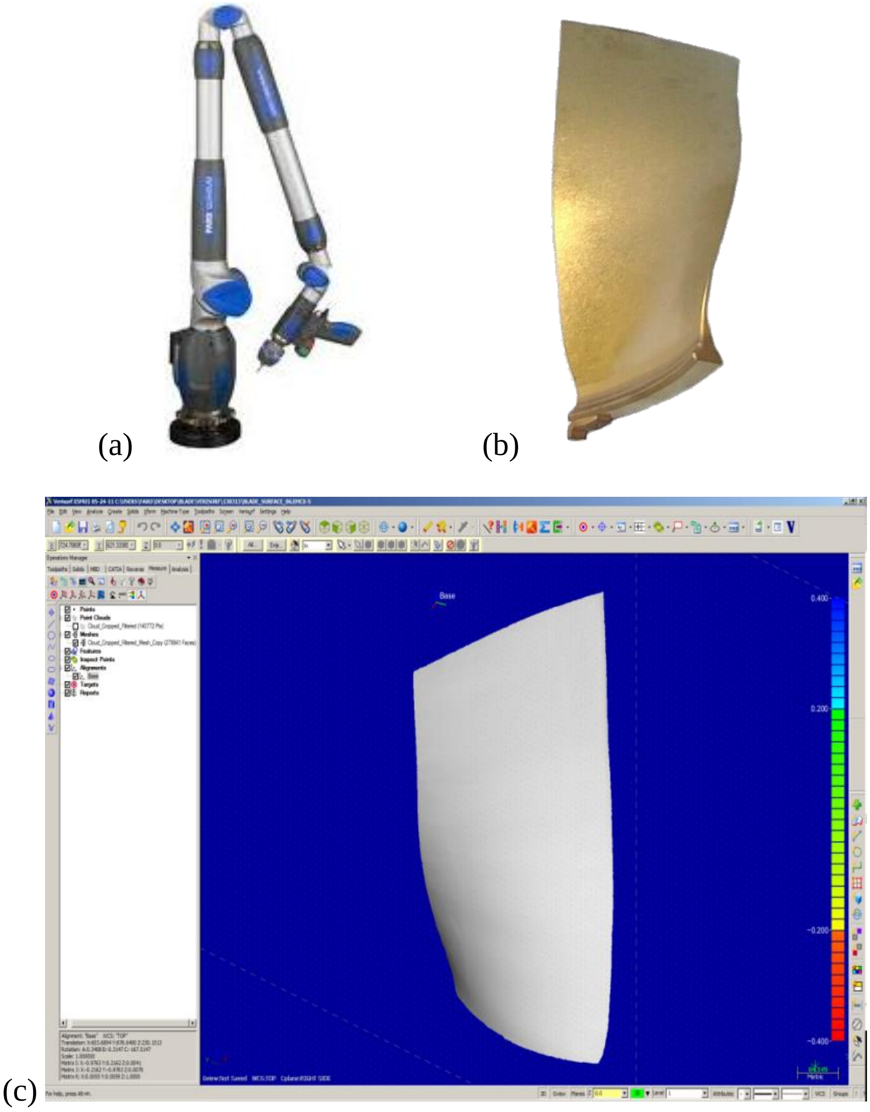

Figure 7-4 Reconstructed CAD model system. (a) FaroArm with a laser probe; (b) Fan blade; (c) Reconstructed CAD model result in software [105]

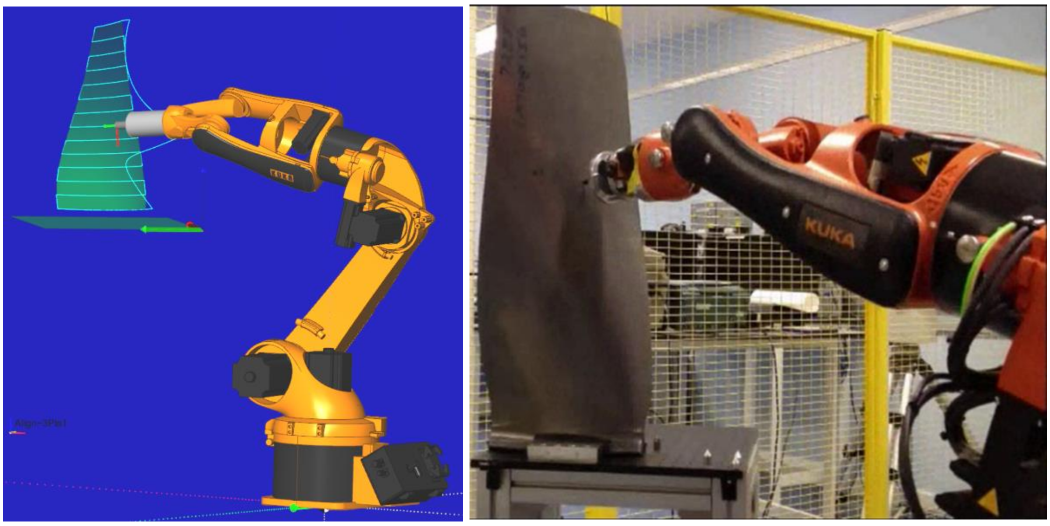

Figure 7-5 Automated toolpath generation system [105]

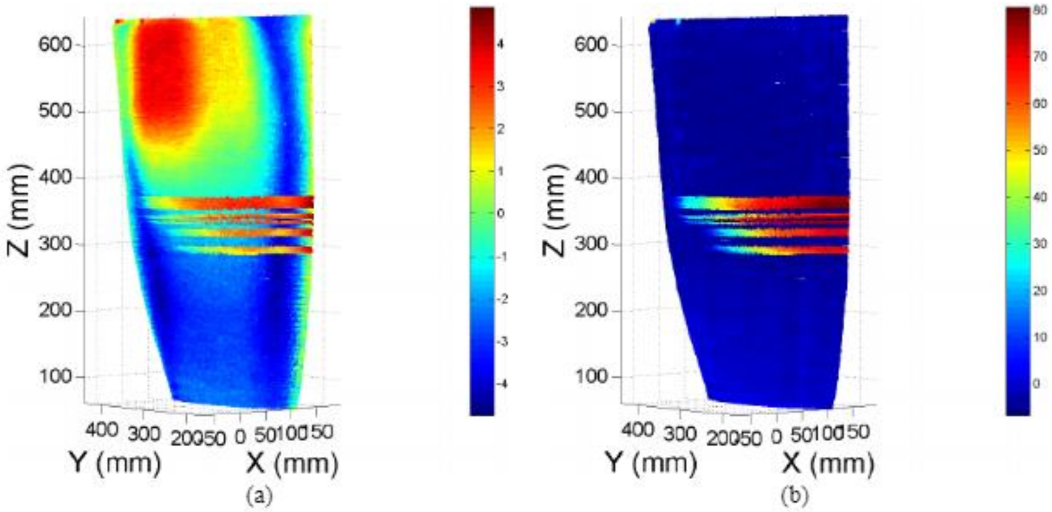

Figure 7-6 Eddy Current probe inductance change during robotic scan of the blade : (a) at 10 kHz, (b) at 1 MHz [105]

These three aspects are currently under consideration within the Centre of Ultrasonic Engineering Group, at the University of Strathclyde, and it is hoped that encouraging results will be published in the future.

References

1) K. F. Lo, S. H. Ni, and Y. H. Huang, “Non-destructive test for pile beneath bridge in the time, frequency, and time-frequency domains using transient loading”, Nonlinear Dynamics, vol. 62, no. 1–2, pp. 349–360, Apr. 2010.

2) A. M. T. Hassan and S. W. Jones, “Non-destructive testing of ultra-high performance fibre reinforced concrete (UHPFRC): A feasibility study for using ultrasonic and resonant frequency testing techniques”, Construction and Building Materials, vol. 35, pp. 361–367, Oct. 2012.

3) Non-destructive Testing Handbook, third edition, American Society for Non-destructive Testing, pp. 222- 224, 1991.

4) NDT Education Resource Centre, 2001-2012. The Collaboration for NDT Education, Iowa State University. From: http://www.ndt-ed.org/index_flash.htm

5) H. E. Bass, L. C. Sutherland, A. J. Zuckerwar, D. T. Blackstock, and D. M. Hester, “Atmospheric absorption of sound: Further development”, J. Acoust. Soc. Am. 97(1), pp. 680–683, 1995.

6) A. Gachagan, “An evaluation of 1-3 connectivity composite transducers for air-coupled ultrasonic applications”, PhD thesis. University of Strathclyde. Glasgow, 1996.

7) ANSI Standard S1-26:1995, “Calculation of the absorption of sound by the atmosphere”, (ISO 9613-1:1996).

8) S. P. Kelly, “An air-coupled ultrasonic array scanning system for rapid through transmission NDT”, PhD thesis. University of Strathclyde. Glasgow, 2000.

9) Wells PNT, “Biomedical Ultrasound”, Academic Press, 1977.

10) A. R. Selfridge, “Approximate material properties in isotropic materials”, IEEE Transactions on Sonics and Ultrasonics, vol. 32, no. 3, pp. 381–394, 1985.

11) M. J. Zipparo, K. K. Shung, and T. R. Shrout, “Piezoceramics for high-frequency (20 to 100 MHz) single-element imaging transducers”, IEEE Trans. Ultrasonics, Ferroelectrics, and Frequency Control, vol. 44, no. 5, pp. 1038–1048, 1997.

12) W. Manthey, N. Kroemer, and V. Magorl, “Ultrasonic transducers and transducer arrays for applications in air”, Meas. Sci. Technol., vol. 249, no. 3, pp. 249–261, 1992.

13) W. A. Grandia and C. M. Fortunko, “NDE applications of air-coupled ultrasonic transducers”, 1995 IEEE Ultrason. Symp. Proceedings. An Int. Symp., vol. 1, pp. 697–709, 1995.

14) M. Deka, “Air-coupled ultrasonic transducer for NDE”, Proc. IEEE US Symp, pp. 543-546, 1987.

15) A. J. Rogovsky, “Development and application of ultrasonic dry-contact and air-contact C-scan systems for non-destructive evaluation of aerospace composites”, Materials Evaluation, vol.49, pp. 1491-1497, 1991.

16) J. Stor-Pellinen and M. Luukkala,”Paper roughness measurement using airborne ultrasound”, Sensors and Actuators A-Physical, vol. 49, pp. 37-40, 1995.

17) H. Kawai, “The piezoelectricity of polyvinylidene fluoride”, J. Appl. Phys. 8 pp. 975-976, Japan, 1969.

18) K. Koga, H. Ohigashi, “Piezoelectricity and related properties of vinylidene fluoride and trifluoroethylene copolymers”, J. Appl. Phys. 56, pp. 2142– 2150, Japan, 1986.

19) K. Snook, S. Rhee, M. Robert, E. Gottlieb, K.K. Shung, “Development of P(VDF– TrFE) ultrasonic transducers operating at 50–120 MHz”, in: Proc. IEEE Ultrason. Symp., pp. 1249–1252, 2002.

20) A. S. Fiorillo, “Design and characterisation of a PVDF ultrasonic range sensor”, IEEE Trans. Ultrasonics, Ferroelectrics, and Frequency Control, vol. 39,no. 6, pp. 688–692, 1992.

21) S. Takahashi and H. Ohigashi, “Ultrasonic imaging using air-coupled P(VDF/TrFE) transducers at 2 MHz.,” Ultrasonics, vol. 49, no. 4–5, pp. 495–498, May 2009.

22) F. Wang, M. Tanaka, and S. Chonan. “Development of a PVDF piezopolymer sensor for unconstrained in-sleep cardiorespiratory monitoring”, J. Intell. Mater. Syst. Struct., 14:185–190, 2003.

23) A. S. Fiorillo, “Layered PVDF transducers for in-air US applications”, IEEE Ultrason. Symp., pp. 663–666, 1993.

24) J. Xu, “Microphone based on Polyvinylidene Fluoride (PVDF) micro-pillars and patterned electrodes”, PhD thesis. The Ohio State University. 2010.

25) K. T. Son and C. C. Lee, “Bonding and impedance matching of acoustic transducers using silver epoxy”, Ultrasonics, vol. 52, no. 4, pp. 555–563, Apr. 2012.

26) J. S. Jeong and K. K. Shung, “Improved fabrication of focused single element P(VDF-TrFE) transducer for high frequency ultrasound applications”, Ultrasonics, vol. 53, no. 2, pp. 455–8, Feb. 2013.

27) T.R. Shrout, Z. P. Chang, N.Kim and S. Markgraf, “Dielectric behaviour of single crystals near the (1-x)Pb(Mg 1/3 Nb 2/3)O3 – (x)PbTiO3 morphotropic phase boundary”, Ferroelect. Lett., vol. 12, pp. 63-69, 1990.

28) C. G. Oakley and M. J. Zipparo, “Single crystal piezoelectrics: a revolutionary development for transducers”, IEEE Ultrasonics Symposium, pp. 1157-1167, 2000.

29) X. M. Lu, T. L. Proulx, “Single crystal vs. PZT ceramics for medical ultrasound applications”, Ultrasonics Symposium, pp. 227-230, 2005.

30) D. Robertson, G. Hayward, A. Gachagan, V. Murray, “Comparison of the performance of PMN-PT single-crystal and ceramic composite arrays for NDE applications”, Insight. 48. 97-100. 10.1784/insi.2006.48.2.97, 2006.

31) R. H. Silverman, J. Cannata, K. K. Shung, O. Gal, M. Patel, H. O. Lloyd, E. J. Feleppa, and D. J. Coleman, “75 MHz ultrasound biomicroscopy of anterior segment of eye”, Ultrason Imaging, vol. 28, no. 3, pp. 179-188, 2006.

32) W. Qiu, Y. Yu, F. K. Tsang, and L. Sun, “An FPGA-based open platform for ultrasound biomicroscopy”, IEEE Transactions on Ultrasonics, Ferroelectrics, and Frequency Control, vol. 59, no. 7, pp. 1432-1442, July 2012.

33) P. A. Wlodkowski, K. Deng, K. Manfred, “The development of high-sensitivity, low-noise accelerometers utilizing single crystal piezoelectric materials”, Sensors Actuators A, vol. 90, Issues 1-2. pp. 125-131, May 2001.

34) P. W. Rehrig, W. S. Hackenberger, X. Jiang, R. J. Meyer, and X. Geng, “Naval device applications of relaxor piezoelectric single crystals”, IEEE Ultrason. Symp., pp. 733–737, 2002.

35) M.F. Wallace, “Single crystal acoustic transducers for high performance underwater sonar systems”, University of West of Scotland, PhD thesis, 2007.

36) J. Park and J. Kim, “Analytical development of single crystal Macro Fiber Composite actuators for active twist rotor blades”, Inst. Phys. Publ., vol. 14, pp. 745–753, 2005.

37) S. E. Park and W. Hackenberger, “High performance single crystal piezoelectrics : applications and issues”, Curr. Opin. Solid State Mater. Sci., vol. 6, pp. 11–18, 2002.

38) H. Luo, G. Xu, H. Xu, P. Wang, and Z. Yin, “Compositional homogeneity and electrical properties of lead magnesium niobate titanate single crystals grown by a modified bridgman technique”, Japan Soc. Appl. Phys., vol. 39, no. 9, pp. 5581–5585, 2000.

39) A. Gachagan, G. Harvey, R. O’Leary, and J. Mackersie, “Investigating the influence of the constituent materials on the performance of periodic piezoelectric composite arrays”, Review of Quantitative Nondestructive Evaluation, vol. 26, pp. 759–766, 2007.

40) J. A. Hossack and G. Hayward, “Assessment of different pillar geometries for 1-3 composite transducers using finite element analysis”, Ultrasonics Symposium, pp. 389–392, 1990.

41) J. A. Hossack and G. Hayward, “Finite-element analysis of 1-3 composite transducers”, IEEE Trans. Ultrasonics, Ferroelectrics, and Frequency Control, vol. 38, no. 6, pp. 618–629, 1991.

42) W. A. Smith and B. A. Auld, “Modeling 1-3 composite piezoelectrics: thickness-mode oscillations”, IEEE Trans. Ultrasonics, Ferroelectrics, and Frequency Control, vol. 38, no. 1, pp. 40–47, 1991.

43) T. Ritter, X. Geng, K. Kirk Shung, P. D. Lopath, S. E. Park, and T. R. Shrout, “Single crystal PZN/PT-polymer composites for ultrasound transducer applications”, IEEE Trans. Ultrasonics, Ferroelectrics, and Frequency Control, vol. 47, no. 4, pp. 792–800, Jan. 2000.

44) A. Gachagan and G. Hayward, “Improving the bandwidth of 1-3 connectivity composite receivers using mode coupling,” J. Acoust. Soc. Am., vol. 103 (6), pp. 3344–3352, 1998.

45) P. Reynolds, J. Hyslop, and G. Hayward, “The influence of constructional parameters on the practical performance of 1-3 piezocomposite transducers”, 1996 IEEE Ultrasonics Symposium, vol. 2, pp. 967–970, 1996.

46) E. Zukauskas, V. Cicenas, R. Kazys, and Prof. K. Barsauskas, “Application of aircoupled ultrasonic technique for sizing of delamination type defect in multilayered materials”, Ultragarsas, vol. 1, no. 54, 2005.

47) L. S. Smith, W. E. Engeler, M. O’Donnell, and J. E. Piel, “Rectilinear phased array transducer using 2-2 ceramic-polymer composite”, Ultrasonics Symposium, IEEE, vol.2, pp. 805–808, 1990.

48) W. Huebner, M.R. Reidmeyer, and J.W. Stevenson, “Fabrication of 2-2 connectivity PZT/Thermoplastic composites for high frequency linear arrays”, IEEE, pp. 206-209, 1995.

49) C. Wang, A. Gachagan, T. O’Leary and J. Mackersie, “High intensity focused ultrasound array transducers using 1 2-2 stacked piezoelectric composite appropriate for sonochemistry applications”, 2012 IEEE International Ultrasonics Symposium proceedings, pp. 2497-2500, 2012.

50) K. Kim, W. zhu, X. Qu, C. Aaronson, W. R. McCall, S. Chen and D. J. Sirbuly, “3D optical printing of piezoelectric nanopartical-polymer composite materials”, Acsnano, vol. 8, no. 10, pp. 9799–9806, 2014.

51) G. Hayward and A. Gachagan. “An evaluation of 1-3 connectivity composite transducers for air-coupled ultrasonic applications.” J. Acoust. Soc. Am. 99(4), Pt. 1, pp. 2148-2157. April 1996.

52) A. Erturk, and D. J. Inman, “Appendix E: numerical data for PZT-5A and PZT-5H piezoceramics”, in Piezoelectric Energy Harvesting, John Wiley & Sons, Ltd, Chichester, UK.

53) D. J. Powell and G. Hayward, “Flexible ultrasonic transducer arrays for nondestructive evaluation applications- Part 11 : performance assessment of different array configurations”, vol. 43, no. 3. IEEE Trans. Ultrasonics, Ferroelectrics, and Frequency Control, pp. 393–402, 1996.

54) W. Galbraith and G. Hayward, “Development of a PVDF membrane hydrophone for use in air-coupled ultrasonic transducer calibration”, IEEE Transactions on Ultrasonics, Ferroelectrics, and Frequency Control, vol. 45, no. 6, pp. 1549–1558, Nov. 1998.

55) A. Barzegar, D. Damjanovic, and N. Setter, “The effect of boundary conditions and sample aspect ratio on apparent d33 piezoelectric coefficient determined by direct quasistatic method”, IEEE Trans. Ultrasonics, Ferroelectrics, and Frequency Control, vol. 51, no. 3, pp. 262–270, 2004.

56) M. Kim, J. Kim, and W. Cao, “Aspect ratio dependence of electromechanical coupling coefficient of piezoelectric resonators”, Am. Inst. Phys., vol. 87, pp. 132901: 1-3, 2005.

57) G. Hayward, J. Bennett, “Assessing the influence of pillar aspect ratio on the behaviour of 1-3 connectivity composite transducers”, IEEE Transactions on Ultrasonics, Ferroelectrics and Frequency Control, vol. 43, no. 1, pp. 98–108, Jan. 1996.

58) A. Caronti, G. Caliano, R. Carotenuto, A. Savoia, M. Pappalardo, E. Cianci, and V. Foglietti, “Capacitive micromachined ultrasonic transducer arrays for medical imaging”, Microelectronics Journal, pp. 1–8, 2005.

59) D. E. Chimenti, “Review of air-coupled ultrasonic materials characterization”, Ultrasonics 54, vol. 54, no. 7, Elsevier B.V., pp. 1804–1816, Sep 2014.

60) Philips innovation services, From:

https://www.innovationservices.philips.com/looking-expertise/mems-micro-devices/mems-applications/capacitive-micromachined-ultrasonic-transducers-cmut/

61) D. W. Schindel, D. A. Hutchins, L. Zou, and M. Sayer, “The Design and Characterization of Micromachined Air-Coupled Capacitance Transducers”, IEEE Trans. Ultrasonics, Ferroelectrics, and Frequency Control, vol. 42, no. 1, pp. 42–50, 1995.

62) M. I. Haller and B. T. Khuri-Yakub, “A surface micromachined electrostatic ultrasonic air transducer”, IEEE Trans. Ultrasonics, Ferroelectrics, and Frequency Control, vol. 43, no. 1, pp. 1–6, 1996.

63) A. Buhudorf, O. Ahrens, and J. Binder, “Capacitive micromachined ultrasonic transducers and their application”, IEEE Ultrasonics Symposium, pp. 933–940, 2001.

64) A. Octavio Manzanares and F. Montero de Espinosa, “Air-coupled MUMPs capacitive micromachined ultrasonic transducers with resonant cavities”, Ultrasonics, vol. 52, no. 4, pp. 482–489, Apr. 2012.

65) J. Knight, J. McLean, and F. L. Degertekin, “Low temperature fabrication of immersion capacitive micromachined ultrasonic transducers on silicon and dielectric substrates”, IEEE Transactions on Ultrasonics, Ferroelectrics, and Frequency Control, vol. 51, no. 10, pp. 1324–1333, Oct. 2004.

66) B. W. Drinkwater and P. D. Wilcox, “Ultrasonic arrays for non-destructive evaluation: A Review”, NDT&E International, pp. 525–541, 2006.

67) F. Blum, J. Jarzynski, and L. J. Jacobs, “A focused two-dimensional air-coupled ultrasonic array for non-contact generation”, NDE&E International, pp. 634–642, 2005.

68) D. T. Yeh, O. Oralkan, I. O. Wygant, A. S. Ergun, J. H. Wong and B. T. Khuri-Yakub, “High-resolution imaging with high-frequency 1-D linear CMUT arrays”, IEEE Ultrasonics Symposium, pp. 665-668, 2005.

69) J. Peng, Z. Hu, H. Tang, X. Chen, T. Wang and S. Chen, “Fabrication and performance of a 10 MHz annular array based on PMN-PT single crystal for medical imaging”, 2013 IEEE International Ultrasonics Symposium (IUS), Prague, pp. 516-518, 2013.

70) C. E. Morton and G. R. Lockwood, “Theoretical assessment of a crossed electrode 2-D array for 3-D imaging”, IEEE Symposium on Ultrasonics, pp. 968-971 vol. 1, 2003.

71) L. G. Ullate, G. Godoy, O. Martinez and T. Sanchez, “Beam steering with segmented annular arrays”, IEEE Transactions on Ultrasonics, Ferroelectrics and Frequency Control, vol. 53, no. 10, pp. 1944-1954, October 2006.

72) B. Diarra, H. Liebgott, P. Tortoli, and C. Cachard, “Sparse array techniques for 2D array ultrasound imaging”, in Proceedings of the Acoustics 2012 Nantes Conference, pp. 23–27, 2012.

73) J. Dziewierz, A. Gachagan, N. Lord and A. Mullholland, “An application-specific design approach for 2D ultrasonic arrays”, In: 51st Annual Conference of the British Institute of Non-Destructive Testing 2012 (NDT 2012). British Institute of NonDestructive Testing, Northampton. ISBN 9781622764372 ,

74) R. Y. Chiao, K. W. Rigby and D. G. Wildes, “Optimization of 1.5D arrays”, 1998 IEEE Ultrasonics Symposium Proceedings, Sendai, pp. 1835-1838, vol.2, 1998.

75) Olympus, “Introduction to phased array ultrasonic technology applications”, USA: Olympus NDT, 2004.

76) T. J. Robertson, D. A. Hutchins, and D. R. Billson, “Capacitive air-coupled cylindrical transducers for ultrasonic imaging applications”, Institute of Physics, Measurement Science and Technology, pp. 758–769, 2002.

77) T. E. Gómez Álvarez-Arenas, J. Camacho, and C. Fritsch, “Passive focusing techniques for piezoelectric air-coupled ultrasonic transducers”, Ultrasonics, vol. 67, pp. 85–93, 2016.

78) G. Liaptsis, D. Liaptsis, P. Charlton, “Demonstration of a novel equation for the near field distance calculation for annular phased array transducers”, Nov. 2014. Available from: http://www.ndt.net/article/ndtnet/2014/95_Charlton.pdf

79) G. Liaptsis, D. Liaptsis, B. Wright and P. Charlton, “Focal law calculations for annular phased array transducers”, Feb. 2015. Available from: http://www.ndt.net/article/ndtnet/2015/100_Charlton.pdf

80) O.Godin, Oleg and G. Voronovich, Alexander. “Fermat’s principle and acoustic tomography in a time-dependent ocean”, The Journal of the Acoustical Society of America. 110(5) : 2725, 10.1121/1.4809017, 2001.

81) M. Toda, “New type of matching layer for air-coupled ultrasonic transducers”, vol. 49, no. 7, pp. 972–979, 2002.

82) S. P. Kelly, G. Hayward, and T. E. Gómez Álvarez-Arenas, “Characterization and assessment of an integrated matching layer for air-coupled ultrasonic applications”, IEEE Trans. Ultrasonics, Ferroelectrics, and Frequency Control, p., Vol. 51, No. 10, pp. 1314–1323, 2004.

83) T. E. Gómez Álvarez-Arenas, “Air-coupled piezoelectric transducers with active matching layers”, IEEE International Ultrasonics Symposium Proceedings, pp. 860–863, 2011.

84) T. E. Gómez Álvarez-Arenas, “Air-coupled piezoelectric transducers with active polypropylene foam matching layers”, Sensors (Basel)., vol. 13, no. 5, pp. 5996–6013, Jan. 2013.

85) T. E. G. Alvarez-Arenas and L. Diez, “Novel impedance matching materials and strategies for air-coupled piezoelectric transducers”, IEEE SENSOR, 2013.

86) T. E. G. Alvarez-Arenas, “Acoustic impedance matching of piezoelectric transducers to the air”, Ultrasonics, Ferroelectrics and Frequency Control, IEEE Transactions, vol.51, no.5, pp.624-633, 2004.

87) Rafael H. Medina-Sanchez, “Beam steering control system for low-cost phased array weather radars: design and calibration”, University of Massachusetts Amherst, PhD Thesis, 2014.

88) Dynaray, Zetec Inc., From:

https://www.zetec.com/products/ultrasound/instrumentation/dynaray-dynaray-lite/.

89) Diagnostic Sonar Ltd (DSL), FIToolbox manual, From:

http://diagnosticsonar.com/index.html

90) H.P. Savakus, K. A. Klicker and R. E. Newnham, “PZT epoxy piezoelectric transducers: a simplified fabrication process”, Materials Research Bulletin, vol. 16, pp. 667-680, 1980.

91) Y. Qian, N. R. Harris, and S. P. Beeby, “Design of a novel high frequency ultrasound annular array”, Procedia Chem., vol. 1, no. 1, pp. 413–416, Sep. 2009.

92) OLYMPUS, From: http://www.olympus-ims.com/en/ndt-tutorials/transducers/pa-definitions/.

93) M. Morozov, J. Riise, R. Summan, S. G. Pierce, C. Mineo, C. N. Macleod, and R. H. Brown, “Assessing the accuracy of industrial robots through metrology for the enhancement of automated non-destructive testing,” in IEEE International Conference on MFI, 2016, pp. 19–21.

94) U. Farooq, A. A. Khurram, M. S. Ahmad, S. A. Rakha, N. Ali, A. Munir, and T. Subhani, “Optimization of the manufacturing parameters of honeycomb composite sandwich structures for aerospace application”, International Conference on Aerospace Science & Engineering, pp. 1–4, 2013.

95) T. Václav and G. T. Bugajski, “Non-destructive inspection of honeycomb sandwich using infrared thermography”, International Conference on Military Technologies (ICMT) 2015, Brno, pp. 1-6, 2015.

96) V. M. do Nascimento, V. L. da S. Nantes Button, J. M. Maia, and E. T. Costa and E. J. V. Oliveira, “Influence of backing and matching layers in ultrasound transducers performance”, Medical Imaging 2003 Ultrasonic Imaging Signal Process., vol. 5035, pp. 86–96, 2003.

97) C. Fei, J. Ma, C. T. Chiu, J. A. Williams, W. Fong, Z. Chen, B. Zhu, R. Xiong, J. Shi, T. K. Hsiai, and K. K. Shung, “Design of matching layers for high-frequency ultrasonic transducers”, Appl. Phys. Lett. 107, vol. 123505, pp. 1–5, 2015.

98) A. Gachagan, G. Hayward, S. P. Kelly, and W. Galbraith, “Characterization of Air-Coupled Transducers”, IEEE Trans. Ultrasonics, Ferroelectrics, and Frequency Control, vol. 43, no. 4, pp.678–689, 1996.

99) A. J. Mulholland, N. Ramadas, R. I. O’Leary, A. C. S. Parr, G. Hayward, A. Troge, and R. A. Pethrick, “Enhancing the performance of piezoelectric ultrasound transducers by the use of multiple matching layers,” IMA J. Appl. Math. (Institute Math. Its Appl., vol. 73, no. 6, pp. 936–949, 2008.

100) S. N. Ramadas, R. L. O’Leary, A. J. Mulholland, G. Hayward, A. R. MacKintosh, A. Troge, and R. A. Pethrick, “Tapered transmission line technique based graded matching layers for thickness mode piezoelectric transducers”, in Proceedings - IEEE Ultrasonics Symposium, 2009, pp. 1–4, January 2015.

101) AD8432 data sheet, From: http://www.analog.com/media/en/technical-documentation/data-sheets/AD8432.pdf

102) AD8129 data sheet, From: http://www.analog.com/media/en/technical-documentation/data-sheets/AD8129_8130.pdf

103) ADP151 data sheet, From : https://www.analog.com/media/en/technical-documentation/data-sheets/adp151.pdf

104) ADM7151 data sheet, From: https://www.analog.com/media/en/technical-documentation/data-sheets/adm7151.pdf

105) C. Mineo, M. Morozov, G. Pierce, I. Nicholson, and I. Cooper, “Computer-Aided Tool Path Generation for Robotic Non-Destructive Inspection”, in 52nd Annual Conference of the British Institute for Non-Destructive Testing, 2013, May 2014.

Appendix A

Appendix A gives the characteristics of the constituent piezocomposite transducer materials used in the Thesis: two ceramics which are PZT5H and PZT5A; and three epoxies which are hard-set material CIBA-GEIGY CY1301/HY1300, the medium-set setting CY221/HY956 and the soft-set one CY208/HY956.

	PZT5A	*PZT5H*
Electromechanical coupling coefficient, $\boldsymbol{k_{33}}$	0.699	0.752
Electromechanical coupling coefficient, $\boldsymbol{k_{31}}$	0.327	0.370
Thickness coupling coefficient, $\boldsymbol{k_t}$	0.469	0.525
Piezoelectric strain constant, $\boldsymbol{d_{31}}$ $(10^{-10}/CN)$	-1.7	-2.43
Piezoelectric strain constant, $\boldsymbol{d_{33}}$ $(10^{-10}/CN)$	4.25	5.74
Piezoelectric voltage constant, $\boldsymbol{g_{33}}$ (Vm/N)	0.0267	0.0226
Relative permittivity, ε_{11}^{S}	916	1700
Relative permittivity, ε_{33}^{S}	830	1470
Stiffness coefficient, c_{11}^{E} $(10^{10}Pa)$	12.03	12.72
Stiffness coefficient, c_{44}^{E} $(10^{10}Pa)$	2.11	2.30
Density, ρ (kg/m^3)	7750	7500
Curie temperature, (℃)	350	235

CY1301/HY1300 *In WATER*		*FREQUENCY (MHz)*	
	0.5	1.0	2.25
Vl(m/s)	2512.7	2535.9	2560
Vs(m/s)	1175	1178.8	1208.7
Density(Kg/m3)	1149	1149	1149
Poisson Ratio	0.3601	0.3622	0.3566
Young's Modulus E (m.s-2Kg)	4.2810E+09	4.3157E+09	4.5187E+09
Impedance Z (Kg.m2s-1)	2.8645E+06	2.8909E+06	2.9184E+06
Bulk Modulus B (m.s-2.Kg)	5.0990E+09	5.2190E+09	5.2505E+09
Shear Modulus G (m.s-2Kg)	1.5739E+09	1.5841E+09	1.6655E+09
c11	7.1976E+09	7.3311E+09	7.4711E+09
c44	1.5739E+09	1.5841E+09	1.6655E+09
s11	2.3360E-10	2.3170E-10	2.2130E-10
s44	6.3540E-10	6.3130E-10	6.0040E-10
Longitudinal Attenuation (dB/m)	139	287	608
Shear Attenuation (dB/m)	356	738	1980

CY221/HY956 *IN WATER*	*FREQUENCY (MHz)*		
	0.5	1.0	2.25
Vl(m/s)	2364.1	2451.5	2440.9
Vs(m/s)	1064.6	1109.9	1084.5
Density(Kg/m3)	1134	1134	1134
Poisson Ratio	0.3728	0.3711	0.377
Young's Modulus E (m/s2Kg)	3.5288E+09	3.8307E+09	3.6732E+09
Impedance Z (Kg/m2s)	2.6809E+06	2.7800E+06	2.7680E+06
Bulk Modulus B (m/s2 Kg)	4.6242E+09	4.9526E+09	4.9780E+09
Shear Modulus G (m/s2Kg)	1.2852E+09	1.3969E+09	1.3337E+09
c11	6.3379E+09	6.8152E+09	6.7564E+09
c44	1.2852E+09	1.3969E+09	1.3337E+09
s11	2.8340E-10	2.6110E-10	2.7220E-10
s44	7.7810E-10	7.1580E-10	7.4980E-10
Longitudinal Attenuation(dB/m)	208	895	1711
Shear Attenuation (dB/m)	2319	4108	8147

CY208/HY956 *low velocity oil*	*FREQUENCY (MHz)*		
	0.5	1.0	1.25
Vl(m/s)	2000.8	1989.2	1998.1
Vs(m/s)	747.8	762	779.8
Density(Kg/m3)	1165	1165	1165
Poisson Ratio	0.4188	0.414	0.4102
Young's Modulus E (m.s-2Kg)	1.8486E+09	1.9130E+09	1.9980E+09
Impedance Z (Kg.m2s-1)	2.3309E+06	2.3174E+06	2.3278E+06
Bulk Modulus B (m.s-2.Kg)	3.7951E+09	3.7079E+09	3.7066E+09
Shear Modulus G (m.s-2Kg)	6.5147E+08	6.7645E+08	7.0842E+08
c11	4.6637E+09	4.6098E+09	4.6512E+09
c44	6.5150E+08	6.7650E+08	7.0840E+08
s11	5.4100E-10	5.2300E-10	5.0100E-10
s44	1.5350E-09	1.4780E-09	1.4120E-09
Longitudinal Attenuation (dB/m)	825	1633	1694
Shear Attenuation (dB/m)	6063	11526	12638

Appendix B

Appendix B presents the full fabrication details of the 600 kHz single element transducers which are used for matching layers' evaluation in Chapter 3.

	Transmitter	*Receiver*
Ceramic material	PZT5H	PZT5A
Polymer material	Hard set CY1301	Hard set CY1301
Volume fraction	72 %	49 %
Diameter	30 mm	30 mm
Saw width	0.15 mm	0.15 mm
Saw pitch	1 mm	0.5 mm
Thickness	2.56 mm	3 mm
Aspect ratio	0.332	0.117


Transmitter


Receiver

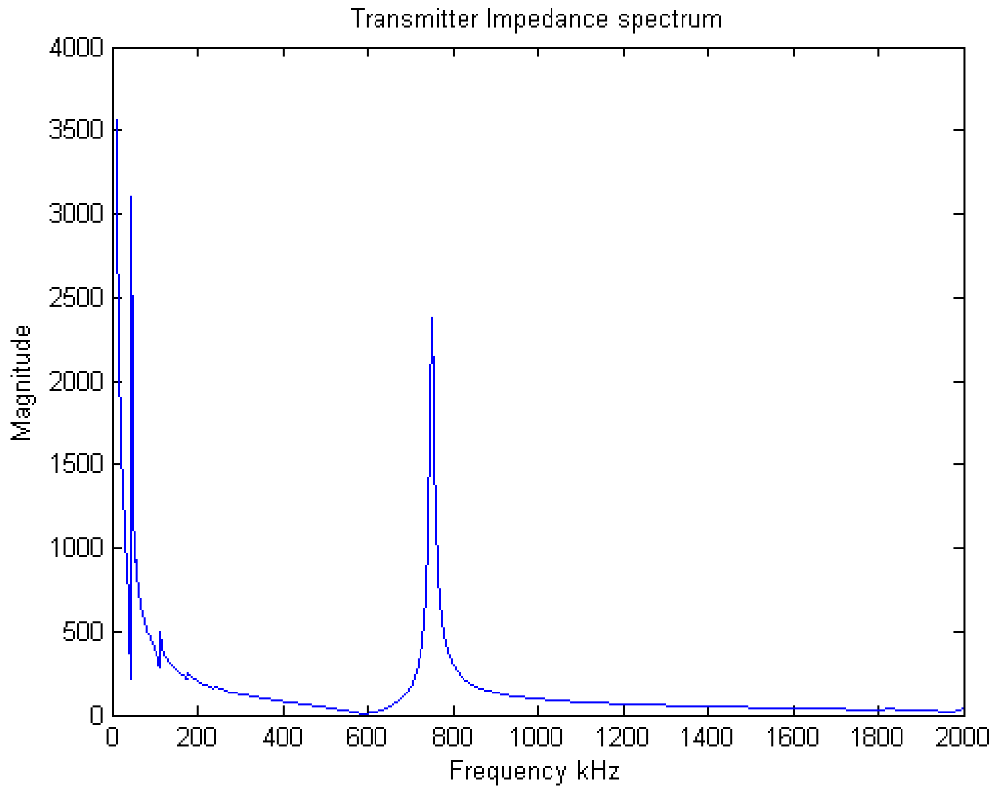
Transmitter Impedance spectrum
Magnitude
4000
3500
3000
2500
2000
1500
1000
500
0
0
200
400
600
800
1000
1200
1400
1600
1800
2000
Frequency kHz

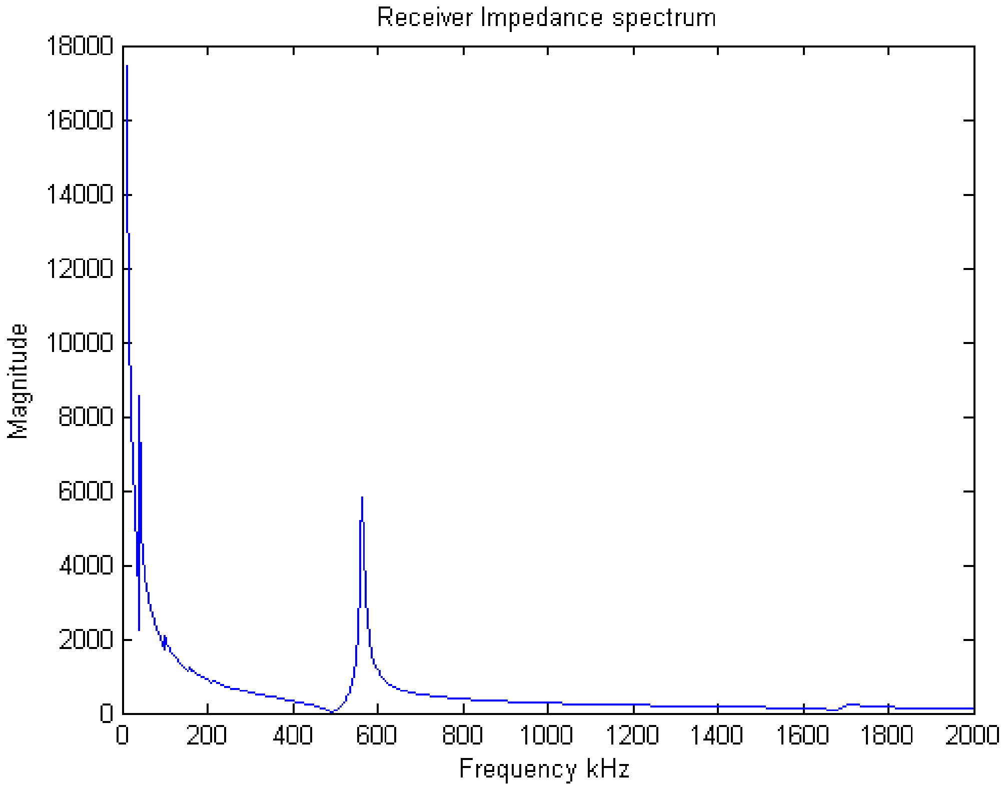
Receiver Impedance spectrum
Magnitude
18000
16000
14000
12000
10000
8000
6000
4000
2000
0
0
200
400
600
800
1000
1200
1400
1600
1800
2000
Frequency kHz

Appendix C

Use these four design criteria are programmed in MATLAB to design the annular array's dimension.

- Every element has an equal active area.
- The element size should be fairly large to transmit/receive more energy.
- The gap width between each ring should be large enough to electrically isolate array elements.
- The width of each element should be determined relative to the ceramic pillar size to ensure at least 1 ceramic pillar across the smallest width array element.

```
g=0.6; % gap
%  -----------------------------------------------------------------
-
%  calculation
n = input('Enter the number of the rings  :  ');
n = n-1 ; % number of rings -1
rimatrix = zeros(n,1) ; % matrix for ri value
romatrix = zeros(n,1) ; % matrix for ro value
rmiddle  = zeros(n,1) ; % matrix for the middle r
while  romatrix(n) - rimatrix(n)<0.9    % the out-most ring should
large than 1
ro=rimatrix(1)-g+0.1;
A= ro^2;
for i = 1:n
    ri = ro + g ;
    ro=(ri^2+A)^0.5;
    rimatrix(i) = ri ;
    romatrix(i) = ro ;
    rmiddle (i) =(ri+ro)*0.5 ;
end
end
%  -----------------------------------------------------------------
--
%  show the result
fprintf('r1 = %g\n' , rimatrix(1) - g )
for i = 1:n
fprintf(['r',int2str(i+1) ,'i= %g\n'] , rimatrix(i)) ; %rimatrix(1)
is r2i
fprintf(['r',int2str(i+1) ,'o= %g\n'] , romatrix(i)) ; %romatrix(1)
is r2o
end
```

Appendix D

Appendix D shows the Matlab code to calculate the rings radius and model the 3-D beam file of the rings designed using algorithm in Appendix C.

```
Freq = input('Enter the excitation frequency (kHz)  :  ');
Freq = Freq * 1000;
Speed = 343;
wavelength = Speed / Freq;
dia = input('Enter txdcr diam. (assumed circular, mm) :  ');
txdcr_resn = input('Enter resolution of TPoints (mm) :  ');
dia = dia / 1e3;
txdcr_resn = txdcr_resn / 1e3;

%calculate the matrix of the transducer points
clear TPoints;
i2=1;
for x = -dia/2 : txdcr_resn : dia/2
    for y = -dia/2 : txdcr_resn : dia/2
        if (((x^2)+(y^2))^0.5 <= ((rimatrix(1)-g)/1000))
            TPoints(i2,1) = x;
            TPoints(i2,2) = y;
            i2 = i2+1;
        end
        for j=1:n
            if ((((x^2)+(y^2))^0.5 >= (rimatrix(j)/1000)) &
(((x^2)+(y^2))^0.5 <= (romatrix(j)/1000)))
%                if (y<=(-sqrt(3)/3*x + sqrt(3)/2/1e3) & y>=(-
sqrt(3)/3*x - sqrt(3)/2/1e3) & y<0)||(y>0 & x>=-0.75e-3 & x<=0.75e-
3)||(y<=(sqrt(3)/3*x + sqrt(3)/2/1e3) & y>=(sqrt(3)/3*x -
sqrt(3)/2/1e3) & y<0)
                if (y<=(-sqrt(3)*x + 1.5/1e3) & y>=(-sqrt(3)*x -
1.5/1e3) & x<0)||(x>0 & y>=-0.75e-3 & y<=0.75e-3)||(y<=(sqrt(3)*x +
1.5/1e3) & y>=(sqrt(3)*x - 1.5/1e3) & x<0)
                else
                    TPoints(i2,1) = x;
                    TPoints(i2,2) = y;
                    i2 = i2+1;
                end
            end
        end
    end
end
plot(TPoints(:,1),TPoints(:,2),'.');
axis square;
xlabel('distance x(m)');
ylabel('distance y(m)');
title('Simulated layout');
TPoints(:,3) = zeros([length(TPoints(:,1)),1]);

zstart = input('Enter start of field in z-direction (mm): ');
zstop = input('Enter end of field in z-direction (mm)  :  ');
```

```
wi = input('Enter width of scan in x-direction (mm; enter 0 for on-
axis plot only)  :  ');
field_resn = input('Enter resolution of field (mm)  :  ');
focpt = input('Enter the focal distance in z-direction (mm) :  ');
focpt = focpt/1000; % scales to m

%---------calculate the time delay (focal law)-----------------------
-------
 tdelay(1)=(((rmiddle(n)/1000)^2+focpt^2)^0.5-focpt)/Speed;
 for i=1:n
     tdelay(i+1)=-(((rmiddle(i)/1000)^2+focpt^2)^0.5-
((rmiddle(n)/1000)^2+focpt^2)^0.5)/Speed;
 end
 for i=1:n+1
     angledelay(i)=tdelay(i)*2*pi*Freq;
 end
%--------------------------------------------------------------------
-------
DoAtten = input('Include attenuation (Yes (1) default) >> ');
z=zstart:field_resn:zstop;
x1=wi/2;
x=-x1:field_resn:x1;
n3=length(x);
c=length(z);
FPoints=zeros((c*n3),3);             % zeros matrix, FPoints in
length
for i=1:c
    FPoints(n3*(i-1)+1:n3*i,3)=z(i);  % builds FPoints n rows at a
time
    FPoints(n3*(i-1)+1:n3*i,1)=x;
end
FPoints=FPoints/1000;               % scales to mm

% If user selects to use atten then calc it, otherwise atten = 0
if isempty(DoAtten)
    DoAtten = 1
end

if DoAtten == 1
    Atten = AirAttenCoeffBenny(Freq)         % attenuation (NP/m)
else
    Atten = 0
end


VVect = 1;

Density = 1.2;

% Get lengths of inputs
n1=length(FPoints);
n2=length(TPoints);
% ------------decide each transducer point's time delay-------------
-------
SVect = ones([length(TPoints),1]);
for i=1:n2
   TPointsr=1000*sqrt(TPoints(i,1).^2+TPoints(i,2).^2);
```

```
   if TPointsr<rimatrix(1)-g
       ExcitationAngle(i,1)= angledelay(1);
   end
   for j=1:n
       if TPointsr<romatrix(j)& TPointsr>rimatrix(j)
         ExcitationAngle(i,1)= angledelay(j+1);
       end
   end
 end
ExcitationMag = 1;
%ExcitationAngle = angle(SVect);
% -------------create the variable of the follow equations----------
-------
radius=ones(n2,1);
K = 2 * pi * Freq/ Speed;
CWpressure=ones(n1,1);
%clear SVect

% Calculate the field at each TPoint
clear j
for i=1:n1
    % calculate the distance from each points of Transducer
    radius=((TPoints(:,1)-FPoints(i,1)).^2+(TPoints(:,2)-
FPoints(i,2)).^2+...
        (TPoints(:,3)-FPoints(i,3)).^2).^0.5;
    % for each i, radius is a matrix of the distance from each
TPoint to the
    % current FPoint (so it is TPoints long)

    CWPressuremag = (-j* Freq/n2) .* ExcitationMag .*...
        exp((j * (-K .* radius - ExcitationAngle))-radius*Atten) ./
(2 * pi * radius);
    % calculates the (complex) contribution to pressure at FPoint(i)
from
    % each individual TPoint
    CWpressure(i)=sum(CWPressuremag);
    % sums each contribution to produce the pressure at FPoint(i)
end

CWPressurereshape =
reshape(CWpressure,length(unique(FPoints(:,1))),length(unique(FPoint
s(:,3))));
CWabspressure=abs(CWPressurereshape);
%/max(max(abs(CWPressurereshape)));

%plot on-axis pressure
figure;
onaxis = int16((length(CWabspressure(:,1))/2));
plot(z, CWabspressure(onaxis,:));
xlabel('distance (mm)');
ylabel('air pressure');
title(['Simulated on-axis pressure ',num2str(Freq/1e3),'kHz;
',num2str(dia*1e3),'mm']);
set (gcf,'Position',[400,100,800,400], 'color','w');
figure
plot(log10(z),log10(CWabspressure(onaxis,:)));
set (gcf,'Position',[400,100,800,400], 'color','w');
```

```
powlaw=polyfit(log10(z(floor(end/2):end)),log10(CWabspressure(onaxis
,floor(end/2):end)),1);
% save matlab figure, png
figroot = ['SimPressAxis' num2str(Freq/1e3) 'kHz' num2str(dia*1e3)
'mmdia' num2str(zstop) 'mmdepth'];
figfile = [figroot '.fig'];
saveas(gcf, figfile);
figfile = [figroot '.png'];
saveas(gcf, figfile);

% rotate so that beam profile is vertical
if wi ~= 0
    CWabspressure = rot90(CWabspressure,3);
%    pause;
    figure;
    contourf(x, z, CWabspressure,20, 'Linestyle', 'none');
    colormap(gray);
    colorbar;
    title(['Simulated pressure ',num2str(Freq/1e3),'kHz;
',num2str(dia*1e3),'mm']);
    set (gcf,'Position',[400,100,800,600], 'color','w');
   xlabel('Distance (mm)');
   ylabel('Distance along airpath (mm)');
%     % save matlab figure, png
%     figroot = ['SimPressField' num2str(Freq/1e3) 'kHz'
num2str(dia*1e3) 'mmdia' num2str(wi) 'x' num2str(zstop) 'mmfield'];
%     figfile = [figroot '.fig'];
%     saveas(gcf, figfile);
%     figfile = [figroot '.png'];
%     saveas(gcf, figfile);
end
```

Appendix E

The impedance characteristic experimental results for every ring array element in both the transmitter and receiver before connecting to the micro-coax cable are detailed in Appendix E.

- Transmitter's impedance characteristic by experiment: no cable

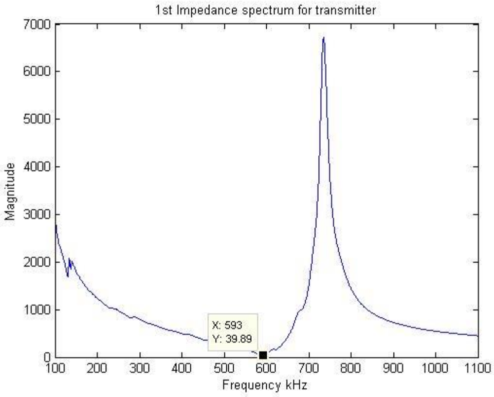
1st Impedance spectrum for transmitter

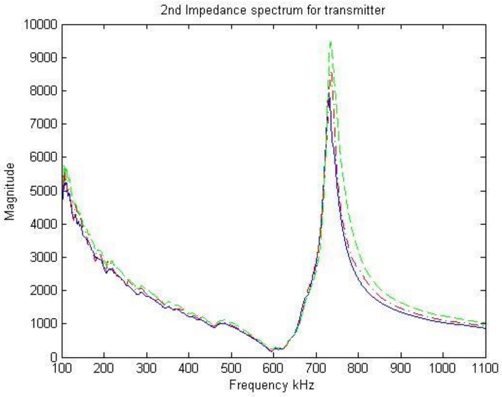
2nd Impedance spectrum for transmitter

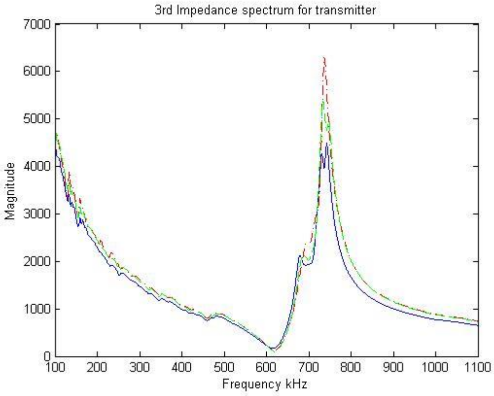
3rd Impedance spectrum for transmitter

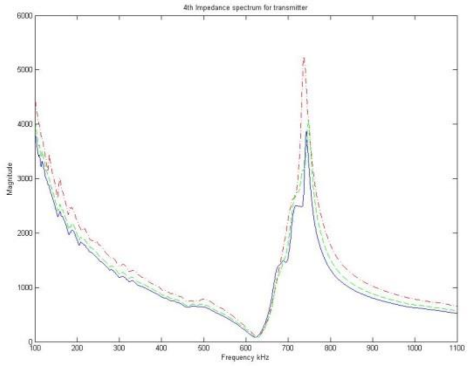
4th Impedance spectrum for transmitter

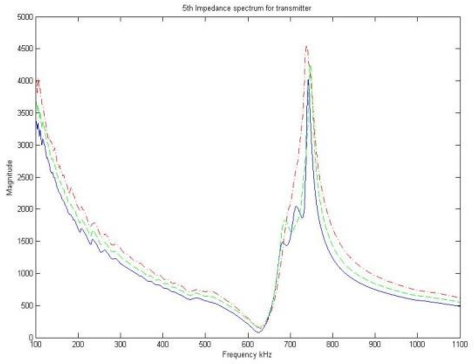
5th Impedance spectrum for transmitter

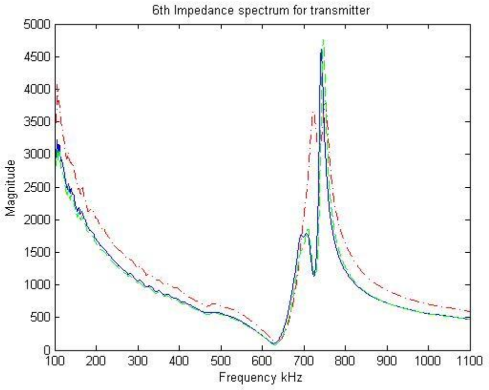
6th Impedance spectrum for transmitter

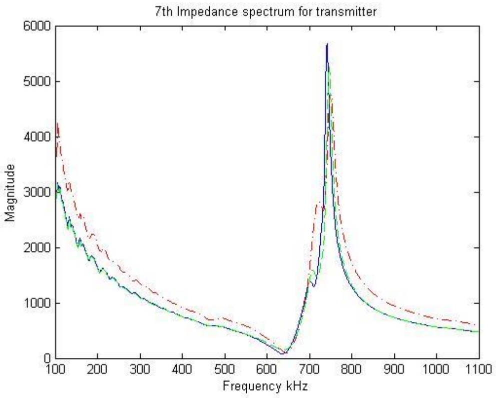

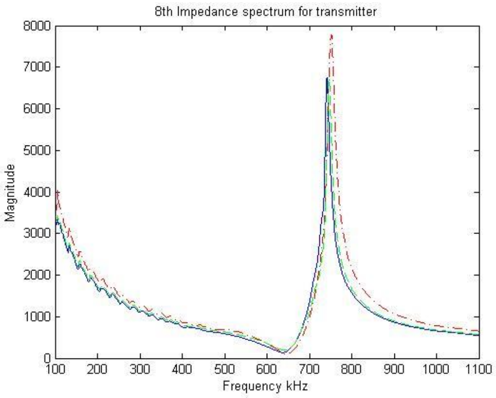

- Receiver’s impedance characteristic by experiment: no cable

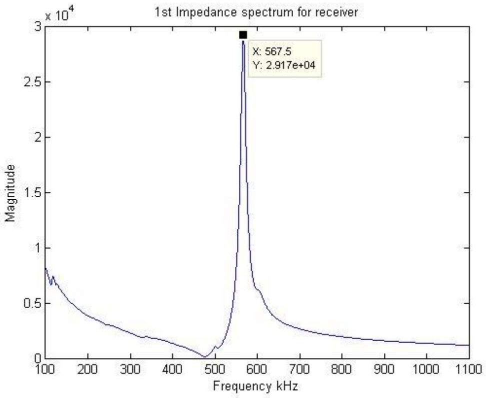

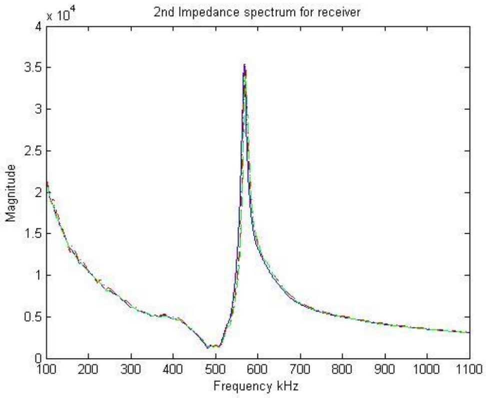

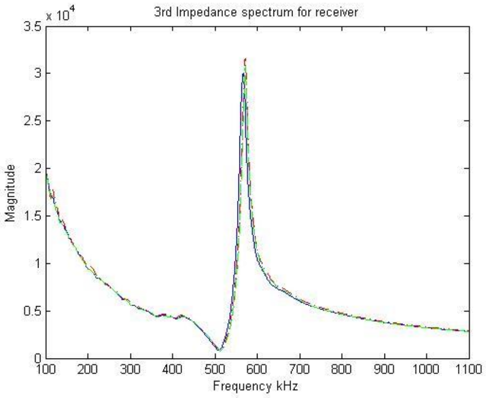

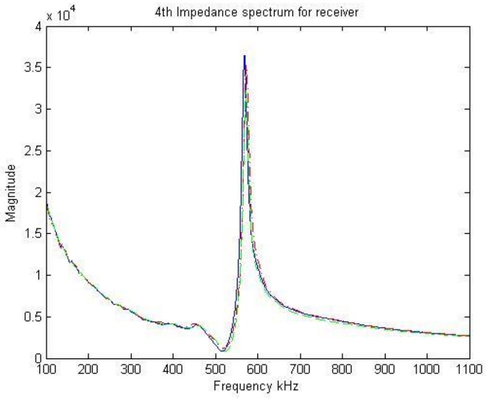

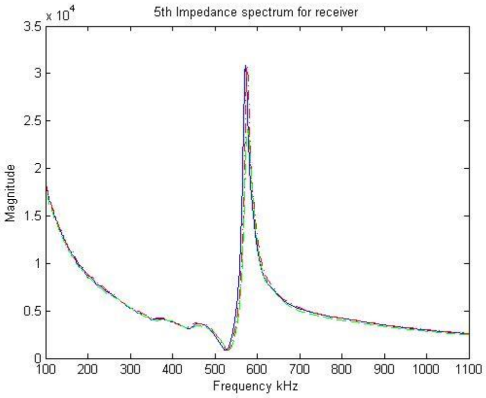
5th Impedance spectrum for receiver
x 10^4
Magnitude
0
0.5
1
1.5
2
2.5
3
3.5
Frequency kHz
100
200
300
400
500
600
700
800
900
1000
1100

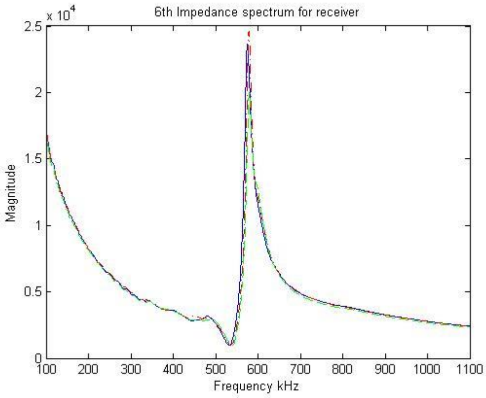
6th Impedance spectrum for receiver
x 10^4
Magnitude
0
0.5
1
1.5
2
2.5
Frequency kHz
100
200
300
400
500
600
700
800
900
1000
1100

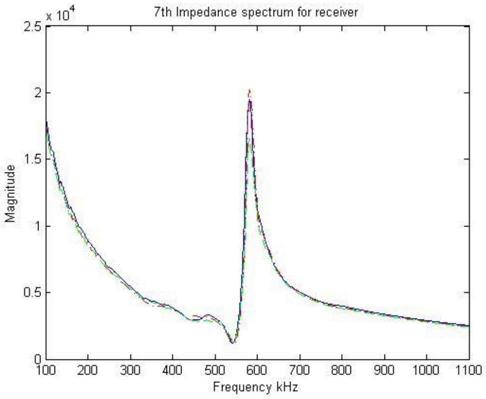
7th Impedance spectrum for receiver
x 10^4
Magnitude
0
0.5
1
1.5
2
2.5
Frequency kHz
100
200
300
400
500
600
700
800
900
1000
1100

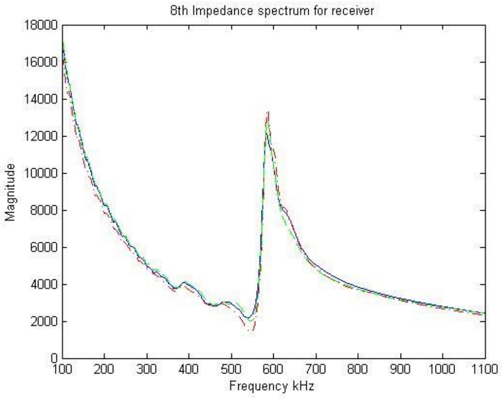
8th Impedance spectrum for receiver
Magnitude
0
2000
4000
6000
8000
10000
12000
14000
16000
18000
Frequency kHz
100
200
300
400
500
600
700
800
900
1000
1100

Appendix F

The array interconnect cables are separated into two distinct areas for both the transmitter and the receiver. The connection detail is shown below:

- Hypertronics connector pin socket layout

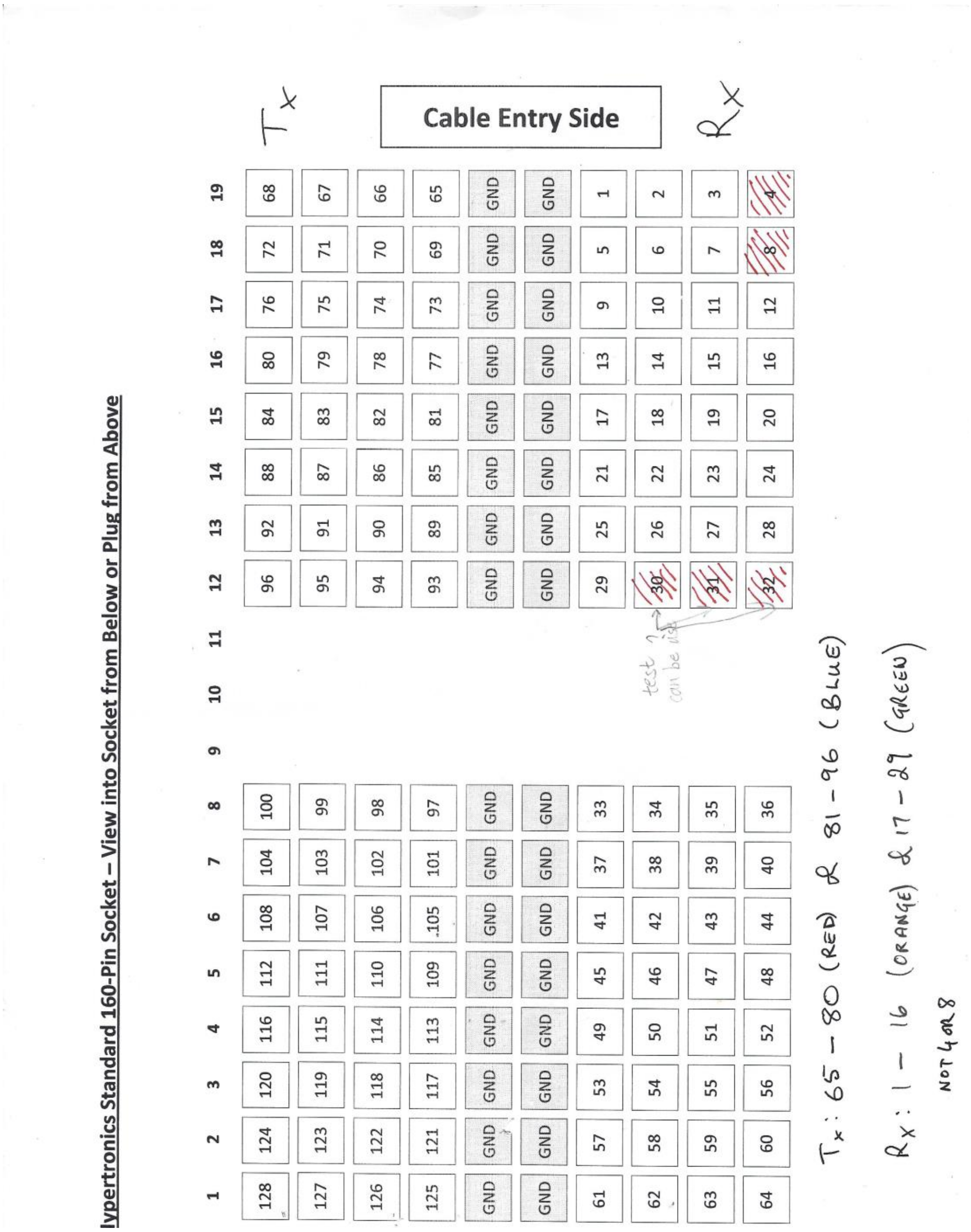

Hypertronics Standard 160-Pin Socket – View into Socket from Below or Plug from Above

1	2	3	4	5	6	7	8	9	10	11	12	13	14	15	16	17	18	19
128	124	120	116	112	108	104	100				96	92	88	84	80	76	72	68
127	123	119	115	111	107	103	99				95	91	87	83	79	75	71	67
126	122	118	114	110	106	102	98				94	90	86	82	78	74	70	66
125	121	117	113	109	105	101	97				93	89	85	81	77	73	69	65
GND	GND	GND	GND	GND	GND	GND	GND				GND	GND	GND	GND	GND	GND	GND	GND
GND	GND	GND	GND	GND	GND	GND	GND				GND	GND	GND	GND	GND	GND	GND	GND
61	57	53	49	45	41	37	33				29	25	21	17	13	9	5	1
62	58	54	50	46	42	38	34				30	26	22	18	14	10	6	2
63	59	55	51	47	43	39	35				31	27	23	19	15	11	7	3
64	60	56	52	48	44	40	36				32	28	24	20	16	12	8	4

Tx

Cable Entry Side

Rx

test ? can be us

Tx : 65 – 80 (RED) & 81 – 96 (BLUE)

Rx : 1 – 16 (ORANGE) & 17 – 27 (GREEN)

NOT 4 OR 8

- Transmitter’s PCB board connection layout

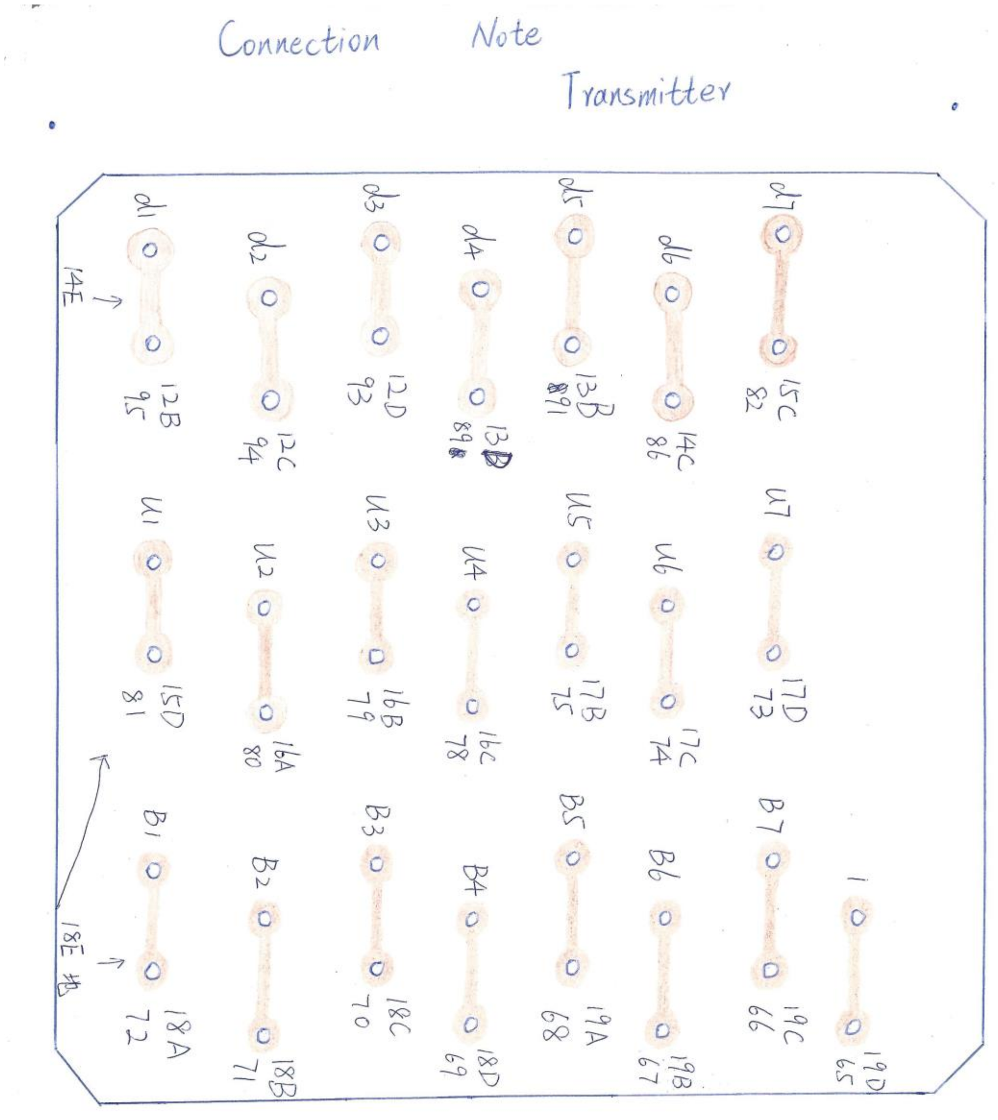

- Receiver's PCB board connection layout

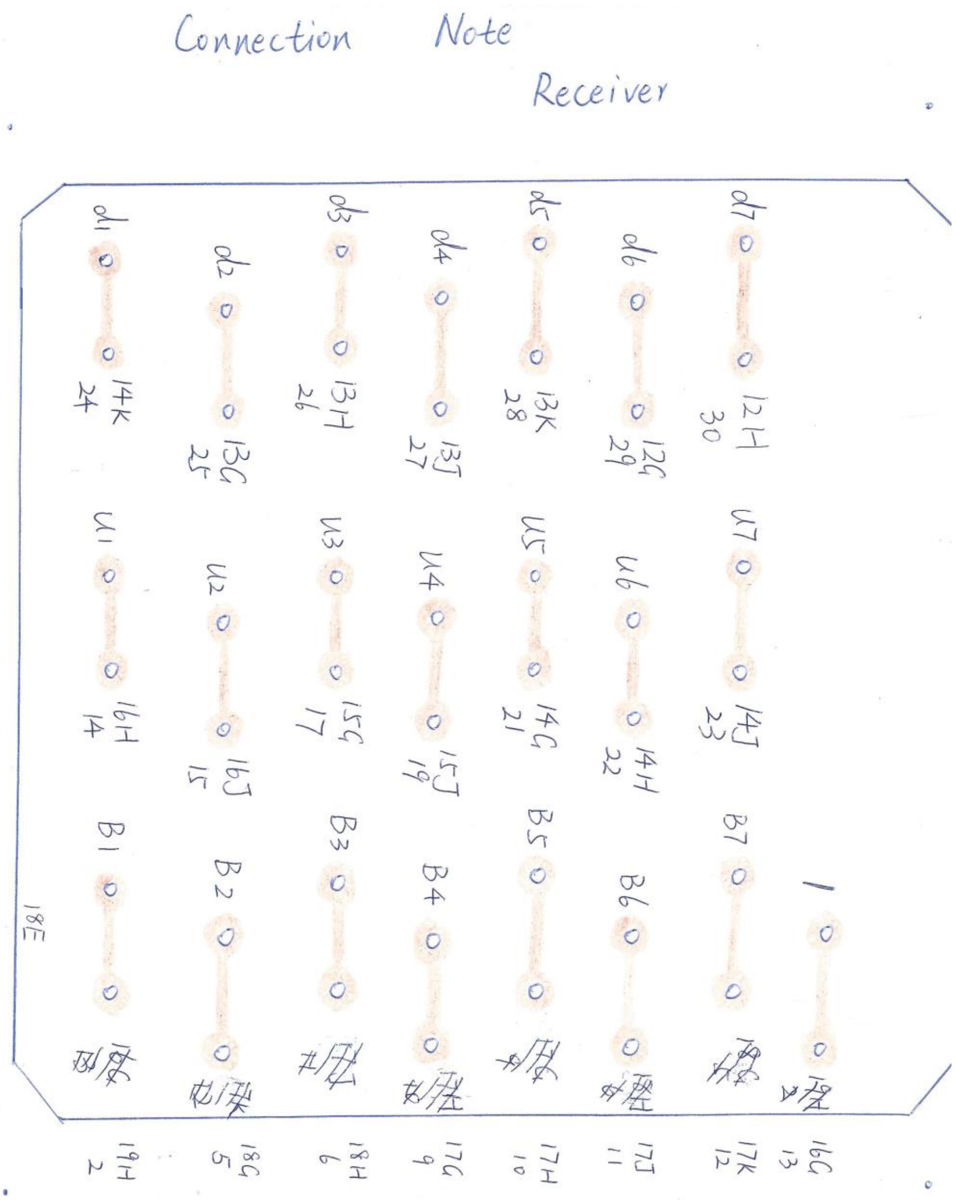

Appendix G

The impedance characteristic experimental results for every ring array element in both the transmitter and receiver after connecting to the 3 m long micro-coax cable are detailed in Appendix G.

- Transmitter's impedance characteristic by experiment: micro-coax cable

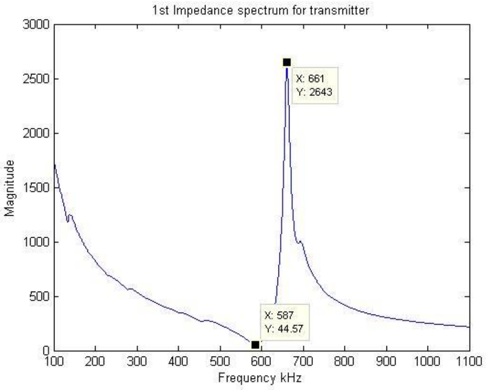

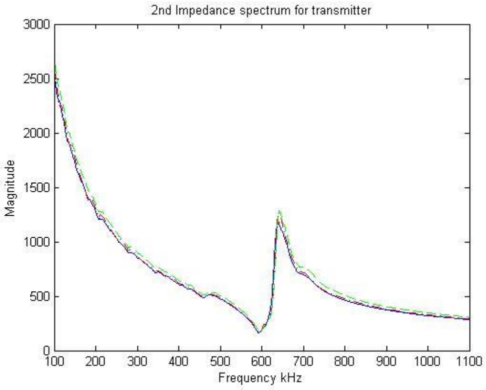

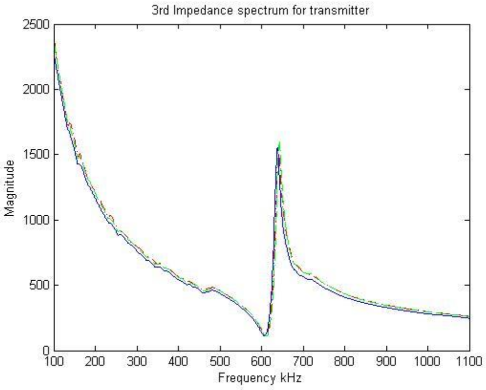

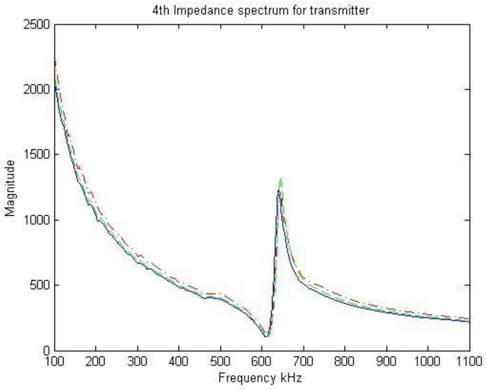

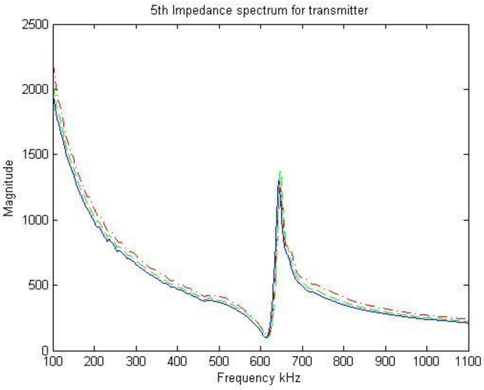

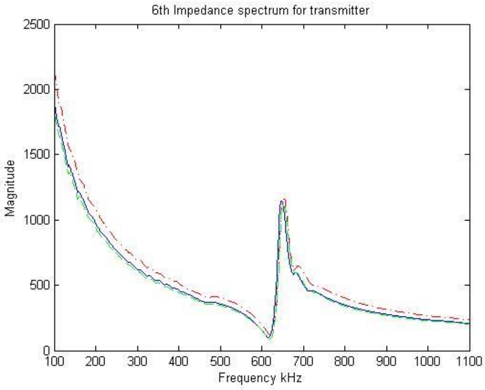

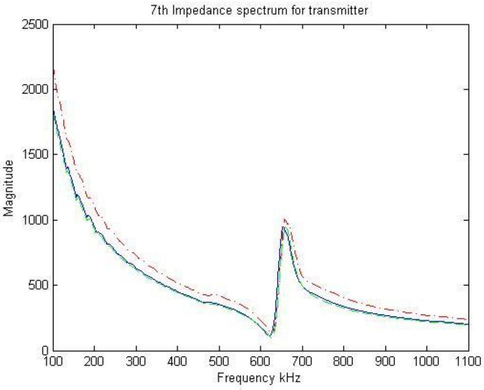

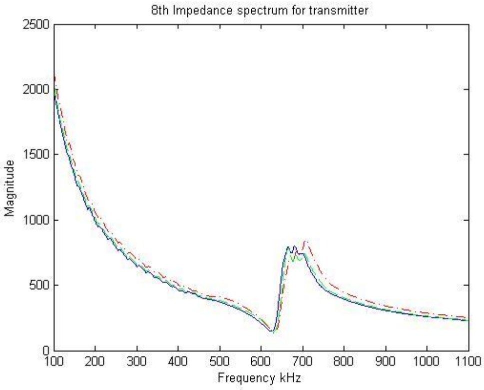

- Receiver’s impedance characteristic by experiment: micro-coax cable

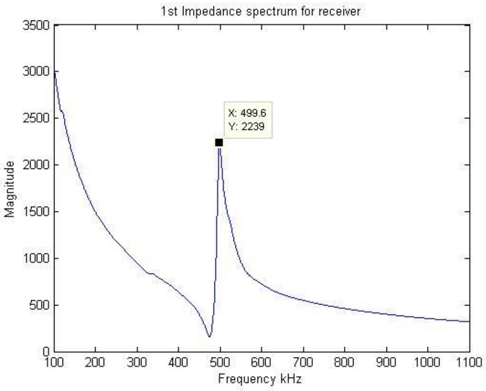
1st Impedance spectrum for receiver
Magnitude
Frequency kHz
X: 499.6
Y: 2239
0
500
1000
1500
2000
2500
3000
3500
100
200
300
400
500
600
700
800
900
1000
1100

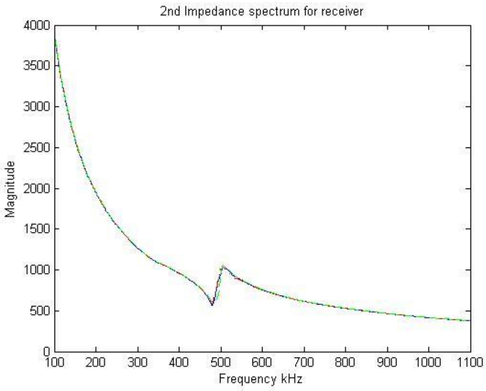
2nd Impedance spectrum for receiver
Magnitude
Frequency kHz
0
500
1000
1500
2000
2500
3000
3500
4000
100
200
300
400
500
600
700
800
900
1000
1100

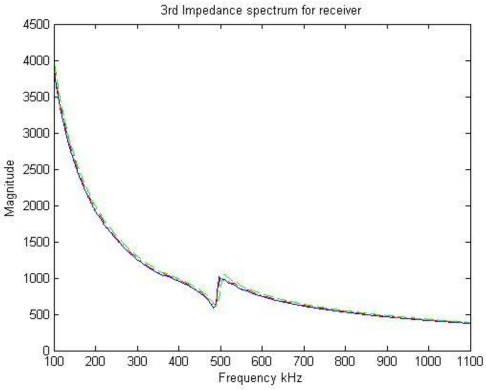
3rd Impedance spectrum for receiver
Magnitude
Frequency kHz
0
500
1000
1500
2000
2500
3000
3500
4000
4500
100
200
300
400
500
600
700
800
900
1000
1100

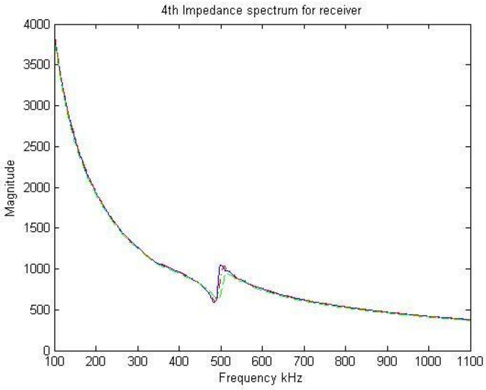
4th Impedance spectrum for receiver
Magnitude
Frequency kHz
0
500
1000
1500
2000
2500
3000
3500
4000
100
200
300
400
500
600
700
800
900
1000
1100

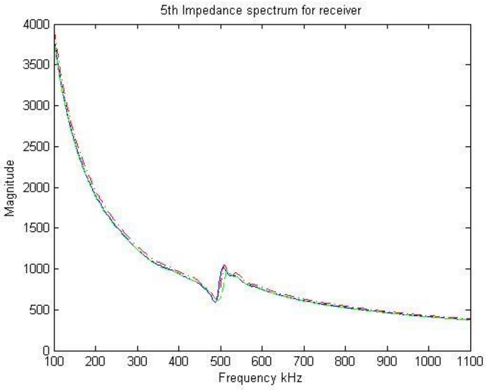
5th Impedance spectrum for receiver
Magnitude
Frequency kHz
0
500
1000
1500
2000
2500
3000
3500
4000
100
200
300
400
500
600
700
800
900
1000
1100

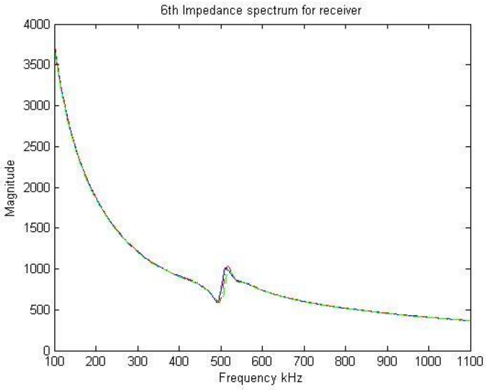
6th Impedance spectrum for receiver
Magnitude
Frequency kHz
0
500
1000
1500
2000
2500
3000
3500
4000
100
200
300
400
500
600
700
800
900
1000
1100

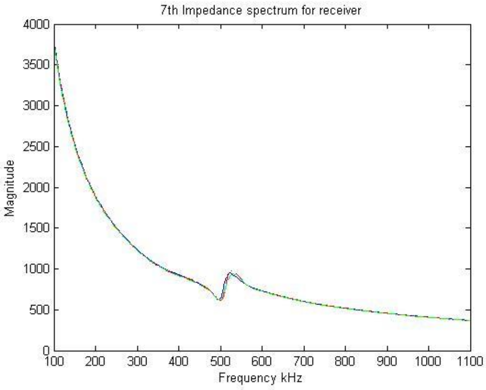
7th Impedance spectrum for receiver
Magnitude
Frequency kHz
0
500
1000
1500
2000
2500
3000
3500
4000
100
200
300
400
500
600
700
800
900
1000
1100

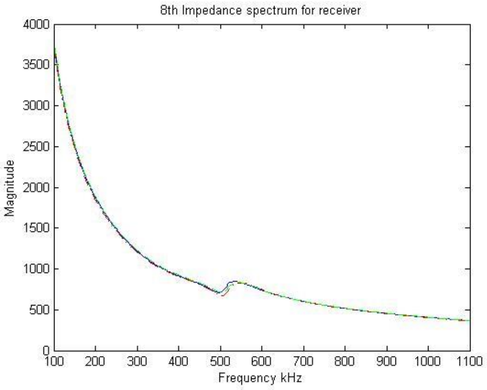
8th Impedance spectrum for receiver
Magnitude
Frequency kHz
0
500
1000
1500
2000
2500
3000
3500
4000
100
200
300
400
500
600
700
800
900
1000
1100

Appendix H

Focal law calculation process example for the ring #1 with multi materials in air path.

```
i=1;
t=1;
X1=0;
X2=0;
for x1=0:0.01:7.64; % rmiddle(n)
for x2=0:0.01:7.64;
T(i) =
1/5200000.*sqrt(13.52^2+x1.^2)+1/345000.*sqrt(x2.^2+36^2)+1/630000.*
sqrt(0.48^2+(7.64-x1-x2).^2);

if T(i)<t
    t = T(i);
    X1 = x1;
    X2 = x2;
end
i=i+1;
end
end
% plot (x1,x2,T);
% [tmin indmin]=min(T);
% X1 = x1(indmin)
% X2 = x2(indmin)
t = min(T)
Z=reshape(T,765,765);
mesh(Z)
X1
X2
xlabel ('X1 ( x10^-5 m)');
ylabel ('X2 ( x10^-5 m)');
zlabel ('t ( s)');
title ('total time ')
```

Appendix I

Each channel of the receiver will acquire the air-coupled signal at the same time and the post-processing applied in MATLAB as shown in Appendix I.

```
function [ Rfocalamplitud,RFocallaw,indexxx ] = inputthename( name )
%UNTITLED Summary of this function goes here
%   Detailed explanation goes here
g=0.6; % gap
Ts = 1/1250000;
Fs = 1250000;
% ------------------------------------------------------------------
-
for j = 1:1:30
    k=1;
    m = [0 0];
Distan = 68/1000:1/2000:123/1000;
for focpt = Distan;
n = 7; % number of rings -1
rimatrix = zeros(n,1) ; % matrix for ri value
romatrix = zeros(n,1) ; % matrix for ro value
rmiddle  = zeros(n,1) ; % matrix for the middle r
while  romatrix(n) - rimatrix(n)<0.9    % the out-most ring should
large than 1
ro=rimatrix(1)-g+0.1;
A= ro^2;
for i = 1:n
    ri = ro + g ;
    ro=(ri^2+A)^0.5;
    rimatrix(i) = ri ;
    romatrix(i) = ro ;
    rmiddle (i) =(ri+ro)*0.5 ;
end
end
r1 = rimatrix(1) - g;
time=1;
X1=0;
t(1)  = 1/345.*sqrt((focpt-0.65/1000).^2)+1/750.*sqrt((0.65/1000).^2);
for i = 1:n
for   x1=0:0.01/1000:rmiddle(i)/1000;
      T(i+1) = 1/345.*sqrt(x1.^2+(focpt-
0.65/1000)^2)+1/750.*sqrt((0.65/1000)^2+(rmiddle(i)/1000-x1).^2);
if T(i+1)<time
    t(i+1) = T(i+1);
    X1 = x1;
end
end
end

%---------------calculate focal law
for i=1:n
```

```
  TimDely(i)=t(8)-t(i);
end
TimDely(8)=0;
cloknum = fix(TimDely*Fs);
%---------------------------------------------------------------------
----------

for i = 100:1:3500
    a(i) = sum(name((j*8-7):(j*8),i));
end

for i = 100:3500
    c(i) = name(j*8-7,i-cloknum(1))+name(j*8-6,i-
cloknum(2))+name(j*8-5,i-cloknum(3))+name(j*8-4,i-
cloknum(4))+name(j*8-3,i-cloknum(5))+name(j*8-2,i-
cloknum(6))+name(j*8-1,i-cloknum(7))+name(j*8,i) ;
end

AA = max(a(100:3500));
CC = max(c(100:3500));
m(k,:) = [AA CC];
k = k+1;
end
% figure;
focpt = 1000*(Distan);
% plot (focpt,m(:,1));
% hold on
% plot (focpt,m(:,2),'r');
% plot (focpt,m(:,3),'b');
% hold off
indexx = find(m(:,2) == max(m(:,2)),1,'first');
RFocallaw(j) = focpt(indexx);

% figure;
% plot (c(100:3500));
% ylabel('1moveback');
% title('TRML Focallaw T:75mm R:best mm');
% set (gcf,'Position',[400,0,600,300], 'color','w');
% Rfocalamplitud(j) = peak2peak(c(100:3500));
end

for j = 1:1:30
    k=1;
    m = [0 0];
for focpt = RFocallaw(j)/1000; %focus distance 75mm 75mm 85mm
n = 7; % number of rings -1
rimatrix = zeros(n,1) ; % matrix for ri value
romatrix = zeros(n,1) ; % matrix for ro value
rmiddle  = zeros(n,1) ; % matrix for the middle r
while  romatrix(n) - rimatrix(n)<0.9    % the out-most ring should
large than 1
ro=rimatrix(1)-g+0.1;
A= ro^2;
for i = 1:n
    ri = ro + g ;
    ro=(ri^2+A)^0.5;
    rimatrix(i) = ri ;
    romatrix(i) = ro ;
```

```
    rmiddle (i) =(ri+ro)*0.5 ;
end
end
r1 = rimatrix(1) - g;
time=1;
X1=0;
t(1) = 1/345.*sqrt((focpt/1000-
0.65/1000).^2)+1/750.*sqrt((0.65/1000).^2);
for i = 1:n
for   x1=0:0.01/1000:rmiddle(i)/1000;
      T(i+1) = 1/345.*sqrt(x1.^2+(focpt/1000-
0.65/1000)^2)+1/750.*sqrt((0.65/1000)^2+(rmiddle(i)/1000-x1).^2);
if T(i+1)<time
    t(i+1) = T(i+1);
    X1 = x1;
end
end
end

%---------------calculate focal law
for i=1:n
  TimDely(i)=t(8)-t(i);
end
TimDely(8)=0;
cloknum = fix(TimDely*Fs);
%-------------------------------------------------------------------
----------

for i = 100:3500
    c(i) = name(j*8-7,i-cloknum(1))+name(j*8-6,i-
cloknum(2))+name(j*8-5,i-cloknum(3))+name(j*8-4,i-
cloknum(4))+name(j*8-3,i-cloknum(5))+name(j*8-2,i-
cloknum(6))+name(j*8-1,i-cloknum(7))+name(j*8,i) ;
end

end

Rfocalamplitud(j) = peak2peak(c(100:3500));
indexxx(j) = find(c(100:3500) == max(c(100:3500)),1,'first');
end

% figure;
% % % plot (RFocallaw);

end
```

Appendix J

The recent development of piezocrystals within (1-x)Pb(Mg1/3Nb2/3)O3-xPbTiO3 (PMN-PT) family provide a means of advancing both the bandwidth and imaging sensitivity simultaneously. The large electromechanical coupling (k_{33} ≈ 90%) and large piezoelectric charge coefficient (d_{33} > 2000 pc/N) of piezocrystals can result in improved resolution, higher SNR, and increased depth of view in NDT ultrasound imaging. The development of the transducer under test was aimed to explore the air-coupled inspection of piezocomposite materials by utilizing PMN-PT piezocrystal's high performances.

Frequency: Due to the increasing attenuation of sound in air with increasing frequency, air coupled transducers usually work at low frequencies <500 kHz. However, since there is a reverse relationship between piezo material layer thickness and operational frequency, operating at lower frequencies means the piezo material layer needs to be thicker. A typical 1-3 PMNPT-epoxy piezocomposite, with a VF of 50% would be around 2.3 mm thick to operate at 450 kHz. The thickness of the available bulk PMN-PT sample, 2 mm, has therefore limited the lowest frequency could be achieved to be 700 kHz.

Microstructure parameters: Piezocrystal needs to be in 1-3 piezocomposite form to take use of its high d_{33} and k_{33} advantages. Conventional dice-and-fill technique was used to fabricate the piezocomposite. Volume fraction (VF) Aspect ratio (AR, Pillar width / pillar height), and dicing kerf are the key parameters considered. All of them were determined taken into account the practical limits during manufacture. The predicted coupling coefficient k_t of the piezocomposite, representing transducer's sensitivity, is presented in fig. x against VF. Although there are only slight differences in kt between VF = 0.5 – 0.65, VF = 0.55 and AR = 0.3 were chosen as two criterions, the resulting pillar kerf is 167 um which can be easily and accurately obtained using existing dicing facility in CUE.

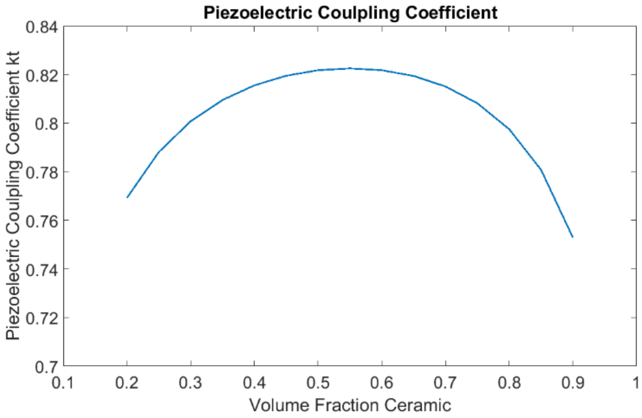

Ref: W.A. Smith et al "Modeling 1-3 Piezocomposite Piezoelectrics...",IEEE Trans UFFC, vol. 38, no. 1, pp. 40-47, 1991.

Transducer parameters for PMN-PT & medium set epoxy 1-3 piezocomposite

	PMN-PT & medium set 1-3 piezocomposite
Thickness	1.594 mm
Piezocomposite area	25 x 25 mm
Pillar width	0.476 mm
Polymer width	0.166 mm
Volume fraction	55%
Aspect ratio	0.298

Passive materials: The diced piezocrystal substrate was then filled with medium set epoxy. Although normally hard set epoxy filler with less loss is considered more suitable filler for this application, medium set was chosen due to the trade-off between limited existing sample thickness, 2 mm, and the final achievable operational frequency of the piezocomposite. The two parts of the epoxy, HY956EN/CY221 were mixed with a 5:1 ratio by weight, and then generally poured into the mould. The whole substrate was then cured under room temperature for 48 hours. The substrate was then lapped at both sides to explore the pillars.

The transducer was air backed, to maximize the energy output at the front of the transducer into air. This would make the transducer to be narrow banded, even though the material itself offers the potential to enlarge the operational frequency range.

Because of the fabrication caused variations, the finished 1-3 piezocomposites of PMN-PT have ARs of 0.27, resonance frequency of 720 kHz, and k_t of 0.758.

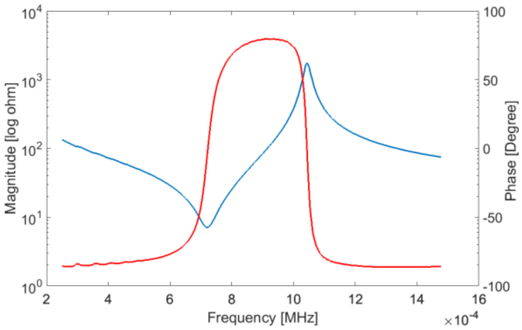

Appendix K

22 elements pre-amplifier design detail.

- First board (bottom board) with 12 pre-amplifiers AD8432

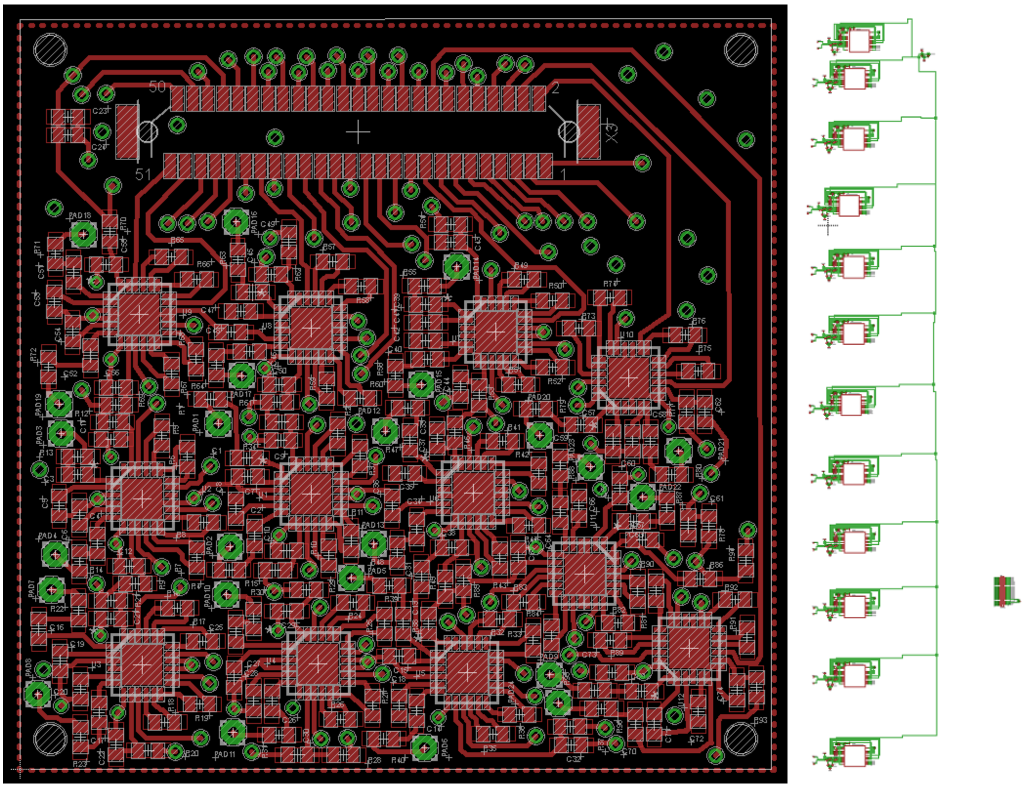

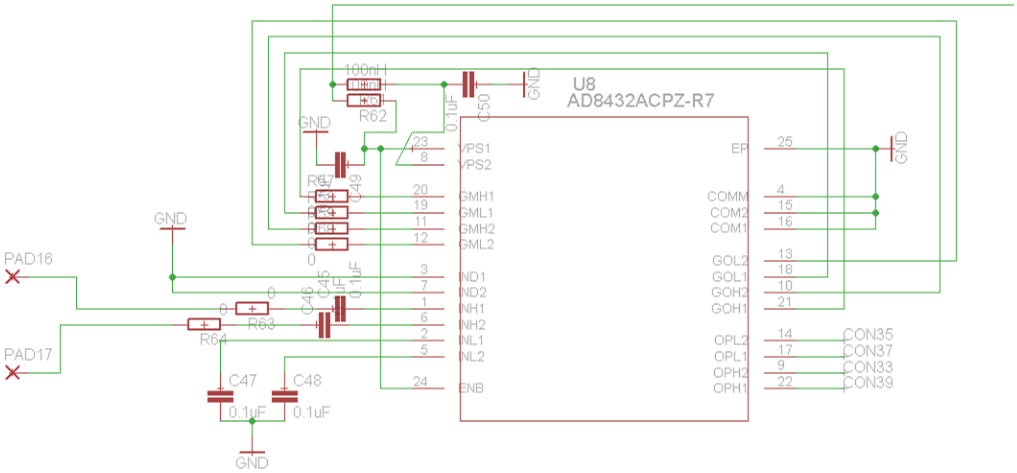

- Middle board with 22 receiver amplifiers (top layer and bottom layer)

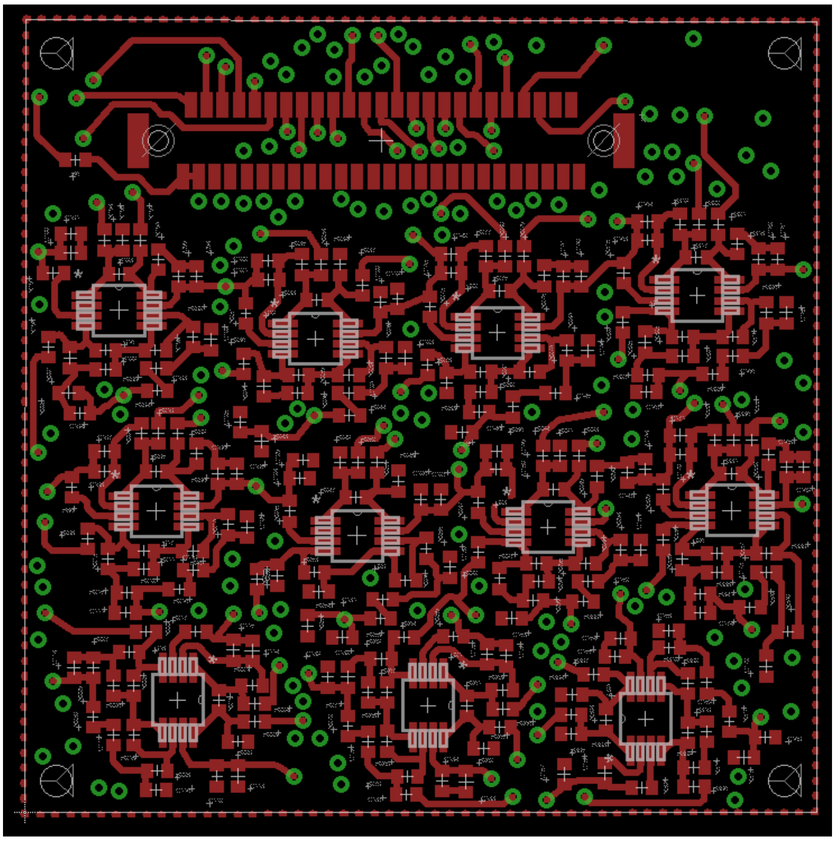

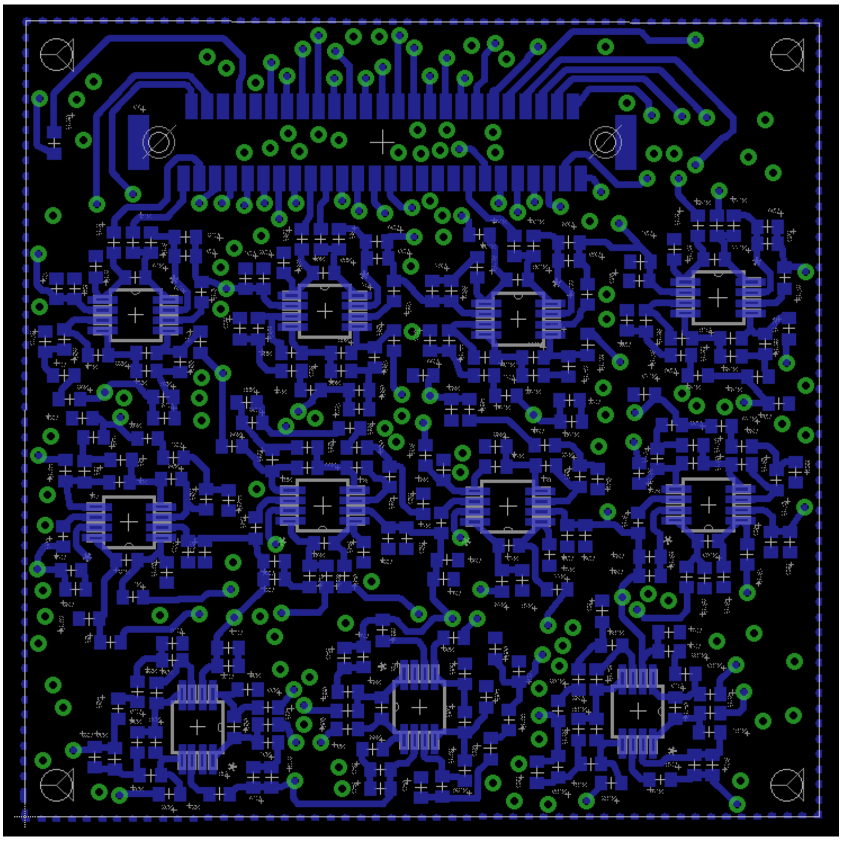

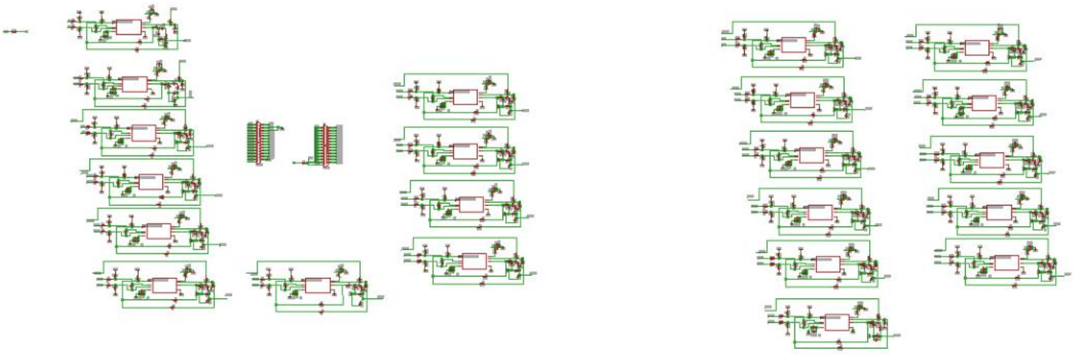

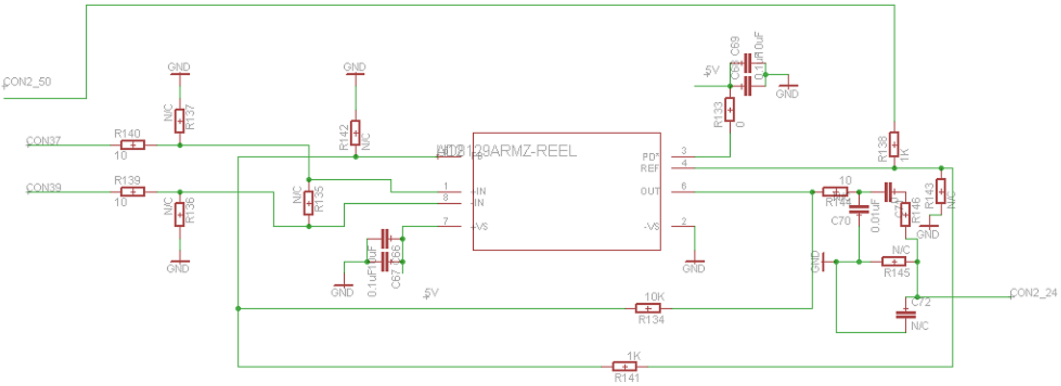
CON2_50
GND
GND
N/C
R137
R142
N/C
+5V
C68
C69
0.1uF
10uF
GND
R133
0
CON37
R140
10
CON39
R139
10
AD8129ARMZ-REEL
+VS
3
PD*
4
REF
R138
1K
1
+IN
8
-IN
N/C
R135
N/C
R136
7
-VS
6
OUT
10
R144
C70
0.01uF
C71
R146
R143
N/C
GND
2
-VS
GND
GND
GND
0.1uF
10uF
C67
C66
+5V
GND
N/C
R145
C72
N/C
CON2_24
10K
R134
1K
R141

- Third board (top board) which offer power supply

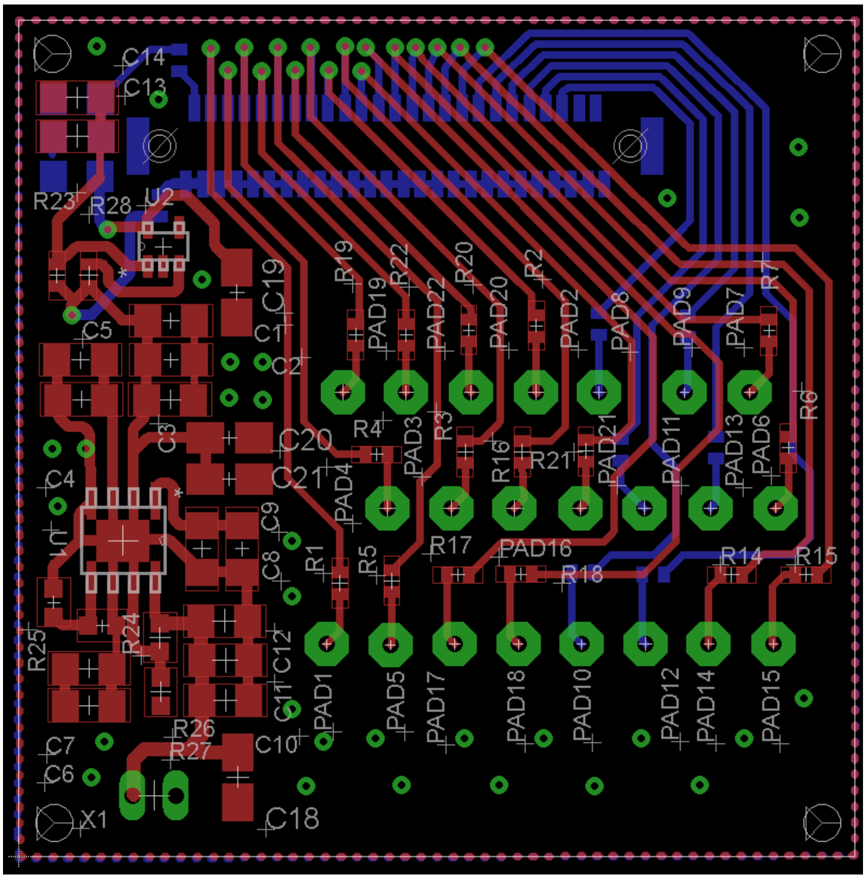

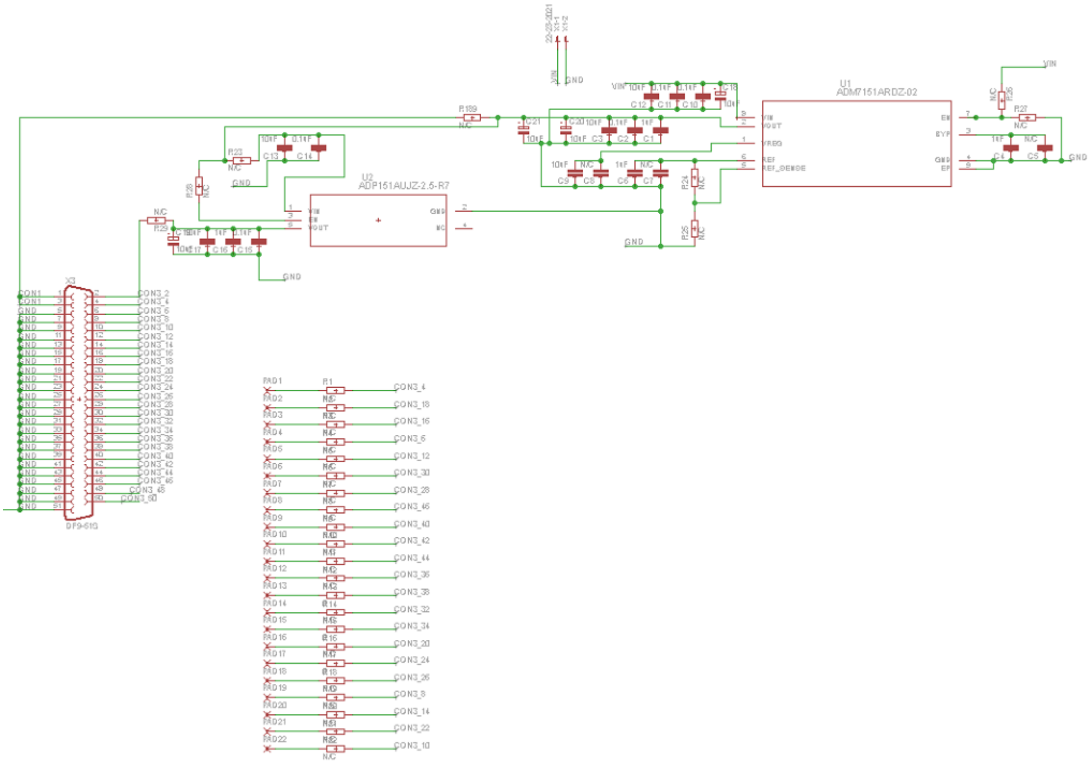

- First and middle board layout